TePA 2015

Proceedings of International Symposium

THUNDERSTORMS & ELEMENTARY PARTICLE ACCELERATION

Edited by

A. Chilingarian

Yerevan Physics Institute

Nor Amberd, Armenia

5-9 October, 2015

Proceedings of International Symposium

TEPA 2015

Thunderstorms and Elementary Particle Acceleration

Nor-Amberd, Armenia
October 5 - 9

Edited by A. Chilingarian

Cosmic Ray Division
Yerevan Physics Institute

INTERNATIONAL SCIENTIFIC ADVISORY COMMITTEE

Lightnings and Particle fluxes from the Thunderclouds

Thunderstorms and Elementary Particle Acceleration (TEPA-2015)

Yerevan, Armenia, 5-9 October 2015

The problem of how lightning is initiated inside thunderclouds is probably one of the biggest mysteries in the atmospheric sciences. Recently established high energy processes in the atmosphere, i.e. Terrestrial Gamma Flashes (TGF) – brief bursts of gamma rays observed by orbiting gamma ray observatories and Thunderstorm Ground Enhancements (TGEs) – sizable long-lasting fluxes of electrons, gamma rays and neutrons detected on Earth's surface are correlated with thunderstorms. However, the relationship among thundercloud electrification, lightning activity, and wideband radio emission and enhanced particle fluxes have not been yet unambiguously established. One of the most intriguing opportunities opened by the observation of the high-energy processes in the atmosphere is their relation to lightning initiation and propagation. Lightning discharges and TGEs are alternative mechanisms for the discharging of the atmospheric "electric engine" and synchronized observations of both phenomena help to understand them better.

With the objective to discuss these high-energy phenomena, the conference on Thunderstorms and Elementary Particle Acceleration was held at the Nor Amberd International Conference Center of the Yerevan Physics Institute (YerPhI) in Armenia. The Cosmic Ray Division of the YerPhI and Skobeltsyn Institute of Nuclear Physics of Moscow State University organized the workshop; YerPhI and the Armenian State Committee of Science sponsored it. Thirty scientists and students from the United States, Japan, France, Germany, Israel, Russia, and Armenia attended.

Presentations focused on observations and models of high-energy emissions in thunderclouds; on the termination of particle fluxes by lightning; multivariate observations of thunderstorms from the Earth's surface and from space; radio emissions produced by atmospheric discharges and particle fluxes;   the influence of the Extensive Air Showers (EASes) on lightning initiation and others.

Discussions covered questions such as the following: Do particle fluxes initiate lightnings? Do EASes help to unleash - CG lightnings? Are TGE and TGF currents competitive with the lightning current? What is a mechanism for the particle flux termination?

The workshop participants agreed that it would be useful to compare the vast amount of experimental data on TGEs observed in Armenia, Japan, Slovakia, Russia and USA in various conditions by different particle detectors to check the models of particle origin in thunderclouds. Armenian physicists suggested the location of sensors developed by other groups at Aragats Space Environmental Center (ASEC) where large TGEs are very frequent in spring and autumn.

With the installation of new fast electronics at Aragats it became possible to relate lightning initiation with fast waveforms of the electric field and with particle fluxes on the microsecond scale. Various particle detectors and fast electric field sensors now are synchronized by GPS receivers providing time stamps with accuracy not worse than a few tens of nanoseconds. The series of large TGEs were observed with renewed ASEC facilities during the workshop. The natural "electron accelerator" at Aragats has provided several interesting events, which was discussed extensively by participants. During the most interesting 7 October TGE particle fluxes and lightnings were synchronized on a millisecond time scale. On the one-second time scales the TGE termination looks like immediate ~10-fold drop of the 1-second count rate measured by large plastic scintillators. The detailed analysis of the 50-ms time series of the electrostatic field, fast waveforms of the electric field and particle fluxes reveals that the TGE decay started simultaneously with abrupt increase of electrostatic field ~200 ms after the return stroke of the lightning. Therefore, the declining of particle flux is connected with rearranging of charge centers in the cloud involving removal of the Lower Positive Charged Region (LPCR).

The presentation slides and discussion videos are available on the conference website, http://crd.yerphi.am/Conferences/tepa2015/home. More details can be found in the supplemental information in the online version of this meeting report. TEPA-2016 symposia is scheduled on October 3-7 in Nor Amberd international conference center.

A. Chilingarian

Table of Contents

Mount Aragats as a stable electron accelerator for atmospheric High-energy physics research

A. Chilingarian, G. Hovsepyan, E. Mnatsakanyan

A.Alikhanyan National Lab (Yerevan Physics Institute), 2, Alikhanyan Brothers, Yerevan 0036, Armenia

Abstract. The observation of the numerous Thunderstorm ground Enhancements (TGEs), i.e. enhanced fluxes of electrons, gamma rays and neutrons detected by particle detectors located on the Earth's surface and related to the strong thunderstorms above it helped to establish a new scientific topic - high-energy physics in the atmosphere. The Relativistic Runaway Electron Avalanches (RREAs) are believed to be a central engine initiated high-energy processes in the thunderstorm atmospheres.

RREAs observed on Aragats Mt. in Armenia during strongest thunderstorms and simultaneous measurements of TGE electron and gamma ray energy spectra proved that RREA is a robust and realistic mechanism for electron acceleration. TGE research facilitates investigations of the long-standing lightning initiation problem.

For the last 5 years we were experimenting with the "beams" of "electron accelerators" operated in the thunderclouds above the Aragats research station. Thunderstorms are very frequent above Aragats, peaking at May-June and almost all of them are accompanied with enhanced particle fluxes. The station is located on a plateau at altitude 3200 asl near a large lake. Numerous particle detectors and field meters are located in three experimental halls as well as outdoors; the facilities are operated all year round.

The key method employed is that all the relevant information is being gathered, including the data on the particle fluxes, fields, lightning occurrences, and meteorological conditions. By the example of the huge thunderstorm that took place at Mt. Aragats on the 28th of August 2015, we show that simultaneous detection of all the relevant data allowed us to reveal the temporal pattern of the storm development and to investigate the atmospheric discharges and particle fluxes

1. INTRODUCTION

The theoretical investigation of the high-energy processes in the atmosphere started 90 years ago by the Nobel Prize winner and creator of one of the first particle detectors C.T.R.Wilson (1924). Numerous papers published in recent decades by A.Gurevich, J.Dwyer, L.Babich, A.Lidvansky and co-authors (see citations to original publications in Dwyer, Smith, and Cummer, 2012) introduce the Runway Breakdown (RB), otherwise cited as Relative Runaway Electron Avalanches (RREA) as a central engine of the high-energy processes in the thunderstorm atmospheres. Measurements of particle fluxes on high mountains and in regions of Japan with low charge centers in thunderclouds prove the existence of particle fluxes that last up to a few tens of minutes correlated with thunderstorm activity (see details and references to original publications in review of Dwyer and Uman, 2014). The first detection of huge fluxes of electrons, gamma rays and neutrons on on Aragats in 2009 (Chilingarian et al., 2010) has unambiguously established a new physical phenomenon - Thunderstorm ground Enhancement – TGE, increased fluxes of electrons, gamma rays and neutrons detected by particle detectors located on the Earth's surface. The in situ observation of RREAs during strongest thunderstorms on Aragats (Chilingarian et al., 2011) and simultaneous measurements of TGE electrons and gamma ray energy spectra (Chilingarian, Mailyan and Vanyan, 2012) proved that RREA is a realistic and robust mechanism for electron acceleration in the atmosphere. In these publications, it was emphasized that lightnings, and TGFs are alternative mechanisms for the discharging of the atmospheric "electric engine"; there was also introduced the origin of the highest energy gamma photons - Modification of the Cosmic ray (CR) electron energy Spectrum (MOS) in the strong electric field of the thundercloud. Chilingarian and Mkrtchyan, 2012, emphasized the role of the transient Lower Positive Charge Region (LPCR) in electron-gamma

ray avalanche unleashing. Detailed measurements of the gamma ray energy spectra by large NaI spectrometers on Aragats (Chilingarian, Hovsepyan, Kozliner, 2013) allow to reliably extend the energy range of the "thunderstorm" gamma rays up to 100 MeV. All these results were obtained at the Aragats research station in Armenia during the last 5 years with "beams of electron accelerator" operated in thunderclouds above the research station. Aragats Space Environmental center (ASEC, Chilingarian et al., 2005) is located at an altitude of 3200 m on the plateau nearby a large lake and clouds usually are formed just above it (see Fig. 1).

Numerous particle detectors and field meters are located in three experimental halls as well as outdoors; the facilities are operated all year round. After understanding the TGE physics, we plan to apply this new evidence, i.e. fluxes of particles from the thundercloud, to approach the long-standing problems of lightning initiation and lightning leader propagation.

The key method employed is that all the relevant information is being gathered, including the data on the particle fluxes, fields, lightning occurrences, and meteorological conditions. By the example of the huge thunderstorm that took place at Mt. Aragats on the 28th of August 2015, we show that simultaneous detection of all the relevant data allowed us to reveal the temporal pattern of the storm development and to investigate the atmospheric discharges and particle fluxes. The paper is comprised of the following sections: instrumentation; chain of positive lightnings; chain of negative lightnings; small size TGE; and large size TGE. Thunderstorms are very frequent above Aragats, the peak activity being in at May-June and September-October. Almost all of them are accompanied with enhanced particle fluxes. In Fig. 1 we see an artistic view of multiple electron-gamma ray avalanches directed to the earth's surface and to the open space. The first ones originated TGEs regis-

tered by the ground based particle detectors; the second ones – originated Terrestrial gamma flashes (TGFs, Fishman et al., 1994) observed by the orbiting gamma ray observatories.
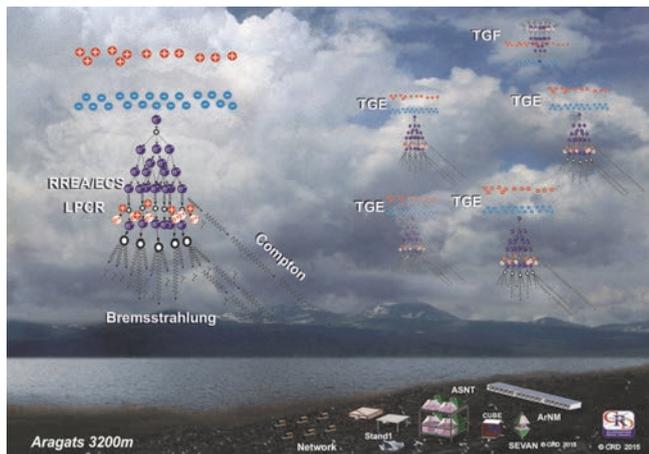

Figure 1. Artistic view of the multiple RREA cascades in the thunderstorm atmosphere directed to earth's surface (TGEs) and - to the space (TGF)

By analyzing a particular stormy day at Aragats, namely 28 August 2015, we will demonstrate the operation of the electron "accelerator" in the vicinity of the station and present the stages of our physical inference on the discovery of the new phenomenon of "Long TGEs" – lasting for several hours enhancements of low-energy gamma ray fluxes (0.4 - 2 MeV).

2. INSTRUMENTATION

The particle detectors of the Aragats Space Environmental Center (ASEC, Chilingarian et al., 2005) can measure the fluxes of the species of secondary cosmic rays (electrons, gamma rays, muons and neutrons), which have different energy thresholds. Numerous thunderstorm-correlated events, detected by the ASEC facilities, constitute a rich experimental set for the investigation of the high-energy phenomena in the thunderstorm atmosphere. The new generation of ASEC detectors consist of 1 and 3 cm thick molded plastic scintillators arranged in stacks and cubic structures (Chilingarian, Chilingaryan and G.Hovsepyan, 2015). The ''STAND1'' detector is comprised of three layers of 1-cm-thick, 1-m^2 sensitive area molded plastic scintillators fabricated by the High Energy Physics Institute, Serpukhov, Russian Federation see Fig. 2. The light from the scintillator through optical spectrum-shifter fibers is reradiated to the long- wavelength region and passed to the photomultiplier FEU-115M. The maximum of luminescence is emitted at the 420-nm wavelength, the luminescence time being about 2.3 ns. The STAND1 detector is tuned by changing the high voltage applied to PM and setting the thresholds for the discriminator-shaper. The threshold should be chosen to guarantee both high efficiency of signal detection and maximal suppression of photomultiplier noise. Proper tuning of the detector provides ~99% efficiency of charged particle detection. The data acquisition (DAQ) system counts and stores all coincidences of the detector channels. Coincidence ''100'' means that a signal has been registered in the upper detector only. This combination registered low- energy electrons with an efficiency of ~99%; the threshold energy of ~1 MeV is one of the lowest among all ASEC detectors.

The gamma ray detecting efficiency of this combination is about 2%. For the coincidence 010, the gamma ray

detection efficiency is increased to ~3% due to creation of the additional electron-positron pairs in the substance of the upper scintillator. Coincidence ''111'' means that all three layers register particles; the minimal energy of charged particles giving a signal in all three layers is ~10 MeV. With the same DAQ electronics are registered the time-series of a similar (but 3 cm thick) particle detector stand aside near the stacked structure.

Figure 2. STAND detector consisting of three layers of 1 cm thick scintillators.
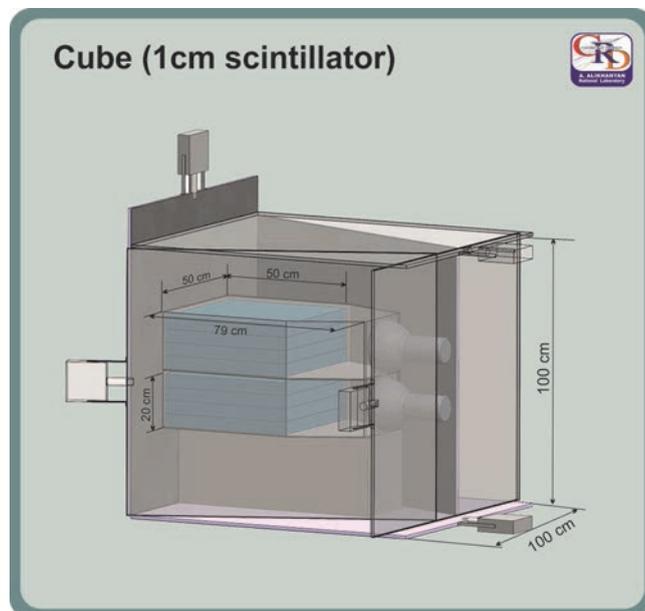
Figure 3. Cube detector; thick scintillators located inside are measuring neutral flux with purity ~98%.

Special experimental facilities were designed and installed at Aragats in order to separate electron and gamma ray fluxes. Two 20 cm thick plastic scintillators are surrounded by 1 cm thick molded plastic scintillators (see Fig. 3). Thick scintillators detect charged flux with a very high efficiency (~99%); they can also detect neutral flux with an efficiency of ~20%. Thin scintillators also detect charged flux with very high efficiency (~99%), though the efficiency of detecting neutral flux is highly suppressed and equals 1%–2%. Thus, using the coincidences technique, it is possible to purify the neutral flux detected by inside scintillators, rejecting the charged flux by the veto signals from surrounding thin scintillators. The calibration of the cube detector proves that the veto system (preventing the counting signal in the thick scintillator if there is a signal in at least one of the six surrounding thin scintillators) can reject 98% of the charged flux (see details in Chilingarian, Mailyan and Vanyan, 2012).

The histograms of the energy deposits in the two inner thick scintillators are stored every minute. The one-minute count rates of the surrounding 6 scintillators are measured and stored as well.

The detector network measuring particle energy consists of four NaI crystal scintillators packed in a sealed 3-mm-thick aluminum housing. The NaI crystal is coated by 0.5 cm of magnesium (MgO) by all sides (because the crystal is hygroscopic) with a transparent window directed to the photocathode of a FEU-49 photomultiplier (PM), see Fig. 4.
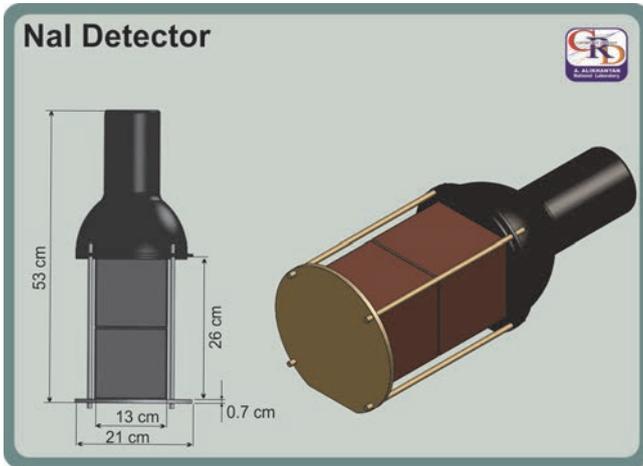
Figure 4. NaI(Tl) crystal assembly.

The large cathode of FEU-49 (15-cm diameter) provides a good light collection. The spectral sensitivity range of FEU-49 is 300–850 nm, which covers the spectrum of the light emitted by NaI(Tl). The sensitive area of each NaI crystal is ~0.0348 m^2; the total area of the four crystals is ~0.14 m^2; the gamma ray detection efficiency is ~80%. A logarithmic analog-digit-convertor (LADC) is used for the coding of PM signals. Calibration of LADC and code-energy conversion was made by detecting the peak from exposed 137Cs isotope emitting 662 keV gamma rays and by high-energy muon peak (55 MeV) in the histogram of energy releases in the NaI crystal. The PM high-voltage was tuned to contain both structures (peaks) in the histogram of LADC output signals (codes) and to ensure linearity of LADC in the energy region of 0.4 - 60 MeV. The detailed description of other ASEC detectors including charts with all sizes is available from the WEB site of the Cosmic Ray Division of Yerevan Physics Institute: http://crd.yerphi.am/ADEI in the WIKI section of the multivariate visualization platform and from (Chilingarian et al., 2010, Chilingarian, Chilingaryan, and Reymers, 2015).

The count rate of a particle detector depends on the chosen energy threshold of the shaper-discriminator, size of the detector and on the amount of matter above it. The inherent discrepancy of the parameters of PMs also can add ~ 15% difference to the particle detector count rates. Significant amount of substance above the sensitive volume of NaI crystals (0.7 mm of roof tilt, 3 mm of Aluminum and 5 mm of MgO) prevents electrons with energy lower than ~3-4 MeV to enter the sensitive volume of the detector. Thus, the network of NaI spectrometers below 4 MeV can detect gamma rays only.

The small sizes of the NaI crystals and short duration of TGE pose a limitation on the lowest gamma ray flux that can be reliably observed. The usual requirement on the minimal amount of particles in a histogram bin is >5; therefore, the minimal flux that can be reliably detected by the NaI network should be above 200 per minute per m^2 (the

area of 4 crystals is 0.14 m^2 and required number of particles in 4 crystals above 20). For smaller fluxes fluctuations overwhelm the signal.

The significance of detecting peaks in the time series of the particle count rates is determined by the p-values of the peak significance test, i.e. by the value of the peak divided by the standard deviation of count rate (number of standard deviations contained in the peak, Nσ). The p-value is the most comprehensive measure of the reliability of detecting peaks in a time series. Large p-value corresponds to small chance probabilities that the observed peak is a background fluctuation and not a genuine signal. Therefore, we can safely reject the null hypothesis (back- ground fluctuation) and confirm the TGE. Very large p-values not only prove the unambiguous existence of a particle flux from the cloud, but also serve as a comparative measure of the TGE observations using different detectors.

The deep negative near-surface electric field is a necessary condition for the TGE origination. Moreover, the observed changes of the electric field, along with detected particle fluxes encompass information on the dynamics of the cloud electrification, which is very difficult to acquire by in-situ measurements. A network of three electric mills continuously monitors the disturbances of electric field on Mt. Aragats. Electrical mill EFM 100 produced by Boltek Company operates with 20 Hz frequency performing 20 measurements of the near-surface electric field per second. Comparisons of electric field strengths obtained by the three identical EFM-100 electrical mills prove reliability and high accuracy (discrepancy of device readings do not exceed 10%) of electric field measurements.

3. SERIES OF POSITIVE LIGHTNINGS AT ~ 12:00 – 13:00

On 28 August, almost all day long, the thunderstorms at Aragats were accompanied with numerous nearby lightnings and several episodes of the enhanced particle fluxes registered by the detectors located at ASEC.

The network of NaI spectrometers had detected an enhanced flux of low energy gamma rays with several episodes of abrupt bursts, as it is shown in Fig. 5. In spite of the fact that the NaI crystals are much smaller than the plastic scintillators, due to the low energy threshold (0.4 MeV) and higher efficiency to register gamma rays the count rate of each of the four spectrometers are higher than the counts of larger plastic scintillators. The ~15% discrepancy of the count rates of the four spectrometers are explained by the differences in PM parameters. This discrepancy does not influence the amplitude of TGE (peak value of the count subtracted by background value), which is the same for all 4 spectrometers.

The matter above the sensitive volume of NaI spectrometer absorbs electrons with energies below 3 MeV. Thus, registration of gamma rays below 0.4 MeV is only feasible; sure the detection of electrons of the higher energy is possible. In Fig. 5 we can see that the time series of CUBE detector (a 20-cm thick detector located inside the veto housing; energy threshold ~4 MeV) demonstrate enhancement only around 23:20 when, as we will see later the gamma ray flux exceeded 4 MeV due to presence of the bremsstrahlung gamma rays from the runaway electrons. The STAND1 detector (energy threshold ~ 1MeV) showing a flux enhancement coherent to NaI at a smaller scale had also demonstrated a pronounced peak around 23:20.

For recovering electron and gamma ray intensity in the TGE flux at energies above 4 MeV we use data from CUBE detector vetoing the charge flux.

Due to the small sensitive area of NaI spectrometers, we can recover differential energy spectra at energies above ~10^3/m²min, equivalent to 5-10 registered particles in an energy bin. Histograms of the energy releases in NaI crystals are collected and stored each minute; therefore we can recover 1440 energy spectra daily. To achieve better statistical accuracy, we use the data from all 4 spectrometers and combine several minutes around the peak values of the count rate. The energy spectra were recovered, according to the methodology described in (Chilingarian et al., 2007) for 4 TGE episodes at 14:49 -14:52; 16:37-16:44; 23:18-23:21 and 23:29-23:31. The relative enhancement was calculated by subtracting from the peak value of the count rates the background measured just before the enhancement started. Only the relative enhancement in measurements with NaI crystals has physical meaning in the described series of measurements. The NaI spectrometers were located just below the iron tilts of the roof. In August at Aragats, the sun is extremely strong and the temperature under the iron roof reached 50-60 C°. The high temperature influenced DAQ electronics and, respectively, the detector count rate increases at peak temperatures up to 10% as compared with nighttime count rate when the temperature drops down to 5-10 C°. Therefore, though the maximal absolute count rate was achieved at ~15:00, the TGE at 23:20 has larger amplitude and was much more significant; it could be explained by the bremsstrahlung gamma rays emitted by the runaway electrons in the thundercloud just above the detectors.
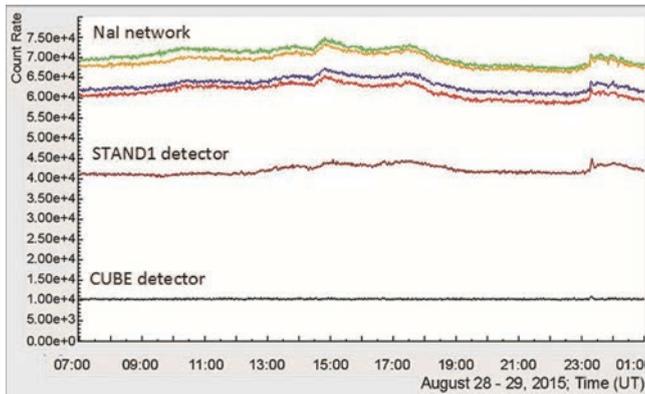

Figure 5. One-minute count rates of the network of 4 NaI spectrometers. TGE at 23:18-23:21 contain high energy gamma rays detected by all ASEC particle detectors.

The electric field disturbances at 28 August 2015 were prolonged and deep reaching -35 kV/m; lightning activity was strong and some of the lightnings were within 5 km from the station. Numerous positive lightnings that started at ~8:00 stipulate small disturbances of the near-surface electric field. The network of three EFM-100 electric mills measured the near-surface electric field. The devices operated according to the "atmospheric electricity" sign convention (a positive electric field at ground is produced by positive charge overhead and negative electric field on the ground is produced by negative charge overhead). Thus, the recorded positive field change corresponds to negative lightning, which decreases the negative charge overhead and negative field change corresponds to positive lightning, which decreases the positive charge overhead. The heavy-duty storm that started at ~12:00 was followed by copious positive lightnings lasting until ~13:00 (Fig. 6). In Fig. 6 we show the electric field disturbances measured by the elec-

tric mill located on the roof of MAKET building, the corresponding distance to the lightning and one-second time series of 1 m² plastic scintillator. The spikes in the particle count rates are due to the showers hitting the scintillator. In one-minute time series they are smoothed by integration over 60 seconds, but in 1-second time series spikes are visible.
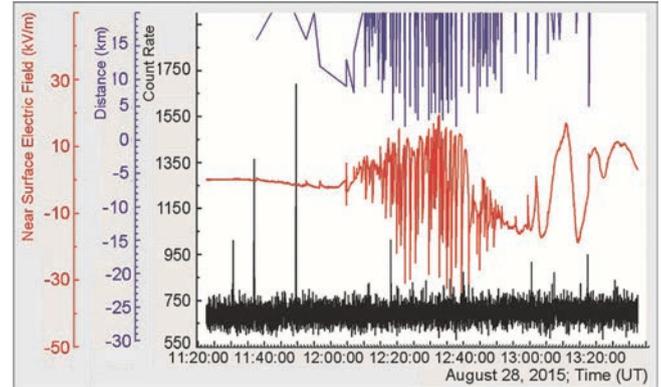
Figure 6. Positive lightnings series observed at 28 August 2015, 12:00 – 13:00; the top lines – distance to lightning, the middle curve – disturbances of near surface electric field; in the bottom – 1-second time series of count rates of 3 cm thick and 1 m² area plastic scintillator.
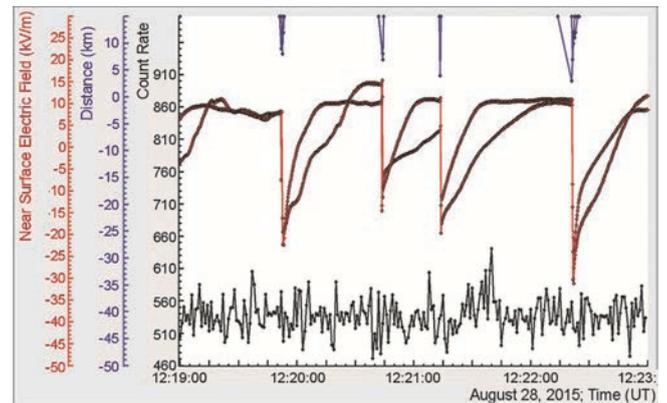
Figure 7. One episode of positive lightning series observed on 28 August 2015 at 12:00 – 13:00; the top lines – distance to lightning, the middle 2 curves – disturbances of near surface electric field measured by electric mills located at a distance of 300 m from each other; in the bottom – 1-second time series of count rates of 3 cm thick and 1 m² area plastic scintillator.

In Fig. 7 we show four minutes of stormy weather matched with 4 positive lightnings (zoomed from Fig. 6).

The pattern of rapid decrease of the electric field was approximately the same for both electric mills located at a distance ~300 m from each other. The abrupt decrease of the near-surface electric field followed by relatively slow recovery indicates the neutralization of a positive charge in the thundercloud. However, the operation of the charging engine permanently recovers the positive charge region in the thundercloud. In Tab. 1 we post the characteristic of 4 positive (+CG) lightnings from ~100 that occurred on 28 August 2015; in the end of an hour-long series of positive lightnings they changed to the negative ones.

From Tab. 1, where we present the main characteristics of the lightnings shown in the previous Figure we can outline typical features of the positive cloud-to-ground lightning that occurred on Aragats on 28 August 2015:

1. Mean electric field before the start of the lightning ~ 8-15 kV/m;

2. Typical values of the drop of electric field ~ -30 - -40 kV/m.

3. After reaching its minimum, the near-surface electric field slowly returned to the pre-lightning values due to continuous charge separation processes in the cloud in 21-31 seconds;

4. Time from the start of electric field sharp decrease till its minimum was ~ 0.1 – 0.65 sec;

5. Distance to lightning was ~ 3-8 km.

Rather large amplitude of the positive lightning field changes (-30 - -40 kV/m) achieved in time less than 1 sec and large recovery time of electric field (tens of seconds) indicates strong discharge processes at nearby distances (10 km). Several high masts are located near the station, from their tops the electron streamers can propagate to the positive charge regions in the thunderclouds above. As usual during a series of positive lightnings no enhancements of particle flux were registered.

The strong rain that started at 13:22 stopped at 14:00. The temperature started to rise from 4 C° at 13:00 till 6 C° at 14:30 and then abruptly dropped till 3.4 C° at 14:50 UT. The relative humidity decreases from 95% at 13:00 till 75% at 14:30.

Electric field was in negative domain - 8 till - 24 kV/m; few lightnings were detected. At 14:30 the gamma ray flux started to rise, reaching maximum at 14:50. The differential energy spectrum of the gamma ray flux is shown in Fig. 8. We fit the energy spectrum with 2 power law dependences; the point where interpolating dependence is changed usually is named the "knee". Knee position is located at ~1 MeV

and is rather smooth. The energy spectrum extends to~ 2 MeV and then fast decays.

$$I_{TGE} = (1.12 \pm 0.05) \, 10^4 E^{-(1.2 \pm 0.07)}$$
$$I_{TGE} = (1.43 \pm 0.14) \, 10^4 E^{-(4.68 \pm 0.18)}$$

28 August 2015
14:49 - 14:52
all det. NaI
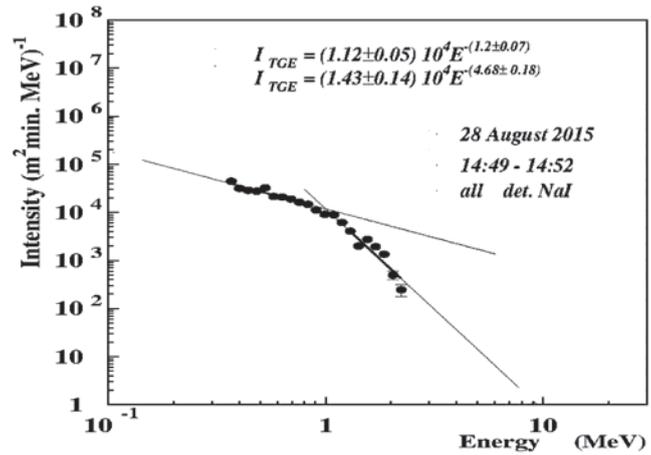
Figure 8. The differential energy spectrum of sum of 4 NaI spectrometers; the background was measured just before the TGE started. Flux intensity - 0.18x10⁵/m²min; knee position 0.9 MeV; intensity after knee 0.50x10⁴/m²min.

Next hour the lightning activity became stronger, see Fig. 9; however, the atmospheric discharges were far from the Aragats station and, therefore, the amplitudes of the near surface electric field disturbances were small, as it is seen in Tab. 2. The relative humidity (RE) successively increased from 75% at 14:30 to 92% at 15:45 when the rain resumed. At the same time, the wind speed decreased from 2 m/sec to 0.2 – 0.6 m/sec and the temperature decreased from 3.4C° till 2.9 C°.

Table 1. Main characteristics of a sample of lightning occurrences at 12:19 – 12:23 28 in August 2015

Start of Lightning (UT) and el. field value (kV/m)	Time of el. field mTime of el. field minimum (UT) and field minimal value (kV/m)	Duration (sec)	Recovering (sec)	Drop of el. field	Dist. (km)	WWLLN time	WWLLN dist.
12:19:52.18	12:19:52.75 -23	0.65	21	-31	8		
12:20:43.7 15	12:20:43.8 -18	0.1	29	-33	7		
12:21:13.8 10	12:21:14.0 -20	0.2	23	-30	4		
12:22:21.3 10	12:22:21.8 -30	0.5	31	-40	3		
12:51:31.15 -14	12:51:31.55 -8	0.4	29	6	8	12:51:31.23 - 12:51:31.47	5-9

4.   SERIES OF NEGATIVE LIGHTNINGS
AT ~ 15:00 – 16:00

After 15:00, as we can see from Fig. 9 and the Tab. 2, the pattern of disturbances of electric field drastically changed as compared with the ones registered 2 hours before (Figs 6 and 7). The lightning locations were 10-20 km from the station (confirmed by WWLLN, see last column of Tab. 2). Therefore, the amplitude of disturbances of the near surface field was small – 3-7 KV/m. Lightnings were mostly negative, i.e. the large amount of negative charge overhead was decreased.

No TGEs were detected. The spike in 1-sec time series of plastic scintillator was due to the particle shower that hit the detector at 15:07:23.

The illustration of the 3 seconds of time series of near-surface electric field, revealing the pattern of an unusual lightning that occurred at 15:59:54.4 - 15:59:55 is given in Fig.10. In 0.6 seconds the negative discharge (abrupt enhancement of the electric field) with amplitude 3 kV/m suddenly turned to a positive one (abrupt decrease of the electric field) with amplitude -7 kV/m (see also Tab. 2).
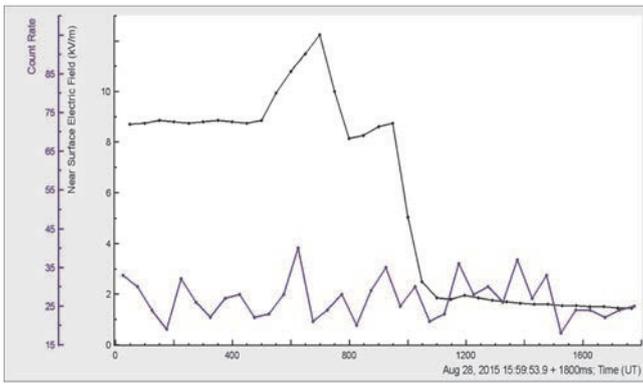
Figure 9. Multiple negative lightnings detected at 14:45 – 16:30; the top lines – distance to lightning, the middle curve – disturbances of near surface electric field; in the bottom – 1-second time series of count rates of count rates of 3 cm thick and 1 m² area plastic scintillator.
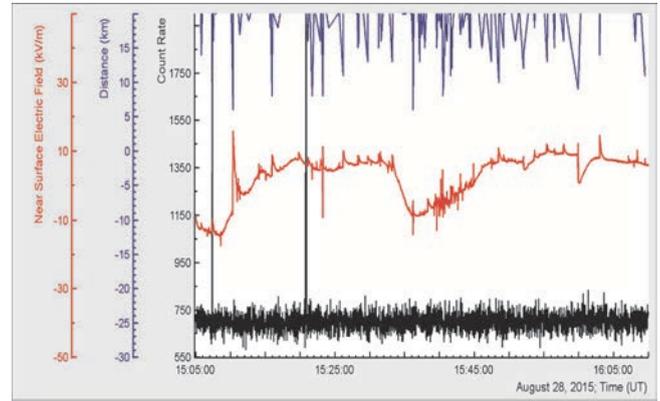

Figure 10. Disturbance of near surface electric field demonstrate starting negative discharge suddenly turned to positive one; in the bottom – 50 msec time series of 3 cm thick 1 m² area outdoor plastic scintillators.

Table 2. Main characteristics of a sample of lightning occurrences at 15:38 – 16:03 28 in August 2015

| Start of Lightning (UT) and el. field value (kV/m)	Time of maximum (UT) and maximum value (kV/m)	Dura-tion (sec)	Reco-vering (sec)	Drop of el. field	Dist. (km)	WWLLN time	WWLLN dist.
15:38:21.8 -7	15:38:22.7 -4	0.9	32	3	14	15:38:22.41	21
15:53:39.4 7	15:53:40.3 (15:53:39.9) 10	0.9	41	3	18	15:53:39.5	14
15:59:54.4 9	15:59:54.6 12	0.2	0.1	3	9	15:59:54.32	14
15:59:54.85 9	15:59:55.0 2	0.15	-	-7	20	15:59:54.34	8
16:03:01.05 8	16:03:01.55 15	0.5	27	7	13,15	16:03:01.0 – 16:03:01.86	11-21

5.   SMALL SIZE TGE WITH MAXIMUM AT ~ 16:40
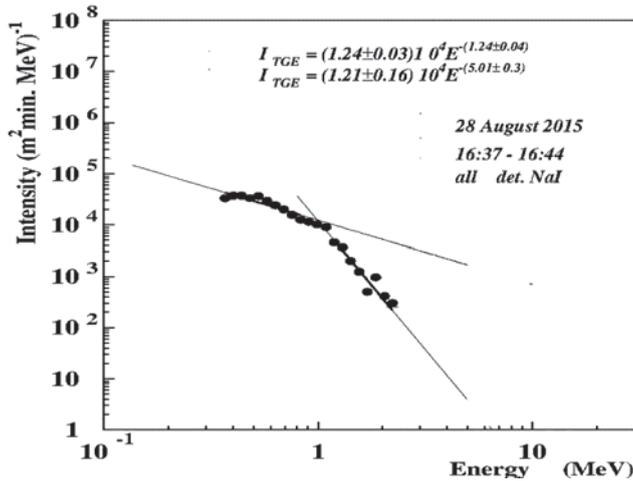
Figure 11. Differential energy spectrum of the "small size" TGE. Flux intensity - 0.95x104/m2min; knee position - 0.9 MeV; intensity after knee - 0.25x104/m2min.

At 16:20 electric field moved to negative domain and at 16:43 dropped to -23 kV/m. Between 16:36 and 16:43 at the large negative electric field there appeared several small "bumps" with an amplitude of less than 5 kV/m. During that "bumpy" time (16:37-16:44) several ASEC particle detectors registered TGE. The intensity of the event was 2 times less than previous TGE see Fig. 11. The "knee" position is analogous to the previous spectrum and the change of interpolating power law function is smooth too. Energy spectrum is continuing till ~ 2 MeV.

The relative humidity (RE) was 92-95% during TGE (high RE is another necessary condition to unleash large TGE) and wind speed was ~1 m/sec. The temperature started to fall at 16:26 from 3.5 C° dawn to 2.9 C° during TGE. Wind direction was 180° N. It stopped raining at 16:27 and resumed at 17:00. Consequently, there was no rain during TGE.

6.   LARGE TGE OCCURRED AT ~ 23:18-23:21

Disturbances of electric field and lightnings prolongs till 17:30, rain till 22:00. After rain stopped electric field start to decrease at 23:00 reaching -28 kV/m at 23:21. The relative humidity (RE) rose from 89% at 23:14 till 92% at 23:17 and remain constant till 23:23. Wind speed abruptly increased from 0 at 23:13 till 7.5 at 23:19, and then increased down to 1 m/sec at 23:23. The temperature started to decrease at 23:13 from 3.9 C° reaching 0.8 C° at 23:23. Wind direction was 200N. The TGE flux reaches maximum at 23:19; energy spectra of TGE extends till 6 MeV, see Figure 12. TGE event duration is ~ 10 minutes; intensity and maximal energy – largest on 28 August. Knee position shifted to 1.12 MeV and knee is sharper than in previous TGEs cconsidered on 28 August 2015.

The veto system of the CUBE detector rejected most of the charged particles by six 1 m² area and 1 cm. thick plastic scintillators shaped in a cubic structure. The located inside two 0.25 m² area and 20 cm thick scintillators with the veto system switched on, registered neutral particles. The CUBE detector with two inner 20 cm thick plastic scintillators with energy threshold ~4 MeV had also demonstrated pronounced peaks (Fig 13). Fig. 13 does not show the time

series of the count rates itself, but the time series of the p-values of the peak significance test. The large p-values of peaks observed by 2 inner 20 cm thick scintillators of CUBE detector allows to estimate charged and neutral fluxes of TGE above ~4 MeV (NaI spectrometers allow to measure pure gamma ray flux below 3-4 MeV and mixed flux above 3-4 MeV).
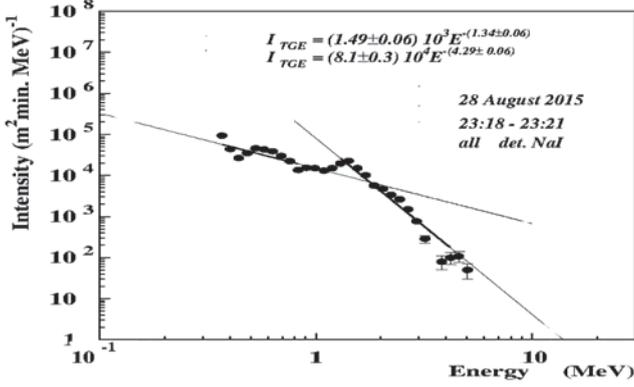

Figure 12. Differential energy spectrum of TGE obtained by 4 NaI spectrometers; Flux intensity - 0.34x10⁵/m²min; knee position – 1.2 MeV; intensity after knee - 0.17x10⁵/m²min.
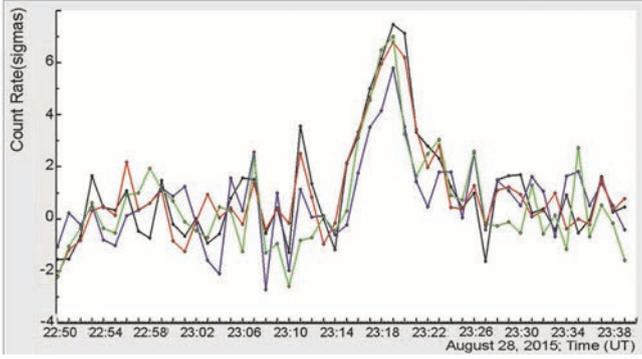
Figure 13. TGE observed by the CUBE detector's two stacked 20 cm thick plastic scintillators with and without veto system switched on.

From the Tab. 3 we can see that at 23:19 the CUBE scintillators registered maximal count rate; for that minute we calculate the electron and gamma ray intensities incident on the CUBE detractor.

Due to non-zero probability of electrons to miss registration in the 1-cm thick plastic scintillator of the veto system, and due to non-zero probability for the detection of the gamma ray by the same scintillator, we have made corrections to recover intensities (see details in Chilingarian, Mailyan and Vanyan, 2012). However, these corrections are below ~2% as compared with calculation of the gamma ray intensity directly from the amplitude of the peak observed by the thick scintillator with the veto switched on (538 counts). The intensity of gamma rays above ~4 MeV

is ~10^4/m²min; and the intensity of electron flux – $8x10^2$/m²min. Thus, the fraction of electrons at energies above 4 MeV does not exceed ~ 7%.

Table 3 Count rate of 20 cm thick plastic scintillator with and without veto (minutes after 23:00 UT)

28 August (UT)				
23:16	10548	8614	4526	3577
23:17	10736	8749	4633	3647
23:18	10853	8797	4735	3739
23:19	**10990**	**8923**	**4802**	**3764**
23:20	10954	8750	4755	3585
23:21	10564	8589	4534	3507
23:22	10508	8516	4418	3548
23:23	10459	8617	4484	3575

In Tab. 4 we show the mean values of count rate, the peak value, amplitudes of the peaks (also in the number of standard deviations); and calculated intensities (integral spectra) of gamma ray and electron flux above ~4 MeV. We assume the efficiency of gamma ray detection by 20 cm thick scintillator to be equal 20% and detection of electrons 99%.

The efficiency of detecting gamma rays by the "veto" 1-cm thick scintillators is 2% and electrons – 99%. Particles to be registered in the bottom thick scintillator (see Fig. 3) should traverse through the upper one therefore due to attenuation of the particle flux intensities measured by the bottom scintillator are significantly lower.

After the decline of TGE at 23:23 the low energy particle flux measured by NaI spectrometers remained high. However, the conditions required for unleashing large TGE did not last and energy spectrum measured at 23:39 - 23:41 contained only low energy particle (see Fig.14).
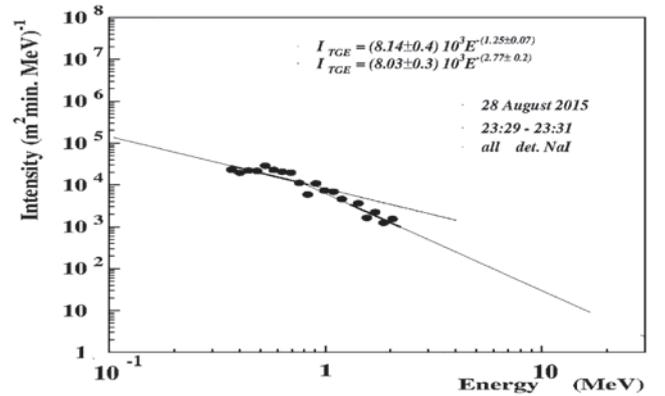
Figure 14. The differential energy spectrum of sum of 4 NaI spectrometers measured after large TGE. Entire intensity 0.21x105/m²min; knee position –1.2 MeV; intensity after knee 0.4x104/m²min.

Table 4. Calculated intensities of TGE electron and gamma ray fraction; threshold 4 MeV

Name	Mean	σ	23:19 peak	TGE -ΔN (Nσ)	e intensity (1/m²min)	γ intensity (1/m²min)	e/ γ
Cube 7	10258	108	10990	742 (6.9)	800	10920	7.3%
Cube 8	8494	81	8923	429 (5.3)	368	6768	5.4%
7 with veto	4294	79	4802	538 (6.8)	-	-	-
8 with veto	3431	47	3764	333 (7.1)	-	-	-

7. DISCUSSION AND CONCLUSIONS

The model of TGEs can be formulated briefly as follows (Chilingarian, 2014): electrons from the ambient population of the cosmic rays (CR) are accelerated downward (towards the Earth) by the positive dipole formed by the main negatively charged layer in the middle of the cloud and a transient lower positive charge region in the bottom of the cloud. In very strong electric fields the energy gained from the field surpasses the electron energy losses in the atmosphere and the intensive process of the electron multiplication and acceleration initiate large particle avalanches reaching and being registered on the earth's surface (TGE). If the strength of electric field is not enough to discharge RREA, nonetheless the energy of an electric field is transferred to the electrons changing their energy spectrum and enhancing the probability of bremsstrahlung (MOS process). Both MOS and RREA processes have been experimentally observed at Aragats high-mountain research station in good agreement with simulations (Chilingarian, Mailyan and Vanyan, 2012). Recently as well intense fluxes of gamma rays were measured by the airborne detector near the end of a downward RREA, consistent with another positive dipole - occurring between the upper positive charge layer and the negative screening layer above it (authors name it "gamma glows" Kelly et al., 2015).

However, in our previous publications we consider TGE events, mostly large ones, when the RREA was unleashed just above the detector site during several minutes. In this paper, we consider data collected on a whole day of 28 August 2015. The day was stormy, electric field disturbances continuous, lightnings enormous and the electron accelerator above provided evidence on several long, low

According to the model of TGE initiation (Chilingarian, 2014) the intense RREA process in the cloud originates bremsstrahlung photons that follow the passage of electrons. The electrons from the ambient population of secondary cosmic rays were accelerated up to energies 30-40 MeV. The size of LPCR does not extend more than 1 km therefore high-energy bremsstrahlung photons illuminate the earth's surface only locally under the thundercloud. The Compton scattered photons of lower energy due to much broader angular distribution can illuminate much larger surface under a cloud. Only on a few occasions when the emitting region is above the detector site we register large TGE with maximal energies above 3-4 MeV. These episodes are usually short because the wind moves the cloud relative to particle detector location. The Compton scatter photons can reach the detector site from several RRE avalanches periodically emerging in the large thundercloud for the much longer time, see Fig. 1. The position of the knee at ~1-1.2 MeV supported our assumption. Intensity of gamma rays with energies above pair production threshold (1.022 MeV) should be abruptly decreased due to catastrophic energy losses of the electrons and positrons in the atmosphere.

In this event, the flux of >10 MeV gamma rays was the highest energy part of the bremsstrahlung photons that are emitted by electrons accelerated to a few tens of MeV. As known from the bremsstrahlung cross-section, such photons, with energies close to that of primary electrons, are projected forward in a narrow cone. In addition, such high-energy photons undergo less Compton scatterings than lower energy photons that tend to be spread over a wide area. Therefore, it is likely that the extent of the >10 MeV gam-

energy TGEs and intensive and energetic enhancements. For the first time we describe and analyze not only isolated TGE events, but also the whole temporal history of the long duration thunderstorm, including high and low energy TGEs, periods of positive and negative lightnings, meteorological conditions, disturbances of the near-surface electric field. Our recent measurements reveal a meaningful relation between TGEs and lightnings (Chilingarian et al., 2015). Scrutinizing a particular stormy day at Aragats we demonstrate operation of the "moving electron accelerator" generated high-energy (up to 6 MeV) bremsstrahlung gamma photons when RREA was above the station and low energy (0.4– 2 MeV) Compton scattered gamma rays when a strong electric field moved from the station.

NaI spectrometers registered totally additional (compared to the fair weather day) ~1.8 million gamma rays. TGE differential energy spectra were estimated by the network of the NaI spectrometers for 4 TGE episodes. Three of them contain only low energy gamma rays with energies below 4 MeV, large TGE with maximal flux at 23:19 contain also gamma rays with energies up to 6 MeV. The spectrometer data is confirmed by the count rate measurements of other ASEC detectors. The 1-minute time series of CUBE detector with energy threshold above ~4 MeV does not demonstrate any enhancements for the low energy TGEs. The same time series demonstrates pronounced peaks with very high statistical significance for the high-energy TGE. The energy spectra are of a broken power law type. Due to the very large number of the registered gamma rays we estimate spectra for each of TGE events. We fit our spectra with 2 power low dependences that allow physical inference on the possible origin of 2 gamma ray populations.

ma rays observed in this event almost equals that of the whole acceleration region.

REFERENCES

- Chilingarian, A., Arakelyan, K., Avakyan, K.et al., 2005. Correlated measurements of secondary cosmic ray fluxes by the Aragats space-environmental center monitors, Nucl. Instrum. Methods A 543, 483.
- Chilingarian A., Melkumyan L., Hovsepyan G., Reymers A., 2007. The response function of the Aragats Solar Neutron Telescope, Nuclear Instruments and Methods in Physics Research, A 574, (255-263).
- Chilingarian, A., A. Daryan, K. Arakelyan, A. Hovhannisyan, B. Mailyan, L. Melkumyan, G. Hovsepyan, S. Chilingaryan, A. Reymers, and L. Vanyan L., 2010. Ground-based observations of thunderstorm-correlated fluxes of high-energy electrons, gamma rays, and neutrons, Phys. Rev. D, 82, 043009, doi:10.1103/PhysRevD. 82.043009.

- Chilingarian, A., Hovsepyan, G., Hovhannisyan, A., 2011. Particle bursts from thunderclouds: natural particle accelerators above our heads. Phys. Rev. D: Part. Fields 83 (6), 062001.

- Chilingarian, A., Mailyan, B., Vanyan, L., 2012. Recovering of the energy spectra of electrons and gamma rays coming from the thunderclouds. Atmos. Res. 114–115, 1–16.

- Chilingarian, A., Mkrtchyan, H., 2012. Role of the lower positive charge region (LPCR) in initiation of the thunderstorm ground enhancements (TGEs). Phys. Rev. D: Part. Fields 86, 072003.

- Chilingarianb A., Hovsepyan G., Kozliner L., 2013. Thunderstorm ground enhancements gamma ray differential energy spectra. Phys. Rev. D: Part. Fields 88, 073001.

- Chilingarian A., 2014. Thunderstorm Ground Enhancements - model and relation to lightning flashes, Journal of Atmospheric and Solar-Terrestrial Physics 107, 68–76.

- Chilingarian, A., Chilingaryan, S., and A. Reymers, 2015. Atmospheric discharges and particle fluxes, J. Geophys. Res. Space Physics, 120, 5845–5853, doi: 10.1002/2015JA021259.

- Chilingarian A., Chilingaryan S., Hovsepyan G., 2015. Calibration of particle detectors for secondary cosmic rays using gamma-ray beams from thunderclouds, Astroparticle Physics 69, 37–43

- Chilingarian A., Hovsepyan G., Khanikyanc G., Reymers A. and Soghomonyan S., 2015. Lightning origination and thunderstorm ground enhancements terminated by the lightning flash, EPL, 110, 49001.

- Dwyer, J. R., and M. A. Uman 2014. The physics of lightning, Phys. Rep., 534(4), 147–241.

- Dwyer, J. R., D. M. Smith, and S. A. Cummer 2012. High-energy atmospheric physics: Terrestrial gamma-ray flashes and related phenomena, Space Sci. Rev., 173, 133–196.

- Fishman, G.J., Bhat, P.N., Mallozzi, R., Horack, J.M., Koshut, T., Kouveliotou, C., Pendleton, G.N., Meegan, C.A., Wilson, R.B., Paciesas, W.S., Goodman, S.J., Christian, H.J., 1994. Discovery of intense gamma ray flashes of atmospheric origin. Science 264 (5163), 1313–1316.

- Kelley N.A., Smith D.M., Dwyer J.R., et al. 2015. Relativistic electron avalanches as a thunderstorm discharge competing with lightning, Nature communications 6, Article number: 7845.

- Wilson C. T. R., 1925. The Acceleration of β-particles in Strong Electric Fields such as those of Thunderclouds, Proc. Cambridge Phil. Soc. 22, 534.

Extensive air showers, lightnings and thunderstorm ground enhancements

A.Chilingarian, G.Hovsepyan, L.Kozliner

A.Alikhanyan National Lab (Yerevan Physics Institute), 2, Alikhanyan Brothers, Yerevan 0036, Armenia

Abstract. For the lightning research, we monitor the particle fluxes from thunderclouds, the so called Thunderstorm Ground Enhancements (TGEs) initiated by the runaway electrons, and Extensive Air Showers (EASs) originated from high energy protons or fully stripped nuclei that enter the Earth's atmosphere. Besides, we monitor the near-surface electric field and the atmospheric discharges with the help of a network of electric field mills.

The Aragats "electron accelerator" produced plenty of TGE and lightning events in spring 2015. Using 1-sec time series, we investigated the relation of lightnings and particle fluxes. Lightning flashes often terminated the particle flux; during some of TGEs the lightning would terminate the particle flux 3 times after successive recovery. It was postulated that a lightning terminates a particle flux mostly in the beginning of TGE or on the decay phase of it; however, we observed two events (19 October 2013 and 20 April 2015) when the huge particle flux was terminated just on a maximum of its development. We discuss the possibility that a huge EAS facilitates lightning leader to find its path to the ground.

1. INTRODUCTION

Considered the highest mountains in the South Caucasus Aragats is a dormant volcano with a 400 m deep crater that has become an ice basin. Its central highlands cover an area of more than 820 square kilometers and generate huge summer storms that flow down its slopes into the surrounding valleys. The four crests that top Mt. Aragats are simple reminders of its once soaring heights leveled over 10, 000m 1.5 million years ago, before a massive eruption lowered the height to its current 4,095m. Only in 100 km to the south from Aragats across the valley of the Araks River stands sister of Aragats – Biblical Mountain Ararat. Lightning activity is enormously strong at Aragats that makes it home of the ancient Armenian god of thunder and lightning Vahagn. Mt. Aragats hosted one of the world's oldest and largest cosmic ray research stations, located on the slopes of the mountain. The Cosmic Ray Division (CRD) of the A. Alikhanyan National lab (Yerevan Physics Institute) during the last 70 years has commissioned and operated on the research stations of Aragats and Nor Amberd numerous particle detectors uninterruptedly registered fluxes of charged and neutral cosmic rays. The research work at Aragats (in the framework of Aragats Space Environment center (ASEC, Chilingarian et al., 2005) includes registration of Extensive Air Showers (EAS) with large particle detector arrays; investigation of solar-terrestrial connections; monitoring of space weather; and observations of high-energy particles from the thunderclouds. More than 300 particle detectors (including plastic scintillators and NaI spectrometers) are registering particle fluxes and sending data online to the CRD headquarters in Yerevan. In addition to particle detectors, ASEC includes facilities that can measure electric and geomagnetic fields, lightning occurrences and locations, and a variety of meteorological parameters. With installing in 2014 of fast electric field recorders and automotive cameras the research in the lightning physics started on Aragats. ASEC facilities are located on the slopes of Mt. Aragats and in Yerevan at altitudes of 3200, 2000, and 1000 m above sea level, respectively (see Fig. 1). The distance between Nor Amberd and Aragats research stations is 12.8 km. The distance from the CRD headquarters in Yerevan to the Nor Amberd and Aragats research stations is 26.5 and 39.1 km, respectively. The Latitude and Longitude coordinates of the stations are: 40.3750° N, 44.2640° E for the Nor Amberd Station,

40.4713° N and 44.1819° E for the Aragats Station, and 40.2067° N and 44.4857° E – for the Yerevan Physics Institute.

Acceleration and multiplication of the Cosmic ray (CR)electrons by the strong electric fields in the thunderclouds are well-established phenomena constituting the core of the atmospheric high-energy physics and are related to the Runaway Breakdown (RB, Gurevich, 1992) recently referred to as Relativistic Runaway Electron avalanches (RREAs, Dwyer, Smith, and Cummer, 2012; Dwyer and Uman, 2014). However, the origin and location of charged centers in the thundercloud (one of the most important aspects in the atmospheric physics) we do not understand exactly until now. In fair weather conditions, the atmosphere is positively charged and the Earth has an opposite-polarity negative charge. A thunderstorm can drastically change the cloud electrification pattern. The simplified sketch of storm-time cloud electrification is shown in Fig. 2. The top of the thundercloud has a positive charge with a negative screening layer just above it; the middle layer has a negative charge and a small local region of positive charge is in the bottom of the cloud (Stolzenburg et al., 1998). If we use the so-called "physics" sign convention (see discussion on the used sign conventions in (Krehbeil, Mazur and Rison, 2014), then the near-surface electrostatic field is negative during fair weather (positive ions are slowly migrated from the atmosphere in the direction to the Earth), and it is negative during thunderstorms (electrons are transported by the lightning from the cloud to the Earth). According to the tripole model (quadruple, if we add a negative screening layer above the main positive layer), in the cloud there exist several dipoles of opposite orientation, which accelerate electrons downward, in the direction of the Earth, and – in the direction to the open space, as it is shown in Fig. 2. The "atmospheric electricity" sign convention is the opposite: the fair-weather near-surface electric field is positive, and the storm time field is mainly negative. The historical basis of this controversy is that the electric mills usually operated according to the "atmospheric electricity" sign convention (a positive electric field at the ground is produced by positive charge overhead and negative electric field on the ground is produced by negative charge overhead).
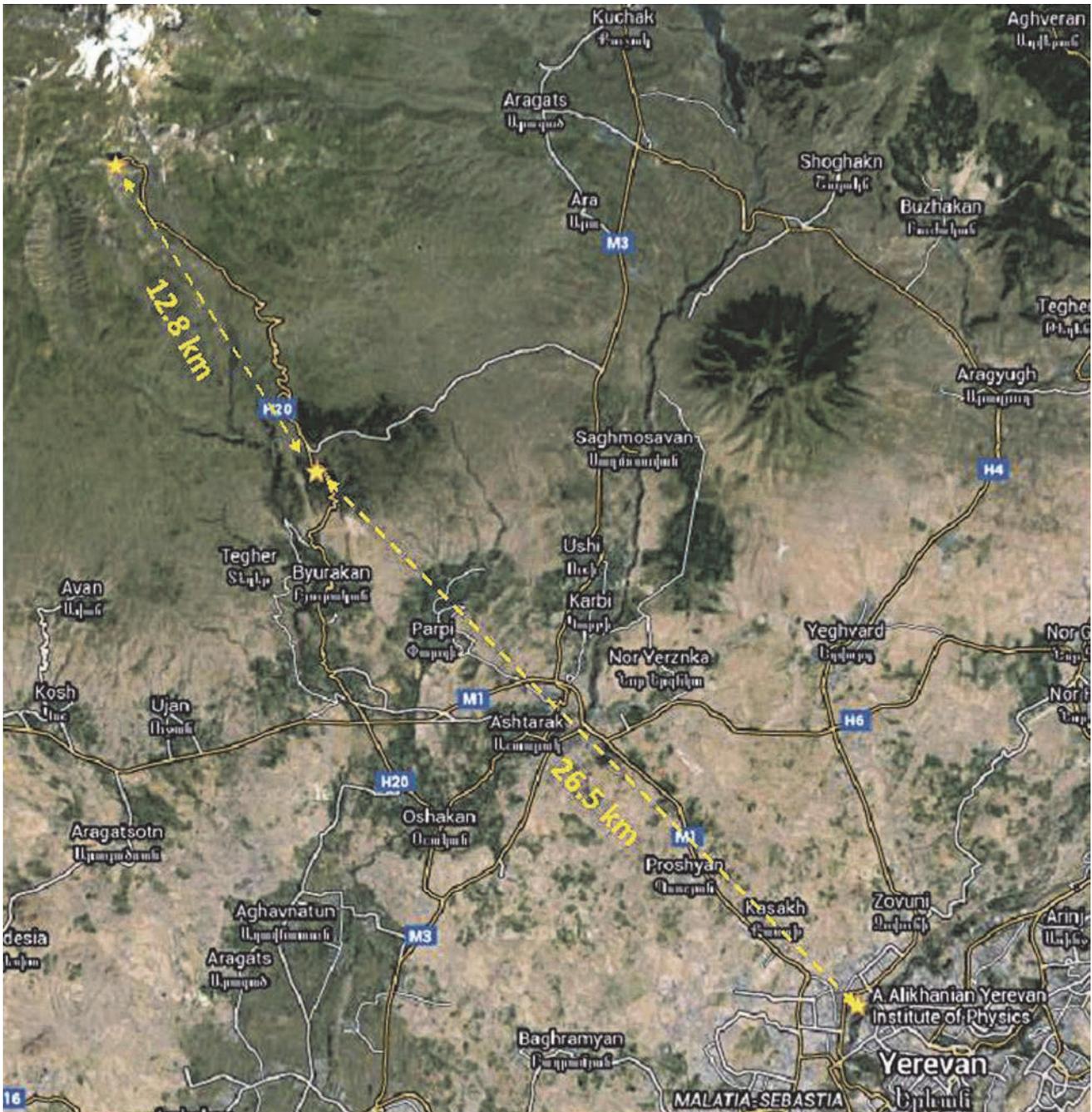
Figure 1. The Google map of Aragats Mountain with Aragats and Nor Amberd research stations and Yerevan headquarters of CRD.

Our key evidence for the lightning research is the monitoring of the particle fluxes from thunderclouds. These fluxes significantly increase the usually stable background of the secondary cosmic rays incident on the Earth's surface and create the so-called Thunderstorm Ground Enhancements (TGEs, Chilingarian et al., 2010, 2011). Development of a Lower Positive Charge Region (LPCR) facilitates the proper direction of the electric field, in order to accelerate the electrons in the direction to the Earth. The upper dipole accelerates electrons upwards and radiated bremsstrahlung gamma rays reaching the satellites are registered by the orbiting gamma ray observatories. These enigmatic bursts of gamma rays are named Terrestrial Gamma Ray Flashes (TGFs, Fishman et al., 1994). The particle burst in the gap between the positive upper layer and the screening layer recently detected by ADELE aircraft (Kelley et al., 2015) is named Gamma flow.

Both, the lightning initiation and leader propagation and the dynamics of TGE are dependent on the cloud elec-

trification and, therefore, on the charged layers in the thundercloud. Thus, by detecting the changing particle fluxes we can monitor the distribution of charged layers above the particle detector site. As the nearest to the ground charged layer, LPCR strongly influenced the development of cloud-to-ground (CG) and intracloud (IC) discharges and TGEs. When LPCR is above the particle detectors, and when the field is strong enough the electric field between LPCR and the main negatively charged region above effectively accelerate electrons downward (Chilingarian and Mkrtchyan, 2012). Thus, the intensity and energy spectra of gamma rays and electrons of TGE can be used for estimating the position and thickness of the LPCR.

At the maximum of the TGE flux, in the time series of the near-surface electric field we usually observe so-called "bumps" rising from deep negative electric field – brief increase of the electric field with amplitude up to 10-20 kV/m. It was postulated (Nag and Rakov, 2009) that especially in the declining phase of the TGE, there often occur

negative cloud-to-ground lightings, which abruptly terminate the particle flux (Alexeenko et. al., 2002, Tsuchiya et al., 2013, Chilingarian et al., 2014). The mature LPCR do not allow a lightning leader to make its path to the ground, declining it horizontally and transforming a –CG lightning attempt to an intracloud (-IC) lightning. A CG lightning becomes energetically preferable than –an - IC when LPCR is thin. However, sometimes we can see a catastrophic decay of TGE near the maximum of the particle flux. High-energy EASs (with primary particle energies above 10^{16} eV) possibly facilitated the propagation of the lightning leader downwards (Gurevich et al., 1999). Therefore, we discuss a large EAS registration by the Aragats Neutron monitor and Muon detectors during thunderstorms.
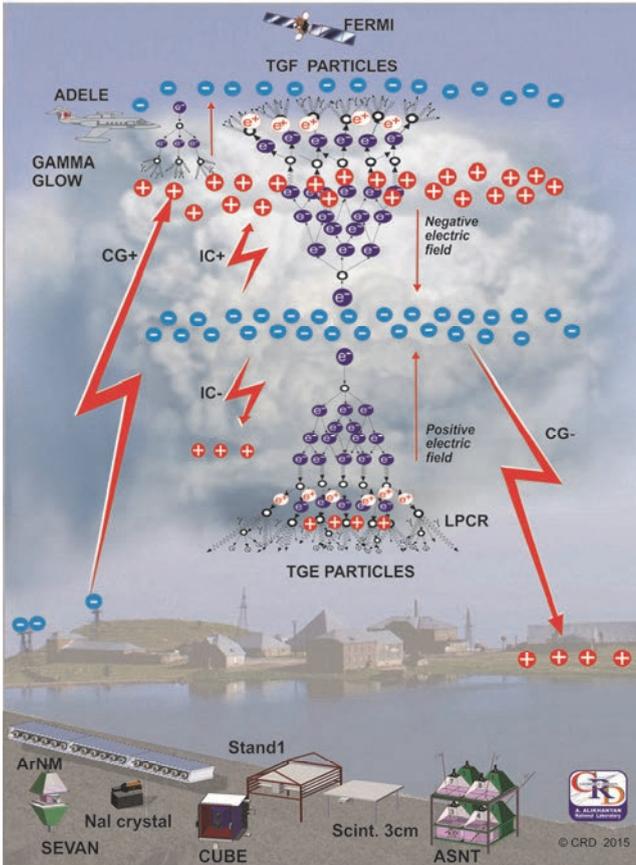

Figure 2. High-energy physics processes in the atmosphere

2. INSTRUMENTATION

The ASEC particle detectors can measure the fluxes of the species of secondary cosmic rays (electrons, gamma rays, muons and neutrons) as well as the electron, muon and neutron content of EASs. Numerous thunderstorm-correlated events, detected by the ASEC facilities, constitute a rich experimental set for the investigation of the high-energy phenomena in the thunderstorm atmosphere. The new generation of ASEC detectors consist of 1 and 3 cm thick molded plastic scintillators arranged in stacks and cubic structures. The ''STAND1'' detector is comprised of three layers of 1-cm-thick, 1m2 sensitive area molded plastic scintillators fabricated by the High Energy Physics Institute, Serpukhov, Russian Federation. The light from the scintillator through optical spectrum-shifter fibers is reradiated to the long- wavelength region and passed to the photomultiplier FEU-115M. The maximum of luminescence is emitted at the 420-nm wavelength, the luminescence time being about 2.3 ns (see details of detectors setup in Chilingarian, Chilingaryan, and Hovsepyan, 2015).

The Aragats neutron supermonitor (ArNM, Fig. 3) consists of eighteen cylindrical proportional counters of CHM-15 type (length 200 cm, diameter 15 cm) filled with BF_3 gas enriched with B^{10} isotope and grouped in three sections containing six tubes each. The proportional chambers are surrounded by 5 cm of lead (producer) and 2 cm of polyethylene (moderator). The cross section of lead producer above each section has a surface of $6m^2$ and the total surface of three sections is $18m^2$. The atmospheric hadrons produce secondary neutrons in nuclear reactions in lead; then the neutrons get thermalized in a moderator, enter the sensitive volume of the counter, and in interactions with boron gas bear Li^7 and the α particle. The α particle accelerates in the high electrical field inside the chamber and gives a pulse registered by the data acquisition electronics. High- energy hadrons generate a large number of secondary neutrons entering the sensitive volume of the proportional counter, and if we want to count all pulses initiated by the incident hadrons, we have to keep the dead time of the NM very low (the ArNM has a minimal dead time of 0.4 μs). If we want to count incident hadrons only (a one-to-one relation between count rate and hadron flux) we have to keep the dead time as long as the whole secondary neutron collecting time (~1250 μs) to avoid double counting.

In (Stenkin et al., 2007) was described detection of so-called neutron bursts in the NM related to occasional hitting of it by a core of high-energy EAS. Huge amount of the EAS hadrons will generate numerous thermal neutrons and enormously enlarged NM's count rate (size of the neutron burst or peak multiplicity). This option of EAS core detection by NM mostly was not recognized because of usually used large dead time not allowing counting of all secondary neutrons. With establishing low dead time and short collecting time for ArNM (usually only 1-minute time series are available for NM), we detect numerous EASs hitting NM, several from them providing multiplicities above 1000. In our terminology, the multiplicity is the number of pulses registered in each particular second. Each counter has the mean multiplicity of usually 30-60 counts per second; at a neuron burst, the multiplicity can reach many hundreds and ever thousands. For each channel we calculate as well the number of standard deviations (N of σ) of the peak multiplicity. The 1-sec time series of ArNM counts are being entered in the MSQL database at CRD headquarters in Yerevan (available online from http://adei.crd.yerphi.am/adei/) as well as in the database of the Euro-Asian consortium of neutron monitors (NMDB@.eu.org).
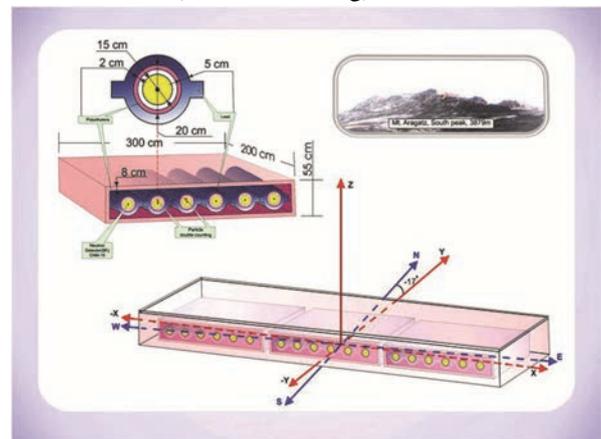

Figure 3. STAND detector consisting of three layers of 1 cm thick scintillators.

The Aragats Muon detector (Fig. 4) consists of three vertically stacked plastic scintillators with an area of 1m². The top 3cm thick scintillator is covered by 7.5cm of lead filter; the middle 1cm thick scintillator is covered by 1.5cm of lead filter and by an ~ 60 cm thick rubber layer (carbon); the bottom 1cm thick scintillator is covered by a 6cm thick lead filter. The energy thresholds to detect muons in three stacked scintillators accordingly are ~170 MeV, ~220 MeV and ~350 MeV accordingly. DAQ electronics provides 50 ms time series of all scintillators.

ArNM and Muon detectors are located at a distance of ~ 6m in the MAKET experimental hall (Fig. 5). Close location of these detectors allows joint detection of several large EASs. Outdoors is located the STAND1 detector comprised of three layers of 1-cm-thick, 1m² area molded plastic scintillators and 3 cm thick plastic scintillator of the same type fabricated by the High Energy Physics Institute, Serpukhov, Russian Federation. The light from the scintillator through optical spectrum-shifter fibers is reradiated to the long-wavelength region and passed to the photomultiplier FEU-115M. The maximum of luminescence is emitted at the 420-nm wavelength, the luminescence time being about 2.3 ns. On the roof of MAKET building are located meteorological devices measuring the near-surface electric field and weather conditions. A deep negative near-surface electric field is a necessary condition for the TGE origination. Moreover, the observed changes of the electric field as well as detected particle fluxes contain information on the dynamics of the cloud electrification; such information is very difficult to acquire by *in-situ* measurements. Electrical mill EFM 100 produced by Boltek Company operates with 20 Hz frequency performing 20 measurements of the near-surface electric field per second. Professional Davis Instruments Vantage Pro2, http://www.davisnet.com/ provides a wide range of meteorological parameters measured each minute. Devices of the same type are located at Nor Amberd research station and in Yerevan.

An array of plastic scintillators located inside and outside the MAKET hall (green "pyramids" in Fig. 6) has been primarily a part of MAKET-ANI experiment (Chilingarian et al. (2004). About 100 detecting channels formed from 5-cm thick plastic scintillators with an area of 1 m² each, were triggered by large EASs corresponding to primary particle with energy greater than 10^{14} eV. At the end of the MAKET-ANI experiment we picked several detectors and implemented special trigger conditions in order to detect large particle bursts due to thunderstorm activity. The MAKET detectors measure the charged species of secondary cosmic rays with very high accuracy. Each of the standalone scintillators can measure incident particle flux and the array, as whole, can also count the so-called EAS triggers (''firing'' of more than 8 detectors of the array within a time window of 400 ns). If the signals from the first 8 scintillators coincide within the trigger window time, then the amplitudes of all photomultiplier signals (proportional to the number of particles hitting each scintillator) are stored. At fair weather the surface array registered EASs initiated by the primary protons with energies above 50 TeV (~25 EASs per minute, 8-fold coincidences) and 100 TeV (~8 EASs per minute, 16-fold coincidences).

Large TGEs are can trigger the MAKET array. When thunderstorm clouds are very low above the scintillators, the TGE electrons reach the MAKET scintillators and the stable EAS count rate suddenly and abruptly goes up. We investigate in details these Extensive Cloud Showers (ECSs) and prove their systematic difference from EASs (Chilingarian et al., 2011). ECSs are individual RREA cascades from a single cosmic ray electron entering the RREA process. Alex Gurevich et al., 1999 called this cascades micro-runaway breakdown (MRB). Registration of ECSs is very difficult due to fast attenuation of electrons in the atmosphere; only at Aragats, due to very low thunderclouds, we can register several huge TGEs accompanied with ECSs (Chilingarian, 2013). ECSs are an analogue of TGFs registered by orbiting gamma ray observatories; however, TGF particles are mostly gamma rays, not electrons. Gamma rays can travel hundreds of kilometres in the open space and occasionally hit fast-moving satellites and give rise to very short bursts of radiation.
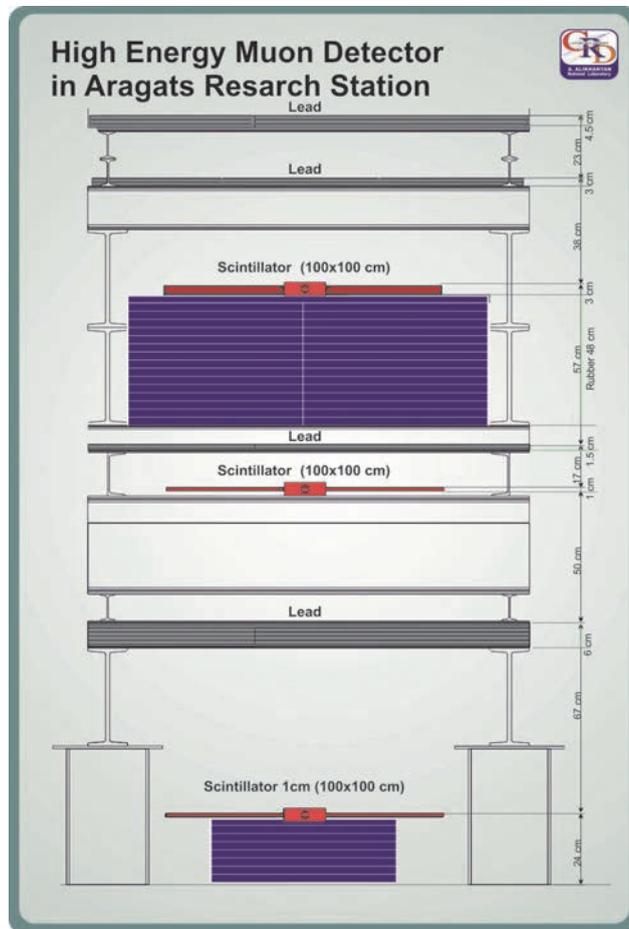

Figure 4. The "muon" stacked detector with large amount of lead and robber between 3 scintillators
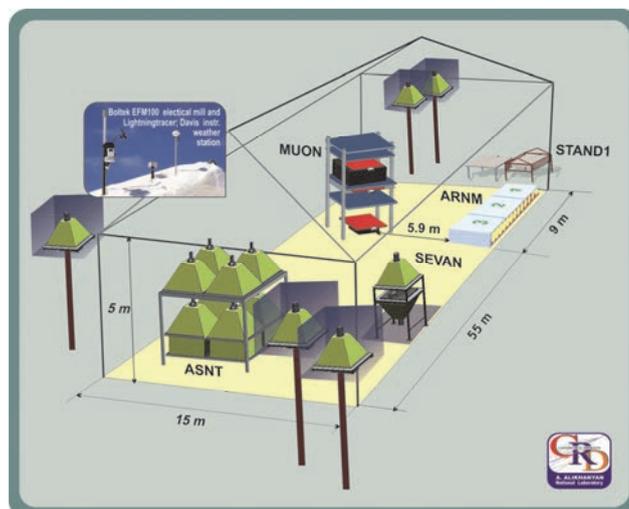

Figure 5. Tree-cm thick plastic scintillator of STAND1 detector.

We investigate in details this Extensive Cloud Events (ECSs) and prove their systematic difference from EASs (Chilingarian et al., 2011). ECSs are individual RREA cascades from a single cosmic ray electron entering the RREA process. Alex Gurevich et al., 1999 called this cascades micro-runaway breakdown (MRB). Registration of ECSs is very difficult due to fast attenuation of electrons in atmosphere; only at Aragats due to very low location of thunderclouds we register several huge TGEs accompanied with ECSs (Chilingarian, 2013). ECSs are an analog of TGFs registered by orbiting gamma ray observatories; however TGF particles are mostly gamma rays, not electrons. In the open space gamma rays can travel hundreds of kilometers and hit occasionally fast moving satellites providing very short bursts of radiation.

3. THUNDERSTORM GROUND ENHANCEMENTS DETECTED IN SPRING 2015

The first spring storm started at Aragats on March 30 at 11:15 UT and continued until 11:50 with numerous nearby lightnings (Fig. 10). Thick clouds covered the sky reducing the solar radiation by a factor of 2.5, from 370 W/m^2 at 11:32 down to 150 W/m^2 at 11:43. The relative humidity was very high - 96%. Numerous lightnings caused frequent near-surface electric field disturbances. Due to a nearby lightning (2 km far from the detector site, measured by EFM-100 electric mill) the near-surface electric field changed its value from -21 kV/m to +38 kV/m in less than a second (Fig. 6). The lightning terminated the particle flux registered by the STAND1 detector. For 3 seconds (from 11:46:59 to 11:47:01), the particle count rate of the 1m^2 scintillator correspondingly increased by 9.2%, 12.2% and 16% above the mean value measured just before the start of the particle flux enhancement. At 11:47:02, the particle flux was abruptly terminated and dropped by ~17%.
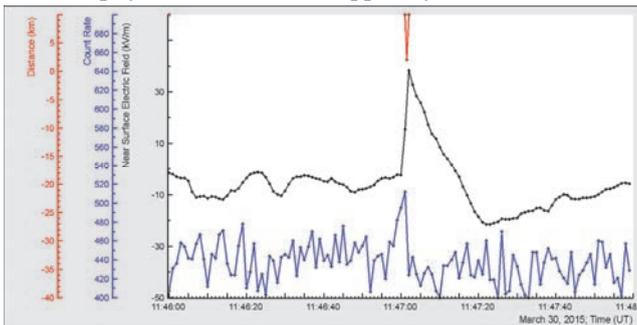

Figure 6. One-second time series of the count rates measured by the outdoor 3 cm thick 1 m^2 area scintillator (bottom); 1-sec time series of the near surface electric field (middle); and distance to lightning (top).

On April 4, the 3-cm thick plastic scintillators detected a large TGE at 16:01. In Fig. 7, instead of particle detector count rates the corresponding p-values of statistical test are shown. The significance of the detected peaks in the time series of the particle count rates is determined by the actual peak values divided by the standard deviation of the count rate, i.e. by the number of standard deviation contained in the peak (number of σ). The p-value is the most comprehensive measure of the reliability of detecting peaks in a time series. Large p-value corresponds to small chance probabilities that the observed peak is a background fluctuation and not a genuine signal. Therefore, we can safely reject the null hypothesis (that peak is a background fluctuation only) and confirm the existence of a TGE. The outdoor 3 cm thick scintillator measures 38σ enhancement; the same type scintillator located indoors at another experimental hall (named SKL) demonstrates ~10σ enhancement;

the scintillator located under deep snow (snow covers Aragats station until end of May) - ~5σ. Note that only the scintillator with a low energy threshold shows the flux enhancement lasting near 2 hours.

In Fig. 8 we show disturbances of near-surface electric field measured at Aragats and Nor-Amberd research stations. The same lightning was detected at both stations; the distance between the stations is ~13 km. Note the same polarity of the electrostatic field on both stations (no electrostatic field reversal occurred).

The near-surface electric field at Aragats increased from -43 kV/m to 35 kV/min in very short time; at Nor Amberd station the electric field increased from -9 kV/m to 23 kV/min. This indicates strong discharge processes at nearby distances in the thunderclouds above Aragats leading to the decline of the particle flux to the background value, decreasing it by 14% in 2 seconds. The start and end of the lightning (time of abrupt enhancing of the near surface electric field and time of reaching the maximal value of it) coincide at both stations within 50 ms (at 16:00:45.2 and at 16:00:45.25); this is a demonstration of the fact that the accuracy of synchronization of the remote on-line computers in Nor Amberd and Aragats is at least 50 ms. Thus, the measurements of ASEC particle detectors and field-meters are synchronized as well with an accuracy of 50 ms as well.
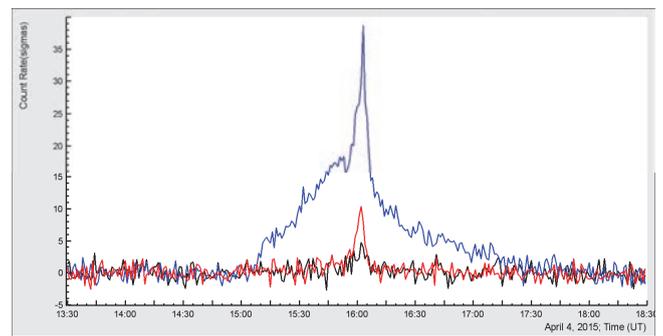
Figure 7. Significance of the particle flux enhancements in number of standard deviations (Nσ); The outdoor 3-cm thick scintillator shows a 2 hour TGE with a maximum of 38σ (upper curve); the same-type indoors scintillator demonstrates only a few minutes TGE with a maximum of ~ 10σ (the second highest peak) and a same-type scintillator under deep snow – only 5σ enhancement (smallest peak).
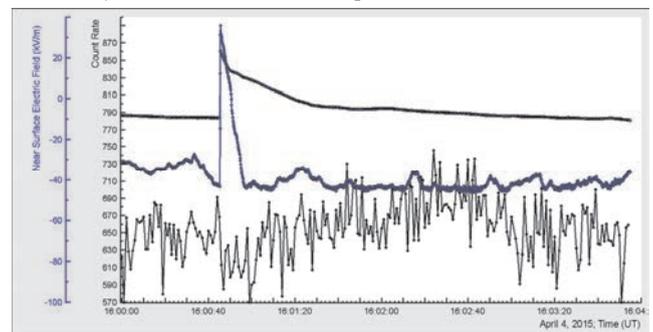
Figure 8. One-second time series of the count rates measured by the outdoor 3 cm thick 1 m^2 area scintillator (bottom); near-surface electric field (middle with larger amplitude – Aragats; top, with lower amplitude – Nor Amberd; Particle flux measured at Aragats declined after lightning by 12% at 16:00:47.

4. LONG-LASTING SPRING STORM AT ARAGATS ON 9-10 APRIL 2015

At 22:00 UT on 9 April 2015, an extensive storm was unleashed on Mt. Aragats. During upcoming 14 hours numerous nearby lightnings occurred near Aragats station and the particle flux several times exceeded the background

values by 2-22%, which corresponds to 3-32 standard deviations (3-32 σ) in the one-minute time series of the 1-m² particle detectors. Humidity was stable high – 98%, temperature – near the freezing point ~ -1; atmospheric pressure was also stable, 684 mbar. Wind was West-North – 160° – 200° N, speed - 5-12 m/sec. In Fig. 9 we post the 1-minute time series of the particle flux measured by the indoors 3 cm thick and 1 m² area plastic scintillator (bottom); the disturbances of electric field measured by EFM-100 electric mill (middle); and estimated distance to the lightning measured by the same electric mill (top). As one can see from Fig. 9, almost all disturbances of the electric field were accompanied with lightnings and TGEs.
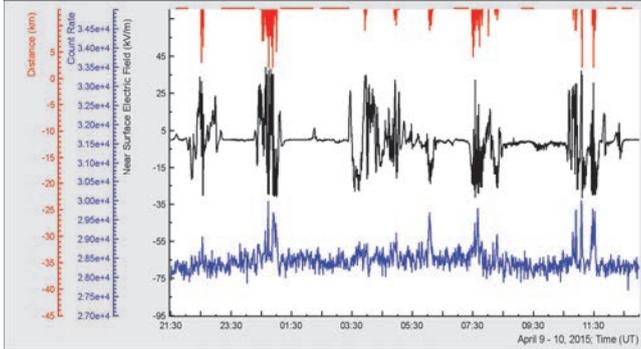
Figure 9. Time series of particle count rate (bottom); disturbances of near-surface electric field (middle) and distance to lightning (top).

In Fig. 10 we again show the 1-minute time series of the same-type particle detectors (3 cm thick and 1 m² area plastic scintillators) located outside, inside and under deep snow. The weather conditions on high mountains are rather challenging and the staff cannot maintain some of the outdoors detectors during the winter-spring months. Few of detectors are operated beneath ~1m of snow, in spring the snow becomes wet and the particle attenuation in it – stronger. From Fig. 10 we can conclude that the energy thresholds of all 3 detectors, in spite that they are the same type are very different due to different amount of matter above them. The outside scintillator with the lowest threshold (upper time series) of ~1 MeV shows the low energy component of the TGE lasting up to 5 hours with emerging peaks of few minute duration due to RREA bremsstrahlung high-energy gamma photons born above detector location (measured as well by the scintillators with higher energy threshold, lower time series).
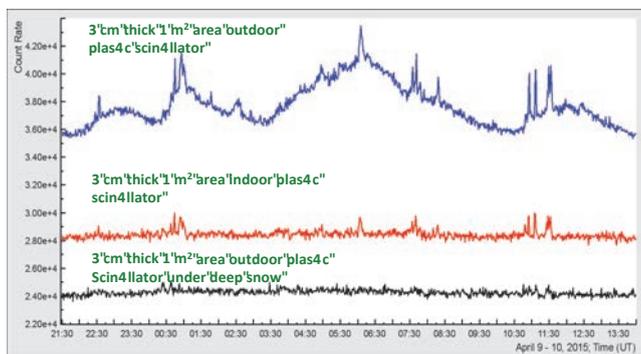
Figure 10. One minute time series of analogical scintillators located under different amount of matter

Thus, the scintillators with higher threshold (3-4 MeV) did not register the low energy component; only peaks from the high-energy gamma rays coincide in time with the ones registered by the low threshold scintillators. From Figs. 9 and 10 we can conclude that the low-energy component of TGE is below 3-4 MeV. The high-energy component of the

TGE is local and is directly connected with RREA process and bremsstrahlung gamma rays; the long-lasting lower energy component of TGE is possibly connected with the distant regions of the thundercloud where RREA is unleashed and from where Compton scattered gamma rays are reaching the detector site.

In Fig. 11 we show the data from another TGE terminated by the lightning. From 00:28 until 1:00 April 10 several abrupt surges of the near surface electric field occurred due to negative lightnings. The near-surface electric field increased from -29 kV/m to 40 kV/min in ~150 ms at 00:44:58; the electric field recovery time was 29 seconds. The TGE flux declined by 14% (from 686 down to 588) the same second when the lightning occurred; and by 21% (down to 541) in the following 4 seconds.

The time delay between the EAS registered by the scintillators of the MAKET surface array and the start of lightning was 2.25 ± 0.05 seconds. Thus, we conclude that, for these events lightning occurrence is not connected with EAS. According to the RB-|EAS theory (Gurevich et al., 1999) only very large EASs (with primary energy above 10¹⁶ eV) can facilitate a negative CG lightning; thus frequent EASs with energies 50-100 TeV cannot be connected with lightning initiation. We need detectors registering cores of very large EASs providing huge ionization in the atmosphere. The small MAKET detector due to fast saturation of scintillators registering EAS electrons cannot outline such events. Usually the core region around the EAS axes is excluded from the recovering of the EAS size and arrival direction. The ArNM and Muon detectors, as we will see in the next section by registration of the neutron burst, which are directly connected with EAS core, can outline the largest EASs.
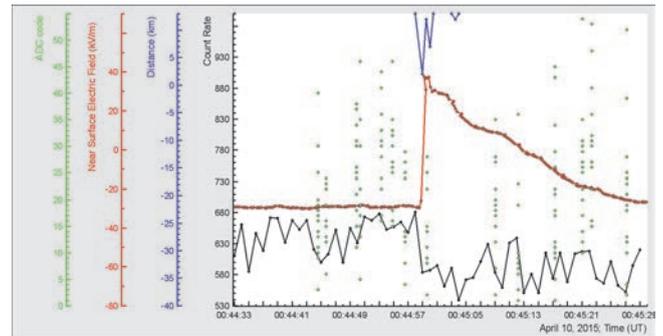

Figure 11. 1-second time series of the count rates measured by the outdoor 3 cm thick 1 m² area scintillator (bottom); near surface electric field |(middle); distance to lightning (top); and EAS triggers: dots are correspondent to "fired" ones from 16 plastic scintillators (ADC code is proportional to the number of electrons hitting the scintillator).

The essential parameters of the selected lightnings that occurred on April 10 2015 are summarized in Tab. 1. In the first column, we put the date of the event, in the second – time of the abrupt change of near-surface electric field. In the third column, we put the time of maximum (for negative lightnings) or minimum (for positive lightnings) and the extreme value of the near-surface electrostatic field. In the fourth column, we put the time of electrostatic field fall or surge. In the next column - the drop of the gamma ray flux (if a TGE is released). In the sixth column, we put the amplitude – the difference of the initial and extreme values of the near-surface electrostatic field and in the seventh – the distance to the lightning measured by the EFM-100 electric mill. In the last two columns, we put the coinciding measurements reported by WWLLN (if any).

Table 1. Main parameters of the lightning occurrences on 10 April 2015

Date (UT)	Start of Lightning (UT) and el. field value (kV/m)	Time of maximum (UT) and maximum value (kV/m)	Duration (msec)	Drop of flux (%)	Drop of el. field	Dist. (km)	WWLLN time	WWLLN dist.
10/04/2015	00:38:42.85 8	00:38:43 45	150	-	37	7		
10/04/2015	00:40:45.65 -14	00:40:45:80 36	150	-	50	7		
10/04/2015	00:43:25.65* 20	00:4325.90 -42	250	-	-62	7	0:43:25.69	12
10/04/2015	00:44:58.85 -30	00:44:59 40	150	15	70	2		
10/04/2015	00:47:47.7 2	00:47:48.25 22	550	-	20	7		
10/04/2015	00:48:49.10 -4	00:48:49:35 32	250	-	36	3		
10/04/2015	00:51:12.45 1	00:51:12:75 26	300	-	25	7		
10/04/2015	00:53:27.7 -3	00:53:27.9 38	200	-	41	2		
10/04/2015	4:58:06.35 -15	4:58:06.65 8	300	-	23	5		
10/04/2015	7:30:56.4 -23	7:30:56.65 7	250	-	30	4	7:30:56.3	2
10/04/2015	7:32:58.6 -22	7:32:58.9 2	300	-	24	6		
10/04/2015	7:34:35.5 -28	7:34:35:6 36	100	12	64	7		
10/04/2015	7:41:25.05 -24	7:41:25.25 26	200		50	3		
10/04/2015	11:06:39.45** 32	11:06:39.5 -32	50	-	-64	2		
10/04/2015	11:26:51.0 -29	11:26:51.2 27	200		56	6		
10/04/2015	11:29:22.15 -27	11:29:22:30 -34	150	10	61	2		
10/04/2015	14:30:11.7** 19	14:30:11.75 -30	50	-	-49	14		

*Positive lightning was detected in Nor Amberd, both electric mills at Aragats registered small negative lighting

** Positive lightnings detected at Aragats station

From the overall 17 lightnings being observed, only three were positive; the positive/negative ratio was ~0.18. Abrupt termination of the TGE flux had been observed only during the negative lightnings. Positive lightnings demonstrate faster dynamics (electric field fall) than negative lightnings surge. TGE's surge above background is rather significant - $35 \pm 12\%$. The abrupt fall of TGE is also sizable $21 \pm 7\%$. From the Tab. 1 we can outline typical features of the negative cloud-to-ground lightning:

1. Mean electric field before the start of the lightning ~ -24.7 ± 2.9 kV/m;
2. The mean maximum value of the enhanced electric field ~ 51 ± 2.7 kV/m. After reaching maximum the near-surface electric field slowly returns to pre-lightning values due to continuous charge separation processes in the cloud;
3. Mean time from the start of electric field sharp change till its extreme value is ~160 ± 50 ms.

The mean distance to the lightning is ~ 4.8 ± 3 km. In Fig. 12 we can see an unusual TGE accompanied with the positive nearby lightning. During a short TGE, the near-surface field was in the positive domain, ~ 37 kV/m, decreasing to 13 kV/m, when the particle flux peaked. The nearby positive lightning (~2 km) in the end of TGE caused the near-surface field to drop from 39 kV/m to -31 kV/m.

It is interesting to note that this positive lightning does not terminate the particle flux as the negative ones do.

In Fig. 13, we demonstrate a TGE several times terminated by the negative lightnings. The largest lightning occurred at 11:29:19 within 2 km from the detector site (see zoomed version in Fig. 14); the particle flux dropped by 22% in 4 seconds. In 200 ms, the near-surface electric field increased from – 30 kV/m to 27 kV/m; recovery of the field took 20 seconds. No coinciding EAS events were detected.
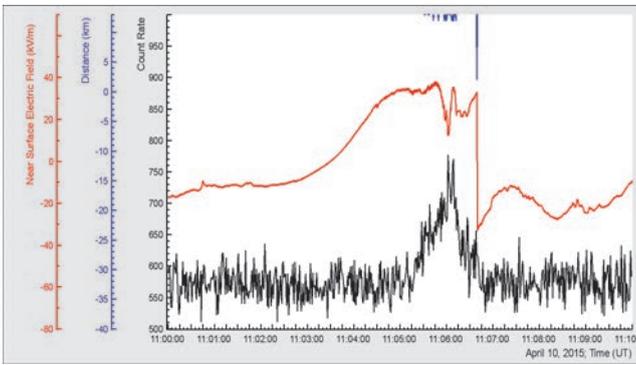
Figure 12. Rare TGE ended by a positive lightning; time series of 1-minute count rate of outdoor 3-cm thick scintillator (bottom); disturbances of near-surface electric field (middle) and distance to lightning (top).
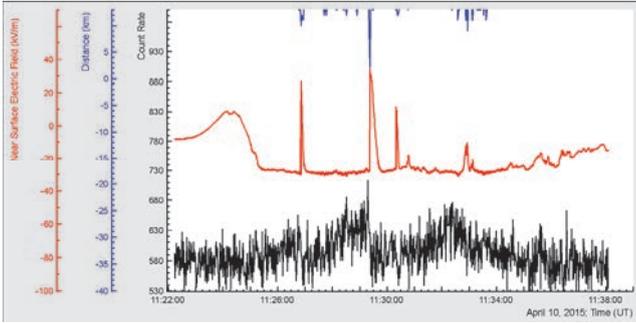
Figure 13. TGE terminated by 4 negative lightnings
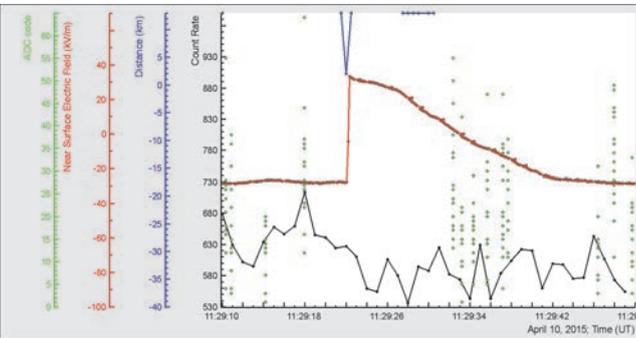

Figure 14. Zoomed version of the Fig. 18. One-second time series of the count rates measured by the outdoor 3 cm thick 1 m² area scintillator (bottom); near-surface electric field (middle); distance to lightning (top); and EAS triggers: dots are correspondent to "fired" plastic scintillators (ADC code is proportional to the number of electrons hitting the scintillator).

5. SUPER-EVENT OF 20 APRIL 2015

The enormously strong storm of April 19 with many nearby lightnings continued into 20 April, producing the largest TGE of the last 5 years. At 17:50 the relative humidity on Aragats was very high - ~97%; the atmospheric pressure was ~682 mbar, outside temperature was ~2C°; the velocity of ~225° N wind was ~3.5 m/sec. The electrostatic field was in the negative domain reaching -5kV/m at 17:50 and after 2 small bums got the near zero strength after 17:58. Particle count rate slowly rose after 17:58 and started to boost at 17:59, reaching the highest value at 18:00. Fig. 15 shows the time series of 1-minute count rate measured by the 1 cm and 3 cm thick plastic scintillators both with 1 m² area; the scintillators are located outdoors and have a minimal energy threshold of ~1 and ~3 MeV. In the middle of the picture, we have posted the near-surface electric field with apparent 2 negative lightnings; on the top – distance to lightning.
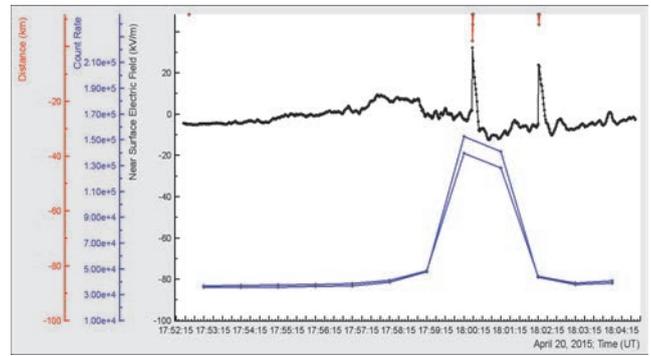
Figure 15. In the bottom – 1 minute count rates of outdoors scintillators (the larger count rate is corresponding to the 1cm thick plastic scintillator with a lower threshold), in the middle – disturbances of the near surface electric field, in the top – distance to lightning, first lightning was at a distance of ~ 2 km and the second one – 8km.

The one-minute time series of count rates demonstrate huge enhancement comparable with the super TGEs observed on Aragats in 2009 (Chilingarian et al., 2010) and 2010 (Chilingarian et al., 2011). In 2 minutes after the TGE started at 17:59, the count rate of the 1 cm thick scintillator boosted from the mean value of 35,540 to 152,430 $(min*m^2)^{-1}$, that is to say the TGE flux was ~117,000 $(min*m^2)^{-1}$. The flux measured by the 3 cm thick scintillator was smaller due to higher energy threshold – growing from the mean value of 36,623 to 139,888 $(min*m^2)^{-1}$, i.e. ~102,000$(min*m^2)^{-1}$. The fluxes were enhanced by 330% and 220% respectively. The mean square deviation of 1-minute count rate of both detectors is ~ 200, therefore the number of standard deviations (Nσ) is very large - 580 and 500 σ.

The detailed image (one-second time series) of the TGE we can see in Fig. 16, where we show the one-second time series of the same 3-cm thick outdoors plastic scintillator, electric field disturbances and distances to lightning. The maximal 1-second count rate was observed at 18:00:13. The 3 cm thick scintillator count rate boosted up to 7863 $(sec*m^2)^{-1}$; comparing it with the mean fair weather value of 587 +/- 22.6 $(sec*m^2)^{-1}$ we obtain 1240% enhancement corresponding to ~320 σ; i.e. the particle flux was enhanced 12.6 times!

Strong discharge processes at the nearby distances in the thunderclouds above Aragats abruptly terminate the ongoing huge TGE. The one-second-count rate of 3 cm thick outdoor scintillator declines from 7863 $(sec*m^2)^{-1}$ at 18:00:13 to 5295 (32%) at 18:00:14 and 598 (92%) at 18:00:15.
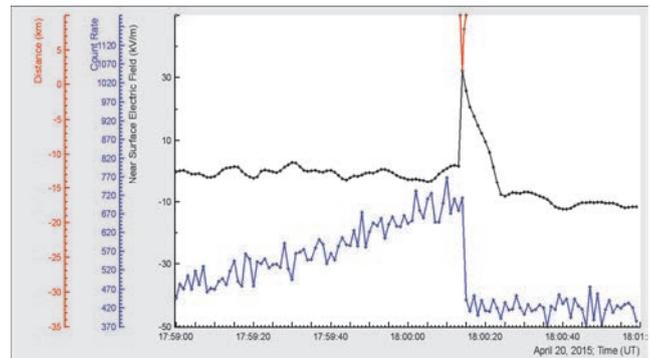
Figure 16. Abruptly declined 1-second count rates of the outdoors scintillator (bottom); disturbances of the near surface electric field (middle); distance to lightning ~ 2 km (top).

A more precise image of the super-TGE event and possible relation to an EAS trigger can be seen in the 50-ms time-series. In Fig. 17 we show the electric field disturb-

ances during the negative lightning observed at Aragats and Nor Amberd stations as well as the 1-second count rates of the 3-cm thick plastic scintillator. The lightning initiation time registered by the EFM-100 electric mills at the Aragats and Nor Amberd research stations was at 18:00:14.1 and 18:00:14.15 respectively. The electric field increased at Aragats from 1.2 kV/m up to 43.4 kV/m in 100 ms and from 2.15 kV/m up to 23.8 kV/m in 400 ms at Nor Amberd. Field recovering time at Aragats was 10 sec (the field decreased down to – 8 kV/m); in Nor Amberd – 30 sec. WWLLN registered a strong lightning at 18:00:14.75 located 6.7 km far from the Aragats station. The distance to the lightning measured by the EFM-100 sensor from Aragats was 1.8 km and 5 km from Nor-Amberd.
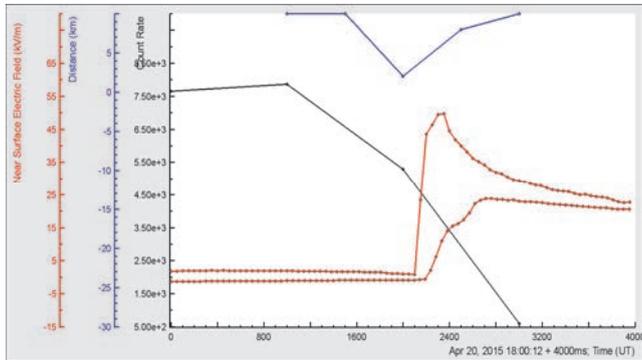

Figure 17. 50-msec time-series of the electric field disturbances during negative lightning observed at Aragats and Nor Amberd and 1 second count rates of 3-cm thick plastic scintillator.

Applying the veto system of the Cube detector, we can estimate the fraction of electrons in TGE. In Fig. 18 we show the 1-minute count rates of two 20 cm thick plastic scintillators stacked on each other and fully covered by six 1-cm thick and 1m² plastic scintillators (CUBE detector, see details in Chilingarian, Chilingaryan and Hovsepyan, 2015). The veto signal (at least 1 hit in 6 scintillators) from the shielding rejects the charged flux and it is supposed that only neutral particles reach the inside scintillators and are registered.

However, as the probability for missing charged particles and for registration of neural particles is other than zero, we have to make corrections in order to obtain the electron and gamma ray fluxes separately.
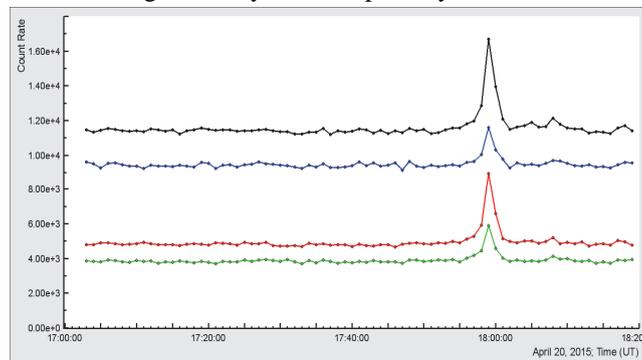

Figure 18. From top to the bottom: - the count rate of the top 20 cm thick scintillator without veto; the count rate of bottom 20 cm thick scintillator without veto; and then the count rates with veto switched on

Using the upper scintillator (with the energy threshold equal to ~ 4MeV) and applying the techniques described in (Chilingarian, Mailyan and Vanyan, 2012), we obtain an electron flux intensity of Ie ~1000 (min*m²)⁻¹ and a gamma ray flux of Iγ ~ 21,500(min*m²)⁻¹. For the bottom scintillator of the same type with higher energy threshold the elec-

tron flux was absent and the gamma ray flux was ~2200 (min*m²)⁻¹.

In Fig. 19 shows the energy spectrum of the gamma ray flux measured by a network of NaI spectrometers (Chilingarian, Hovsepyan and Kozliner, 2013) with an energy threshold of ~ 4 MeV. The MeVelectrons from the ambient population of the secondary cosmic rays were accelerated in the strong electric fields of the thundercloud and run away, unleashing an electron-photon avalanche. The maximal energy of runaway electrons can be as high as 50 MeV and that of bremsstrahlung gamma rays – 30-40 MeV. The very high intensity of TGE means that the thundercloud is just above the detector location site. Thus, the bremsstrahlung gamma rays can reach the detector and be registered. Each of the five NaI spectrometers stores each minute a histogram of energy releases. These histograms are added up and a power-law fit is applied to the joint histogram.
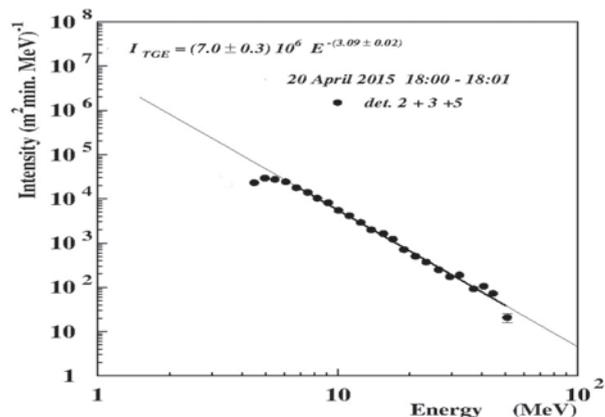
Figure 19.. The differential energy spectrum of the super-event that occurred on 20 April 2015. The spectrometers number 2,3 and 5 involved from the NaI network consisted of 5 units.

6. EXTENSIVE AIR SHOWERS DETECTED BY ARAGATS NEUTRON MONITOR AND MUON DETECTOR

Extensive air showers are initiated by protons or stripped nuclei, which in the interaction with the atmosphere unleash an electron-hadron cascade. Dependent on the energy of primary particles EAS can penetrate the Earth's surface and beneath it (high energy muons and neutrinos). EAS duration as registered by the surface particle detectors does not exceed a few tens of nanoseconds. However, several detectors that contain a lot of absorbing matter can prolong the "life" of EAS to ~ 1 ms. In the Neutron monitor's 5 cm lead producer the EAS hadrons generate many hundreds of neutrons and in the polyethylene moderator they slow the neutrons down to thermal energies before entering the proportional counters. Due to multiple scattering in the absorber and moderator, the time distribution of the secondary neutrons became significantly broader. Thus, the time distribution of the pulses from the proportional counters of the neutron monitor after EAS propagation extends to ~ 1 ms, thousands of times larger than the EAS passing time (Balabin et al., 2011). The measurements on Tien-Shan demonstrated that EASs with energy greater than 10 PeV with axes in 3-10 meters from NM could produce multiplicities above 1000 (Antonova et al., 2002).

The Aragats neutron monitor (Fig. 3) has a special option for the EAS detection. Usually the dead time of NM is set to ~1 ms for one-to-one relation of incident hadrons and detector counts. Thus, all neutrons entering the proportional

chamber after the first one will be neglected. In ArNM we use several dead times and the shortest one, the 400 nsec, can count almost all the secondary neutrons that enter the proportional chambers. Thus, if ArNM with the shortest dead time registers much more signals than with ~ 1ms dead time it means that the EAS core is hitting the detector. Within 1 ms, if we assume very large (continuous) thermalized neutron flux, 2500 thermal neutrons can be registered. Sure, only extremely energetic EASs hitting NM can produce this very large multiplicity.

In Fig. 20 we demonstrate one of such events with a total multiplicity of 2310 measured by the shortest dead time of 0.4 μs. The count rate corresponding to larger dead times also enhanced; however, only by 17% (250 μs dead time) and by 14% (250 μs dead time) of the shortest dead time. The distribution of multiplicity among 8 operational proportional chambers (see insert in fig. 20) is more or less uniform with the center of gravity of counts in the second section of ArNM (counters 7 and 8).

Name	Mean	σ	Min	Max
ArNM #3	42.58	7.57	27 (-2.06σ)	214 (22.63σ)
ArNM #4	44.49	7.74	31 (-1.74σ)	218 (22.42σ)
ArNM #8	56.9	9.87	35 (-2.22σ)	450 (39.82σ)
ArNM #9	60.8	10.12	41 (-1.96σ)	284 (22.06σ)
ArNM #13	20.56	5.66	9 (-2.04σ)	268 (43.74σ)
ArNM #14	35.02	7.09	21 (-1.98σ)	373 (47.66σ)
ArNM #16	23.29	6.36	12 (-1.77σ)	230 (32.49σ)
ArNM #17	38.95	8.15	22 (-2.08σ)	259 (27.01σ
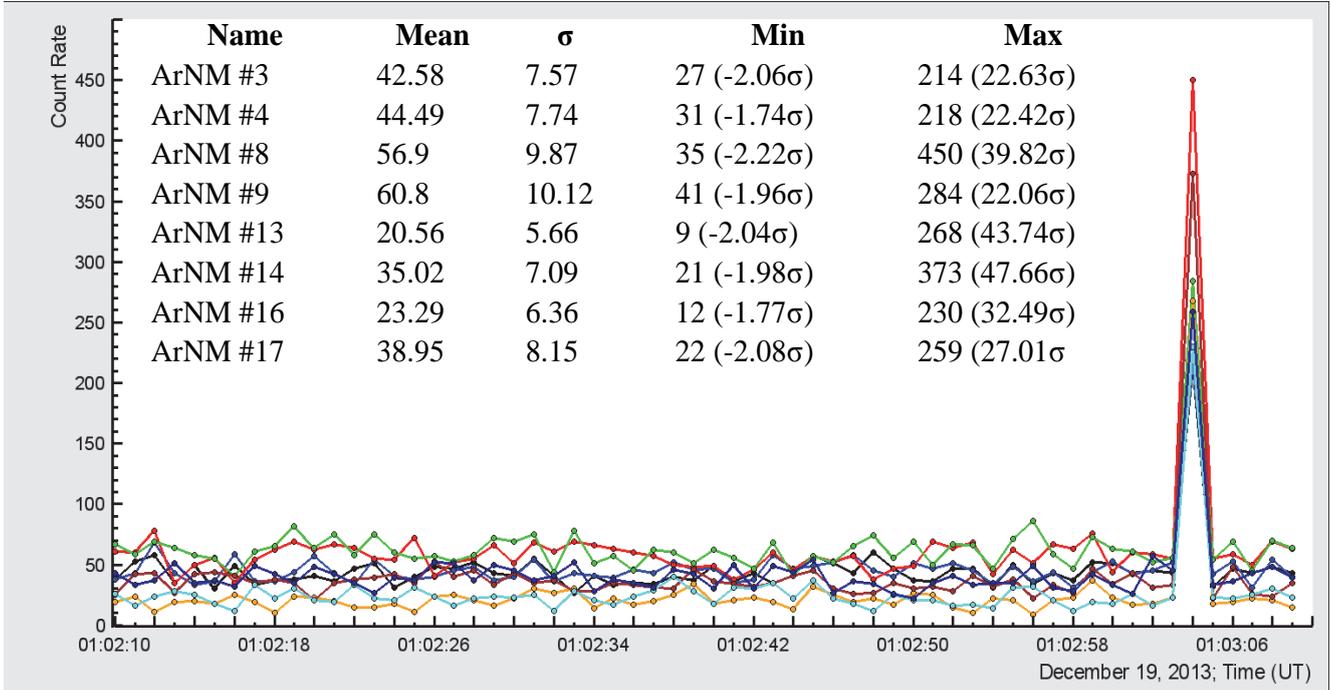
Figure 20.. Time series of ArNM proportional counters registered a large neutron burst at 1:03:4 on 19 October 2013. The mean value and variance of the one-second time series of each counter were calculated by 59 ArNM counts from 1:02:10 to 1:03:9 with the second of the neutron burst excluded.

Name	Mean	σ	Min	Max
Dead time 0.4μs	338.47	27.37	276 (-2.28σ)	2060 (62.72σ)
Dead time 250μs	307.03	22.55	250 (-2.53σ)	440 (5.9σ)
Dead time 1250μs	278.63	19.19	230 (-2.53σ)	337 (3.04σ)
3cm scint. 7.5cm Lead	261.95	13.58	232 (-2.21σ)	541 (20.56σ)
1cm scint. 9cm Lead	178.97	12.9	156 (-1.78σ)	390 (16.35σ)
1cm scint. 15cm Lead	125.27	11.12	92 (-2.99σ)	313 (16.88σ)
3cm thick scintillator	478.83	18.74	440 (-2.07σ)	479(0.01σ)
Coinc. of Muon scint.	4.9	2.36	1 (-1.65σ)	47 (17.87σ)
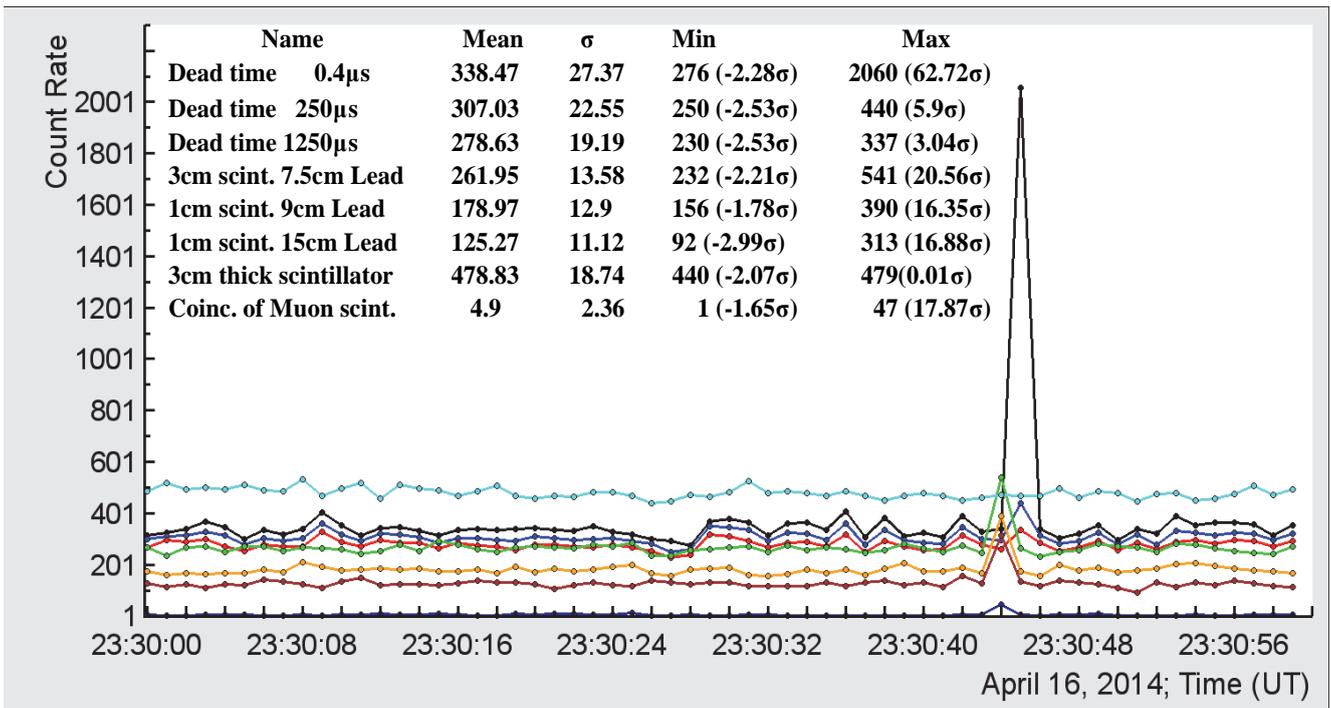
Figure 21.. Large neutron burst detected by the ArNM with dead time 0.4 us. All 3 layers of Muon detector and coincidences also demonstrate large enhancement (see insert). 3 cm thick plastic scintillator shows no enhancement. The 1 sec shift in time series of ArNM and Muon detectors is explained by the accuracy of time series detected by separate DAQ systems.

19

| Name	Mean	σ	Min	Max
ArNM #3	39.19	6.97	24 (-2.18σ)	184 (20.77σ)
ArNM #4	43.05	6.56	30 (-1.99σ)	218 (26.67σ)
ArNM #8	56.49	10.9	40 (-1.51σ)	293 (21.69σ)
ArNM #9	64.29	9.93	45 (-1.94σ)	292 (22.93σ)
ArNM #13	17.54	4.45	9 (-1.92σ)	178 (36.05σ)
ArNM #14	36.14	8.84	18 (-2.05σ)	283 (27.92σ)
ArNM #16	22.03	5.27	10 (-2.28σ)	252 (43.65σ)
ArNM #17	35.8	6.9	18 (-2.58σ)	278 (35.11σ)
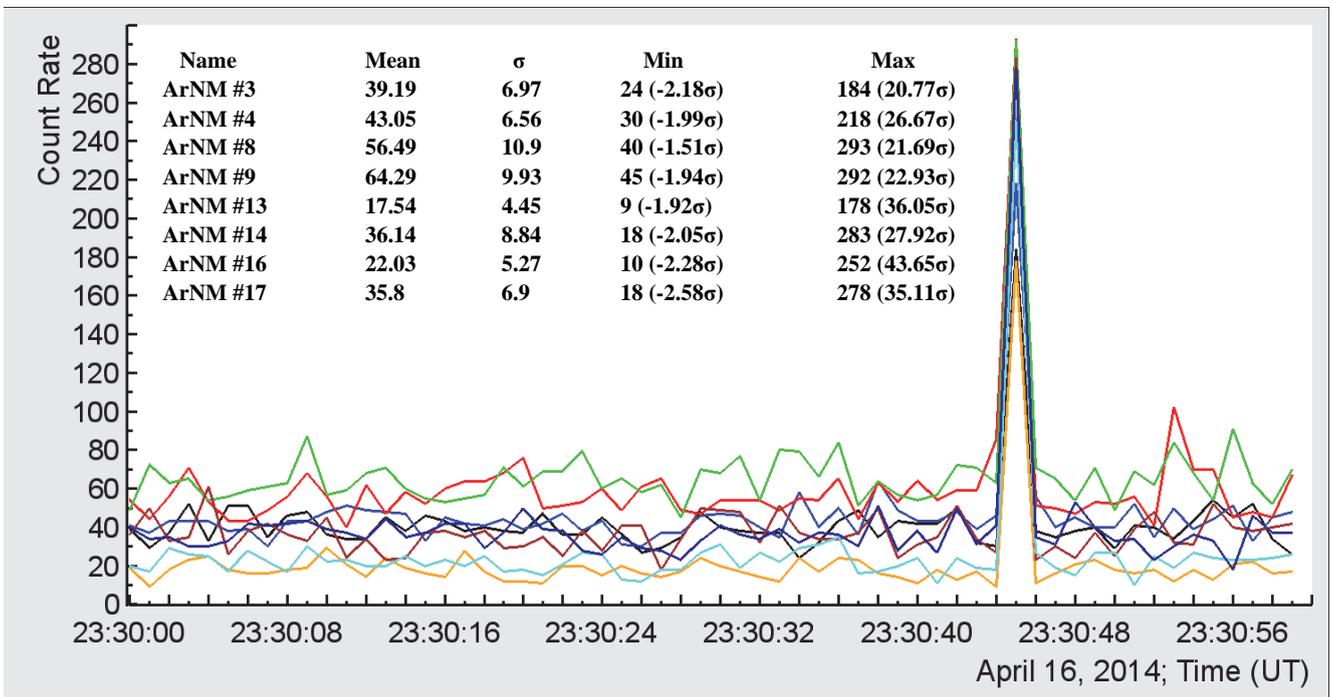
Figure 22. Time series of ArNM proportional counters registered a large neutron burst at 23:40:45 on 16 April 2014. The mean value and variance of the one-second time series of each counter were calculated by 59 ArNM counts from 23:30 to 23:30:59 with the second of the neutron burst excluded.

In Fig. 21 we show another large neutron burst this time detected also by the Muon detector. In the insert to Fig. 21 we show the enhancement of proportional counters and scintillators of ArNM, Muon and outdoors scintillator without any matter above. The multiplicity (size of the neutron burst) in ArNM equals 2060. All 3 scintillators of Muon detector show huge enhancements. The number of coincidences in 3 scintillators exceeds by an order of magnitude. The outdoors scintillator demonstrates no enhancement at all.

In Fig. 22 we show the corresponding enhancements in 8 proportional counters of ArNM. The uniform distribution of counts in all sections of ArNM and huge enhancements in Muon detector located at a distance of 6 m from ArNM verifies very large size of EAS core, exceeding 10m. Thus, the energy of the primary particle initiate EAS was enormously large.
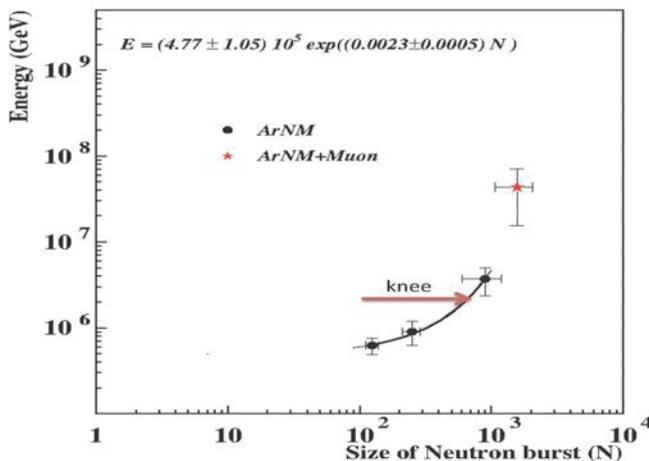

Figure 23. The dependence of the multiplicity (size) of neutron burst on energy of primary particle, which initiated EAS (obtained by relation of the frequency of different observed multiplicities (neutron burst sizes) to integeral energy spectrum measured by MAKET array (Chilingarian et al., 2004). By arrow we show the knee position of the all particle spectrum and by asterics – the primary particle energy corresponding to the frequency of detecting bursts both in ArNM and muon detector.

In Fig. 23 shows the neutron burst multiplicity as a function of the energy of the primary proton initiated EAS. The relation was obtained by the frequency analysis through the counting intensities of multiplicities (one-second peak counts) of different magnitude and relating them to the integral energy spectrum measured by the MAKET array at the same place several years ago (Chilingarian et al., 2004).

The multiplicities above 2000 are extremely rare, 1-2 per month; neutron bursts detected by both ArNM and Muon are even rarer, 3-4 per year. The primary particle energies corresponding to these events are well above 10^{16} eV. In the last 3 years we detect only 2 strong negative cloud-to-ground lightnings (-CG) coinciding with enhancements in muon detector. Unfortunately, at 11:20:53 on 19 October 2013, the lightning was so strong that several ASEC particle detectors (including ArNM) remained "blind" for several seconds, including the second of a huge enhancement in Muon detector. At 18:00 on 20 April 2015 the ArNM was switched off due to electronics failure. Thus, we have 2 coinciding events of a strong nearby lightning and a very high-energy EAS, which possibly facilitate the propagation of the lightning leader through mater LPCR. These lightnings also abruptly terminated a huge TGE on the stage of its maximal flux (Fig. 16 and 17).

7. CONCLUSION

April thunderstorms, as usual, also in 2015, bring a lot of TGEs observed by Aragats Space Environment center particle detectors and field meters. Using 1-sec time series we investigate the relations of lightnings and particle fluxes. For the first time we bring vast evidence on simultaneous detection of TGEs, disturbances of the electrostatic field and lightnings. Lightning flashes terminated the particle fluxes very often; during some of TGEs the lightning terminated the particle flux 3 times. Only a negative lightning can terminate TGEs. We have no TGE terminated by a positive lightning. We classify positive and negative lightnings by the characteristic pattern of disturbance of near-surface electrostatic field that we

measure 20 times per second with a network of EFM-100 electric mills. According to the model (Nag and Rakov, 2009), lightnings terminate the particle fluxes mostly in the beginning of TGE or on the decay of it, when the Lower positive charge region is "thinning" and the lightning leader can make a path through it and connect the negative charge region in the cloud and ground. However, we observed two events (19 October 2013 and 20 April 2015) when huge TGEs were terminated just on the maximum of their development, i.e. when LPCR was thick and mature and should prevent the lightning leader to reach the Earth's surface. The Muon detector fixed a huge EAS in the same second when the TGE abruptly terminated. Thus, in one and the same second we observe: abrupt termination of TGE at maximal particle flux, a large EAS and a negative cloud-to-ground lightning. Unfortunately, we do not detect all the 3 processes on the microsecond time scales. However, following the theory of a combined effect of RB-EAS effect (Gurevich, et al., 1999), we can assume that the strong ionization in the atmosphere due to passage of a high-energy EAS (E > 10^{16} eV) under RB conditions, produced a strong local pulse of electric current that initiated a lightning leader and, thereafter, a negative cloud-to-ground lightning. Of course, our findings need to be confirmed by measurements with a microsecond time resolution, which are planned for 2016-2017 at Aragats. It is very important to correlate particle flux enhancements and lightnings on millisecond time scales. The lightnings are a powerful source of electromagnetic radiation and can influence DAQ electronics and produce fake signals. However, as we demonstrate in (Chilingarian et al., 2016), the particle flux is changing not immediately with a huge pulse of electromagnetic radiation, but with the rearrangement of the electric fields in the cloud after depositing the negative charge to the ground by a lightning. And there is a delay of at least several tens of milliseconds between these processes. Therefore, to avoid possible interferences and fake signals in the particle detectors, we plan to add a precise time stamp to each registration in the Muon detector.

By detecting TGEs with the same type of detectors although different amount of matter above and, therefore, having different energy thresholds, we prove the existence of two-components of particle population in the TGE. The high-energy one (from 3-4 till 40-50 MeV) is local and short in time (several minutes) and is connected with RB/RREA process above the detectors resulting in bremsstrahlung gamma photons. The second, low- energy component (0.4-3 MeV) lasted several hours and, as we admit, is connected with the Compton-scattered gamma rays that reach the detectors from the distant regions of the cloud.

ACKNOWLEDGEMENT

REFERENCES

- Alexeenko V.V., Khaerdinov N.S., Lidvansky A.S., and Petkov V.B., 2002. Transient Variations of Secondary Cosmic Rays due to Atmospheric Electric Field and Evidence for Pre-Lightning Particle Acceleration, *Physics Letters A*, 301, 299-306.

- Antonova A.P., Chubenko A.P., Kruychkov S.V. et al., 2002. Anomalous time structure of extensive air shower particle flows in the knee region of primary cosmic ray spectrum, J. Phys. G: Nucl. Part. Phys. 28, 251–266.

- Balabin, Yu. V., Gvozdevsky B. B., Vashenyuk E. V., and Dzhappuev D. D., 2011. EAS hadronic component as registered by a neutron monitor, Astrophys. Space Sci. Trans., 7, 507-510.

- Chilingarian, A., Gharagyozyan, G., Hovsepyan, G., Ghazaryan, S., Melkumyan, L., Vardanyan, A., 2004. Light and heavy cosmic-ray mass group energy spectra as measured by the MAKET-ANI detector. Astrophys. J. 603, L29–L32.

- Chilingarian, A., Arakelyan, K., Avakyan, K., et al., 2005. Correlated measurements of secondary cosmic ray fluxes by the Aragats Space-Environmental Center monitors. Nucl. Instrum. Methods Phys. Res., Sect. A 543 (2–3), 483–496.

- Chilingarian, A., Daryan, A., Arakelyan, K., et al., 2010. Ground-based observations of thunderstorm-correlated fluxes of high-energy electrons, gamma rays, and neutrons. Phys. Rev. D 82, 043009.

- Chilingarian, A., Hovsepyan, G., Hovhannisyan, A., 2011. Particle bursts from thunderclouds: natural particle accelerators above our heads. Phys. Rev. D 83, 062001.

- Chilingarian A., Mailyan B., and Vanyan L., 2012. Recovering of the energy spectra of electrons and gamma rays coming from the thunderclouds, Atmospheric Research 114–115, 1–16.

- Chilingarian, A., Mkrtchyan, H., 2012. Role of the lower positive charge region (LPCR) in initiation of the thunderstorm ground enhancements (TGEs). Phys. Rev. D: Part. Fields 86, 072003.

- Chilingarian A., Hovsepyan G., and Kozliner L., 2013. Thunderstorm ground enhancements: Gamma ray differential energy spectra, Physical Review D 88, 073001.

- Chilingarian A., 2014. Thunderstorm Ground Enhancements - model and relation to lightning flashes, Journal of Atmospheric and Solar-Terrestrial Physics 107, 68–76.

- Chilingarian A., Chilingaryan S., Hovsepyan G., 2015. Calibration of particle detectors for secondary cosmic rays using gamma-ray beams from thunderclouds, Astroparticle Physics 69, 37–43.

- Chilingarian A., Hovsepyan G., Khanikyanc G., Reymers A. and Soghomonyan S., 2015. Lightning origination and thunderstorm ground enhancements terminated by the lightning flash, EPL, 110 49001.

- Chilingarian A., Hovsepyan G., Khanikyants Y., Pokhsraryan D., and Soghomonyan S., 2016. Atmospherics discharges - particle flux relations in the TGEs terminated by the lightning flash, Proceedings of TEPA 2015, Nor Amberd, Tigran Mets

- Dwyer, J.R., Smith, D.M., Cummer, S.A., 2012. High-energy atmospheric physics: terrestrial gamma-ray flashes and related phenomena, Space Sci. Rev., 173, 133–196.

- Dwyer J.R., Uman M.A., 2013. The physics of lightning, Physics Reports Phys. Rep., 534(4), 147–241.

- Erlikin A.D., 2007. The neutron 'thunder' accompanying the extensive air shower, J.Phys, G33, 565-576.

- Fishman, G.J., Bhat, P.N., Mallozzi, R., Horack, J.M., Koshut, T., Kouveliotou, C., Pendleton, G.N., Meegan, C.A., Wilson, R.B., Paciesas, W.S., Goodman, S.J., Christian, H.J., 1994. Discovery of intense gamma ray flashes of atmospheric origin. Science 264 (5163), 1313–1316.

- Gurevich A.V., Milikh G.M. and Rouseel-Dupre R, 1992. Runaway electron mechanism of air breakdown and preconditioning during a thunderstorm, Physics Letters A 1992, v.165, pp.463 – 468.

- Gurevich A.V., Zybin K.P, Roussel – Dupre R.A., 1999. Lightning initiation by simultaneous of runaway breakdown and cosmic ray showers, Phys.Lett. A 254, 79.

- Kelley N.A., Smith D.M., Dwyer J.R., et al. 2015. Relativistic electron avalanches as a thunderstorm discharge competing with lightning, Nature communications, 6, Article number: 7845.

- Krehbeil P., Mazur V., Rison W., Standardizing the sign convention for atmospheric electric field measurements 2014. Newsletter on Atmospheric Electricity Vol. 25 No 2, 5.

- Nag A. and Rakov V. A., 2009. Some inferences on the role of lower positive charge region in facilitating different types of lightning Geophys. Res. Lett., 36, L05815.

- Stenkin Yu. V., Djappuev D. D., and Valde's-Galicia J. F., 2007. Neutrons in Extensive Air Showers , Physics of Atomic Nuclei, 70, 1088–1099.

- Tsuchiya H., Enoto T., Iwata K., et al., 2013. Detection of high-energy gamma rays from winter thunderclouds, Phys. Rev. Lett., 111, 015001.

- Stolzenburg M, Rust W, Marshall T., 1998. Electrical structure in thunderstorm convective regions 3. Synthesis. J Geophys Res, 103: 14097—14108.

Fast Data Acquisition system based on NI-myRIO board with GPS time stamping capabilities for atmospheric electricity research

D. Pokhsraryan

A.Alikhanyan National Lab (Yerevan Physics Institute), 2, Alikhanyan Brothers, Yerevan 0036, Armenia;

Abstract. In the investigation of the fast physical processes, such as propagation of a lightning leader and detection of the correspondent radio emission waveforms, it is crucial to synchronize the corresponding signals in order to be able to create a model of the lightning initiation. Therefore, the DAQ system should be equipped with a GPS synchronization capability. In the presented report, we describe the DAQ system based on a NI-myRio board that provides detection of particle fluxes, the near-surface electric field disturbances and waveforms of radio signals from atmospheric discharges, all synchronized with an accuracy of tens of nanoseconds. The results of the first measurements made at Aragats high-altitude station of Yerevan Physics Institute in Summer-Autumn 2015 are presented and discussed.

1. INTRODUCTION: REQUIREMENTS ON DAQ SYSTEM

When designing a Data Acquisition Electronics (DAQ) system to be used in the high-energy physics and astrophysics experiments, the standard requirement is to achieve reliable and consistent registration of all electronic signals from the particle detectors with inherent correlations. The parameters of DAQ system should be continuously monitored to keep them stable. Electronics should not introduce any uncertainty in the particle detection due to changing efficiency and variations of the "dead times". The particle energy released in the bulk of the plastic scintillators provides additional information on the type and energy of particles. DAQ electronics should be able to measure and store not only the number of registered particles in a definite time span (usually 1 sec or 1 minute), i.e. time series of count rates, but also histograms of energy releases, i.e. amplitudes of the Photomultiplier (PM) signals.

The PMTs, High Voltage Power Supplies, Buffer Preamplifiers as well as the Logarithmic Analog-to-Digital Converter (LADC), the 8-channel counter board (8CNT) with a programmable threshold are the same as were previously used in the Aragats Space Environmental Center (ASEC, Chilingarian et al., 2005, Arakelyan et al., 2009) DAQ systems. All these elements are highly integrated into the ASEC infrastructure; they proved to be robust and demonstrating a reliable performance for many years under severe climatic conditions.

The buffer preamplifier with a +1 voltage gain amplifies the PMT signals. The amplifier with the output resistance of 50 Ohm sends the pulse signal, completely repeating the shape of PMT anode current pulse, through the impedance matched 50-Ohm coaxial transmission line to the control room for further processing. Thus, the whole information about the event registered by the detector is delivered to the LADC without any losses. To transform the analog measurement in digital form the PMT signals are rectified, smoothed and compared with a reference voltage, which varies exponentially. To ensure the correct work of LADC and to control the threshold of comparator we use a voltage from the output of the Digital-to-Analog Converter. For investigation of such fast physical processes as propagation of lightning leader and detection of correspondent

fast waveforms of radio emitting, the accuracy of the time stamp of the registered events should be several tens of nanoseconds. Therefore, the DAQ system should be equipped with a GPS synchronization capability. The registration of an Extensive Air Shower (EAS) – a gigantic cascade of particles propagating in the atmosphere with a velocity reaching the speed of light, the synchronization of different registration channels is very important as well. In the presented report, we describe the DAQ system and the first measurements made at Aragats high-altitude station of Yerevan Physics Institute in Summer-Autumn 2015.

2. THE NI-MYRIO BOARD

The heart of the DAQ system is National Instrument's NI-myRIO board (see Fig. 1 and attachment). It combines the Xilinx Zynq All Programmable SoC with a ready-to-go Linux-based real-time OS (RTOS). It places 40 GPIOs (general propose input output), wireless capabilities, a dual-core ARM real-time processor, and a customizable Xilinx FPGA. The output pulses of the 8CNT board are fed to the FPGA of the myRIO board where the logic of event identifying, pulses counting and GPS time stamping is implemented.

A custom PCB is made based on a myRIO Expansion Port (MXP) Breakouts KIT. It includes the GPS module connection UART for NMEA sentences and a 1PPS signal for FPGA time keeping algorithm. The board is also equipped with a 20 pin 2.54mm pitch PCB IDC Connector to feed the output pulses of the 8CNT board to the FPGA of the myRIO board via a ribbon cable. With the reconfigurable FPGA technology, we perform high-speed signal processing, high-speed control, inline signal processing, and custom timing and triggering. For the control systems, one can also run advanced control algorithms directly in the FPGA fabric to minimize latency and maximize loop rates.

LabVIEW FPGA Module", which extends the LabVIEW graphical development platform, provides an alternative to HDL (Hardware description language) graphical programming approach that simplifies the task of interfacing to I/O and communicating data. This greatly improves the embedded system design productivity and reduces the time of project accomplishment.
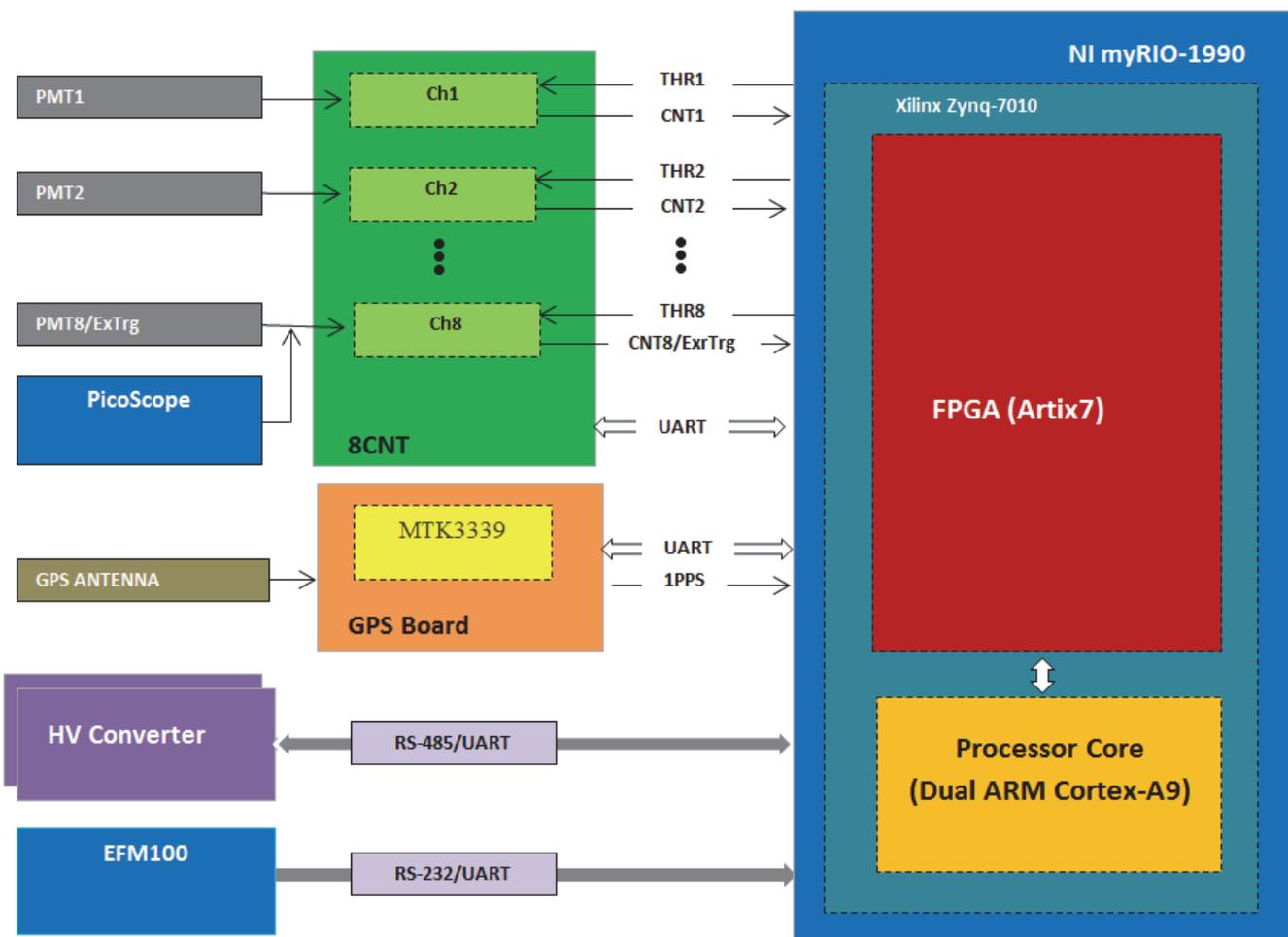
Figure 1. The DAQ system: Photomultipliers (PMT) FEU49, PM30 or other types; Programmable Local High Voltage Power Supply for PMT with RS-485 interface; Buffer Preamplifier; Board of 8 Logarithmic Analog-to-Digital Converter (LADC)/or 8-channel counter board (8CNT); GPS Module with an active antenna FGPMMOPA6H; NI-myRIO -1990.

The commercial GPS module directly supplies the date and "coarse" UTC time and reports geographic location (latitude and longitude) down to the equivalent of a few tens of meters. The GPS receiver sends two types of datastreams to the board. The first is RS-232 ASCII data, telling what time it is, at what latitude, longitude and altitude the receiver is, and information about the satellites the receiver is attaching. An embedded 25 MHz counter on FPGA gives the exact time of the event. The 1PPS (one pulse per second) stream of the 5V, 100-ms pulses resets this counter at each second. The leading edges of 1PPS signals from GPS receivers anywhere in the world are all synchronized within the accuracy of the non-military GPS system (about 100 ns.) This feature allows accurate time synchronization; the estimated resolution to meet is 100 ns. However, the GPS module FGPMMOPA6H (a 4th generation stand-alone GPS module with lightning fast TTFF (Time-to-First Fix), ultra-high sensitivity -165dBm, and low power consumption gives us 10 nsec resolution.

3. HIGH PRECISION DAQ SYSTEM IN HIGH-ENERGY ATMOSPHERIC RESEARCH

The research of the high-energy physics in the atmosphere is still in the earliest stage and each year new interesting phenomena are discovered (Chilingarian et al., 2010, 2011, Chilingarian, 2014). Measurements of the amplitude, duration, energy spectra of the particle fluxes from the thunderstorm atmosphere, the so-called Thunderstorm Ground Enhancements (TGEs) performed at Aragats Space Environmental center (ASEC) prove vast variability and richness of new phenomena. Recently at ASEC, we started the correlation analysis of the TGEs and lightnings that pose additional requirements on the time resolution and synchronization of particle detectors, near surface electric field sensors and sensors of the fast radio waveforms of atmospheric discharges. The DAQ electronics being developed can solve such problems.

The four inputs of DAQ (Fig. 1) are used for feeding signals from STAND1 detector comprised of 3 vertically stacked 1 cm thick and 1 m^2 area plastic scintillators and 1 stand-alone 3 cm thick plastic scintillator of the same area (near the SKL experimental hall). The DAQ pulse counting system can provide very short time series down to 1 millisecond that will enable to investigate in much more details the dynamic of TGE development and its relation to the lightning initiation.

Signals from the sensor of "slow" near surface electric field disturbances (from the "electric mill" EFM-100 of Boltek company) are fed to the myRio board by the TCP-IP connection (WiFi). The firmware application provided by Boltek has a feature to share E-Filed data via network. It acts as a server for a client running under myRIO for E-Field measurements.

The EFM-100 has also an analog output for direct measurements but, unfortunately, it is not optically isolated. It is directly connected to the field mill and a lightning hazard exists at those connections. There are plans to implement optical connection and use direct analog measurements utilizing 500 kHz 12 bit analog inputs on the myRIO device.

One channel is reserved for the synchronization pulse (the trigger) from the device recording a fast waveform. A flat-plate antenna followed by a passive integrator is used to record fast electric field change waveforms. The output of the integrator is directly connected to the digital oscilloscope (Picoscope 5244B) with 60 cm long RG58 coaxial cable. The waveforms are recorded with a sampling rate of 62.5MS/s, (sample interval 16ns) and 8-bit resolution. Data capture length is 500ms, including 100ms pre-trigger and 400ms post-trigger time. The oscilloscope trigger is connected to the GPS time-stamping system described above. Any fast electric field waveform recorded by the oscilloscope that is above the trigger threshold forces the GPS system to trigger and produce a timestamp. *A special output will be generated at any triggering signal* containing precise times of each particle arrival 100 msec before and 400 msec after trigger, near surface electric field value and other information (number of satellites used by GPS system, etc). Thus, the fast waveform patterns will be synchronized with particle arrival to detector with an accuracy of a few tens of nanoseconds.

Two from three units of the STAND1 type detectors that compose a network for the TGE and lightning research are equipped with the new DAQ system (the third one will be equipped with myRio board electronics in summer 2016). Universality of the system will allow solving of the EAS registration problem as well. The unit installed in MAKET experimental hall is attached also to 3 channels of the muon detector (channels 5-7) comprised of 3 vertically stacked plastic scintillators interlayered with a total of 15 cm of lead and 60 cm of carbon. Several channels of 18NM Neutron Monitor located nearby will be attached to the DAQ system too. The Neutron Monitor and Muon detector are sensible to Extensive Air Shower (EAS) cores that occasionally hit the MAKET building (Chilingarian, Hovsepyan and Kozliner, 2016). Thus, DAQ electronics will register simultaneously EAS particles, near surface electric field and TGE.

The mechanism of particle acceleration is due to the existence of free electrons in the atmosphere as well as on the origination of a Lower positive charge region (LPCR, Chilingarian and Mkrtchyan, 2012), which, together with the negatively charged region in the middle of the cloud, forms a positive dipole that accelerates the ambient cosmic-ray electrons downward to the Earth. A mature LPCR is a necessary condition for unleashing of a Relativistic Runaway electron avalanche (RREA) and registering a TGE on the Earth's surface. LPCR as well do not let a lightning leader to reach the Earth, changing its direction horizontally. Usually no cloud-to-ground lightnings (-GC) are registered during TGE, just intracloud (-IC) lightnings are. The second mechanism that connects the lightning discharge with EASes postulates that the lightning leaders follow the EAS path in the atmosphere. If a large EAS hits the thundercloud during TGE, the huge amount of EAS electrons can enable the lightning leader propagation through the LPCR and TGE will abruptly terminate. The new DAQ electronics will help us to observe in details these very complicated phenomena and unambiguously establish the relation between EAS, TGE and lightning initiation. Large EAS detection is a rather rare event and registration of EAS on the nanosecond time scale will help to reveal the 3-dimensional structure of these gigantic particle showers. The DAQ system will store the current data from the muon detector and neutron monitor channels by the abruptly enhanced muon detector coincidences, reflected passage of numerous high-energy muons from EAS core through particle detectors.

4. FIRST DETECTION OF PARTICLE FLUXES AND ATMOSPHERIC DISCHARGES

In August and September 2015, two myRio boards were installed in MAKET and SKL experimental halls at Aragats station. To the myRio boards are attached 4 channels of the STAND1 detector, see Fig. 2. The top row of the picture shows the photo and the drawings of STAND1 detector. The three plots in the middle show the correlations
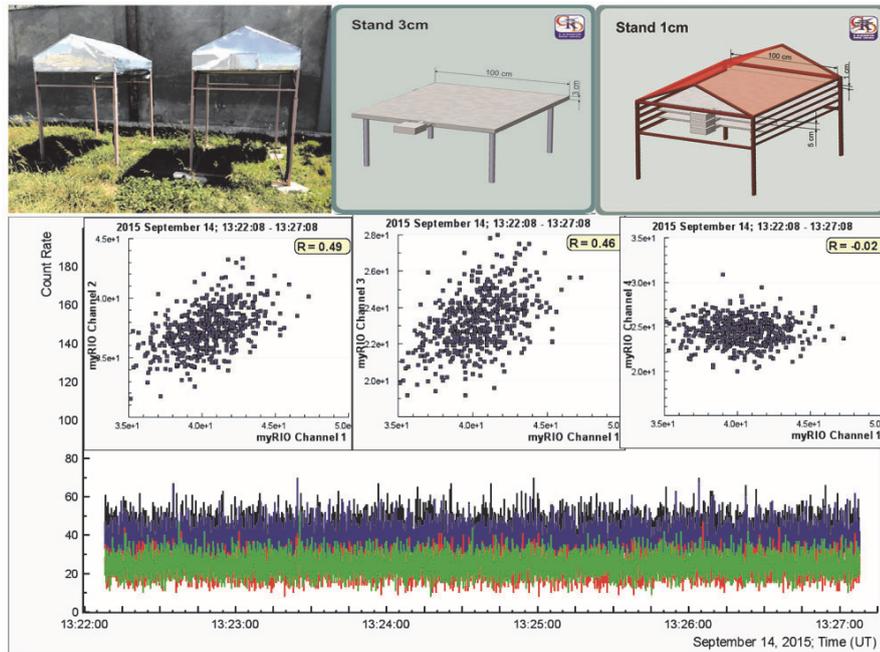
Figure 2. Correlations of 50 msec time series; top row – the photo of detector near the SCL experimental hall and charts of detector; the middle row – correlations of top scintillator with other 3; bottom row – 50 msec time series of 4 scintillators.

of the STAND1 detector's layers. The correlation of the top scintillator and stand-alone 3 cm thick scintillator is minimal, due to small fraction of particle showers with size of ~

1 m and larger. The correlation of stacked scintillators is significantly larger due to the penetrating high-energy mu-

ons and electrons. In the bottom of Fig. 2, the 50 msec time series of STAND1 detector's scintillators are shown.

First large TGE of Autumn 2015 occurred on 7 October at 14:42-14:47, (see Fig. 3). One-minute time series of the STAND1 detector demonstrate huge enhancement, reaching ~100 standard deviations (100σ).
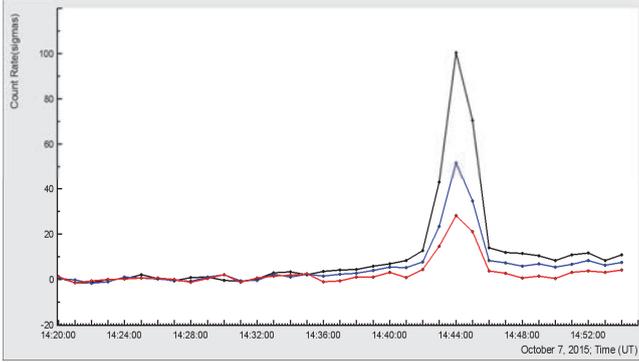
Figure 3. The TGE observed by STAND1 scintillators by 1-minute time series of count rates in number of standard deviations; the upper curve corresponds to upper scintillator, middle curve – to the middle scintillator and bottom curve to the bottom scintillator.

In Fig. 4, we show the two-second time series of the 60 cm thick scintillator of the ASNT detector; the abrupt decay of the count rate is apparent at 14:45:07. From 14:45:05 to 14:45:11 the count rate diminished by 11.6% (from 3263 to 2839 – the background value). The negative lightning that occurred in this time span raises the near surface electric field from -29 to +43 kV/m, i.e. the amplitude of lightning as measured by the near-surface electrostatic field was 72 kV/m (measured by the EFM-100 electric mill located on the roof of MAKET building).
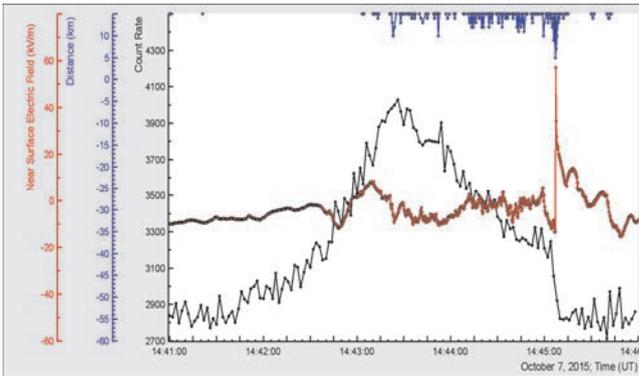

Figure 4. The same TGE as in Figure r observed in 2-second time series of the 60-cm thicj scintillator of the ASNT detector.; in the middle – disturbances of electric field with lightning coinciding with particle flux decline; in the top – distance to lightning by EFM-100 MAKET.

The 50 ms time series of STAND1 detector can bring additional evidence on the relations of lightning and particle flux decay. In Fig. 5 we demonstrate four seconds of the count rates of 3 cm thick outdoors plastic scintillator including the lightning time and particle flux decline time. In the left two "pre-lightning" seconds the count rate is larger than in the two "right" seconds. The lightning started at 14:45:07 and reached its maximum at 14:45:07.10 (the start and maximum are denoted by arrows in Fig. 5). The count rate declined at 14:45:7.175 and returned to the background level after the electric field reached its maximum, i.e. after the return stroke deposited the negative charge on the ground and the overall electric field in the cloud generally rearranged. Thus, after charge redistribution in the thundercloud the electric field, which accelerates electrons downward during TGE declines and particle flux abruptly termi-

nates. The synchronization signal from Picoscope arrives before the lightning struck at 14:45:6:95.
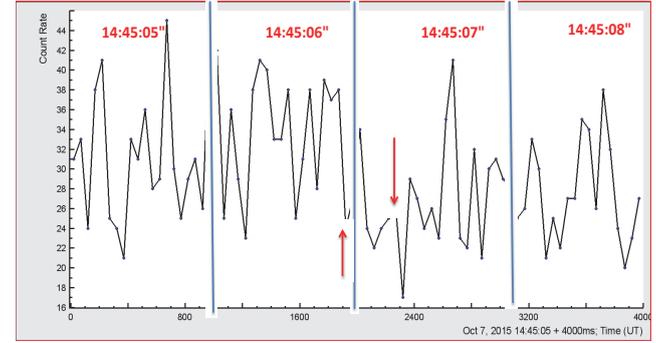

Figure 5. Four seconds of 50 msec time series before and after sharp decline of particle flux at 14:45:07 as measured by 1-sec time series; seconds are separated by the vertical lines; the picoscope (fast waveforms) trigger at 14:45:06.95 and maximum of near surface electric field (return stroke) at 14:45:07.15 is denoted by an arrows.

The exact time synchronization can be checked by the Picoscope trigger pulse and by the corresponding myRio registrations. In Fig. 6a we show the TGE occurred on October 14 2015 along with disturbances of the near-surface electrostatic field and solar radiation. As usual, the particle flux increased when the field was in the negative domain. Before the TGE several lightnings occurred, some of which generated triggers in the picoscope. In the zoomed Fig 6.b we show the time of the picoscope triggers. The corresponding GPS time stamps from myRio were as follows: 13:22:25.291, 13:23:17.586 and 13:24:23.634. Thus, we have now time stamp of picoscope trigger with at least one-millisecond accuracies. In this way we can synchronize particle fluxes and fast waveforms with the same accuracy.
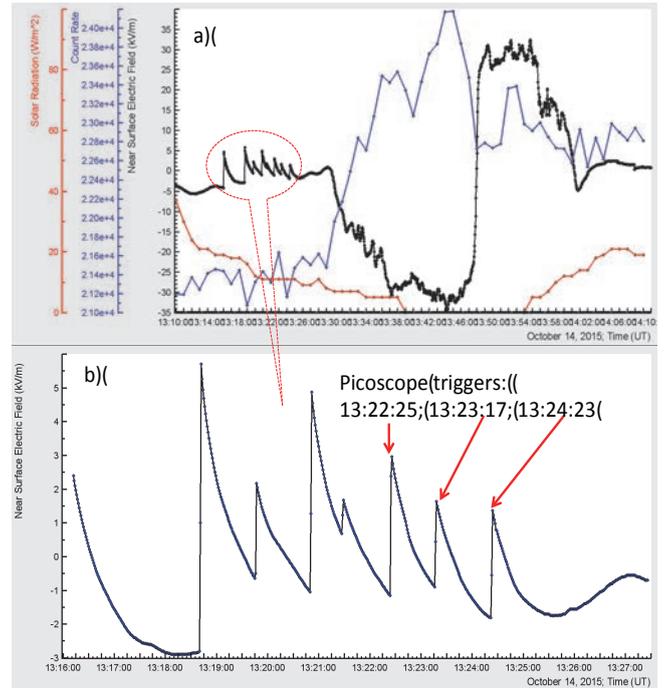
Figure 6 .The enhancement of the particle flux by the 1-minute time series of the upper scintillator of STAND1; in the bottom solar radiation decreasing till zero at TGE time (thick cloud was sitting just on the station. In the Fig. 6b zoomed version of the 5 negative discharges, 3 of which generate picoscope trigger.

5. CONCLUSION

New DAQ electronics based on NI myRio boards proves high effectiveness for the lightning-TGE research. DAQ electronics provides continuous registration of the 50 msec time series of count rates from 10 particle detectors.

The time stamp from the external trigger provides synchronization of the particle fluxes and fast waveforms of electric field with an uncertainty not worse than 1 μc.

The dynamics of the TGE events will be registered with all necessary details. For the first time it will be possible to solve long standing problems of the particle-lightning relations (Chilingarian et al., 2015a and 2015b):

Are particles born in the lightning bolt?

Do lightnings follow the path of Extensive air showers (EASes)?

On what stage of its development does a lightning abruptly cease the particle fluxes?

Do particle avalanches from the thundercloud initiate lightning?

Do LPCR prevent cloud-to-ground lightning, transforming it to an inter-cloud one?

The achieved synchronization accuracy will be very helpful in the lightning initiation researches planned in 2016.

REFERENCES

- Arakelyan K., et al., Proceedings of the International Symposium on Forecasting of the Radiation and Geomagnetic Storms by Networks of Particle Detectors (FORGES 2008) [Nor Amberd, Armenia, (Alikanyan Physics Institute, printed by Tigran Mets, Yerevan) 2009], pp. , pp. 105–116.

- Chilingarian, A., Arakelyan, K., Avakyan, K.et al., 2005. Correlated measurements of secondary cosmic ray fluxes by the Aragats space-environmental center monitors, Nucl. Instrum. Methods A 543 (2–3) 483.

- Chilingarian, A., A. Daryan, K. Arakelyan, A. Hovhannisyan, B. Mailyan, L. Melkumyan, G. Hovsepyan, S. Chilingaryan, A. Reymers, and L. Vanyan L.,2010), Ground-based observations of thunderstorm-correlated fluxes of high-energy electrons, gamma rays, and neutrons, Phys. Rev. D, 82, 043009.

- Chilingarian, A., Hovsepyan, G., Hovhannisyan, A., 2011. Particle bursts from thunderclouds: natural particle accelerators above our heads. Phys. Rev. D: Part. Fields 83 (6), 062001.

- Chilingarian A., Thunderstorm Ground Enhancements - model and relation to lightning flashes, Journal of Atmospheric and Solar-Terrestrial Physics 107 (2014) 68–76.

- Chilingarian, A., Chilingaryan, S., and A. Reymers, 2015a. Atmospheric discharges and particle fluxes, J. Geophys. Res. Space Physics, 120, doi: 10.1002/2015JA021259.

- Chilingarian A., Hovsepyan G., Khanikyanc G., Reymers A. and Soghomonyan S., 2015b. Lightning origination and thunderstorm ground enhancements terminated by the lightning flash, EPL, 110, 49001.

- Nag A. and Rakov V. A., (2009) Some inferences on the role of lower positive charge region in facilitating different types of lightning, Geophys. Res. Lett., 36, L05815.

- Pokhsraryan D, Very fast Data Acquisition system based on NI-myRIO with GPS time stamping capabilities, Proceedings of TEPA 2015, Nor Amberd, Tigran Metz, 2016, in preparation

ATTACHMENT: HARDWARE DETAILS

NI myRIO-1900

The National Instruments myRIO-1900 portable reconfigurable I/O (RIO) device integrates a dual-core ARM real-time processor, and a customizable Xilinx FPGA, and I/O on a single printed circuit board (PCB). It is ideal for low- to medium-volume applications and rapid prototyping.

- Xilinx FPGA and dual-core ARM Cortex-A9 processor
- Wireless, USB Host Port, USB Device Port
- 10 analog inputs (12bit, 500 kS/s)
- 6 analog outputs (12bit, 345 kS/s)
- 40 digital I/O lines

GPS Module

MediaTek MT3329 is a compact solution for adding GPS functionality to any device.
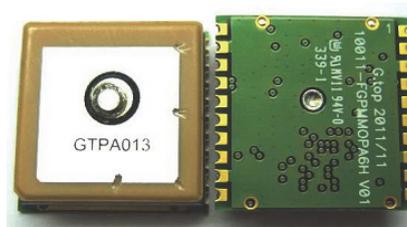
It features a high performance positioning engine with up to 12 multi-tone active interference canceller. It supports up to 210 PRN channels with 66 search channels and 22 simultaneous tracking channels. There is also an "Antenna Advisor" that helps with the detections of different antenna statuses, including active antenna connection, antenna open circuit and antenna shortage.

And the most attractive there is a high accuracy 1-PPS timing support with only 10ns jitter.

Programmable Local High Voltage Power Supply

Features:

- Voltage programming in two hardware selectable ranges ± 900V to 2100V and ±1500 to 3000V in 2V steps
- Output voltage ripple less than 1mV
- Max. output current 1.2 mA for ± 900V to 2100V range; 0.8 mA for ±1500 to 3000V range
- Input voltage from +12V to +15V
- Absolute output voltage regulated to accuracy ±1V
- Optional temperature sensor
- RS-485 half-duplex 2-wire 9600 baud interface for programming and monitoring the output voltage

Development of atmospheric polarization LIDAR System

A.S. Ghalumyan, V.R. Ghazaryan

A.Alikhanyan National Lab (Yerevan Physics Institute), 2, Alikhanyan Brothers, Yerevan 0036, Armenia;

Abstract LIDAR (**Li**ght **D**etection **A**nd **R**anging) system sensitive to the polarization of the backscattered signal is being developed in Yerevan Physics Institute. The system is designed primarily for remote sensing of the atmospheric electric fields. At present, the system is being tuned for measuring vertical atmospheric backscatter profiles of aerosols and hydrometeors, analyze the depolarization ratio of elastic backscattered laser beams and investigate the influence of external factors on the beam polarization [1]. In this paper, we describe the complete LIDAR system – the laser transmitter, receiving telescope and the polarization separator. The data acquisition and processing techniques are also described.

1. INTRODUCTION

Intensive studies in fields of high-energy phenomena in the atmosphere revealed electron acceleration and the bremsstrahlung photons generation caused by the electric field emerging in the thunderclouds [2]. Further studies demand knowledge of electrical field distribution inside clouds [3]. We are suggesting a measurement technique of the electrical field inside the clouds based on the continuous observations by a LIDAR (**Li**ght **D**etection **A**nd **R**anging) system. This technique is based on precise measurement of the backscattered laser radiation polarization changes in the clouds [4].

The real time measurements of the spatial and temporal distribution of the electric field in and around thunderclouds is important for understanding of the thundercloud formation mechanisms, for the prediction of lightning strokes initiation and for understanding of the processes of acceleration of cosmic ray electrons and generation of bremsstrahlung photons caused by the electric field of clouds.

The electric field meters, currently used for this purpose, are set on the Earth's surface or on board of balloons. These techniques are limited as electrostatic field on the Earth's surface significantly differs from that in the clouds; and balloons typically provide a single sample at discrete altitudes at one time. LIDAR systems are the main instrument which allows to realize real time remote measurement of the electric field strength and direction with high spatial and temporal resolution. LIDAR systems are based on the absorption and/or scattering of light by the gas, liquid or solids. The atomic and molecular spectra can be in a sensitive manner and very accurately measured by spectroscopy.

2. LIDAR SYSTEM OVERVIEW

LIDAR systems consist of three main parts: a Laser Emitter (LE), a Receiving System and a registration and control system.

The Laser Emitter of the polarized laser radiation is a solid state, flash-lamp pumped, Q-switched YAG: Nd3+ laser with a second harmonic generator (SHG) and a beam expander. It generates linearly polarized 10 ns pulses with 1064 nm and/or 532 nm wavelengths and a repetition rate of 10-20 Hz.

The Laser oscillator was designed to have a positive branch confocal unstable resonator and a polarization output. Designing the laser oscillator resonator we adopt that the focal length of the thermal lens is induced in the active medium. With the help of a SHG the output laser oscillator beam with 1064 nm wavelength, after amplification, is converted into the second harmonic with 532 nm wavelength. The SHG was designed to have a nonlinear crystal KD*P with angular phase matching.

The laser construction is shown in Fig. 1. The Laser beam output is equipped with an additional polarizer (a Glan prism) to obtain a higher linear polarized output beam.
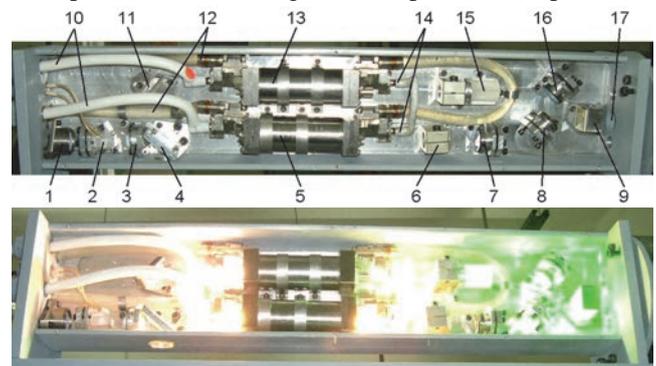
Figure 1. The Laser construction (left): 1 - Convex mirror, 2 – Electro optical Q-Switch, 3 – Diaphragm, 4 – Output polarizer, 5 – laser oscillator pump chamber, 6 – Quarter wave-plate, 7 – Concave mirror, 8 and 16 – Two wavelength mirrors, 9 – Glan prism, 10 – Flash-lamp driver cables, 11 – mirror, 12 – Cooling system pipes, 13 – Laser amplifier pump chamber, 14 – Flash-lamps, 15 – SHG, 17 – Hole for the output beam. The Laser in operation (right).

The LE Beam Expander is an extra cavity Cassegrain telescope with 14^X magnification, which allows to expand the 8 mm across laser output beam to 112mm diameter and reduce the laser beam divergence down to < 0.1 mrad.

The Laser with the beam expander mounted on the receiving telescope (RT) is shown in Fig.2.
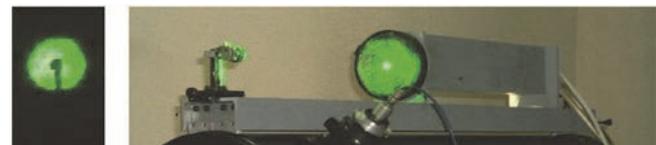
Figure 2. The Laser Emitter, including the beam expander in operation mounted on the RT (in the right) and the Laser Emitter output beam-spot on the distance of 2 meters (in the left).

Receiving System of backscattered radiation contains 250mm aperture Receiving Telescope (RT) and polarization separator (PS).

The PS is placed on the output of the receiving telescope and its function is to separate the orthogonal to

each other polarization components of the back scattered signals. To reduce an additional depolarization of the signal in the optics, the PS was designed with minimum optical components before polarization separation. Calculations shows the possibility of polarization separation without using collimation optics in the RT and overcome the difference between the working angles of the Glan prism and the RT concave mirror.

For polarization separation is used a Calcite prism and two prisms with different refractive indexes (to reduce the abberations in the calcite prism). For this configuration the beams with orthogonal to each other polarization have been refracted under different angles and separated from each other in space for more than 8 mm. The separated beams are channeled into two optical fiber bundles with 4 mm apperture and transported to photo receivers.

Designed and assembled PS is presented on the Figure 3. The PS mount has two angular and two parallel (in crossed directions perpendicular to RT optical axis) alignment capabilities and also can be aligned parallel to RT optical axis (RT focus finder). The polarization separation angle against LE beam polarization can be controlled by means of stepper motor and play free gear system.

The PS was aligned on the optical table for checking the calculations as well, as to design the procedure of alignment for its integration into RT. The points are the separated cross-polarized 532 nm diode laser beams (Figure 3).
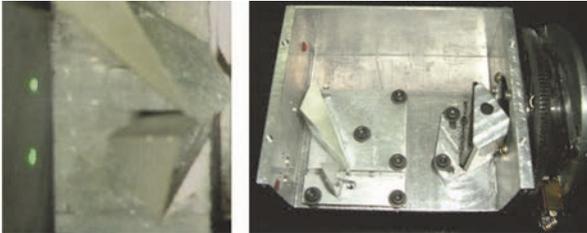

Figure 3. The Polarization Separator

Signal Detection and Processing System registers the orthogonal to each other polarized components of the backscattered radiation by means of photomultipliers (PMT). It allows reducing the optical background noise by means of filters to separate the signal according to wavelength as well as changing the field of view of the receiving telescope.

3. THE LIDAR SYSTEM

The developed LIDAR system is presented on three photos below.

By means of the RT mirror the backscattered radiation is directed and focused on the inputs of the fiber bundles. On its way the radiation is passing through PS which separates orthogonal to each other polarized components of the backscattered radiation. Two fiber bundles transport the separated optical signals to PMT boxes. After optical filtering, signals enter into PMTs, which amplifies and converts them into electrical signals.

The electrical signals from PMTs passed to the signal registration system. The signal observations are realized by means of 500 MHz oscilloscope. The triggering of the registration system is organized by means of photodiode system optically communicated with outgoing laser pulse.

The angle of the PS can be controlled by means of stepper motor and play-free gear allowing orient the polari-

zation separation angle perpendicular to LE beam polarization plane as well, as to any angle to it.

In the LIDAR Registration and Control System the CAMAC crate is used as a framework for custom made blocs and as a power supply for different subsystems and modules. The NI USB DAQ system, custom made BNC module for DAQ inputs and outputs, PMT power supplies, custom made power supplies for system electronics, etc. are installed into CAMAC crate (Figure5).
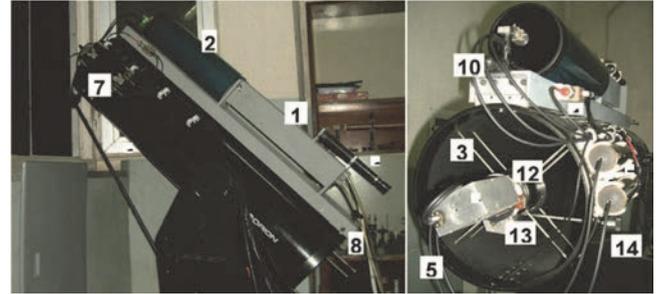
Figure 4. The LIDAR system. 1 - The Laser; 2 – Laser Beam Expander; 3 - RT; 4 - PS; 5 - Signal optical fiber bundles; 6 - Optical filter boxes; 7 - PMTs; 8 - LE alignment platform; 9 - Aiming optics; 10 - Triggering and output energy control optical fiber bundles; 11 - Triggering photodiode; 12 - PS alignment mount; 13 - Stepper motor with Play-free Gear; 14 - RT mirror focus finder.

The system is used for the digitizing observed signals and to control the LIDAR system, including:

- LE beam 1064nm output energy.
- LE beam 532nm output energy.
- LE beam repetition rate.
- LE Q-Switch driver pulse delay.
- LE beam polarization finder.
- PS – LE beam polarization angle.
- Registration delay, etc.

Figure 5. The LIDAR Registration and Control System.

1 - Stepper Motor Driver;

2 - PD and PMT Amplifier Power Supplies;

3 - NI DAQ BNC Inputs and Outputs;

4 - NI USB DAQ;

5 - PMT Power Supplies;

6 - Oscilloscope 500MHz.

The main specifications of the LIDAR system are listed in the Table 1.

Table 1. LIDAR System Specifications.

Laser Emitter	
Laser source	YAG:Nd3+ Custom made
Wavelength	1064 nm 532 nm
Pulse energy	300 – 500 mJ (@ 1064nm) 100 – 200 mJ (@ 532nm)
Beam Expander	14x
Beam divergence	<10-4 rad (after beam expander)
Pulse width	10 ns

Laser Emitter	
Repetition rate	10 – 20 Hz
Polarization linearity	<10-3
Receiving Telescope	
Diameter	250 mm
Field of view	2 x10-4 rad
Polarization Separator	Custom made
Optical fiber bundle aperture	4 mm
PMT	FEU-100 and FEU-83 (Russia)
Range	0.1 – 15 km
Spatial resolution	5 m
Signal and data processing	
Oscilloscope	HMO 3054 (Hameg)
Oscilloscope	PicoScope 5444B
DAQ	NI USB DAQ
Software interface	NI LabVIEW

4. THE FIRST OBSERVATIONS OF THE BACKSCATTERED SIGNALS

Fig. 6a and b present the first observations of the signals scattered from the clear atmosphere and the clouds. It highlights the backscattered signal amplitude above the noise level for the distance of ~7.5 km. The oscillograms are the direct output signals from the PMTs (without amplification and processing) received from the atmosphere per one laser shot/each. The triggering signals are at the beginning of the oscillograms.

In Fig.6.1, the (a) curve is the backscattered signal parallel to the laser emitter beam polarization component and the (b) curve is the crossed one (depolarization channel). The laser emitter output beam is at the beginning of the oscillogram. Taking into account the light velocity in the air, the full scale of oscillogram indicates approximately 7.5 km distance (50 usec - laser pulse time of flight). The signal from depolarization channel shows, that the LIDAR receiving system birefringence is negligibly small.

The oscillograms are obtained with one 100-mJ laser emitter pulse (without averaging or special processing). The PMT supply Voltage 2 kV also is not on maximum and the output signals of the PMTs are without amplification.

The estimations show that the reserve of the system is enough to realize elastic backscattering measurements from not less than 15 km distances.

The second oscillogram (Fig.6.2.) indicates the backscattered signal with the same laser emitter beam and with reduced PMT supply voltages allowing observing the amplitude of the backscattered from the clouds signals (about 6 km far from the system). On the oscillogram one can notice that the laser radiation in the clouds is depolarized ((b) one), which is an indication of the existence of ice droplets in the cloud. From the oscillogram can be easily calculated the heights, the thickness and distribution of the cloud by measuring the attenuation of the laser radiation in the clouds, and so on.

These first observations of the backscattered signals from the atmosphere and clouds by means of the designed LIDAR system show that its completion with a signal digitizing system and a signal processing PC program will allow to use it in the numerous applications of atmospheric research for distances not less than 15 km.
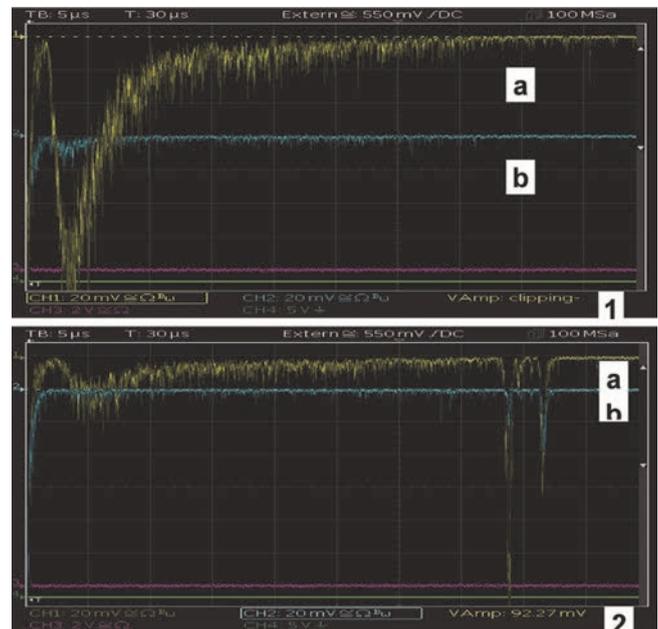

Figure 6. The Scattering from Atmosphere and Clouds received signal oscillograms. a – parallel with laser beam polarization channel, b – crossed with laser beam polarization channel (Horizontal - 5us/div; Vertical -20mV/div).

5. SUMMARY AND FUTURE PERSPECTIVES

A LIDAR system for remote sensing of the atmosphere was designed at the Yerevan Physics Institute and current plans are to use the system for backscatter measurements from aerosols and hydrometeors. It is directed to investigate the influence of the external factors on the backscatter signals including influence of the atmospheric electric fields. It is planned also to add a nitrogen and water Raman channels into the receiver to investigate the cloud and aerosol backscatter and extinction, as well, as the influence of the external factors (including the el A LIDAR system for remote sensing of the atmosphere was designed at the Yerevan Physics Institute and current plans are to use the system for backscatter measurements from aerosols and hydrometeors. It is directed to investigate the influence of the external factors on the backscatter signals including influence of the atmospheric electric fields. It is planned also to add nitrogen and water Raman channels into the receiver to investigate the cloud and aerosol backscatter and extinction as well as the influence of the external factors (including the electric fields) on the deformation of the spectral bands.

REFERENCES

[1] K. Sassen. Bull. Am. Meteorol. Soc. 12, p. 1848 (1991).

[2] A. Chilingarian, A. Daryan, K. Arakelyan, et al. Phys. Rev. D 82, 043009 (2010).

[3] A. Chilingarian, G. Hovsepyan, L. Vanyan. EPL, 106 (2014) 59001.

[4] Ghalumyan, R. Hakhumyan, H. Hakhumyan. Proceedings of the International Symposium TEPA-2013, ed. Chilingarian A. (TIGRAN METS, Yerevan) 2013, p. 102.

First results from the measuring equipment SEVAN on Lomnický štít: possible connections with atmospheric phenomena

Marek Kollárik, Karel Kudela, Ronald Langer, Igor Strhárský

Institute of Experimental Physics, Slovak Academy of Sciences, Watsonova 47, 040 01 Košice, Slovakia

Abstract. The measuring equipment of cosmic rays SEVAN on Lomnický štít was put into operation on March 20, 2014. Since then we have been recording continuous data with 1 min resolution. During the time interval covered by the measurements, several significant changes have occurred that are probably connected with atmospheric electricity phenomena – lightning. The records of thunderstorms on Lomnický štít are from visual observations as well as from data of lightning detector network. The examples of almost simultaneous increases on SEVAN and lightning events are shown. All short time increases in cosmic rays are far not accompanied by lightning events.

1. INTRODUCTION

Lomnický štít (LS, 2634 m above sea level in High Tatras Mountain, coordinates 49.40ºN, 20.22ºE) is a suitable location for high altitude solar, meteorological and cosmic ray (CR) observations. CR measurements at Lomnický štít (geomagnetic vertical cutoff rigidity ~ 4GV) started in 1957 in connection with the IGY [1]. Recording system of the measurements used at present is shortly described in [2]. During years 2010-2013 the reconstruction of the infrastructure at the mountain allowed to extend the measurement to higher energies by SEVAN device described in [3, 4]. We illustrate the first results from the measuring equipment SEVAN that can be related to thunderstorm effects in vicinity of LS.

During recent years, relations between atmospheric discharges and the responses observed in secondary CR ground based observations, as well as in thermal neutron detection, have been reported in several papers (e.g. [5-8]). A huge event observed at ASEC by several detectors supports the existence of long-lasting particle multiplication and acceleration mechanisms in the thunderstorm atmosphere [9].

Nowadays there are operating several systems/ networks of lightning observations, some of them described e.g. in [10,11]. Using the in-situ observations of lightning (at LS there is steady service by technical staff of IEP SAS) and the data from LINET - professional lightning detection network (http://www.nowcast.de, one of many stations within the network is situated in Kosice) [12], we show examples of possible coincidences between the CR short-time increases observed by SEVAN and the lightning events. Possibilities of the progress in the study is shortly discussed.

2. INSTALLATION

The measuring container of the Institute of Experimental Physics of the Slovak Academy of Sciences was installed in its final position on Lomnický štít on June 30, 2012. The container has been designed so that SEVAN device was installed in its higher part on the left (Fig.1). Due to spacing issues the initial height of the caps for upper and lower 5 cm scintillator was lowered to cca 67 cm. After the testing period in Košice (from Sep. 2012 to March 2013) the SEVAN instrument started its measurements at Lomnický štít on March 20, 2014. The data with 1 minute resolution are stored automatically on the online server. The measurements, namely three channels with the total counting rate, four types of coincidences and pressure, are recorded continuously.

Figure 1.. SEVAN is situated on the roof of the main building at Lomnický štít in the new measuring container highlighted by the red frame.

3. INTERVALS WITH THUNDERSTORM ACTIVITY

Several periods with thunderstorm activity occurring in the vicinity of LS have been checked for short-term variations at SEVAN, particularly in the upper channel (channel 1). Counting rate in the channels 1 – 3 (upper, middle and lower ones) is plotted in Figure 2 for the interval of 18 days.
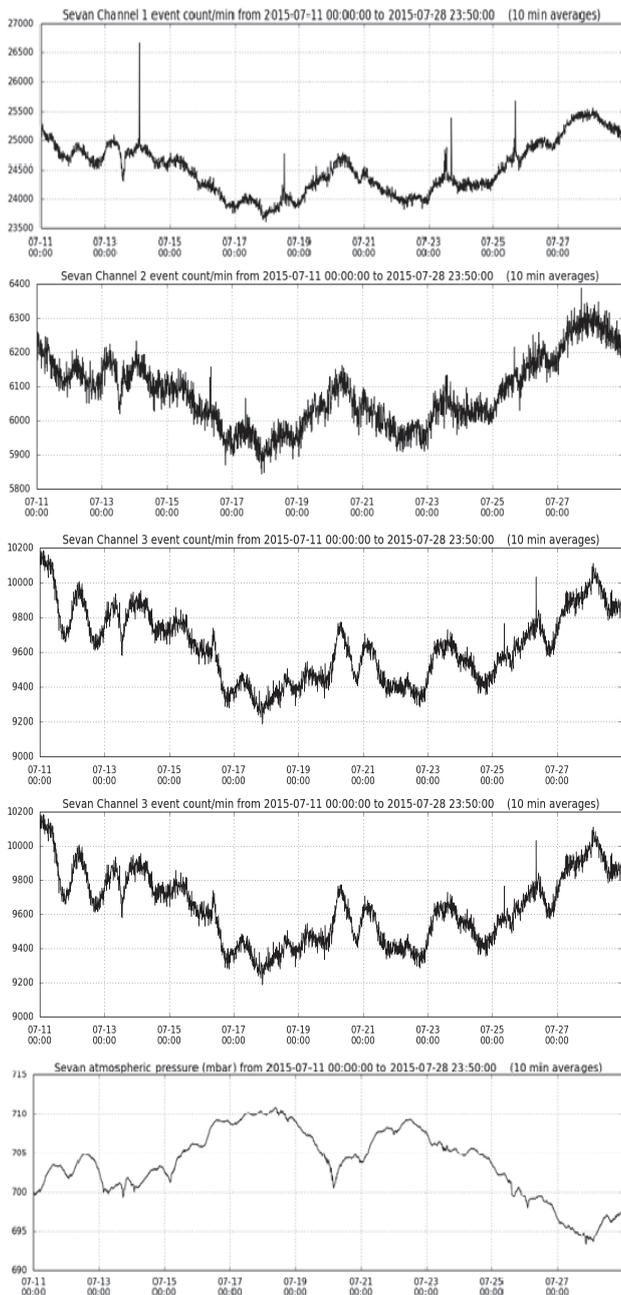
Figure 2. SEVAN 1 min data for period of 18 days (July 11 – 28, 2015) along with barometric pressure. Short spikes in channel 1 are related largely with thunderstorm activity. However, it is not a rule: e.g. first increase on 2015-07-14 in the morning is not related to lightning.

3.1 STORMY DAY 2014-04-28.

Relatively clearly was observed the increase on April 28, 2014 (Figure 3).
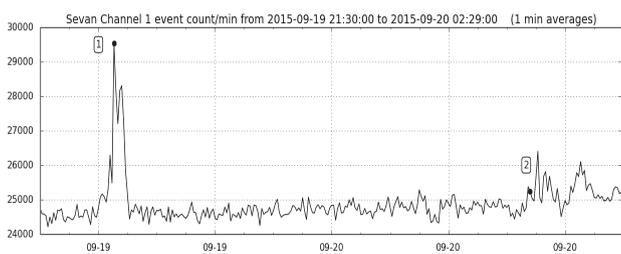
Figure 3. SEVAN LS recorded a rapid increase in the counting rate of channel 1 starting from ~ 13:50 UT, April 28, 2014. A direct hit into Lomnický štít was observed at 13:55UT. Time corresponds to the end of measurement interval

For comparison we have used the LINET records from the region including Slovakia territory (obtained from [12]).

Table 1 indicates the series of discharges in the neighbourhood of LS position during the interval 13:50 till 13:55 UT.

Table 1. Data from LINET [12].

Time	LAT	LON	Dist.(km)
13:51:00.397	49.3463	20.3008	17.982
13:52:03.681	49.3251	20.2754	15.149
13:52:03.718	49.3435	20.2596	16.845
13:53:08.841	49.3397	20.2638	16.497
13:53:08.841	49.3361	20.2664	16.151
13:53:40.719	49.3234	20.2586	14.645
13:55:05.830	49.3241	20.2578	14.708
13:55:05.830	49.3219	20.2496	14.347
13:55:05.832	49.3231	20.2572	14.590
13:55:05.912	49.3430	20.2749	17.049
13:55:05.916	49.2713	20.4207	17.309

3.2 STORMY DAY 2015-05-20.

Intensive thunderstorm activity has been observed during the day May 20, 2015. Direct hits and hits in the immediate surroundings of Lomnicky štít (<10km) according to LINET system have been recorded. Figure 4 and Table 2 present the measurements by SEVAN and LINET data.
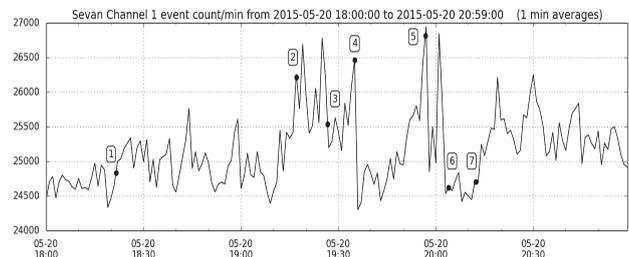

Figure 4. Observed direct hit (point 7), and hits in the immediate surroundings of Lomnický štít (points 1 - 6).

Table. 2 List of hits in the surroundings of Lomnický štít on May 20, 2015, interval 18 -21 UT [12].

Nr.	Time	Estimated Termination of TGE	LAT	LON	Dist. (km)	Type
1	18:21:30.229	18:26	49.22	20.09	9.361	CC
2	19:17:05.641	19:19	49.17	20.21	2.808	CG
3	19:26:40.437	19:25	49.21	20.20	1.903	CG
4	19:34:59.208	19:35	49.17	20.29	6.256	CC
5	19:56:46.562	19:57	49.19	20.31	7.072	CC
6	20:03:51.598	20:03	49.18	20.09	9.101	CG
7	20:12:19.958	20:12	49.17	20.26	4.415	CC

Figure 4 indicates all significant short time increases in the counting rate of SEVAN channel 1 are related to the discharges identified by LINET (Table 2). Later on May 20, 2015 (after 21:50 UT), the relations between discharges and short time increases of counting rate at SEVAN (channel 1) are presented in Figure 5 and Table 3.
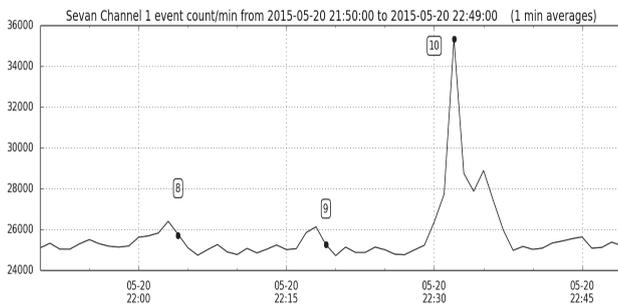
Figure 5. Counting rate in channel 1 from 21:50 until 22:50. Labelling:8 - (increase at 22:03 associated with direct hits (five times) CG into Lomnický štít;9 - decrease observed at 20:19 - after an increase with the peak 22:18 UT - could be associated with direct hits (13 times) of CG in the Lomnický štít surroundings; 10 - increase at 22:32 – without any hits in the surroundings (<10 km))

Relatively clearly was observed the increase on April 28, 2014 (Figure 3).

For comparison we have used the LINET records from the region including Slovakia territory (obtained from [12]). Table 1 indicates the series of discharges in the neighbourhood of LS position during the interval 13:50 till 13:55 UT.

Intensive thunderstorm activity has been observed during the day May 20, 2015. Direct hits and hits in the immediate surroundings of Lomnicky štít (<10km) according to LINET system have been recorded. Figure 4 and Table 2 present the measurements by SEVAN and LINET data.

Table 3. Series of discharges from LINET data around event 8 in Fig. 5. [12].

Nr.	Time	LAT	LON	Dist. (km)	Type
1	22:03:58.451	49.2000	20.2200	0.739	CG
2	22:03:58.482	49.2000	20.1900	1.759	CG
3	22:03:58.534	49.1900	20.2200	0.765	CG
4	22:03:58.538	49.1900	20.2200	0.765	CG
5	22:03:58.557	49.1900	20.2300	1.360	CG
6	22:03:58.572	49.1900	20.2200	0.765	CG
7	22:03:58.604	49.1600	20.1900	4.255	CG
8	22:03:58.606	49.1900	20.2200	0.765	CG
9	22:03:58.611	49.1600	20.1900	4.255	CG

3.3 STORMY DAY 2015-09-19.

On September 19, 2015 the thunderstorm activity was observed in the evening/night hours. Figure 6 displays the counting rate of SEVAN.
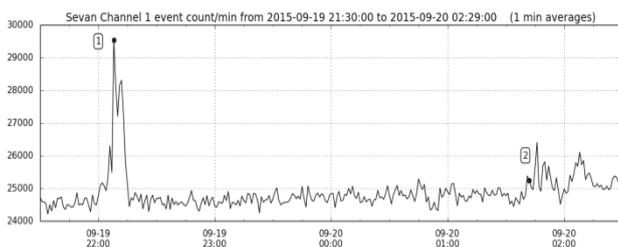

Figure 6. Counting rate in channel 1 on Sep. 19, 2015 since 21:30 UT. Labelling: 1 – the increase with the peak at 22:08 could be associated with discharge in the LS surroundings (visually observed and associated with hits recorded by LINET system); 2 - moderate increase in counting rate on Sep. 20, 2015 at 01:42 – indirect hit to LS.

4. DISCUSSION AND SUMMARY.

Analysis of the relations between the thunderstorms and short – time increases in counting rate of CR at LS – illustrated by the examples here – is in its initial phase. The TGE (Thunderstorm ground enhancement) related effects in several cases are seen in the upper channel of SEVAN. However, the observations also indicate that not all the discharge effects (including also direct hits to LS position) are impacting the upper channel. Moreover, there are recorded short-time increases that are not connected to any nearby surrounding discharges.

The usefulness of the LINET system in the type of the study started here, is apparent. In order to obtain more accurate results in the future, we are planning to include the measurements of electrostatic field at LS. Thus combination of LINET, visual observations and in situ measurement of electric field is expected to provide more information for comparison of atmospheric discharges and CR variations observed at LS altitude.

To discriminate at least roughly the type of secondary CR particles related to discharges, various coincidences provided by SEVAN measurements should be checked in relation to TGEs. The same is valid for simultaneously measured profile of counting rate at neutron monitor (NM) LS having relatively high statistical accuracy and independent measurements by several counters. Higher temporal resolution of both SEVAN an NM LS is assumed for the future.

Since paper [13] the intense γ ray flashes of atmospheric origin are observed on satellites. Recently, significant progress obtained from measurements of FERMI satellite [14] is reported. Terrestrial gamma flashes (TGFs) must be created at altitude > 30 km to escape absorption in the atmosphere. The TGEs are observed on the ground (e.g. [15]). High mountain measurements of TGEs can contribute to the understanding of the possible relations between TGFs and TGEs, if correlated measurements with those on satellite(s) can be done in future [16]. One of the positions (among others) for TGE checking at high mountains can be Lomnický štít.

REFERENCES

[1] Kudela, K. and R. Langer, Cosmic ray measurements in High Tatra mountains: 1957–2007. Advances in Space Research, **44** (10), p. 1166-1172, 2009.

[2] Strhárský, I., Langer, R., Kudela K., Recording System for Cosmic Ray Measurements at Lomnický štít, ESWW10, Nov 18-22 2013, Antwerp, Belgium.

[3] Chilingarian, A., Hovsepyan, G., Arakelyan, K. et al, Space Environmental Viewing and Analysis Network (SEVAN) – characteristics and first operation results, Journal of Physics: ConferenceSeries **409** (2013) 012222.

[4] Chilingarian, A. et al., Space Environmental Viewing and Analysis Network (SEVAN), Central European Astrophysical Bulletin **31**, pp. 259-272, 2007.

[5] Chilingarian, A. et al., Ground-based observations of thunderstorm-correlated fluxes of high energy electrons, gamma rays and neutrons, Phys. Rev. **D 82**, 043009, 2010.

[6] Martin, I.M. and Alves, M.A., Observation of a possible neutron burst associated with a lightning discharge?, J. Geophys. Res., **115**, A00E11, 2010

[7] Gurevich, A.V., The time structure of neutron emission during atmospheric discharge, Atmos. Res., **164-165**, 339-346, 2015

[8] Chilingarian, A. et al., Neutron bursts associated with thunderstorms, Phys. Rev. **D 85**, 085017, 2012

[9] Kozlov, V.I. et al., Neutron bursts associated with lightning cloud-to-ground discharges, Journal ofPhysics:ConferenceSeries **409**, 012210, 2013

[10] Betz, H.-D. et al., LINET - An International VLF/LF Lightning Detection Network in Europe, Atmospheric Research, **91**, p. 564¸S573, 2009.

[11] Höller, H. et al., Lightning characteristics observed by a VLF/LF lightning detection network (LINET) in Brazil, Australia, Africa and Germany, Atm. Chem. Phys., **9**, 7795, 2009

[12] Betz, H.-D., personnal communication 2014, 2015.

[13] Fishman, G.J. et al., Discovery of Intense Gamma-Ray Flashes of Atmospherc Origin, Science, New Series, **264**, No 5163, 1313-1316 (May 27, 1994)

[14] Briggs, M.S. et al., Terrestrial gamma-ray flashes in the Fermi era: Improved observations and analysis methods, J. Geophys. Res., **118**, 3805–3830, doi:10.1002/jgra.50205, 2013

[15] Chilingarian, A. et al., Thunderstorm ground enhancements: Gamma ray differential energy spectra, Phys. Rev. **D 88**, 073001 (2013)

[16] Kudela, K. and J. Blecki, Possibilities of selected space weather and atmospheric studies in JEM-EUSO project?, PoS(ICRC2015)113, 2015

2015

5-th International TEPA Symposium
Thunderstorms and Elementary Particle Acceleration
October 5-9 | Nor Amberd | Aragatsotn Province | Armenia

The Baksan experiment on thunderstorm CR variations: history, results, and prospects

N.S. Khaerdinov, A.S. Lidvansky

Institute for Nuclear Research, Russian Academy of Sciences, Moscow, Russian Federation

Abstract. Variations of cosmic rays in thunderstorm atmosphere, as measured at the Baksan Neutrino Observatory with the Carpet air shower array, are discussed. Their underlying mechanisms and accompanying phenomena are also considered. The observed effects in cosmic rays include regular variations with the near-ground electric field of the soft (electrons, positrons and gamma-rays) and hard (muons) components of secondary cosmic rays and sporadic changes in intensity of both these components (bright events). Associated phenomena occurring simultaneously with bright events in cosmic rays include geomagnetic pulsations (observed by high-sensitivity magnetic variation station deep underground) and large-scale atmospheric high-altitude discharge of a new type (observed by a video camera placed at a distance of 75 km from the Carpet array). Implications of all these results and prospects for further studies are discussed.

1. INTRODUCTION

Thunderstorm variations of secondary cosmic rays during thunderstorms were first proved to be related to the strong electric field (measured near the ground surface) in a pioneering experiment carried out by A.E. Chudakov with collaborators in early 1980s (for references see Lidvansky, 2003). The new version of the same experiment (Alexeenko et al., 2002; Khaerdinov et al., 2005) yielded a lot of data on variations of cosmic rays during thunderstorms, a part of which is discussed below. We consider two types of experimental data: (i) regular variations of the counting rates of the soft and hard components correlated with the near-earth electric field of the atmosphere during thunderstorms and (ii) bright events or strong changes in the counting rate of these components. The soft component under study is represented by electrons, positrons, and gamma-rays in the energy range 10-30 MeV, while muon intensity was investigated at three different energy thresholds. In this paper we present a brief overview of the most important experimental results and discuss their interpretation.

2. EXPERIMENTAL DATA AND MODEL OF PARTICLE GENERATION

Experimental data on variations 'intensity versus field' published in Khaerdinov et al., 2005 are shown in Fig. 1 together with theoretical estimation of the predicted transformation in the near-earth field made in Lidvansky et al., 2004. The plot of Fig.1 is constructed using 52 carefully selected thunderstorm events detected in Baksan Valley (North Caucaus) in 2000-2002.

The red solid curve in Fig. 1 is the weighted mean of approximations by second-degree polynomials made in each thunderstorm event. The left part of Fig. 1 (negative field) corresponds to acceleration of electrons (all electrons of secondary cosmic rays gain additional energy in the electric field so that their counting rate increases at a constant threshold of detection). Similarly, the right branch of the curve of Fig. 1 should correspond to acceleration of positrons in the field of the opposite sign. The blue dashed and dot-dashed lines represent theoretically calculated effect for two extreme values of calibration coefficients. The curve best fitting the experimental data is selected to subtract expected behavior from the real data. The result is shown in Fig. 2.
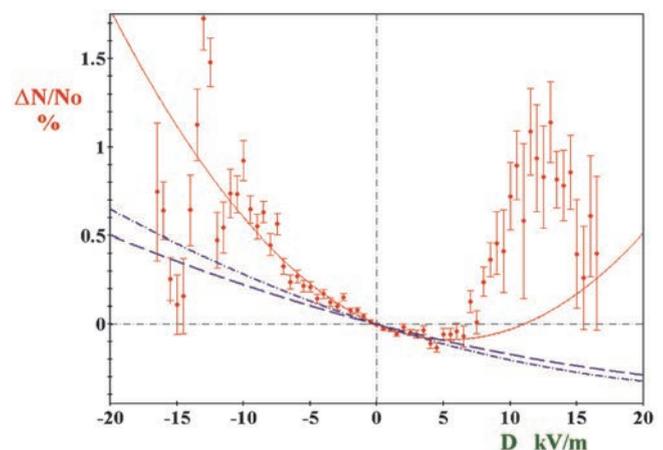

Figure 1. Experimental deviation of the soft component count rate versus near-ground electric field. The result is obtained for 52 thunderstorms selected from 106 having occurred in 2000-2002 seasons in the Baksan valley. Also shown are calculated expectations for electron spectrum transformation in the field at two extreme values of calibration coefficients of electric field meter.
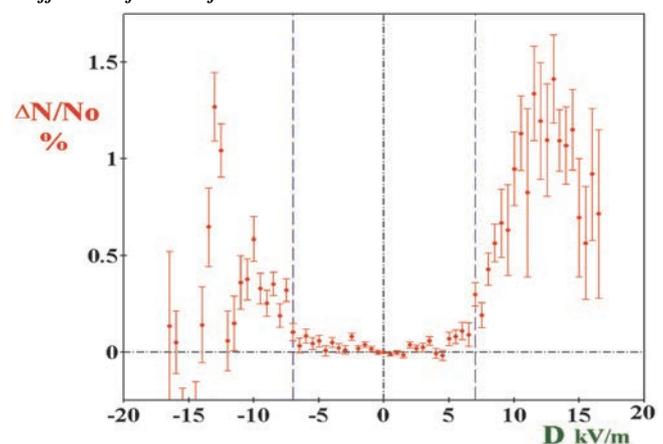

Figure 2. Experimental data of Figure 1 after subtraction of theoretical curve obtained as weighted mean of two calculated curves of Figure 1. See text for explanations.

The effect of spectrum transformation in the near-ground field is pretty small. The linear term of this dependence is such that when field strength changes by 1 kV/m the counting rate changes 20 times weaker than when atmospheric pressure changes by 1 mm of Hg. Nevertheless, this effect is observable (as show the data of Fig. 1) and reason-

ably well described by calculations in the range of near-ground field from − 7 kV/m to + 7 kV/m. Beyond these limits there are bumps of excess particles whose origin is rather obvious.

According to experimental measurements of the vertical profile of electric field during thunderstorms, it has a layered structure and quite frequently the strong field in the cloudy layer has opposite sign with rather weak near-ground field. Electrons accelerated in the strong field (runaway electrons) and their avalanches produce gamma-ray emission that is detected at the observation level.

The regular part of distribution in Fig. 1 has linear and quadratic terms. The same situation is with the muon intensity, the difference being in the fact that the quadratic coefficient in the data of Fig. 1 is positive, while for muons it is negative. Also, it is strongly dependent on the muon energy threshold (for details see Lidvansky et al., 2004). In both cases the linear terms are connected with charge asymmetry of the particle flux, and quadratic terms are determined by the character of energy spectra (dominated in case of muons by particle decays).
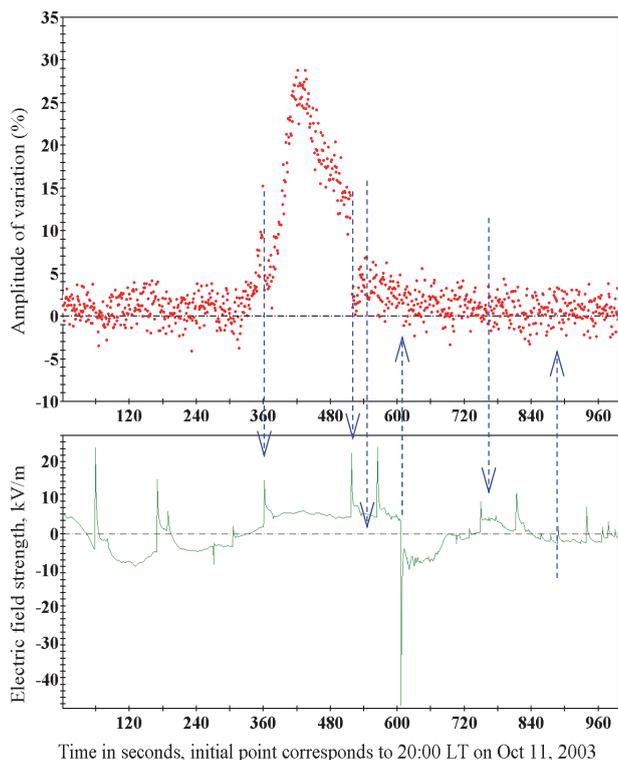

Figure 3. The strong enhancement of the soft component intensity during a thunderstorm on October 11, 2003. The lower panel presents the electric field meter record with lightning discharges clearly seen.

Another experimental fact is observation of strong enhancements of the soft component intensity. The most powerful event of this type was detected on October 11, 2003 and is shown in Fig. 3. This event is remarkable not only by its amplitude. We observe in it two interruptions of regular process simultaneously with lightning discharges and natural saturation of the generation of particles with subsequent decay.

The analysis has shown that such large variations of intensity cannot be produced by simple transformation of energy spectra even in the strong field of thunderclouds. Two lightning discharges marked by arrows that change the region of particle acceleration are rather distant (estimated as 4.4. and 3.2 km). The third lightning discharge marked by arrow is very close and produces no effect on the particle intensity. One can conclude that the acceleration region

is located rather far, and it is impossible to get so strong disturbance of intensity without additional generation of particles. The model of this generation was suggested by us and described in some detail in Lidvansky & Khaerdinov, 2007a. The main points of this model are as follows.
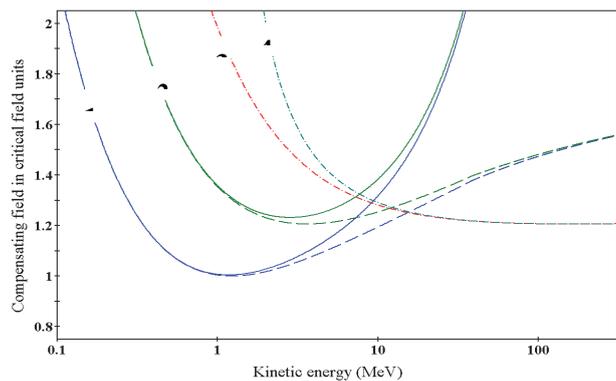

Figure 4. Admissible regions for runaway (2) and feedback (4) particles.

Figure 4 presents in a simplified form the result of analytical calculations made in Lidvansky & Khaerdinov, 2007b for trajectories of particles moving with Coulomb scattering in a homogeneous electric field. Curve 1 represents energy losses of particles (dashed line for ionization only), and ordinate axis gives a field strength that compensates them. Accordingly, in the standard theory of the runaway electron breakdown (Gurevich et al, 1992; Roussel-Dupre et al, 1994) this curve is a separatrix: above it any charged particle becomes a runaway particle. However, proper account for Coulomb scattering gets curve 2 as a separatrix for the zone of runaway particles. As a result, the critical field (minimum of the curve) turns out to be higher by approximately 25% in comparison with the field used by Gurevich et al., 1992. And (what is even more important) the minimum of the separatrix is displaced to the region of higher energies

Owing to the last circumstance, contribution of bremsstrahlung to the total losses becomes significant, and this process leads to generation of gamma rays that are still sufficiently energetic to produce electron-positron pairs. One component of each pair continues acceleration along the field direction, while another one, moving in decelerating field has some chances to make a turn by 180° and become a runaway particle in the opposite direction. Thus, a flux of runaway positrons originates in the field accelerating electrons. For this flux the same scheme of reasoning is valid. These positrons produce an additional flux of runaway electrons, and a positive feedback loop arises. If this feedback is sufficiently stable and efficient, exponential increase of intensity should take place.

The allowed region for such a process is shown in Fig. 4. It is located between curve 4 and the right branch of curve 2. As is seen in Fig. 4, the minimum field necessary for this process is higher than critical field of runaway breakdown theory only by 30%. This minimum is achieved at energy of about 10 MeV (this is just the energy threshold in our experiment). This process has some advantages over mere cascade multiplication of runaway electrons, for which a field of long extension is needed (many characteristic lengths). In addition, this is the process that can ensure temporal properties of observed events (long duration).

Usual runaway avalanches are developed very quickly, while the above feedback process can have different duration: this depends on the filed strength and extension. Fig-

ure 5 presents the calculated minimum possible field strength for which effective cyclic generation is allowed. Each curve represents a fixed time of exponential increase. The ordinate represents the field strength in the units of Gurevich critical field (216 kV/m at sea level), and the field extension is laid as the abscissa. Thick blue line corresponds to 10 s (really observed time in our event on September 7, 2000 published in Alexeenko et al., 2002. Red curve corresponds to infinite time. Empty circles mark the curve calculated by J. Dwyer for absolute instability due to the runaway avalanches. The regime of our model lies deep in the region which he defined as semi-stable. It is worthy of noting that the rate of exponential growth of intensity in Fig. 5 depends on the product $D \times d$, where D is the excess (in comparison to critical value) strength of the field and d is its extension (complete analogy with the Paschen's law, where breakdown voltage depends on the product of pressure and distance).
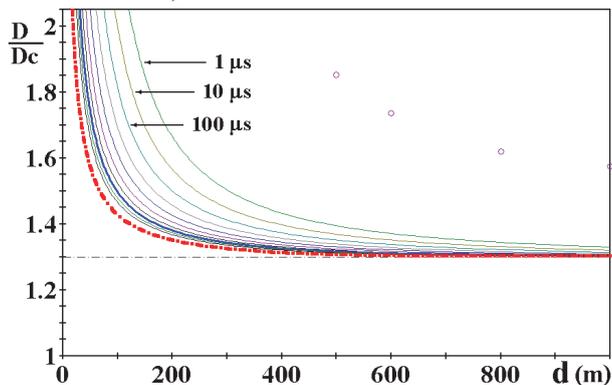

Figure 5. Electric field strength (in critical field units) versus field extension for particle generation process with different rise time.

3. THE BRIGHT MUON EVENTS

Figure 6 presents for the event of September 24, 2007 the following averaged data from top to bottom: the recorded strength of the near-ground electric field (upper panel), the intensity of the hard component (mostly, muons with a threshold of 100 MeV), and the recorded precipitation electric current (bottom panel). Following these data one can trace the evolution of the thunderstorm that has started approximately at 19:50 with an increase of negative electric field, which soon has changed its polarity.

In the meantime, two lightning events approximately at 22:11 and 22:30 have caused jump-like changes of the intensity again to the mean level with the subsequent recovery of the depressed muon intensity in a time of order of a few minutes. Arrows in Fig. 6 mark these disturbances of the muon intensity associated with lightning strokes. So long suppression of muon intensity is obviously connected with the elevation of thundercloud higher than the effective level of muon production. The lightning effects are extremely important as a direct proof of the fact that the suppression is indeed connected with electric field changes: no other factor can give so fast jump of intensity. Not so impressive muon events take place in virtually every thunderstorm. Statistical properties of them are presented in Khaerdinov and Lidvansky, 2011. It is shown in the latter paper that the amplitude of muon variation does not exceed 1%, and their mean duration is about 8 min. Some theoretical considerations about variations of the muon flux in atmospheric electric field are given in Khaerdinov and Lidvansky, 2005 and in Khaerdinov and Lidvansky, 2013b.
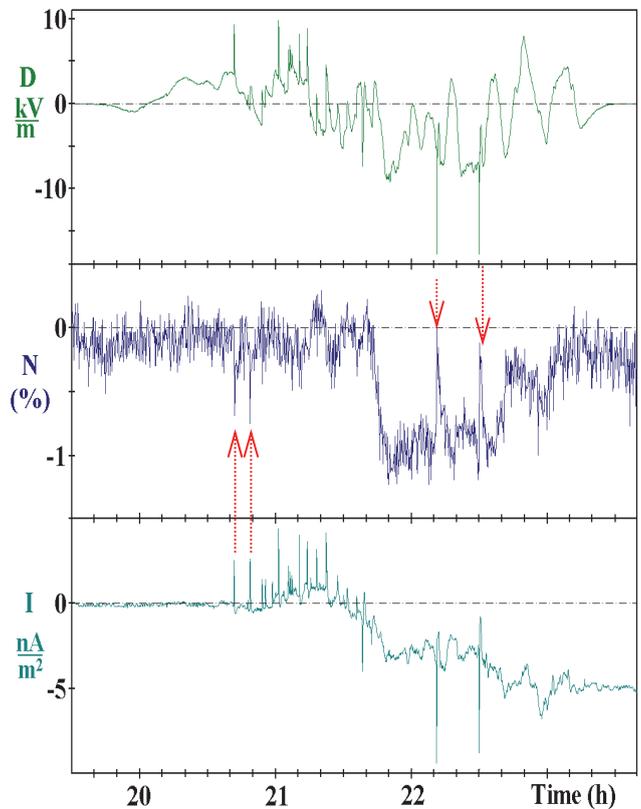

Figure 6. Event on September 24, 2007. The largest and longest decrease of the hard component intensity throughout the entire period of observation with well-pronounced lightning effects.
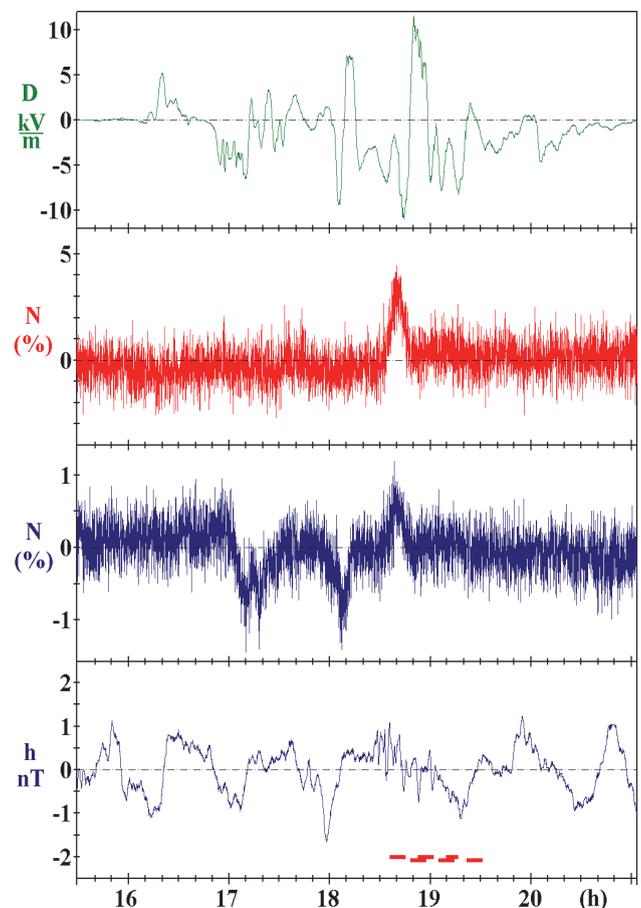
*Figure 7. Thunderstorm event observed in Baksan Valley on October 15, 2007. Interval of averaging is 4 s. From top to bottom the panels represent the strength of the near-earth electric field, intensity of the soft component 10-30 MeV (percent deviation from daily mean value), the hard component (muons > 100 MeV) and the h-component of the geomagnetic field with subtracted trend of the daily wave.*

Approximately at 20:40 a strong lightning activity began, being accompanied by a small positively charged rain. In this case, there are two unequivocal disturbances in the muon flux associated with lightning strokes recorded simultaneously (at 20:41 and 20:48). Finally, at about 21:40 the thunderstorm pattern changes radically: negatively charged rain begins and is permanently intensified, lightning signals becomes stronger and less frequent, while (the most interesting effect for us) the muon intensity drops down approximately by 1% for a pretty long time.

4. GEOMAGNETIC PULSATIONS

The event of October 15, 2007 presented here (Fig. 7) is discussed in more detail in Kanonidi et al., 2011. The amplitudes of enhancements in the soft and hard components are not outstanding. But a remarkable feature of this event is the presence of simultaneous pulsations of geomagnetic field measured deep underground in a tunnel of the Baksan Neutrino Observatory and far (4 km) from the EAS array.

The pulsations are shown in Fig. 7 for one component (bottom panel) where the daily trend of the geomagnetic field is subtracted. The red dashed horizontal bar marks the region of pulsations with typical duration of pulses 100 s. Other details of this event also deserve attention, and they have been partially given in Kanonidi et al., 2011.

5. NEW TYPE OF HIGH-ALTITUDE DISCHARGE

Thus, it was established in this experiment that the active period of a thunderstorm was frequently accompanied by anomalous disturbances of muon intensity whose interpretation needs to assume the potential difference of about 100 MV in the stratosphere (Khaerdinov & Lidvansky, 2013a). These disturbances can coincide with anomalous disturbances in the electron-photon component (see Fig. 7), which can be explained by generation of bremsstrahlung photons produced by avalanches of runaway electrons accelerated in the stratosphere (Khaerdinov & Lidvansky, 2013b).

So, experimental facts and their model explanation give a lot of indirect evidence in favor of existence of a rather slow high-altitude large-scale discharge resulting in electric breakdown of the stratosphere. In recent years an attempt has been made to observe this new atmospheric phenomenon directly. For this purpose the sky region above the array was continuously viewed by two video cameras CS-265-IP, whose information is stored on hard disks. The distances from the experimental setup to the cameras were 1 km and 75 km, observations being carried out in night time in the BW mode, without color resolution. The exposure time is 0.7 s, and sensitivity of recording brightness variations is 10^{-8} lx (10^{-10} W/m^2) of illumination. The field of view of the remote camera (75 km) is 60° x 45°. The lower edge of frames is set to make an angle of 3° with the horizon.

 Thunderstorm event on September 15, 2013 (Fig. 8) occurred in the night and had two active periods. Due to technical problems no data of electric field measurements and near camera were available at this moment. The distant camera recorded a luminous front in the middle atmosphere moving from north to south. Figure 9 presents images (with brightness intensified by a factor of 25) corresponding to different stages of development of this glow.

Simultaneously with emergence of the glow (Fig. 9a) rain is getting heavier and thunderstorm begins. This is obvious from a sharp increase of precipitation electric current, growing pressure, and lightning indicator data. With the appearance of glow the intensity of muons started decreasing, which means formation of a negative potential difference in the troposphere. At the maximum of the decrease (Fig. 9b) the glow is observed for 2 min in the region lower than 6.5 km a.s.l. (altitudes of less than 4 km are screened by mountains). At the same time, there is a large-scale glow at altitudes higher than 20 km above sea level. The moment of Fig. 9c corresponds to a maximum of fast positive disturbance of the muon intensity. One can see a descent of the glow region in the stratosphere, now it correspond to altitudes 12.5 - 20.5 km above sea level.

Its intensification in comparison with the moment of maximum negative disturbance of muons is evident. The moment when thunderstorm activity has stopped corresponds to Fig. 9d. It is seen that the process supporting the glow continues on a smaller scale and slightly to the right from the array. The air transparency was good during the first active period, and this allowed us to observe by the distant camera the lightning discharges recorded by the lightning indicator and precipitation electric current meter.
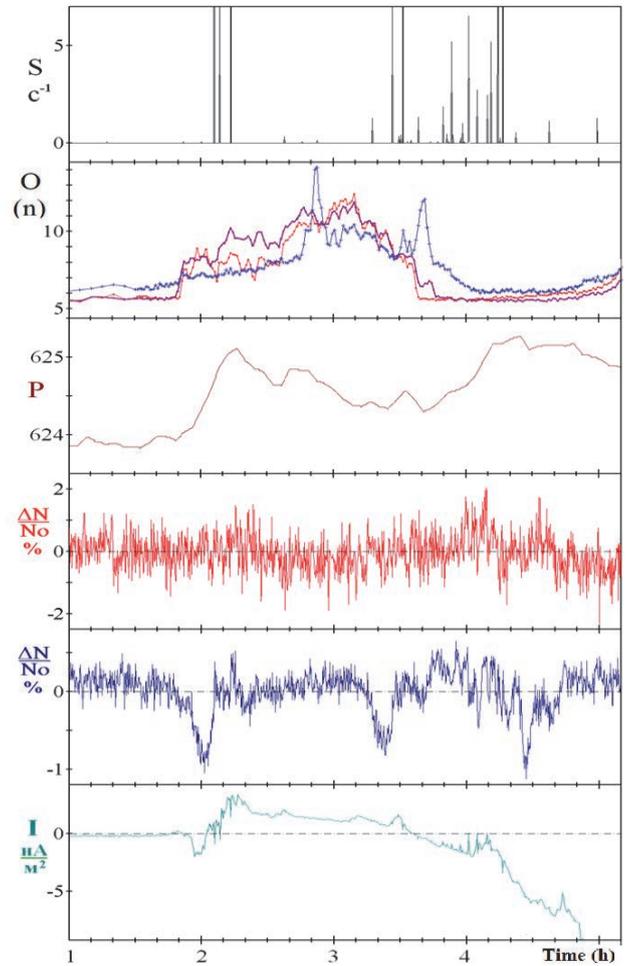

Figure 8.   Thunderstorm event on September 15, 2013. Interval of averaging is 15 s in all cases except for two upper panels. From top to bottom: 1. lightning indicator (arbitrary units proportional to amplitude of electromagnetic signal from lightning discharges), 2. mean brightness of different sky areas on distant camera images (red colour for ionosphere, violet for stratosphere, and blue for troposphere), 3. pressure, 4. variations of the soft component, 5. variations of the hard component, 6. precipitation electric current. Units of optical data in the second panel 10^{-7} lx (data are presented with one-minute intervals averaged over four adjacent frames).

Later the thunderstorm front propagated in the direction of the remote observation point, which caused deterioration of transparency and appearance of diffuse glow near the ground.

Approaching lightning discharges are also recorded by the camera. The quick termination of recorded glow is apparently caused by degradation of air transparency due to beginning of rain at the place of camera location.
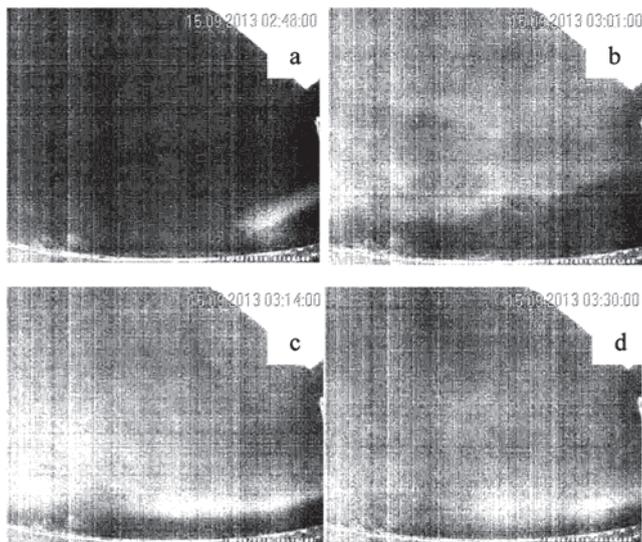

Figure 9. Development of glow in the atmosphere for thunderstorm event on September 15, 2013. Brightness of images is intensified by a factor of 25.

6. DISCUSSION AND CONCLUSIONS

This paper includes neither description of experimental facilities and methods of processing, nor details of calculations made. The aim of it is just to present a list of most interesting results, so that it is a sort of guide over publications where necessary information is given in some detail. We also do not cite experimental data of other groups, since most of them are concentrated on recording radiation associated with lightning and make use of detectors of relatively small area. Some of these experiments, like those at Tien Shan, Tibet and Mt Aragats in Armenia are carried out at higher atmospheric level, where particle effects during thunderstorms are more frequent and have larger amplitudes. At the same time the proximity to the region of strong electric activity should make experimental conditions more dangerous as far as induced interference is concerned. Our experimental setup is located deep in the atmosphere (the altitude of observation is 1700 m a. s l., while the heights of surrounding mountains is about 3900 m), and even in this case the electric interference effects are important. For example, in order to obtain the picture of Fig. 1 we had to take into analysis less than a half of detected thunderstorms. The rest of data were excluded as more or less suspicious with respect to noise. Due to so strict criteria of selection we can be sure in reliability of presented material. In addition, we study variations of cosmic rays with large area detectors (54 m^2 for the soft component observations, and 200 m^2 and 175 m^2 for detecting muons with thresholds of 100 MeV and 1 GeV, respectively), which allows us to have sufficiently high statistical accuracy of particle detection.

The data on optical observations are described above in more detail in comparison with other results, since they were obtained after purposeful search: the entire set of previous data and models interpreting them had led us to a hypothesis of existence of a new type of high-altitude discharge simultaneously with disturbances of cosmic ray muon intensity, and this effect was indeed observed. Thus, some predictive power of our concepts was demonstrated.

Summarizing, we can conclude that the experimental data accumulated for a period longer than a decade have produced a lot of information about processes occurring with cosmic rays and caused by them in thunderstorm atmosphere. Some new effects have been discovered that require confirmation and further investigation. It should be noted that it became possible to observe some new effects due to adding new types of data to original set, first magnetic measurements, and then visual observations.

Accumulation of data in this experiment is rather long, since the rate of bright events is pretty low: a few events per thunderstorm season. For optical data the number of observable events is even less (only night thunderstorms and only at favorable geometry of cloudy layer position and motion are suitable).

So, in the future it is naturally planned to continue observations in order to increase statistics and to include more additional data into analysis in order to make investigations as comprehensive as possible. Also, based on the results and knowledge obtained up to now, one can plan some new experiments in the field of atmospheric research using cosmic rays.

REFERENCES

- Alexeenko, V.V., Khaerdinov, N.S., Lidvansky, A.S., and Petkov, V.B., 2002. Transient Variations of Secondary Cosmic Rays due to Atmospheric Electric Field and Evidence for Pre-Lightning Particle Acceleration, Phys. Lett. A, 301, 3-4, 299-306.

- Dwyer, J.R., 2003. A fundamental limit on electric fields in air, Geophys. Res. Lett., 30, 2055.

- Gurevich, A.V., Milikh, G.M., and Roussel-Dupre, R.A., 1992. Runaway electron mechanism of air breakdown and preconditioning during a thunderstorm, Phys. Lett., A165, 463-468.

- Kanonidi, K.Kh., Khaerdinov, N.S., Lidvansky, A.S., and Sobisevich, L.E., 2011. Strong variations of cosmic ray intensity during thunderstorms and associated pulsations of the geomagnetic field, Astrophysics and Space Science Transactions (ASTRA), 7, 279–282

- Khaerdinov, N.S. and Lidvansky, A.S., 2013a. Heights of Generation of Runaway Electrons in Bright Cosmic Ray Events Observed on the Ground during Thunderstorms, J. Phys.: Conf. Ser., 409, 012225

- Khaerdinov, N.S. and Lidvansky, A.S., 2013b. Variations of Cosmic Ray Muon Flux during Thunderstorms, J. Phys.: Conf. Ser., 409, 012230.

- Khaerdinov, N.S., Lidvansky, A.S., and Petkov, V.B., 2005. Electric Field of Thunderclouds and Cosmic Rays: Evidence for Acceleration of Particles (Runaway Electrons), Atmospheric Research, 1-4, 346-354.

- Khaerdinov, N.S., Lidvansky, A.S., Variations of Intensity of Cosmic Ray Muons due to Thunderstorm Electric Fields, 2005, 29th Intern. Cosmic Ray Conference, Pune, India, vol. 2, pp. 389-392.

- Khaerdinov, N.S., Lidvansky, A.S., Specific Features of Variations of Cosmic Ray Muons during Thunderstorms, 32nd Intern. Cosmic Ray Conf., Beijing, 2011, DOI: 10.7529/ICRC2011/V11/0279.

- Lidvansky, A.S., 2003. The Effect of the Electric Field of the Atmosphere on Cosmic Rays, J. Phys. G: Nucl. Part. Phys., 29, 925-937.

- Lidvansky, A.S. and Khaerdinov, N.S., 2007. Effect of the near-Earth electric field on the intensity of the soft component of cosmic rays, Bulletin of Russ. Acad. Sci., Phys. Ser., 71, no. 7, 1024-1027. doi: 10.3103/S1062873807070398

- Lidvansky, A.S. and Khaerdinov, N.S., 2007. Dynamics of cosmic rays in the atmospheric electrostatic field and production of particles by thunderclouds, Bulletin of Russ. Acad. Sci., Phys. Ser., 71, no. 7, 1032-1034. doi: 10.3103/S1062873807070416

- Lidvansky, A.S., Petkov, V.B., and Khaerdinov, N.S., 2004. Variations of the intensity of cosmic ray muons due to thunderstorm electric fields, Bulletin of Russ. Acad. Sci., Phys. Ser., 68, no. 11, 1605-1607.

- Roussel-Dupre R.A., Gurevich A.V., Tunnell T., and Milikh G.M., 1994. Kinetic theory of runaway air breakdown, Phys. Rev. E, 49, 2257-2271.

Study of TGEs and Gamma-Flashes from thunderstorms in 20-3000 keV energy range with SINP MSU Gamma-Ray spectrometers

V.V. Bogomolov [1, 2], S.I. Svertilov[1, 2], I.A. Maximov[1, 2], M.I. Panasyuk[1, 2], G.K. Garipov[1]

1. D.V.Skobeltsyn Institute of Nuclear Physics, M.V.Lomonosov Moscow State University, Russian Federation;
2. Physical Department, M.V.Lomonosov Moscow State University, Russian Federation

Abstract. SINP MSU provided a number of experiments with scintillator gamma-spectrometers for study of spectral, temporal and spatial characteristics of TGEs as well as for search of fast hard x-ray and gamma-ray flashes probably appearing at the moment of lightning. The measurements were done in Moscow region and in Armenia at Aragats Mountain.

Each instrument used in this work was able to record data in so called "event mode": the time of each interaction was recorded with ~15 mcs accuracy together with detailed spectral data. Such design allowed one to look for fast sequences of gamma-quanta, coming at the moments of discharges during thunderstorms. The pulse-shape analysis made by detector electronics was used to separate real gamma-ray events and possible imitations of flashes by electrical disturbances when discharges occur.

During the time period from spring to autumn of 2015 a number of TGEs were detected. Spectral analysis of received data showed that the energy spectrum of coming radiation in 20-3000 kev range demonstrate a set of gamma-ray lines that can be interpreted as radiation from Rn-222 daughter isotopes. The increase of Rn-222 radiation was detected during rainfalls with thunderstorm as well as during rainy weather without thunderstorms. Variations of Rn-222 radiation dominate in low energies (<2.6MeV) and must be taken into account in the experiments performed to measure low energy gamma-radiation from the electrons accelerated in thunderclouds.

In order to determine the direction from which the additional gamma-quanta come the experiment with collimated gamma-spectrometer placed on rotated platform was done. The results of this experiment realized in Moscow region from august, 2015 will be presented as well as the results of comparison of different TGEs measured in Moscow region and in Armenia.

1. INTRODUCTION

It is known from many experiments that sometimes the gamma radiation additional to constant background appears during thunderstorms. The nature of detected gammas is usually explained by the acceleration of electrons in large electric fields existing in thunderclouds. Spectral characteristics can be described in general by the model of relativistic electrons avalanche (Gurevich, 1992, Dwyer, 2012a).

Phenomena in gamma rays connected with atmospheric electricity are observed in wide range of time scale including such fast flashes as so-called Terrestrial gamma flashes (TGFs) lasting for less than 1ms (Briggs et al, 2013) and such slow phenomena as so-called Thunderstorm ground enhancements (TGEs) lasting up to several hours (Chilingaryan, 2014). TGFs are usually studied in orbital experiments with gamma spectrometers working in "classical" energy range from several hundreds of keV to several MeV, but there are several observations of TGFs from lightnings at the ground level (Dwyer et al, 2012b). It must be noted that the radiation from TGFs is hard up to several tens of MeV. The best conditions for study of TGEs are present in mountains because of low absorption of measured radiation in atmosphere and low distance between the clouds and the detector. Many measurements of gamma-ray and electron flux variations were made with large detectors based on organic scintillators specialized for cosmic ray study (Chilingaryan, 2014). These detectors usually measure count rates in high energy range from MeVs to GeVs and unfortunately can't provide accurate spectral measurements of gamma radiation in energy range of several hundred keV and below (Chilingaryan et.al. 2013). To complete the observations in low energy range well-calibrated detectors based on scintillator crystals are needed. The instruments must have stable (up to ~1%) characteristics for long-lasting measurements and enough time resolution to detect possible short flashes. Energy resolution must be suitable for detection of discrete gamma-ray lines.

In this paper the design and characteristics of couple of such gamma-ray spectrometers produced in SINP MSU will be described. Then the results of measurements made with these instruments in Moscow region and in Armenia will be presented and discussed.

2. DESIGN AND CHARACTERISTICS OF GAMMA-RAY SPECTROMETERS

The instruments used in this work are scintillator gamma-ray spectrometers based on common non-organic scintillators. Electronic circuits used in these spectrometers can work with single-crystal detectors as well as with phosvich multilayer detectors providing determination of the crystal where interaction took place by pulse-shape analysis. Such kind of analysis also allows one to remove imitations of gamma-events by thunderstorm electric discharges because the shape of the imitated pulse will differ from one produced by scintillation.

The design of the detector electronics is very similar to one of DRGE instrument developed in SINP MSU for space experiment RELEC on-board "Vernov" satellite (Panasyuk et.al. 2015). Such transient phenomena as TGFs, GRBs and some other were studied during the space experiments with this instrument.

The structural diagram of electronics of gamma-spectrometer is presented at fig.1. It consists of three boards. First one is "Power supplying unit" providing high voltage (~1000V) for PMT and low voltage (+/-5V) for analog and digital electronics. Second board is "Event" card, containing analog electronics such as preamplifier, discriminator producing event trigger pulse and circuits for pulse shape analysis. The switch controlled by delayed trigger signal is used for separate integrating of first and last

parts of PMT current pulse. The signals of so-called "fast component" and "slow component" proportional to correspondent part of PMT pulse are formed and then digitized by two ADCs of microcontroller located on "Data collecting card"
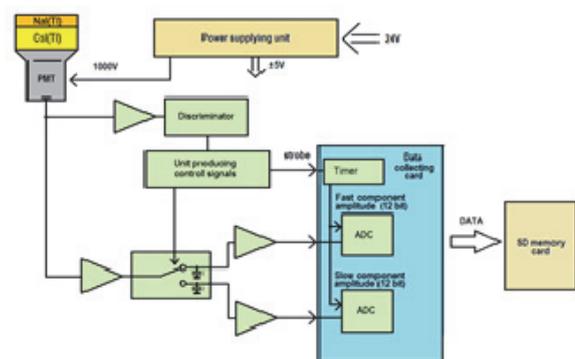

Figure 1. Design of scintillator gamma-ray spectrometer

"Data collecting card" is based on the board STM32F4DISCOVERY with Cortex M4 microcontroller. The program of microcontroller provides the next works:

- Producing time data with accuracy 1s. Stability of internal timer is ~1s/day
- Forming data frames for each second.
- Producing ~15 mcs timer data starting from the beginning of the frame
- Interrupting on the request from "Event" card and digitizing pulses of fast and slow components
- Digitizing signal on the additional analog input at the beginning of the frame

The output data are recorded to SD card for each second. The data frame format is presented in table 1. For reliability it was decided to group data frames to automatically numbered files with size ~10Mb. A new folder is automatically created for every new session when power is on.

Table.1. Data frame format

Size	What is recorded	Details
7b	Frame start marker	E4 57 B4 C0 3F 66 99
4b	Frame number	
6b	Time	YY MM DD hh mm ss
2b	Number of events in the frame	
4b	Number of counts of 15mcs timer during the frame	
2b	ADC data for external analog input	
N*(3b+3b)	Data records	ADC data + timer value
4b	end marker	CC 11 00 00

Two gamma-ray spectrometers were produced for the study of TGEs and the search for gamma-flashes from lightnings. First one has detector based on 80x80 mm CsI(Tl) crystal coupled with Hammamatsu R1307 PMT. It provides measurements in 20-3000 keV energy range with energy resolution 7.2% at 662 keV. Second spectrometer has considerably small NaI(Tl) detector with size 40x40 mm coupled with Russian PMT FEU-176. It is designed for measurements in 20-1000 keV range. The resolution of this instrument is ~12% at 662 keV.

The spectrometer with 80 mm crystal was modified for experimental determination of the predominant direction of detected gamma-radiation if this radiation if not uniform. The instruments detector was collimated by lead layer shielding half of its FOV and placed to the platform rotated with frequency 2 min^{-1}. The sensor of the direction was made as a resistive divider, changing output voltage in dependence on the instrument orientation. The voltage from the divider was recorded in data frames for every second as ADC data for external analog input (see tab.1).

Photos of both small instrument equipped with 40mm NaI(Tl) detector and large one equipped with collimated 80 mm CsI(Tl) detector placed on the platform are presented at fig.2.

Both gamma-ray spectrometers were calibrated with a number of radioactive sources. Some of energy spectra obtained during calibrations are presented at fig. 3, 4.
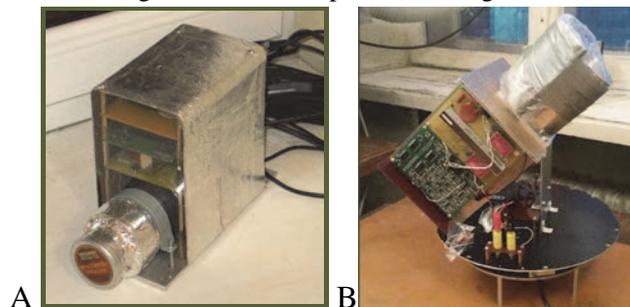

Figure 2. A) Photo of the gamma-spectrometer equipped with 40mm NaI(Tl) detector, B) Photo of the gamma-spectrometer equipped with collimated 80 mm CsI(Tl) detector placed on the rotating platform (without cover)
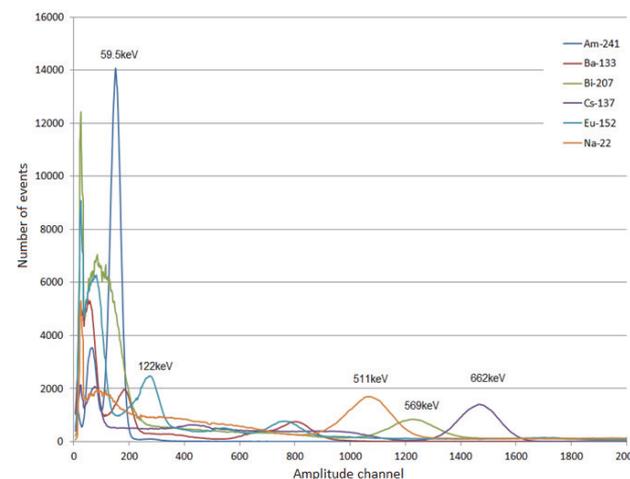

Figure 3. Energy spectra of several radioactive sources obtained during calibration of gamma-spectrometer equipped with 40mm NaI(Tl) detector

Autocalibration algorithm was used during large detector data processing: every 300s of the data the computer program determined actual position of well seen 1.46 MeV background gamma-ray line of K-40, then the energy of gamma-quanta in keVs was calculated. Such procedure allowed minimizing the effects of false variations caused by temperature drift of the detector characteristics. It is important for long-lasting observation series because day and night temperature can differ more than 20 degrees. The temperatures taken during sunny day and thunderstorm can also greatly differ.

It must be noted that 1.46 MeV line can't be used for auto-calibration of small detector because it is out of its range. There were attempts to use 609 keV background line from Bi-214 for auto-calibration but the results appeared to

be not enough reliable because this line is not bright and stop-factor of small NaI(Tl) detector described above is not enough high.

Measurements of radiation of Cs-137 source placed ~3 m far from rotating spectrometer were used to estimate its angular characteristics. The source was positioned at three different angles from the ground plane: 0º, 30º and 70º. Then the data from the rotating instrument were recorded and the numbers of events in 662 keV peak were compared. Correspondent modulation curves are presented at fig. 5. One can see that the depth of modulation is about 2 times for all three positions of the source.
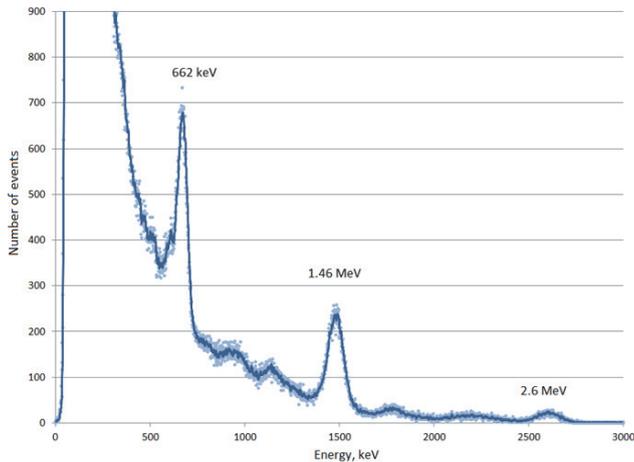

Figure 4. Energy spectrum of Cs-137 gamma-ray source (E=662 keV) placed far from detector obtained during calibration of gamma-spectrometer equipped with 80mm CsI(Tl) detector. Background lines from K-40 (E=1.46 MeV) and Tl-208 (2.6 MeV) are seen
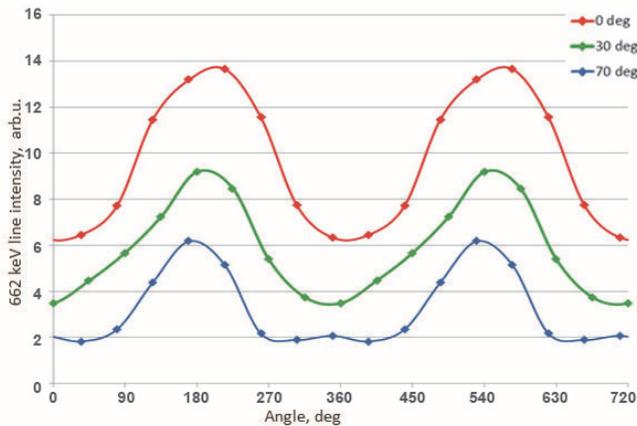

Figure 6. Modulation curves of Cs-137 radiation measured with 80 mm CsI(Tl) collimated detector placed on rotating platform.

3. RESULTS OF MEASUREMENTS IN MOSCOW REGION

The measurements in Moscow region were made ~50 km North from Moscow from July to September of 2015 with 80 mm CsI(Tl) collimated detector. The detector covered by thin film for rain protection was placed in the garden. The data were recorded continuously. The data of the experiment contain considerably long segments of sunny weather, some segments with continuous rain and several segments with showers and thunderstorms.

An example of Moscow region data is presented at fig.7. These data were taken from late 27 to 30 of July, 2015. There were two local thunderstorms correspondent to the peaks at the first day of the data (28.07.2015). These thunderstorms were accompanied with lightnings and intensive showers. Then the weather became fine for next three days. Narrow peaks appearing during the thunderstorms in

gamma-ray data are well seen. The amplitude of the enhancements reaches ~30% of common gamma-ray background.

Energy spectrum for thunderstorm interval correspondent for the second peak at fig.7 is presented at fig.8 together with the spectrum obtained during the sunny weather interval. One can see a lot of gamma lines over all energy range of the spectrometer. Background lines from K-40 (E=1.46 MeV) and Tl-208 (2.6 MeV) are seen with the same brightness for thunderstorm and sunny weather time intervals. Other lines are connected with Rn-222 isotope being one of the most important sources of natural gamma-ray background. Radon is a daughter isotope of Ra-226 appearing from its decay in the ground. The lifetime of Rn-222 is 3.9 days so this heavy radioactive gas has enough time to get to the atmosphere. After series of Rn-222 decay some short-living isotopes, in particular Bi-214 with half-life ~20 min, appear producing linear gamma radiation that is observed.

Gamma-ray lines from Rn-222 are seen during all time intervals but their amplitudes are much greater during the thunderstorm than during the fine weather segments. The result of subtraction of thunderstorm and sunny weather spectra, presented at fig.8, shows that most of the additional gamma-ray flux can be explained by radiation of Rn-222 and its daughters. Some small increase of gamma-ray rate above 2.6 MeV seen at fig.8 is much less than one from Rn-222 radiation.
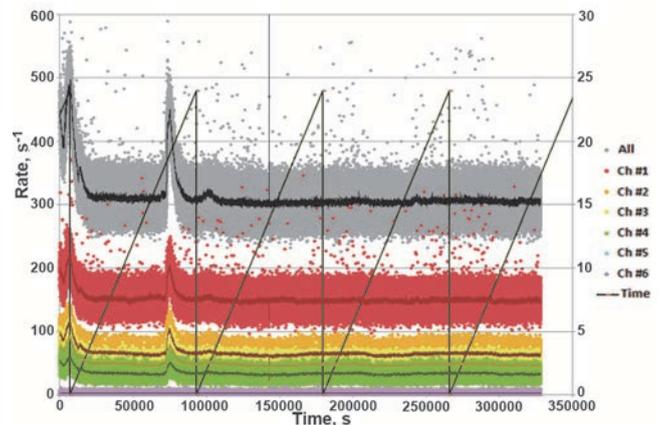

Figure 7. Monitoring data for 27-30 of July, 2015 obtained in Moscow region. Readings in several energy channels are plotted. The sawtooth line displays the time of the day (right scale)
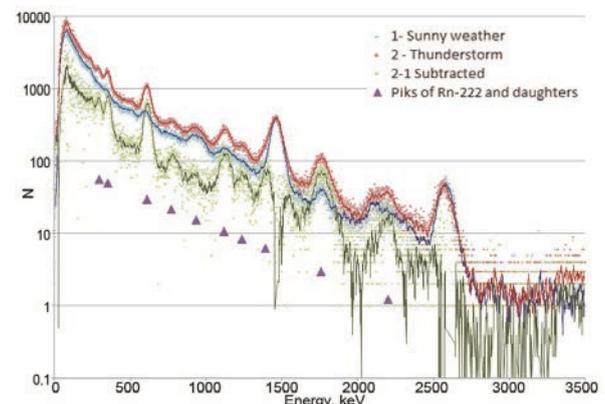

Figure 8. Energy spectra for 27 of July, 2015 obtained in Moscow region.

Monitoring data at fig. 9 and energy spectra at fig. 10 correspond to the data of measurements made 05.09.2015. There was a rainy day with cloudy sky and there was no thunderstorm. However one can see large variations of gamma-ray count rate. Comparison of spectra obtained for regions of large and small flux leads to the conclusion, that

the observed variations are connected with changes of Rn-222 concentration near the instruments.
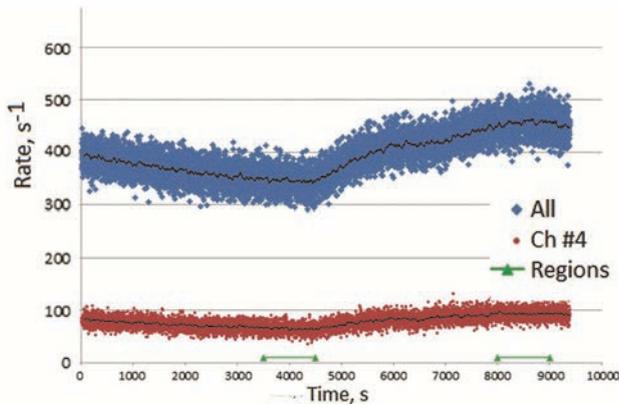

Figure 9. Monitoring data obtained 05 of September, 2015 in Moscow region
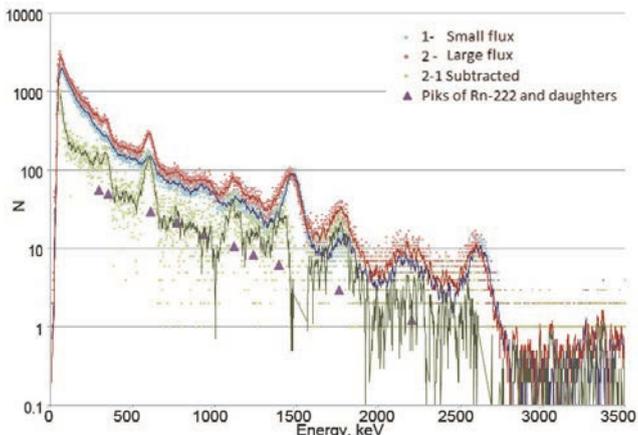

Figure 10. Energy spectra obtained 05 of September, 2015 in Moscow region.

The conditions of observations on 27 of September, 2015 provided the possibility to estimate the rate of additional Rn-222 appearance near the detector. Detailed monitoring data curves are presented at fig.11. There was a clear weather more than for a day, then the thundercloud suddenly appeared and thunderstorm with rain shower rapidly started for ~5 min. After that there was ~5 min pause when there was no rain. Then the thunderstorm with intensive shower started again. The rain with thunderstorm continued for ~1.5 hours and then stopped and the sun appeared.

The spectrum of the observed enhancement is similar to one presented at fig. 8. That means that the additional radiation was produced by radon and its daughters. One can see a step at the front of the curve at fig. 11 that shows that Rn-222 appears together with rain. Possible explanation of the details of its behavior is that Rn-222 was solved in the water of raindrops. Radon could be collected from air during the movement of the storm cloud. Other way of experimental data description is to propose that near-ground concentration of Rn-222 is changed with the change of the conditions of Rn-222 escape from ground. However it is difficult to explain the observed speed of Rn-222 by this way.

After the rain stopped the intensity of radiation dropped with characteristic time ~0.5-1h. It can be explained by the decay of daughter isotopes of Bi-214 and Pb-214. Other processes leading to the fall of the experimental curve are the diffusion of gaseous radon in the air and the leakage of the rain water to the ground.

The monitoring data selected for the time intervals correspondent to definite orientation of the instrument are pre-

sented at fig.12. There is no significant difference in the shape of the curves so one can conclude that the observed radiation is omnidirectional.
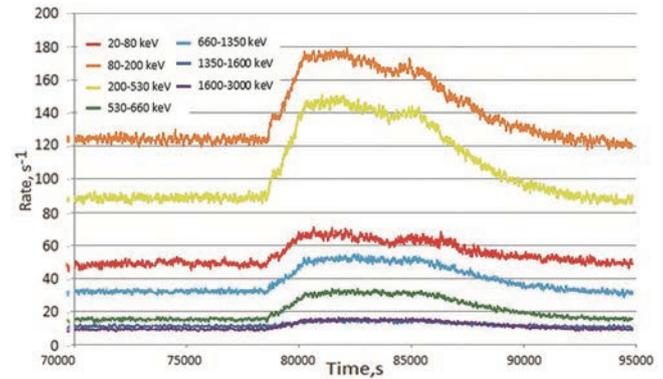

*Figure 11. Monitoring data for 27 of September, 2015 obtained in Moscow region*
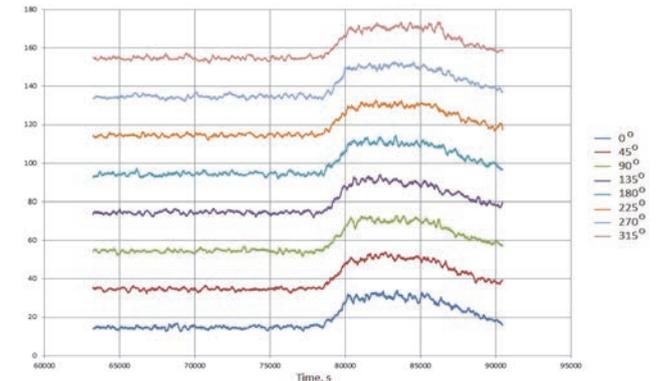
Figure 12. Monitoring data selected for the time intervals correspondent to definite orientation of gamma-ray spectrometer

In order to search for the short bursts possibly appearing at the moment of lightning gamma-by-gamma data of thunderstorm 27.09.2015 were processed. The moments of the short burst candidates with >7 gammas occurring in 1 ms were determined. They are plotted with yellow triangles at fig.13. It is seen that most of the burst candidates group inside the thunderstorm segment of data. However the probability of random imitation for this segment also increases because of the increase of background rate in this time.
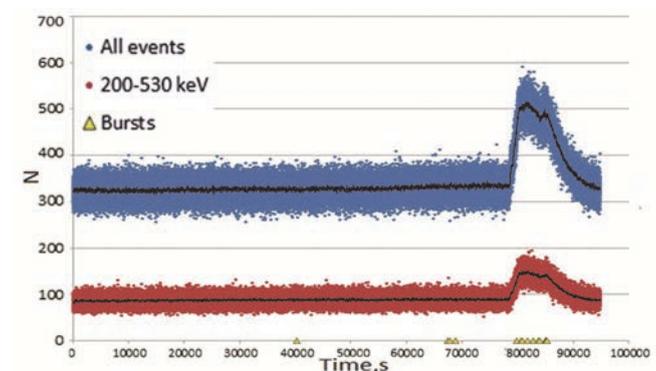
Figure 13. Monitoring data of gamma-ray spectrometer(curves) and the moments of short burst candidates with >7 gammas occurring in 1 ms (triangles)

The graph of expected number of imitations versus threshold value for thunderstorm region and before it is plotted at fig. 14. It definitely shows that probably all candidates pointed on the fig. 13 are random and the criterion must be some harder with threshold of 9 gammas per 1 ms. such events were not observed.

44

Another way to detect gamma-ray flashes from lightnings is to look at the detailed data of gamma-spectrometer at the moment of lightning. Several nearby lightnings happened during the thunderstorm of 27.09.2015. The time between lightning and thunder sound for some of them was less than 1 s. Data analysis shows that there was no significant fast data increase on the millisecond scale within several seconds around these moments.
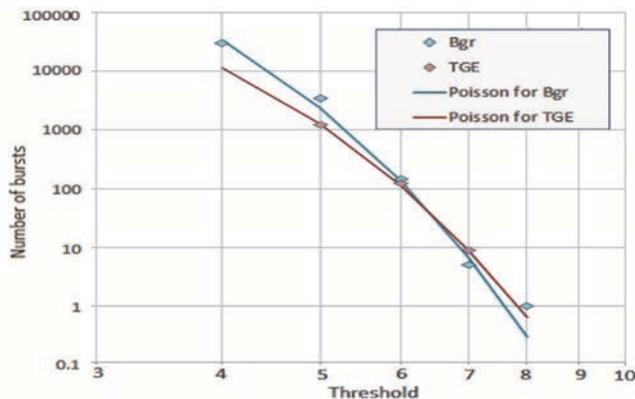
*Figure 14. Expected number of 1 ms pulse imitations versus threshold value.*

4. RESULTS OF MEASUREMENTS IN ARMENIA

A ~2 hour long TGE was observed 22.09.2014 by the instrument with 40 mm NaI(Tl) detector in Nor-Amberd during TEPA-2014 conference. The measurements were made from the balcony of the building during the thunderstorm located considerably far from the instrument in the Erevan direction. Monitoring data sequence for this TGE is presented at fig. 15. Non-intensive rain started approximately at the same moment when the rise of gamma-ray data readings was observed.
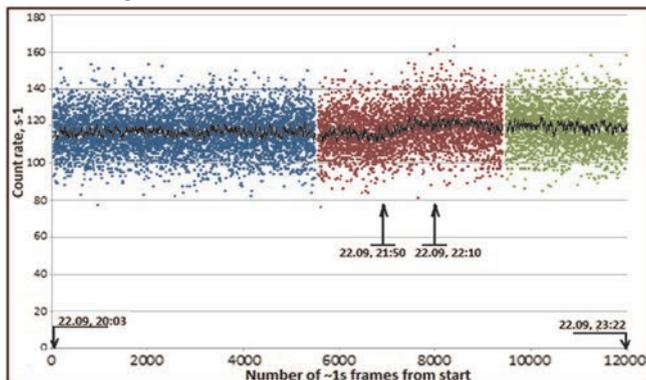

Figure 15. Monitoring data sequence for TGE measured 22.09.2014 in Nor-Amberd.

The spectra measured 22.09.2014 in Nor-Amberd are presented at fig. 16A. The comparison of the spectra at fig.16A with calibration spectra presented at fig. 16B allows one to propose that the peculiarity near 1200 channel is connected with 609 keV gamma-ray line of Bi-214. This line is not seen in the spectrum of the difference between TGE and background segment taken before TGE. But the statistics is very poor and there is no reason to conclude that no 609 keV line is present in additional radiation from TGE source.

The energy spectra of the background gamma-radiation without TGEs were measured at the site of Aragats cosmic ray station (h=3200m) in several places. These spectra (see fig.17) were measured inside one of the buildings and outside near the lake. Also a spectrum measured with fiber absorption block between the concrete of the building and

detector was measured. The peculiarity seen some above 600 keV can be associated with 609 keV line from Bi-214. It is visible on all graphs having different intensity. One can see that this line is very contrast on the spectrum of difference between spectra measured in the building and near the lake. It is possible to conclude that some part of the radiation in the building comes from isotopes generated in decay cascades of Ra-226 existing in concrete.
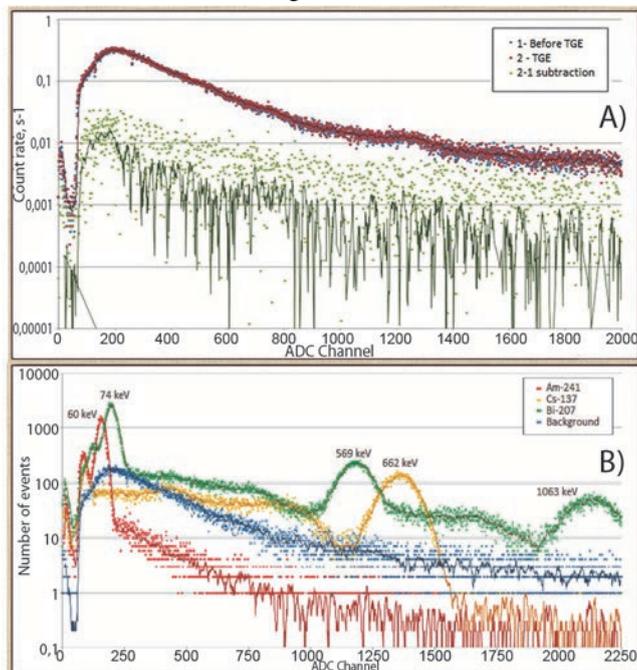
Figure 16. A) Spectra obtained before TGE and during TGE measured 22.09.2014 in Nor-Amberd. B) Calibration spectra of several gamma-ray sources. The scale is the same as at Figure16A.
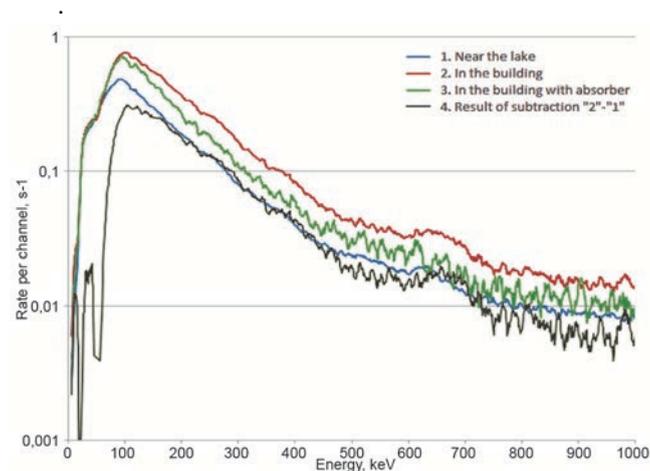
Figure 17. Energy spectra of the background gamma-radiation without TGEs measured at the site of Aragatz cosmic ray station (h=3200m) in several places.

A segment of long-time monitoring data from Aragats are presented at fig. 18. There are variations of gamma-spectrometer readings of different nature. Regular maxima appearing almost every day at 8h time can be described as the reaction of the detector on temperature. Such changes can be removed by auto-calibration method described about if the detector has enough energy range and resolution. There is a channel considerably non-sensitive to such variations (from 230 keV to 450 keV). One can see a peak with considerably hard spectrum that appeared at ~18h on 11.11.2015. The energy spectrum of this increase is presented at fig 19. The peculiarity around 600 keV allows one to propose that Rn-222 is responsible for this gamma-ray flux variation.
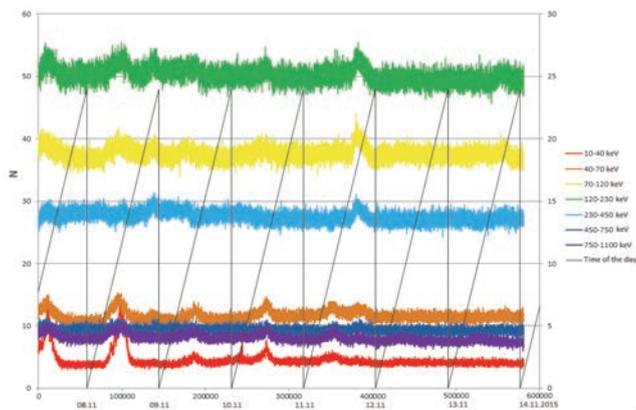
Figure 18. Monitoring data for period from 07.11.2015 to 14.11.2015 obtained with 40mm NaI(Tl) gamma-ray spectrometer on Aragatz mountain (3200 m).
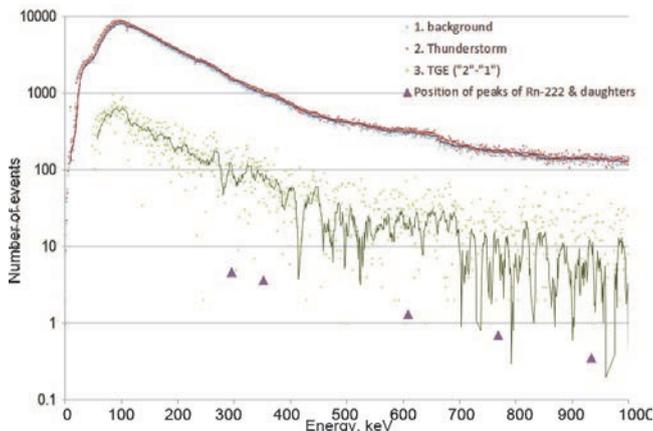
Figure 19. Energy spectra obtained during thunderstorm 11.11.2015 with 40mm NaI(Tl) gamma-ray spectrometer on Aragats mountain (3200 m)

5. DISCUSSION

All energy spectra obtained in 20-3000 keV energy range during thunderstorms in Moscow region show the presence of gamma-ray lines associated with Rn-222 and daughters. Radon radiation is well-known background component. The results of measurements allow one to conclude that the concentration of Rn-222 near the ground has great variations usually increasing at the periods of rain. Dynamic of the background increase probably can be explained by coming of Rn-222 from the cloud with rain water. Maybe atmospheric Rn-222 is solved in this water during the formation of the cloud and its movement above the ground surface. The measurements made on rainy days without thunderstorm demonstrate similar variations of Rn-222 concentration.

The measurements made on Aragats Mountain also allow to conclude that additional Rn-222 background appears during thunderstorms. The amplitude of such variation must depend on various weather conditions such as speed of wind and rain intensity. It is obvious that variations of Rn-222 gamma-ray background are much greater than ones expected from bremsstrahlung of the electrons accelerated in thunderclouds in the same energy range. However variations of natural radioactivity do not influence on gamma-spectra in the high energies above 3 MeV. It is important to use an instrument with wide energy range lasting for more than 3 MeV for TGE study. It must have good stop-factor and energy resolution in order to estimate the amount of radiation connected with Rn-222. The amplitude of 609 keV line on the energy spectrum can be a good indicator for it.

There were no indications on gamma-flashes observed at the moments of lightning. Instruments with larger effective area placed in mountains will improve the quality of measurements.

REFERENCES

- Briggs, M.S., Xiong S., Connaughton, V., et al., (2013) Terrestrial gamma-ray flashes in the Fermi era: Improved observations and analysis methods, Journal of Geophysical Research: Space Physics, vol. 118, 3805–3830, doi:10.1002/jgra.50205

- Chilingaryan A., Hovsepyan G and Kozliner L., (2013), Thunderstorm Ground Enhancements: gamma ray differential energy spectra. Proceedings of International Symposium TEPA-2013, Nor-Amberd, Armenia, 32-41

- Chilingarian A., (2014) Thunderstorm Ground Enhancements - model and relation to lightning flashes, Journal of Atmospheric and Solar-Terrestrial Physics 107 68–76.

- Gurevich A.V., Milikh G.M., Roussel-Dupre R. (1992) Runaway electron mechanism of air breakdown and preconditioning during a thunderstorm. Phys. Lett. A. V. 165, 463– 468.

- Dwyer, J.R., D.M. Smith, and S.A. Cummer (2012a), High-energy atmospheric physics: Terrestrial gamma-ray flashes and related phenomena, Space Sci. Rev., 173, 133-196, doi: 10.1007/s11214–012-9894-0.

- Dwyer, J. R., Schaal, M. M., Cramer, E. et al, (2012b) Observation of a gamma-ray flash at ground level in association with a cloud-to-ground lightning return stroke, Journal of Geophysical Research, vol. 117, A10303, doi:10.1029/2012JA017810

- Panasyuk M.I., Svertilov S.I., Bogomolov V.V., et.al. (2015), RELEC Mission: Relativistic Electron Precipitation and TLE study on-board small spacecraft, Advanced Space Research, doi:10.1016/j.asr.2015.11.033

Angular dependence of muon intensity disturbances detected during thunderstorms

M.N. Khaerdinov, N.S. Khaerdinov, A.S. Lidvansky

Institute for Nuclear Research, Russian Academy of Sciences, Moscow, Russian Federation

Abstract. The possibility of probing the geometry of a thunderstorm near the place of observation using experimental data on count rates of a large-area muon detector is investigated for the conditions of high surrounding mountains with a complex profile. A method of analysis is suggested and demonstration to one particular event of this type recorded by the Carpet air shower array of the Baksan Neutrino Observatory.

1. INTRODUCTION

Anomalous disturbances of particle intensity recorded in the experiment studying variations of cosmic rays during thunderstorms at the Baksan Neutrino Observatory are explained using a model of slow electric breakdown of the stratosphere under the action of avalanches of runaway electrons. In this case, according to the theory of formation of intensity disturbances for muons detected by a horizontal array, significant angular dependence should exist for the effect amplitude. Indeed, for vertical muons the preferential decay of decelerated particles is the main effect, and it forms a strong negative quadratic field dependence of the total intensity. At the same time, for particles moving at large zenith angles the effect of focusing by vertical field is most significant: it increases the effective detection area for them, forming as a result a positive quadratic regression.

Studying the disturbances of muon intensity during thunderstorms at different zenith angles, one can get some information about geometry of the process of the stratosphere breakdown, that is, about its dimensions and distance from the observation point. In addition, one could determine the potential difference in the stratosphere associated with the breakdown. Below, a method of determining parameters of the breakdown region with the use of data on variations of secondary cosmic rays during thunderstorms at different angles is described.

The Carpet air shower array of the Baksan Neutrino Observatory is located in the Baksan Valley, North Caucasus at an altitude of 1700 m above sea level. The tops of surrounding mountains (4-5 km a.s.l...) are at a distance of about 5 km. The particle fluxes of secondary cosmic rays are permanently recorded by the array together with atmospheric pressure, temperature, near-ground electric field and precipitation electric current. Detected particles are divided in two components. The soft component (electrons, positrons and photons) is recorded in the energy range 10-30 MeV. The hard component is represented mainly by muons (83%) with energy higher than 100 MeV. These two components form two independent channels of recording secondary cosmic rays. They are going through the atmosphere whose diagnostics can be performed by deciphering variations of their intensity. Fig. 1 present the angle of elevation above horizon of the upper edge of mountains for an observer looking from the center of the Carpet air shower array.

2. METHOD

Groups of muons with different effective angle of arrival are experimentally selected. The method is based on separation of detected particles into channels with different energy release in the detector (the incident angle and energy release are interconnected). Variations in the channels during thunderstorms should be substantially different (N. Khaerdinov et al., 2013a). This is connected with focusing action of the vertical electric field upon muons. This action increases with increasing zenith angle. Analyzing variations in separated channels one can determine model parameters of the thunderstorm field that forms these variations.
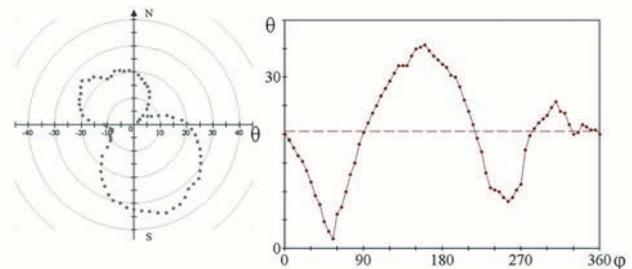

Figure 1. Elevation angle of mountain upper edge around the array center (on the left); and azimuth distribution of elevation angle of mountains around the array center (on the right).

We describe the thunderstorm region forming muon variations in the form of a cylinder with constant potential difference between its bases. The upper base corresponds to the effective height of generation of detected muons (11.5 km above sea level). The lower base corresponds to zero isotherm level of about 3.3 km above sea level (N. Khaerdinov et al., 2015). Such a model allows one to characterize the action of a thundercloud on detected muons by three unknown parameters: potential difference, radius of bases, and distance from the array to the thunderstorm region center. Near-ground part of the field is estimated by direct measurements made with the electric field meter. In order to determine basic characteristics of thunderstorm activity, it is sufficient to have three independent channels recording muon intensity variations and sounding the region under different angles. However, one cannot distinguish azimuth orientation of the center of the thunderstorm region.

3. IMPLEMENTATION

During thunderstorms the variations of instrumental origin are possible, and they reveal themselves as instability of thresholds and maximum position of the energy release spectrum. Therefore, in addition to three information chan-

nels one should have the fourth independent channel characterizing the maximum position. We divide the spectrum of detected muons in four parts with equal intensities (Fig. 2). Taking into account fluctuations of energy release of muons in the detector, the accuracy of angle determination using this method is about 20%. Hence, the regions of spectral maximum (regions 1 and 2) correspond to vertical muons. Comparing their behavior one can get information about stability of variation detection. The first (30-50 MeV) and second (50-62 MeV) parts of the spectrum correspond to arrival angles 0°-35°. Accordingly, the third (62-90 MeV) and fourth (>90 MeV) parts correspond to angular ranges 35°-55° and more than 55°, respectively.
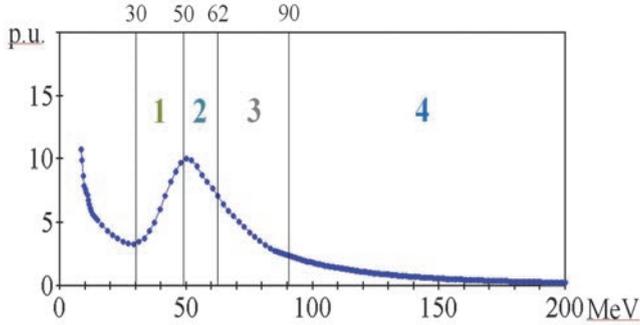

Figure 2. The spectrum of detected muons with partition in equal intensity parts that correspond to different directions of muon arrival. The first part is soft component, next follow angular intervals from 0° to 35° (1 and 2), from 35° to 55° (3), and higher than 55° (4). Electron-photon component is cutoff by energy threshold with the best stability (30 MeV).

Surface topography of surrounding mountains prevents a major part of muons with large zenith angles from being detected. This fact reveals itself in the behavior of muon variations caused by thunderstorm fields. In (N. Khaerdinov et al., 2013b) regression coefficients for the case of infinite field extension in the horizontal plane were calculated, as well as potential differences. Fig. 3 present, for the case of infinite field extension in the horizontal plane, distributions of angular coefficients of linear and quadratic regression of muons with allowance made for mountain border line.
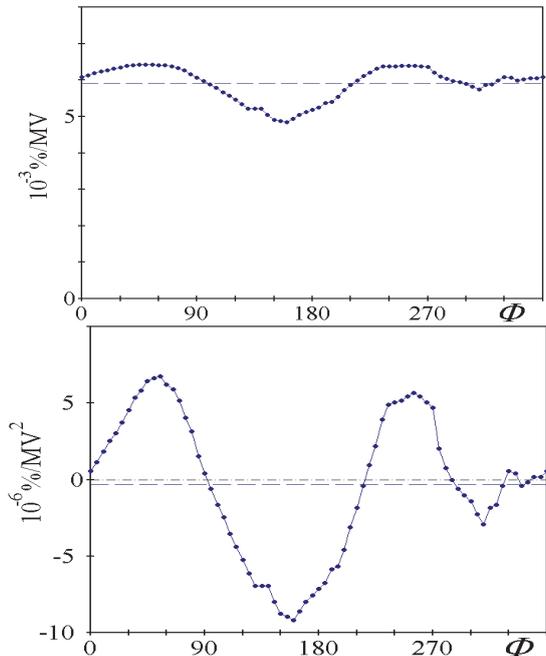

Figure 3. Azimuth distribution of angular coefficients of linear (left) and quadratic (right) regression with potential difference in the stratosphere. Regression coefficients are for muons with energy higher than 100 MeV. The mean values correspond to a zenith angle of 65°.
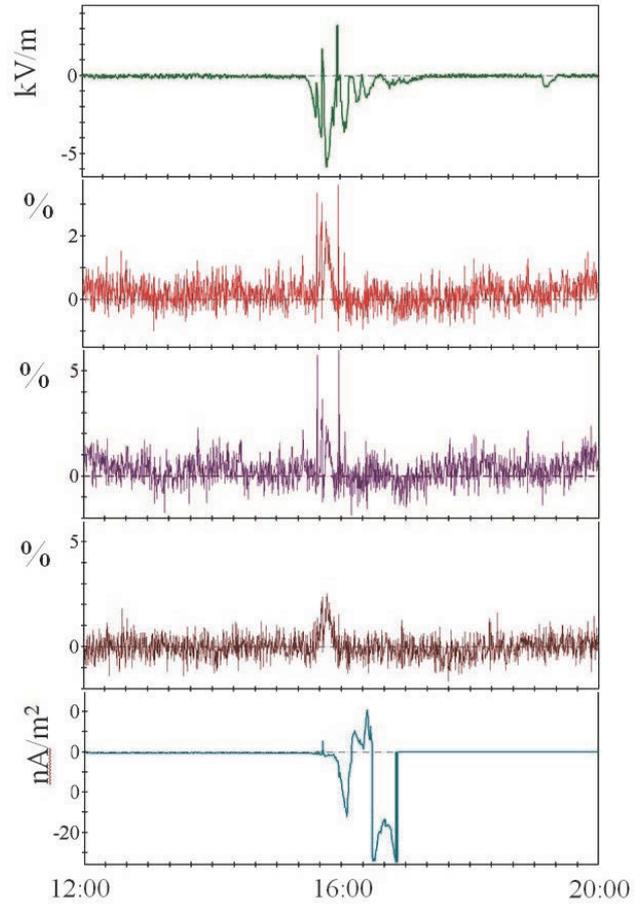

Figure 4. Thunderstorm event on June 20, 2014. The time of averaging is 20 s. Local time. From top to bottom variations of: 1) electric field; 2) soft component (10-30 MeV); 3) soft component (10-17 MeV); 4) soft component (17-30 MeV); 5) precipitation electric current (nA/m²).

The mean values of these regression coefficients correspond to a zenith angle of 65°. Hence, this is the characteristic angle of formation of muon variations.

The linear regression coefficient varies with azimuth within the range of 10%, while the quadratic coefficient variation is more significant. This fact shows stronger dependence of variations in the amplitude of the muon intensity on geometry of the thunderstorm field, which was not taken into account before.

4. DATA ANALYSIS

Let us demonstrate the method application using the thunderstorm event on June 20, 2014 as an example. Figs. 4 and 5 present the plots of different parameters measured by the Carpet array in this period. The recorded disturbances of the soft and hard components correspond to realization of a runaway electron breakdown in the stratosphere region. This follows from the flat spectrum of disturbances of the gamma-ray intensity and anomalous disturbance in muons detected at 15:55. Details of analysis of such experimental data are described in paper (N. Khaerdinov et al., 2013b). The method described here allows one to characterize specific features of the active thunderstorm region that forms these anomalous disturbances.

Fig. 5 present successive channels of detection for muons sounding the thunderstorm region at various angles. Two upper panels represent intensity variations for vertical muons, their synchronous behavior demonstrates stability of detection. The existence and character of the anomalous disturbance variation with channels corresponds to the

model of formation of disturbances by thunderstorm field as described in (N. Khaerdinov et al., 2013b).
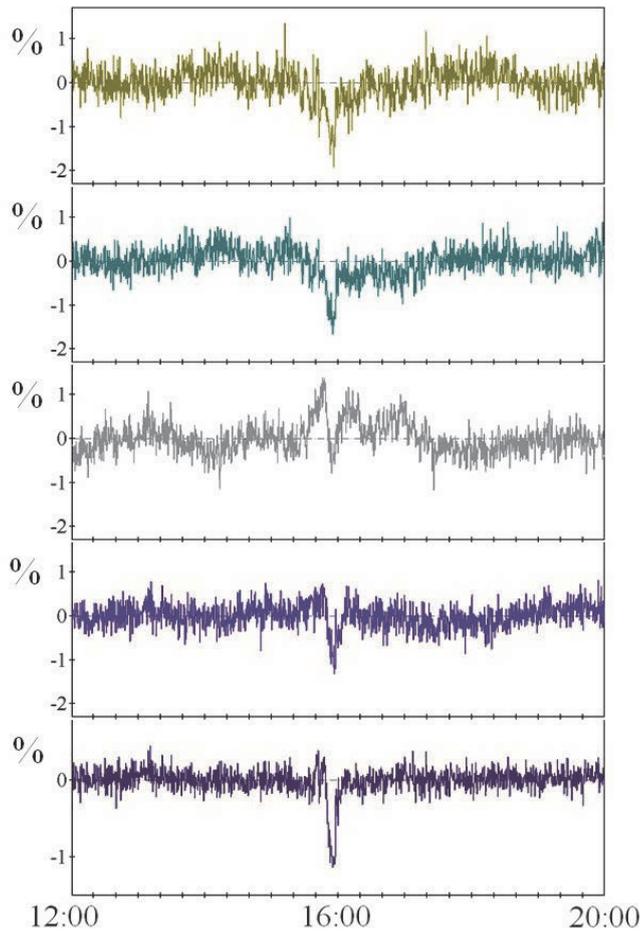
Figure 5. The same event as in Figure 4. From top to bottom variations of: 1) muon intensity 30-50 MeV (0°-35°); 2) muon intensity 50-62 MeV (0°-35°); 3) muon intensity 62-90 MeV (35°-55°); 4) muon intensity > 90 MeV (> 55°); 5) total muon intensity (> 30 MeV).

5. CONCLUSIONS

An example of experimentally detected anomalous disturbances of the intensity of muons with energies above 100 MeV, as measured by the Carpet air shower array, is presented and analyzed for different ranges of zenith angles. The possibility of estimating experimentally the geometry of thunderstorm field is demonstrated. A method to correct the obtained data for variations of apparatus origin is described. The effect of surrounding mountains on formation of muon intensity disturbances during thunderstorms is estimated.

ACKNOWLEDGMENTS

REFERENCES

- N. Khaerdinov and A. Lidvansky. Variations of cosmic ray muon flux during thunderstorms. 2013a J. Phys.: Conf. Ser. 409 012230.
- N. Khaerdinov and A. Lidvansky. Heights of Generation of Runaway Electrons in Bright Cosmic Ray Events Observed on the Ground during Thunderstorms. 2013b J. Phys.: Conf. Ser. 409 012225.
- N. Khaerdinov, A. Lidvansky, M. Khaerdinov, Characteristic electric state of thunderstorm atmosphere as derived from data on cosmic ray variations, Izv. Ros. Akad. Nauk. Ser. Fiz. 2015, vol. 79, no 5, pp.:736-738.

Design of a fiber optical sensor for atmospheric electric field measurement

H.V. Baghdasaryan[1], A.V. Daryan[2], T.M. Knyazyan[1]

1. Fiber Optics Communication Laboratory, National Polytechnic University of Armenia, 105 Terian str., Yerevan 0009, Armenia;
2. A.Alikhanyan National Lab (Yerevan Physics Institute), 2, Alikhanyan Brothers, Yerevan 0036, Armenia

Abstract. All-optical sensor for atmospheric electric field detection and measurement is suggested and numerically modelled. Thin electro-optical crystal sandwiched between two distributed Bragg reflectors (DBRs) forming multilayer Gires-Tournois (G-T) microresonator is used as a sensitive part of the electric field sensor. In the sensor device, an optical fiber delivers the wideband light spectrum to the sensing multilayer structure of G-T microresonator. The reflectance spectrum of the sensor contains information on the electric field strength and direction. The relevant reflectance peaks' shift in the reflected spectrum can be observed by an optical spectrum analyzer (OSA). Numerical modelling has been done by the method of single expression that is a suitable tool for multi-boundary problems solution. The obtained results of modelling will be useful in a new type of non-distorting sensor's elaboration for atmospheric electric field detection and measurement.

1. INTRODUCTION

The magnitude of atmospheric electric field is an important parameter in evaluation of the atmosphere state [1-3]. Measurements of the atmospheric electric field provide information about the thunderstorm activity and are useful for weather forecasting and lightning alert. Conventional instrument used for measuring the strength of electric fields in the atmosphere near thunderstorm clouds is the "field mill" [4, 5]. Different types of "field mills" and E-field probes for electric field measurement and relevant devices are under exploitation [4-9]. However, all these devices are prepared by or contain metallic parts and wires, which distort the electric field distribution [10, 11]. Use of electro-optical sensors makes possible creation of metallic free electric field meters. Devices of this type are widely used in high voltage (HV) engineering, antenna and electromagnetic compatibility (EMC) measurements, etc. [9, 12-14].

Photonic field meters utilize the Pockels effect or linear electro-optic (EO) effect, which produces birefringence in an optical medium. Substances such as KDP (Potassium Dihydrogen Phosphate), KD*P (Deuterated KDP) and LiNbO$_3$ (Lithium Niobate) show large Pockels effect and are very popular in electro-optic modulators [15].

Electric field measurement by use of the Pockels effect implies some means of measuring a change in refractive index caused by the applied electric field. Change in refractive index causes phase change of light passing through the EO crystal. Therefore, the problem reduces to the determination of the phase shift. There are devices exploiting direct measuring of phase shift by means of non-resonant interference methods [13, 16, 17].

We consider another type of electro-optical sensors using nonlinear resonator. These sensors contain an optical fiber and electro-optical crystal within micro-resonator mounted on the end of the fiber [10, 11, 13, 18-20]. Change in the refractive index induced by an external electric field causes shift of the reflectance spectrum. Resonator is irradiated by a wideband optical source via optical fiber and optical spectrum analyzer is used for detection of the reflected light. The same configuration can operate by using monochromatic light source performing phase shift measurement. In this case, phase shift is more sensitive than that in non-resonant case.

The wide range of atmosphere electric field's variation complicates the operation of electro-optical sensor and requires thorough computer simulations before specific device realization. In this paper the relevant method for simulation of light propagation and reflection in the proposed optical design is presented.

2. CONSTRUCTION AND MEASUREMENT SCHEME OF ELECTRO-OPTICAL SENSOR

For measurement of atmospheric electricity the following construction of all-optical sensor is suggested (Fig.1.):
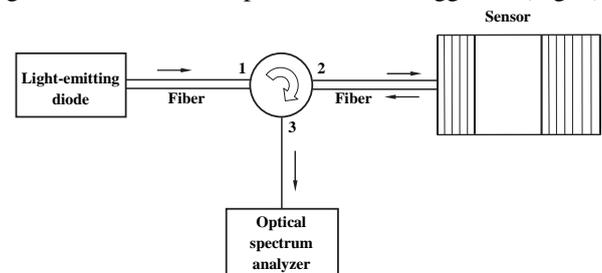
Figure 1. All-optical sensor for atmospheric electric field measurement.

A wideband optical source (light-emitting diode) illuminates reflective microresonator and the spectrum of reflected light is observed by optical spectrum analyzer (OSA). The sensor is a reflective type of Fabry-Perot microresonator (Gires-Tournois (G-T) [21]) where electro-optical crystal is sandwiched between DBR mirrors (Fig. 2).
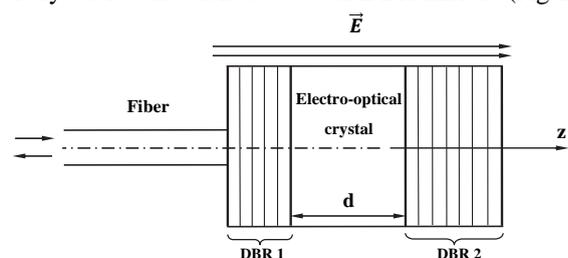
Figure 2. All-optical sensor consists of optical fiber and Gires-Tournois microresonator formed by electro-optical crystal sandwiched between two DBR mirrors of high (DBR 2) and medium reflectivity (DBR 1).

The z-cut electro-optical crystal is sensitive to the electric field strength $\vec{E}$ directed parallel or anti-parallel to the z-axis. Let us consider an application of electro-optical

crystal LiNbO$_3$ as a sensitive part of micro-resonator. It is known that the variation of the refractive index of LiNbO$_3$ crystal by the amplitude of applied electric field is expressed as:

$$\Delta n = n^3 r_{33} E / 2 , \qquad (1)$$

where $n = \sqrt{\varepsilon}$ is the refractive index at the absence of external electric field, $r_{33} \approx 30.8 \cdot 10^{-12}$ m/V is an electro-optic coefficient of the material [22]. The sign of the index change depends upon the polarity of the voltage applied to the crystal [15].

Atmospheric electric field is changed in the range of $E = 10^2 - 10^5$ V/m and relevant interval of permittivity change by (1) is: $\Delta\varepsilon = 0.79 \cdot 10^{-6} - 0.79 \cdot 10^{-3}$. Here $n = 2$ is taken at the light wavelength $\lambda_0 = 1.55 \ \mu m$.

Multilayer DBR mirrors are alternating quarter-wavelength bilayers of low and high permittivity providing high reflectance of mirrors necessary for microresonator operation. To determine optical characteristics of the micro-resonator the numerical simulation by means of the method of single expression (MSE) is carried out [23-28]. In the MSE, the solution of Helmholtz equation in each layer of the structure is searched in the form of a single expression, but not in the form of counter-propagating waves as in the traditional approach. Due to this, a prior assignment of the waveform in each layer of the structure is not required, which makes the MSE a convenient tool in studies of optical structures consisting of layers with any complex values of permittivity and permeability. The MSE is a valid tool for solving intensity-dependent non-linear problems since it does not rely on superposition principle.

3. CONCISE DESCRIPTION OF THE MSE

The backbone of the MSE for wave normal incidence on a multilayer structure is presented [23-28]. From Maxwell's equations in 1D case the following Helmholtz's equation can be obtained for linearly polarized complex electric field component $\dot{E}_x(z)$:

$$\frac{d^2 \dot{E}_x(z)}{dz^2} + k_0^2 \tilde{\varepsilon}(z) \, \dot{E}_x(z) = 0 , \qquad (2)$$

where $k_0 = \omega / c$ is the free space propagation constant, $\tilde{\varepsilon}(z) = \varepsilon'(z) + j\varepsilon''(z)$ is the complex permittivity of a medium. The essence of the MSE is presentation of a general solution of Helmholtz' equation for electric field component $\dot{E}_x(z)$ in the special form of a single expression:

$$\dot{E}_x(z) = U(z) \cdot \exp\left(-jS(z)\right) \qquad (3)$$

instead of traditional presentation as a sum of counter-propagating waves. Here $U(z)$ and $S(z)$ are real quantities describing the resulting electric field amplitude and phase, respectively. Time dependence $\exp\left(j\omega t\right)$ is assumed but suppressed throughout the analysis. Solution in the form (3) prevails upon the traditional approach of counter-propagating waves and is more general because it is not relied on the superposition principle. This form of solution describes all possible distributions of electric field amplitude, corresponding to propagating or evanescent waves in a medium of positive or negative permittivity, respectively. No preliminary assumptions concerning the Helmholtz's equation solutions in different media are needed in the

MSE. This gives advantages in investigation of wave interaction with any longitudinally non-uniform linear and intensity dependent non-linear media that can be done with the same ease and exactness.

Based on expression (3) the Helmholtz's equation (2) is reformulated to the set of first order differential equations regarding the electric field amplitude $U(z)$, its spatial derivative $Y(z)$ and a quantity $P(z)$ - proportional to the power flow density (Poynting vector) in a medium:

$$\begin{cases} \dfrac{dU(z)}{d(k_0 z)} = Y(z) \\[2mm] \dfrac{dY(z)}{d(k_0 z)} = \dfrac{P^2(z)}{U^3(z)} - \varepsilon'(z) \cdot U(z) \\[2mm] \dfrac{dP(z)}{d(k_0 z)} = \varepsilon''(z) \cdot U^2(z) \end{cases} \qquad (4)$$

where $P(z) = U^2(z) \dfrac{dS(z)}{d(k_0 z)}$. The sign of $\varepsilon'(z)$ can take either positive or negative describing relevant electromagnetic features of dielectric or metal (plasma), correspondingly. The sign of $\varepsilon''(z)$ indicates loss or gain in a medium.

The set of differential equations (4) is integrated numerically starting from the non-illuminated side of a multilayer structure, where only one outgoing travelling wave is supposed. Initial values for integration are obtained from the boundary conditions of electrodynamics at the non-illuminated side of the structure. Numerical integration of the set (4) goes step by step towards the illuminated side of the structure taking into account an actual value of structure's permittivity for the given coordinate at each step of integration. In the process of integration any variable of the set (4) is possible to record in order to have full information regarding distributions of electric field amplitude, its derivative and power flow density inside and outside of the structure. At the borders between constituting layers of the multilayer structure ordinary boundary conditions of electrodynamics bring to the continuity of $U(z)$, $Y(z)$ and $P(z)$. From the boundary conditions of electrodynamics at the illuminated side of the structure the amplitude of incident field E_{inc} and the power reflection coefficient R are restored at the end of calculation. The power transmission coefficient T is obtained as the ratio of the transmitted power to the incident one.

4. NUMERICAL ANALYSIS OF A GIRES-TOURNOIS MICRORESONATOR WITH DBR MIRRORS AND LiNbO$_3$ LAYER AS A SPACER

The electromagnetic modelling of the G-T microresonator structure presented in Fig.2 is performed. Corresponding permittivity profile and distribution of optical wave's electric component along the structure are presented in Fig.3.

In Fig. 3, the thickness of the electro-optical layer between DBR mirrors is taken about $5 \ \mu m$ for demonstration only. In the modelled structure, the thickness of the electro-optical crystal is taken as $d = 200 \ \mu m$. The character of internal field distribution in the microresonator at $d = 200 \ \mu m$ looks like in Fig.3, only the increased number of field oscillations within the electro-optical crystal is observed. Highly reflective DBR mirror consists of 13 SiO$_2$/N-LASF9 bilayers and the front mirror consists of 7 bilayers.
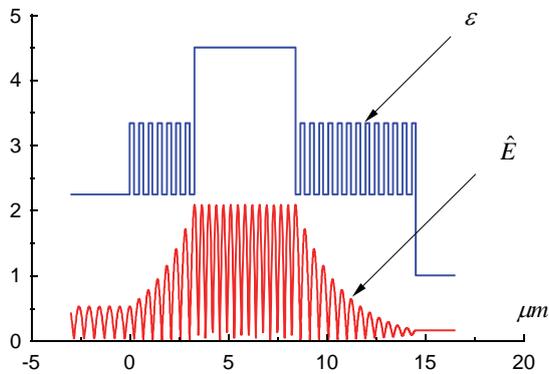
Figure 3. Permittivity profile ε and distribution of the amplitude of optical wave's electric field component $\hat{E}$ along the G-T microresonator at the point of the lowest reflectance ($R = 0.766$). Here the thickness of the electro-optical crystal is $d = 5.115\ \mu m$, the layers of the mirrors are: $L_{SiO_2} = 258\ nm$ of permittivity $\varepsilon = 2.25$ and $L_{N-LASF\ 9} = 212\ nm$ of permittivity $\varepsilon = 3.34$ at $\lambda_0 = 1.55\ \mu m$.

For detection of atmospheric electric field, the sensor's z-axis should be oriented along external field. To model electric field influence on spectral dependences relevant calculation has been done for unperturbed permittivity of the electro-optical crystal ($\varepsilon = 4.5$) and at its change at the value $\varepsilon = 4.505$. This permittivity change is relevant to the change under the highest electric field amplitude. The results of calculations are presented in Fig.4.
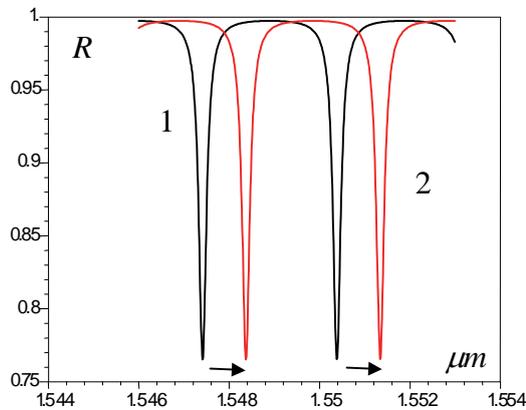

Figure 4. Spectral dependences of reflectance of microresonator (1) at unperturbed ($\varepsilon = 4.5$) and (2) perturbed ($\varepsilon = 4.505$) permittivity of electro-optical crystal. The right shift of spectral dependences stipulated by electrical field directed along crystal's z-axis.

At the change of external field direction, the permittivity of the crystal decreases and spectral peaks are shifted to the left.

The modelling permits to obtain information on the optimal multilayer mirrors suitable for the best observation of spectral peaks' shifts and information regarding influence of crystal thickness on the sensitivity of the sensor from the value of external electric field.

The obtained results will be useful in design and realization of all-optical atmospheric electric field detecting and measuring device. The directional sensitivity of the electro-optical crystal will permit to detect also the direction of atmospheric field that is also important in atmospheric field monitoring.

ACKNOWLEDGEMENTS

REFERENCES

[1] X. Qiea et al. The possible charge structure of thunderstorm and lightning discharges in northeastern verge of Qinghai–Tibetan Plateau. Atmospheric Research, **76** (2005), pp. 231–246.

[2] M. J. Rycroft et al. An Overview of Earth's Global Electric Circuit and Atmospheric Conductivity. Space Sci. Rev., **137** (2008), pp. 83–105.

[3] A.J. Bennett1, R.G. Harrison. Variability in surface atmospheric electric field measurements. Journal of Physics: Conference Series, **142** (2008), 012046.

[4] J. Montanya` et al. A new electrostatic field measurement method: The coherent-notch field mill, Journal of Electrostatics, **65** (2007), pp. 431–437.

[5] P. Tant, Design and Application of a Field Mill as a High-Voltage DC Meter, IEEE Trans. Instrument. Measur. **56** (2007), pp. 1459-1464.

[6] A. Fort, Design, Modeling, and Test of a System for Atmospheric Electric Field Measurement, IEEE Trans. Instrum. Measur. **60** (2011), pp. 2778-2785.

[7] N. A. F. Jaeger, Integrated-Optic Sensors for High-Voltage Substation Applications, SPIE **3489** (1998), pp. 41-52.

[8] Hong-Sik Jung, Electro-optic Electric Field Sensor Utilizing Ti: LiNbO3 Symmetric Mach-Zehnder Interferometers, Journal of the Optical Society of Korea, **16** (2012), pp. 47-52.

[9] R. Zeng et al. Design and Application of an Integrated Electro-optic Sensor for Intensive Electric Field Measurement, IEEE Trans. Dielectr. Electr. Insulat, **18** (2011), pp. 312-319.

[10] Dong-Joon Lee et al. Recent Advances in the Design of Electro-Optic Sensors for Minimally Destructive Microwave Field Probing. Sensors, **11** (2011), pp. 806-824.

[11] V.M.N. Passaro et al. Review: Electromagnetic field photonic sensors. Progress in Quantum Electronics, **30** (2006), pp. 45–73.

[12] R.C.S.B.Allil, M.M. Werneck. Optical High-Voltage Sensor Based on Fiber Bragg Grating and PZT Piezoelectric Ceramics. IEEE Trans. Instrument. Measurem., **60** (2011), pp. 2118-2125.

[13] H. Togo et al. Optical Fiber Electric Field Sensor for Antenna Measurement. NTT Technical Review, 7 (2009), pp.1-6.

[14] M. Miki et al. Electric fields near triggered lightning channels measured with Pockels sensors. Journal Geophys. Resear, **107** (2002), pp. 1-11.

[15] H. Nishihara, M. Haruna, T. Suhara. Optical Integrated Circuits. McGraw-Hill Book Company, 1989.

[16] R. Forber et al. Dielectric EM Field Probes for HPM Test & Evaluation. Annual ITEA Technology Review, August 7-10, Cambridge, MA. Non-Intrusive Instrument. Technol. (2006), pp. 1-6.

[17] F. Pan et al. An Optical AC Voltage Sensor Based on the Transverse Pockels Effect. Sensors, **11** (2011), pp. 6593-6602.

[18] S.M. Chandani, Fiber-Based Probe for Electrooptic Sampling, IEEE PHOTON. TECHNOL. LETTERS, **18** (2006), pp.1290-1292.

[19] Sh. Wakana et al., Fiber-Edge Electrooptic/Magnetooptic Probe for Spectral-Domain Analysis of Electromagnetic Field, IEEE Trans. Microwave Theory and Technol. **48** (2000), pp. 2611-2616.

[20] K. Yang et al., Electric Field Mapping System Using an Optical-Fiber-Based Electrooptic Probe, IEEE Microwave Wireless Component. Lett. **11** (2001), pp. 164-166.

[21] F. Gires, and P. Tournois. Interferometre utilisable pour la compression d'impulsions lumineuses modulees en frequence. C. R. Acad. Sci. Paris, **258** (1964), pp. 6112–6115.

[22] D. A. Cohen et al. High-Q Microphotonic electro-optic modulator, Solids-State Electron., **45** (2001), pp. 1577–1589.

[23] H.V. Baghdasaryan, A.V.Daryan, T.M. Knyazyan, K.U. Nikolaos. Modelling of nonlinear enhanced performance Fabry-Perot interferometer filter, Microwave and Optical Technology Letters, **14** (1997), pp.105-108.

[24] H.V.Baghdasaryan, Method of backward calculation, in the book: Photonic Devices for Telecommunications: how to model and measure/ Editor G.Guekos, Springer-Verlag, (1999), pp.56-65.

[25] H.V. Baghdasaryan, T.M. Knyazyan, Problem of Plane EM Wave Self-action in Multilayer Structure: an Exact Solution, Optical and Quantum Electronics, **31** (1999), pp.1059-1072.

[26] H.V. Baghdasaryan, T.M. Knyazyan, S.S. Berberyan, A.A. Mankulov, Correct Analysis of Gires-Tournois Absorbing Interferometer by the Method of Single Expression, Microwave and Optical Technology Letters, **37** (2003), pp. 64-67.

[27] H.V. Baghdasaryan, T.M. Knyazyan, T.H. Baghdasaryan, B. Witzigmann, and F. Roemer, Absorption loss influence on optical characteristics of multilayer distributed Bragg reflector: wavelength-scale analysis by the method of single expression, Opto−Electronics Review, **18** (2010), pp. 438–445.

[28] H.V. Baghdasaryan, Basics of the Method of Single Expression: New Approach for Solving Boundary Problems in Classical Electrodynamics. Monograph: Chartaraget, Yerevan, (2013), 164 pages.

Research of the thundercloud electrification by facilities of Aragats Space Environmental Center

A. Chilingarian, T. Karapetyan, D. Pokhsraryan

A.Alikhanyan National Lab (Yerevan Physics Institute), 2, Alikhanyan Brothers, Yerevan 0036, Armenia

Abstract. The problem of thundercloud electrification is one of the most difficult ones in the atmospheric physics. Structure of electric fields in the cloud escape from the detailed *in situ* measurements; few balloon flights recognize rather complicated structure much more sophisticated than a simple dipole or triple. To get insight into the problem of charge structure of thundercloud we use new key evidence – the fluxes of particles from thundercloud, the so-called Thunderstorm Ground Enhancements – TGEs. TGEs originate from electron acceleration and multiplication processes in the strong electric fields in the thundercloud and the intensity and energy spectra of electrons and gamma rays as observed at the Earth's surface are directly connected with the charge structure of the cloud.

In the presented paper we demonstrate that experimentally measured patterns of the near-surface electrostatic field during TGEs are consistent with triple structure of the cloud electrification. The maximal particle flux and energy spectra extended above 4 MeV coincide with special pattern of the disturbances of the near surface electrostatic field–the "bumps" arising from deep negative electrostatic field domain. These features we identify with development of mature Lower Positively Charge Region (LPCR), with development of which the electric field in the cloud get enough strength to unleash the Runaway Breakdown (RB) process accelerated electrons downward in the direction of earth.

1. INTRODUCTION

One of the main problems of the atmospheric electricity is the research of the spatial-temporal structure of the electric field in the thunderclouds. Accurately measuring the electric potential within thunderclouds is extremely difficult because of the large time variability and the need to make spatially separated simultaneous measurements within the highest field regions of the storm (Dwyer, 2005). Qie et al., 2005 observed a triple charge structure with a large Lower Positively Charge Region (LPCR) in thunderclouds over the Tibetan Plateau of China, and noticed that the large LPCR prevents negative CG flashes from occurring and, instead, facilitates negative IC flashes. Nag and Rakov, 2009 investigated the dependence of both of lightning types on the magnitude of the LPCR region. They also inferred that when the magnitude of LPCR region is large, inverted IC flashes are expected to occur; when the LPCR starts to decay negative CG flashes became possible. Therefore, LPCR has a great impact on the lightning initiation and type. Thus, how do the size and thickness of LPCR affect lightning discharges? And how to estimate the charge magnitude and distribution range of a LPCR?

To answer these questions, we use a new type of key evidence in the atmospheric electricity research, namely particle fluxes from the thunderclouds, the so-called, Thunderstorm Ground Enhancements (TGEs, Chilingarian et al., 2010, 2011). Origin of the fluxes of electrons, gamma rays and neutrons detected on the earth's surface are the Runaway Breakdown (RB) process (Gurevich et al., 1992) nowadays mostly referred to as Relativistic Runaway Electron Avalanches (RREA, Babich et al., 2001, Dwyer, 2003) and Modification of the energy Spectra of the electrons (MOS, Chilingarian, Mailyan and Vanyan, 2012). Chilingarian and Mkrtchyan, 2012 relate particle fluxes to the origination of the LPCR. The technique of detecting particle fluxes simultaneously with measuring near-surface electrostatic field and lightning occurrences, first developed on Aragats, allows to monitor the creation of the LPCR and its contraction. The maximal intensity of TGE pointed on the maximal

electric field in the cloud and, correspondingly, on the maximal dimension and charge of the LPCR. Fading of the gamma ray flux evidences the degradation of the LPCR.

In (Chilingarian, 2014) we demonstrate that TGEs occur when relative humidity exceeds 95% at near freezing temperatures and that the rain abruptly terminates TGE. Thus, we conclude that LPCR resides on the rain droplets and the polarization of the droplets can play a role in the enhancement of the electric field strength in the cloud. Investigation of the Lightning-TGE relations based on one-second time series of particle fluxes reveals that usually the lightning terminates particle fluxes (Chilingarian et al., 2015). In the time less than one-second particle flux can diminish 2 and more times and return to the background value. Recent observations with microsecond-scale electronics (Chilingarian et al, 2016) proved that the initiation of TGE is connected with the very first stages of the lightning initiation and the space-temporal structure of the TGE can map fast processes of lightning initiation.

2. INSTRUMENTATION

The main goal of the GAMMA detector (also referred to as Aragats Multidirectional Muon Monitor – AMMM, Chilingarian et al., 2003) measuring the Extensive Air Showers (EASes, Fig. 1) is to recover the energy spectra of cosmic rays to understand their origin and particle acceleration mechanisms. About three hundred 5-cm thick $1m^2$ scintillators overviewed by photomultipliers are measuring the number of electrons in the EAS and estimate the size and the "age" of shower and finally the energy and type of the primary particle. EAS detectors are triggered arrays; however, each detector separately counts all incident particles, thus measuring the one-minute time series of the changing fluxes of the secondary cosmic rays. GAMMA detectors consist of 2 parts: the surface array consists of 50 scintillators and the underground muon-detecting array consists of 200 scintillators. The muon array is located in the underground hall of the ANI experiment under 15 meters of soil and concrete and 12 cm of iron bars. Only mu-

ons with energies greater than 5 GeV can reach this underground detector. The 1-minute time series of the 90 scintillators located in the underground hall continuously monitor the 5 GeV muons flux to register violent solar events (see for instance Bostanjyan and Chilingarian, 2007) or nearby supernovae explosions.

Large area of the surface array makes it ideal for measuring additional electron flux correlated with thunderstorms (relative error of the 1-minute count rates is 0.13%, we use only 27 scintillators from the 50 located on the roof of GAMMA calorimeter, see Fig. 1).
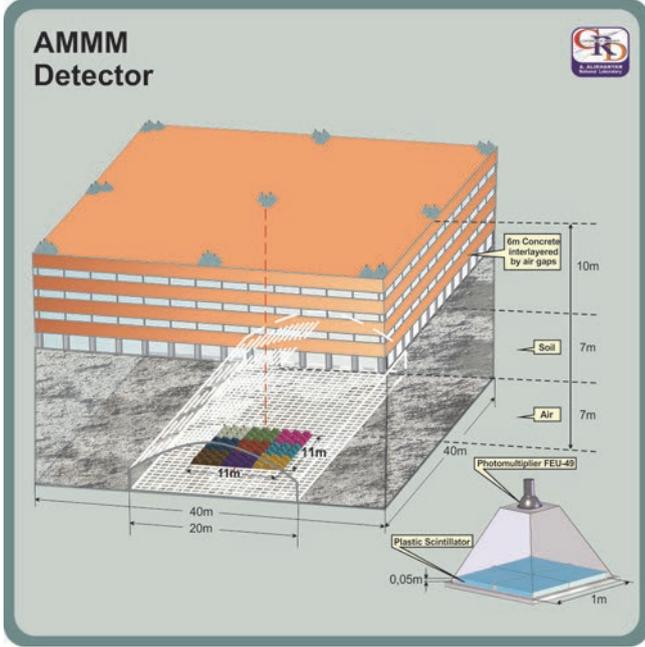

Figure 1. The GAMMA (AMMM) detector.

## 2.1. NETWORK OF STAND1 DETECTORS AND EFM-100 ELECTRIC FIELD MILLS
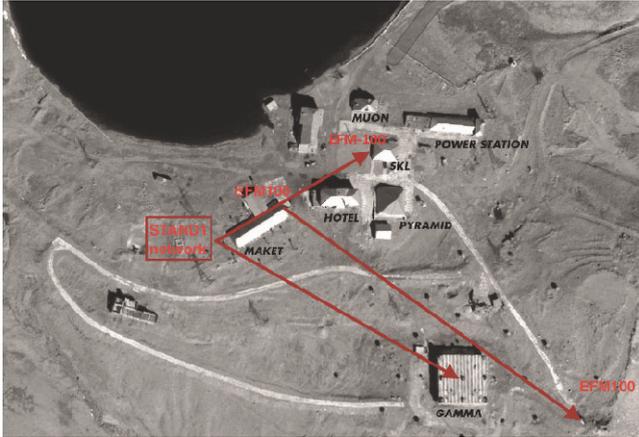
Figure 2. Network of STAND1 detectors and EFM-100 electric field sensors (electric mills); distance from MAKET to SKL ~ 100 m, from MAKET and SKL to GAMMA ~ 300 m

The STAND1 detector consists of 3 vertically stacked one-cm thick 1m² plastic scintillators and a stand-alone 3cm thick plastic scintillator of the same type (see top of Fig. 3). In the bottom of Fig. 3 we show 50msec time series of count rates of upper scintillators of the STAND1 detectors located near the experimental halls MAKET and SKL 100 m apart from each other. Both scintillators enhance the count rate at 14:42 – 14:46 on October 7 2015, registering strong TGE (the minute of the maximal flux has enhanced by ~100 standard deviations). The scatter plot shown in the center of the middle row of Fig. 3 demonstrates strong cor-

relation of count rates measured by remote scintillators proving that radiation region in the cloud illuminates at least an area of ~ 5 x 10⁴ m². The count rates after and before TGE, as expected, do not demonstrate any correlation (left and right scatter plots of the middle row of Fig. 3). Maximums of TGE at ~14:44 is registered by STAND1 scintillators approximately at the same time; thus it was not possible to estimate the structure of the emitting region in the cloud by measuring the time delay and comparing it with the wind velocity and direction. With the new, installed on the roof of GAMMA calorimeter (see Fig. 1), third STAND1 detector located at a larger distance, ~ 300 m, from other detectors it will be possible to investigate the structure of the LPCR above the detectors location site.
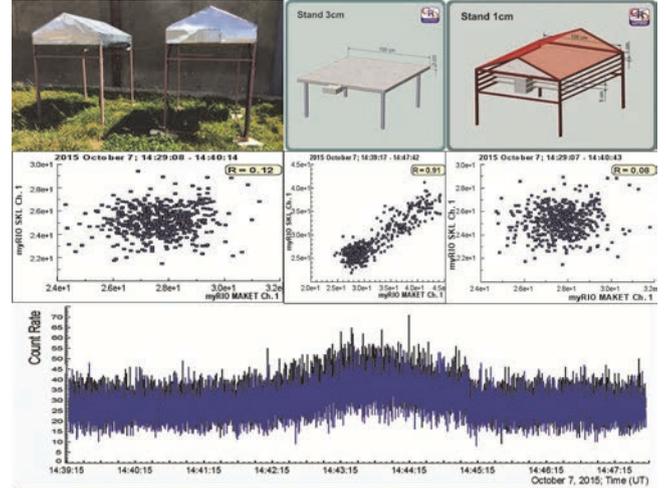

Figure 3. STNAD1 detector located nearby SKL building and its chart (top); scatter plots of count rates of the upper scintillators of 2 remote detectors (distance ~100m, middle); 50 msec time-series of the upper scintillator of the same detectors (bottom).

3. PATTERNS OF THE DISTURBANCES OF ELECTROSTATIC FIELD AND DYNAMICS OF TGEs

In Fig. 3 we depicted the algebraic sum of the electrostatic fields generated by the 3 point charges of the triple structure above according to superposition equation:

$$E_{total} = E_N + E_P + E_{LP} =$$

$$= \frac{1}{2\pi\epsilon_0} \left\{ \frac{Q_N H_N}{(H_N^2 + r^2)^{1.5}} + \frac{Q_P H_P}{(H_P^2 + r^2)^{1.5}} + \frac{Q_{LP} H_{LP}}{(H_{LP}^2 + r^2)^{1.5}} \right\}$$

$$\epsilon_0 = 8.85 * 10^{-12} \frac{F}{m}$$

where Q, E and H are the charge, induced electrostatic field and height of the 3 charged regions in the thundercloud: the main negative charged layer in the middle of the cloud (N, blue); the main positive charged layer on the top of the cloud (P, red) and transient lower positive charge region (LP, green). E_{total} (black) is the superposition (algebraic sum) of all 3 electrostatic fields; ϵ_0 - is vacuum permittivity measured in Farads per meter units; r (distance, horizontal axis) – is the location of the sensor measuring electrostatic field strength.

We assume a plausible value of charges and heights for our simplified model (see caption of Fig. 3). We recognize that the charges in the cloud are distributed horizontally and vertically specific for each thundercloud and these values will significantly differ from the assumed. We made a variety of calculations with different sets of charges and heights. However, what is important, every time when we

introduce LPCR there appeared a "bump" arising from the negative field domain. We will look for the similar structures in the experimentally measured near-surface electrostatic field time series.
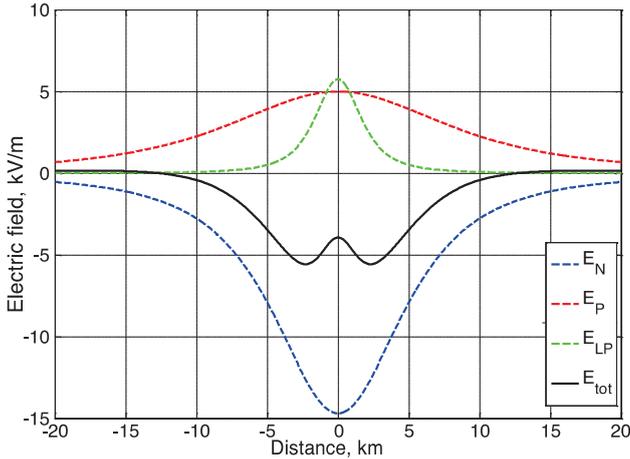

Figure 4. The electrostatic field measured on the ground due to the vertical tripole according to the "atmospheric electricity" sign convention; $Q_P= 40$ C;$Q_N = -40$C; $Q_{LPCR} = 2.5$C; $H_P=12$ km; $H_N=7$km; $H_{LP}=2.5$ km

In Fig. 5 we show a large TGE that occurred on August 28 2015. At 23:15 the near-surface electrostatic field already in negative domain (-12 kV/m) started to decrease; TGE started at the same time from the mean value of 2690 +/- 78 (2-sec time series of 60 cm thick. 1 m^2 area plastic scintillator). At 23:18 the electrostatic field dropped to -24 kV/m and the TGE reached the maximum of ~2890 (+~7%) and sustained near the maximal flux 1.5 minutes, until 23:19:30. With the TGE flux reaching its maximum, the near-surface electrostatic field started to rise, reaching -14 kV/m at 23:19:30. After 23:19:30 TGE slowly faded, recovering the "pre-TGE" value at 23:28. Electrostatic field in the same time abruptly declined, reaching -27 kV/m at 23:20; after reaching minimum, it started to rise again, touching the positive domain at 23:23 and reaching +9 kV/m after 30 seconds. Thus, at TGE maximal flux we see a well-developed bump of 12 kV/m amplitude and 2 minutes duration coinciding in time with TGE maximal flux on rising phase.
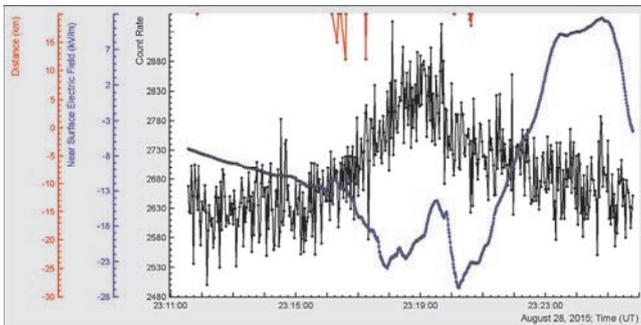

Figure 5. 2-second time series of 60 cm thick and 1 m^2 area plastic scintillator and 1-sec time series of near-surface electrostatic field with a "bump" at particle maximal flux; on the top – distance to lightning.

The emerging structures in the time series of the near-surface electrostatic field are comparable with the structures in the calculated superposition of electrostatic fields induced by 3 charges mimicking a tripole structure of the thundercloud (Fig. 4). Of course, the theoretical curve reveals the spatial distribution of the electrostatic field and the experimental ones – temporal distribution. However, the wind during TGEs is moving the cloud above particle detectors "mapping" the space distribution of the electrostatic field to the temporal one. We speculate that when the ma-

ture LPCR arrives (or emerges) above the detector location the lower dipole accelerates the electron in the direction of earth providing maximal flux of bremsstrahlung gamma rays. Electron flux reaching maximum when LPCR is above detectors and with moving of the cloud from the detector site the TGE subsequently terminates. Thus, the maximal flux of a TGE corresponds to the matureness (maximal thickness - maximal charge) of LPCR. In the time series of the electrostatic field measured at particle detector site, this episode reflected in the sizeable "bumps" rising from the deep negative domain of the near-surface electrostatic field. Note also that during the maximum of particle flux (mature LPCR) usually no lightning occurred (on the special case of TGEs terminated by lightnings see Chilingarian and al., 2016).

In the Fig. 6 we show the time series of count rate of a network of twenty-seven five cm thick 1m^2 plastic scintillators of the AMMM array (Large TGE occurred on 25 August 2015). We can notice the same bump-like structure coinciding with maximal TGE flux.
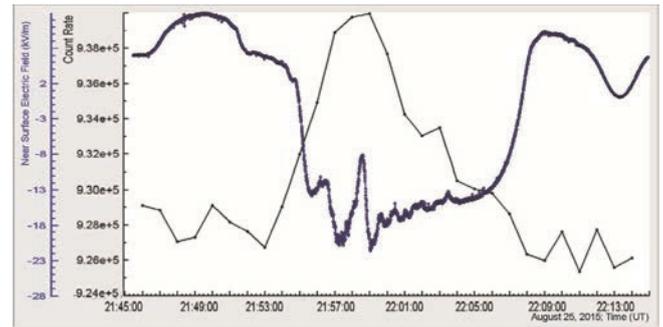

Figure 6. 1-minute time series of 5 cm thick plastic scintillator array and 1-sec time series of near-surface electrostatic field with a "bump" at particle maximal flux.
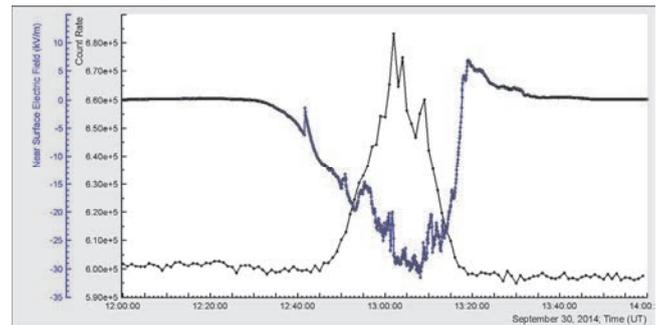
Figure 7. 1-minute time series of 5 cm thick plastic scintillator array and 1-sec time series of near-surface electrostatic field with several "bumps" corresponding to the particle flux bursts.

Another example of the disturbances of near-surface electrostatic field during a TGE we show in Fig. 7. A network of twenty-seven 5 cm thick 1m^2 scintillators measures TGE. Prolonged TGE, lasting 35 minutes demonstrate several peaks (the largest is 13% height above background equivalent to 70σ statistical significance). Carefully examining the Figure, we can outline several small "bumps" corresponding to TGE peaks.

4. CONCLUSIONS

From the observed patterns of electrostatic field disturbances during the TGE occurrences we deduce that rising "bumps" in the time series are an essential characteristic of the thunderstorm, evidencing creation of the LPCR and, as a rule - development of a large TGE. Experimentally measured patterns of the near-surface electrostatic fields during TGEs are consistent with tripole structure of the

calculated electrostatic field in the cloud. The maximal particle flux coincides with the "bumps" rising from negative electrostatic field. This feature we categorize with the development of mature LPCR, which with the main negative charge layer above forms dipole, accelerated electrons downward in the direction of earth. Thus, the scenario of the TGE development (Chilingarian, 2014) finds its proof also in the measured shapes of the electrostatic field disturbances during TGEs observed on Aragats.

However, the large variability in duration, amplitude and shape of TGEs detected by ASEC facilities (see Chilingarian, Karapetyan and Melkumyan, 2013) as well as fluctuating patterns of the near-surface electrostatic field disturbances support different scenarios of the emergence of electric field strong enough to accelerate electrons downwards. Recently was discovered downward RREA occurred between the negative screening layer and the upper positive charge layer just below it (Kelly et al., 2015). Following this discovery we can consider possibility of the particle flux initiation by the electric field originated between main negatively charged region and its "charge image" of the opposite sign on the ground. Extension of the negative layer's image should be much larger than size of the LPCR due to much smaller size of the LPCR.

In 1963 Richard Feynman wrote: "The top of the thunderstorm has a positive charge, and the bottom a negative one— except for a small local region of positive charge in the bottom of the cloud, which has caused everybody a lot of worry. No one seems to know why it is there, how important it is—whether it is a secondary effect of the positive rain coming down, or whether it is an essential part of the machinery. Things would be much simpler if it weren't there". To our present knowledge LPCR is an essential condition for the TGE development and, in turn, TGE is vital for the realizing of the lightning stroke. Thus, without this "local region of positive charge" maybe no lightning will be possible and our planet will be silent and dark.

REFERENCES

- Babich, L.P., et al., 2001. Comparison of relativistic runaway electron avalanche rates obtained from Monte Carlo simulations and kinetic equation solution. IEEE Trans. Plasma Sci. 29 (3), 430–438.

- Bostanjyan N., Chilingarian A., 2007. On the production of highest energy solar protons at 20 January 2005, J. Adv. Space Res. 39, (1456-1459).

- Chilingarian, A. Avakyan K., Babayan, V. et. al, 203. Aragats Space-Environmental Center: Status and SEP Forecasting Possibilities. Journal of Physics G: Nucl.Part.Phys, 29, 939-952.

- Chilingarian, A., Arakelyan, K., Avakyan, K.et al., 2005. Correlated measurements of secondary cosmic ray fluxes by the Aragats space-environmental center monitors, Nucl. Instrum. Methods A 543 (2–3) 483.

- Chilingarian, A., A. Daryan, K. Arakelyan, A. Hovhannisyan, B. Mailyan, L. Melkumyan, G. Hovsepyan, S. Chilingaryan, A. Reymers, and L. Vanyan L.,2010. Ground-based observations of thunderstorm-correlated fluxes of high-energy electrons, gamma rays, and neutrons, Phys. Rev. D, 82, 043009.

- Chilingarian, A., Hovsepyan, G., Hovhannisyan, A., 2011. Particle bursts from thunderclouds: natural particle accelerators above our heads. Phys. Rev. D: Part. Fields 83 (6), 062001.

- Chilingarian, A., Mkrtchyan, H., 2012. Role of the lower positive charge region (LPCR) in initiation of the thunderstorm ground enhancements (TGEs). Phys. Rev. D: Part. Fields 86, 072003.

- Chilingarian A., Karapetan T, Melkumyan L., 2013. Statistical analysis of the Thunderstorm Ground Enhancements (TGEs) detected on Mt. Aragats. J. Adv. Space Res., 52, 1178.

- Chilingarian A., Hovsepyan G., Khanikyanc Y., Reymers A. and Soghomonyan S. 2015. Lightning origination and thunderstorm ground enhancements terminated by the lightning flash, EPL, 110, 49001.

- Chilingarian, A., S. Chilingaryan, and A. Reymers, 2015. Atmospheric discharges and particle fluxes, J. Geophys. Res. Space Physics, 120, 5845–5853.

- Chilingarian A., Mailyan B., and Vanyan L., 2012. Recovering of the energy spectra of electrons and gamma rays coming from the thunderclouds, Atmospheric Research 114–115, 1–16.

- Feynman R., Leighton R.B., Sands M., 1963.The Feynman Lectures on Physics Vol. II Ch. 9- Electricity in the Atmosphere,edited by M.A. Gottlieb and R. Pfeiffer, California Institute of Technology.

- Gurevich, A.V., Milikh, G.M., Roussel-Dupre, R., 1992. Runaway electron mechanism of air breakdown and preconditioning during a thunderstorm. Phys. Lett. A 165 (5-6), 463–468.

- Dwyer, J.R., 2003. A fundamental limit on electric fields in air.Geophys. Res. Lett. 30 (20), 2055.

- Dwyer, J. R. 2005.The initiation of lightning by runaway air breakdown, Geophys. Res. Lett., 32, L20808.

- Kelley N.A., Smith D.M., Dwyer J.R., et al., 2015. Relativistic electron avalanches as a thunderstorm discharge competing with lightning, Nature communications, DOI: 10.1038/ncomms8845

- X. Qie, T. Zhang, C. Chen, G. Zhang, T. Zhang, and X. Kong, 2009. Electrical characteristics of thunderstorms in plateau regions of China, Atmos. Res. 91, 244.

Ultraviolet and infrared emission from lightning discharges observed at Aragats

A. Chilingarian[1], T. Karapetyan[1], D. Pokhsraryan[1], V. Bogomolov[2], G. Garipov[2],

M. Panasyuk[2], S. Svertilov[2], K. Saleev[2]

1. A.Alikhanyan National Lab (Yerevan Physics Institute), 2, Alikhanyan Brothers, Yerevan 0036, Armenia;
2. D.V.Skobeltsyn Institute of Nuclear Physics of M.V. Lomonosov Moscow State University, Leninskie Gory 1, Moscow 119234, Russian Federation

Abstract. The ultraviolet and infrared optical sensors previously used at RELEC space missions were installed at the high-altitude research station Aragats at 3200 m above the sea level. The spectral composition and temporal structure of the recorded optical signals and measurements of the electrostatic field and atmospheric discharges obtained by "fast" and "slow" field sensors have been compared. Measurements of lightning and related to them phenomena observed at the mountain altitude and on board of orbiting satellites are compared.

1. INTRODUCTION

The thundercloud electrical structure and its evolution during thunderstorm have not been yet described and classified. The thunderstorm dynamics, lightning initiation, and electron acceleration in the cloud, multiple atmospheric discharges and their optical counterparts have to be measured simultaneously, and a nontrivial correlation in the measurements can shed light on the underlying physical models.

The discovery of the so-called transient optical phenomena in the upper atmosphere observed between thunderclouds and ionosphere increased the interest to the study of the electric discharges in the electric circuit formed in the cloud - ionosphere-near earth space. To study the properties of the electric discharges and their interaction with particle fluxes, it is necessary to perform measurements within a single storm system at the mountains. A low elevation of the clouds allows to locate sensors just inside the cloud during a thunderstorm.

On the other hand, to observe the global phenomena of thunderstorms we need sensors located on board of satellites having a polar orbit. These two methods of surface and space research complement each other. Studies at the mountains have the advantage to be in close proximity to the thunderclouds where the electric charge is accumulated and distributed and very complicated processes of the self-organizing of discharges are triggered. Such measurements are performed at Aragats Space Environmental Station (ASEC, Chilingarian et. al., 2005) of the Yerevan Physics Institute with the help of a broad variety of particle detectors that measure the neutral and charged particle fluxes, also using field meters, weather stations and lightning detectors. The data collected on numerous nearby thunderstorms accompanied by huge particle flux enhancements (so-called Thunderstorm ground enhancements, which are the subject of the study at Aragats station, Chilingarian et al., 2010 and 2011) can be useful for the analysis of the global data obtained from satellites, which are far above the thunderstorms.

2. DETECTOR FOR UV AND IR EMISSION AND DETECTORS OF ARAGATS COSMIC STATION USED FOR JOINT OPTICAL AND TGE MEASUREMENTS.

The measurements of the transient optical flashes were performed by a detector of ultraviolet and red-infrared emissions (DUVIR), which contains of UV (wavelength 240-380 nm) and IR detectors (wavelength, 610-800 nm) (Garipov et al., 2006). R1463 photomultipliers with a multialkali photocathode and an ultraviolet glass window have been used as photo sensors of ultraviolet and infrared radiation. The bandwidth in the ultraviolet region of the photomultiplier is limited by filter UFS-2; in the infrared region - by filter KS-11 with a thickness of 2.5 millimeters each. Crosstalk between IR and UV sensor signals is less than 0.05 percent. Crosstalk between UV and IR sensor signals is less than 1 percent. Selected were such multialkali photocathodes which could maintain their parameters over a wide range of illumination of the atmosphere, day and night, and also maintain stable sensitivity for a long exposure time. The block diagram of the detector electronics is shown in Fig.1.

The signals from the photomultiplier are amplified by the charge-sensitive preamplifiers with an integration time of ~20 microseconds and fed to the 2-input multiplexer with a switching frequency of 0.5MHz. The output signals from the multiplexer and ADC are transmitted to the programmable logic FPGA unit. This unit selects useful events, implements the scientific program algorithms, performs PMT gain control, and transmits the useful information to an on-line PC. The selected events are recorded in a waveform that is comprised of 256 measurement points each with duration of record time of 128 milliseconds. A waveform of a signal with the largest amplitude is selected every 20 seconds and transmitted to the PC for further processing. Adjustable high voltage power supply provides tuning of the PMT high voltage supply in a way to keep the average current in the middle of the dynamic range of the ADC under all expected levels of the illumination of the atmosphere.

The selected time constant of the automatic adjustment of the high voltage is a few seconds which is considerably larger than the duration of the expected signals, so that the PMT gain remains constant during the signal registration.

58
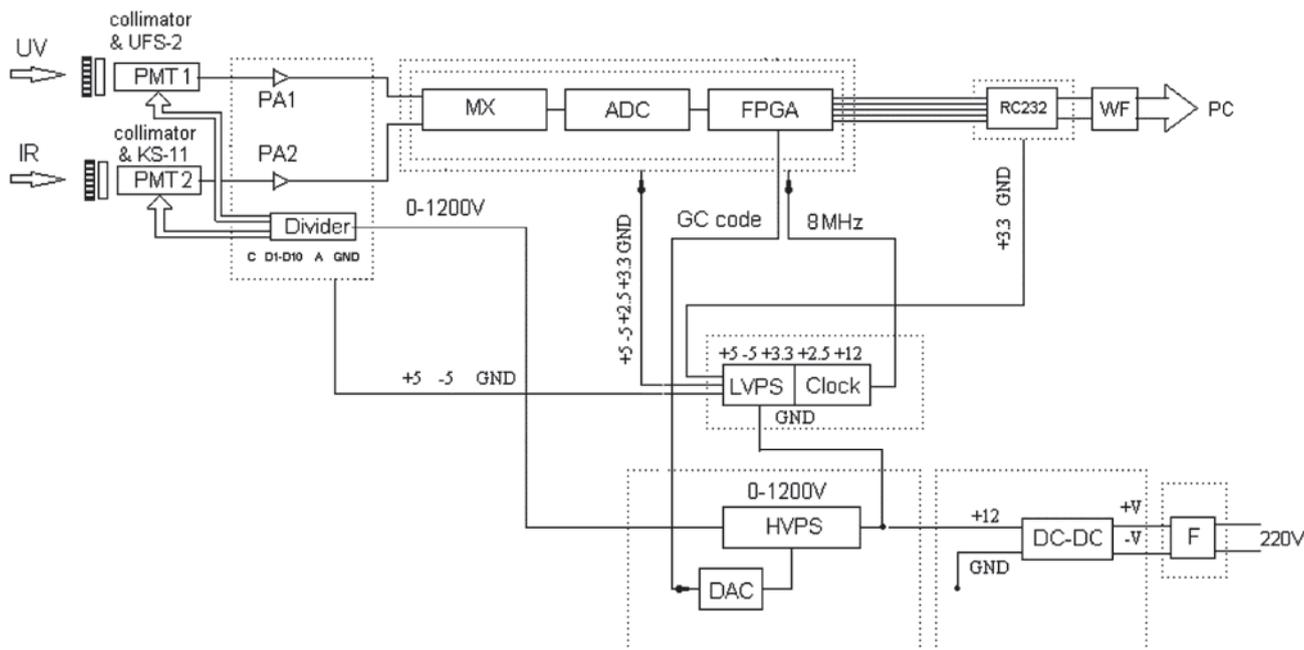
Figure 1. Diagram of the electronics of the DUVIR device.

PMT 1 and PMT 2 are the photomultiplier tubes, PA1 and PA2 - charge sensitive amplifiers, MX - analog multiplexer, ADC- analog to digital converter, FPGA - a logic programmable unit, RS232- communication port, WF- communication line, LVPS- low voltage power supplier, HVPS - controlled high-voltage PMT power supplier, DAC- digital to analog converter for the PMT gain control, DC-DC - common galvanic isolation transformer and circuit of preliminary voltage stabilization, F- noise protection filter

3. DETECTION OF UV AND IR RADIATION AT ARAGATS STATION AND ON BOARD OF VERNOV SATELLITE.

On 15 June 2015 at 18:00 -18:48 a huge storm with numerous lightnings occurred above the Aragats station. The electric field disturbances were prolonged and deep, reaching -28 kV/m; the lightning activity was strong and some of the lightnings were within 5 km from the station. The network of three EFM-100 electric mills monitored the near-surface electric field. The devices operated according to the "atmospheric electricity" sign convention (a positive electric field at ground is produced by positive charge over-head and negative electric field on the ground is produced by negative charge overhead). Thus, the recorded positive field change corresponds to negative lightning, which de-creases the negative charge overhead and negative field change corresponds to positive lightning, which decreases the positive charge overhead. The heavy-duty storm that started at ~18:00 was followed by copious positive light-nings lasting until ~18:45 (Fig. 2). In Fig. 3 (zoomed from Fig. 2) we show the electric field disturbances measured by the electric mills during 10 minutes when the UV and IR radiation was detected by DUVIR device.

The pattern of rapid decrease of the electric field was approximately the same for 3 electric mills located at a maximal distance of ~300 m from each other. The abrupt decrease of the near-surface electric field followed by a relatively slow recovery is an indication for the neutraliza-tion of the positive charge in the thundercloud, i.e. the posi-tive lightning. However, the operation of the in-cloud charging engine permanently recovers the positive charge in the thundercloud. After very-well-pronounced 5 positive lightnings at 18:29 – 18:32, another, a negative lightning

started at 18:34:90 after a prolonged recovery and contin-ued as a positive one with a very long recovery time. At the same time very strong light flash was registered at the sta-tion.
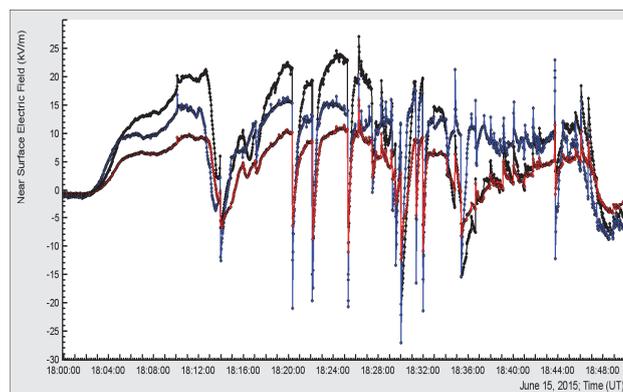
Figure 2. Disturbances of near-surface electrostatic field measured by the network of EFM-100 type electric mills at Mt. Aragats on June 15 2015
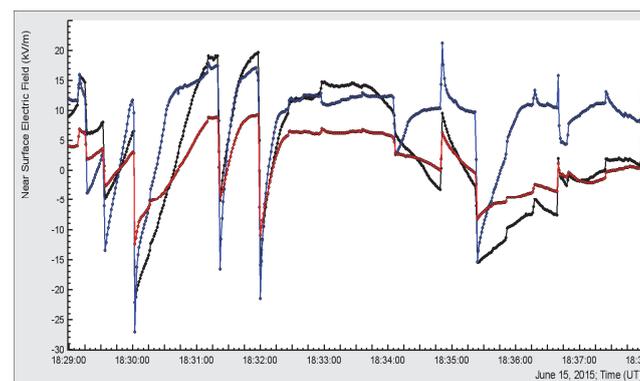

Figure 3. Disturbances of near-surface electrostatic field measured by the network of EFM-100 type electric mills at Mt. Aragats on June 15 2015 (zoomed version of 10 minutes from Fig.2)
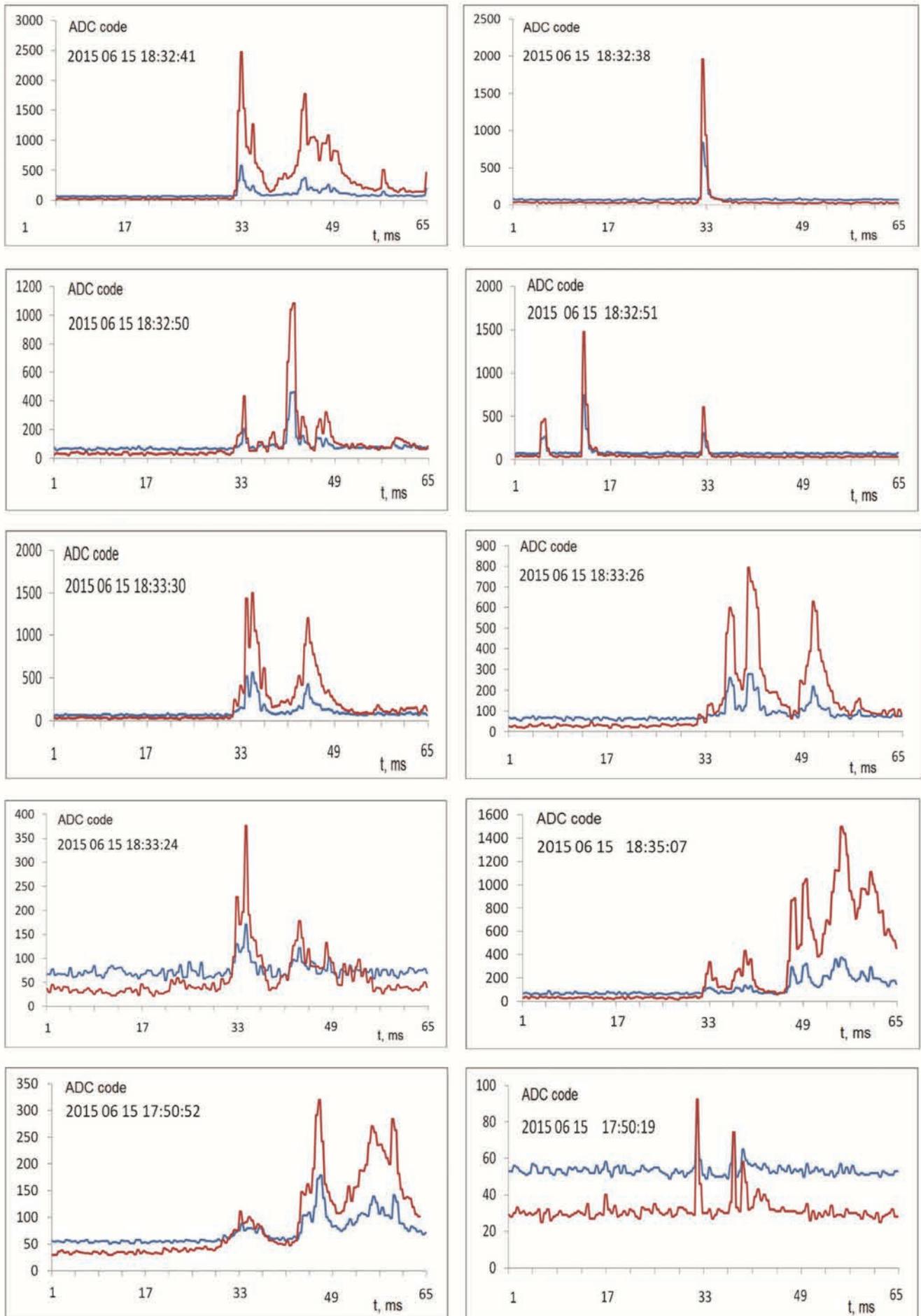
Figure 4. UV and IR radiation from the lightning flashes registered at Aragats station on 15 June 2015

Unfortunately, at that time the on-line computer of DUVIR was not connected to the synchronized NTP computer network of ASEC. That is why we cannot identify each episode of UV/IR radiation with a particular lightning on the millisecond time scale. However, the selected episode of storm shown in Fig. 3 overlaps with the UV/IR radiation peaks.

In Figs. 5 and 6 we show negative and positive lightnings overlapping in time with another episode of intense UV/IR radiation on 4 October 2015 at 16:07 – 17:28.

Figure 6. Positive nearby lightning detected by the network of electric mills and particle count rate (at the bottom)

At the bottom of the pictures we show 50-msec time series of count rates of the 1 m² plastic scintillator located outdoors at an altitude of 3200 m.

The selected lightnings shown in Figs. 5 and 6 coincide within 1sec with the UV/IR radiation spikes (Fig. 7). In Fig 8. we show zoomed pictures of the fast wave forms registered from atmospheric discharges (see details in Chilingarian et all., 2016) coinciding with one of the episodes of UV/IR radiation.

Figure 5. Negative lightning detected by the network of electric mills and particle count rate (at the bottom)
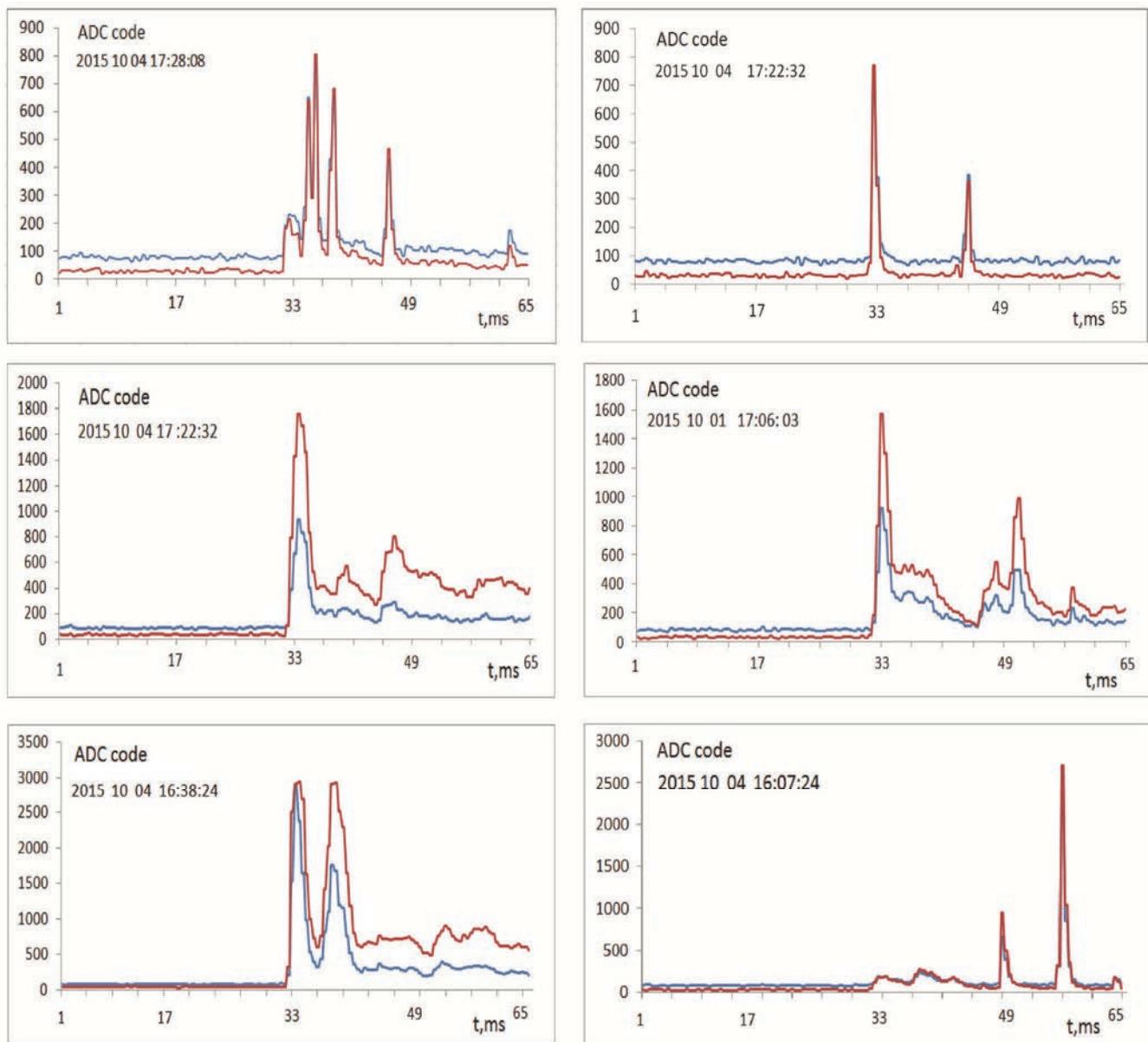
Figure 7. UV and IR radiation from the lightning flashes registered at Aragats station on 4 October 2015

61
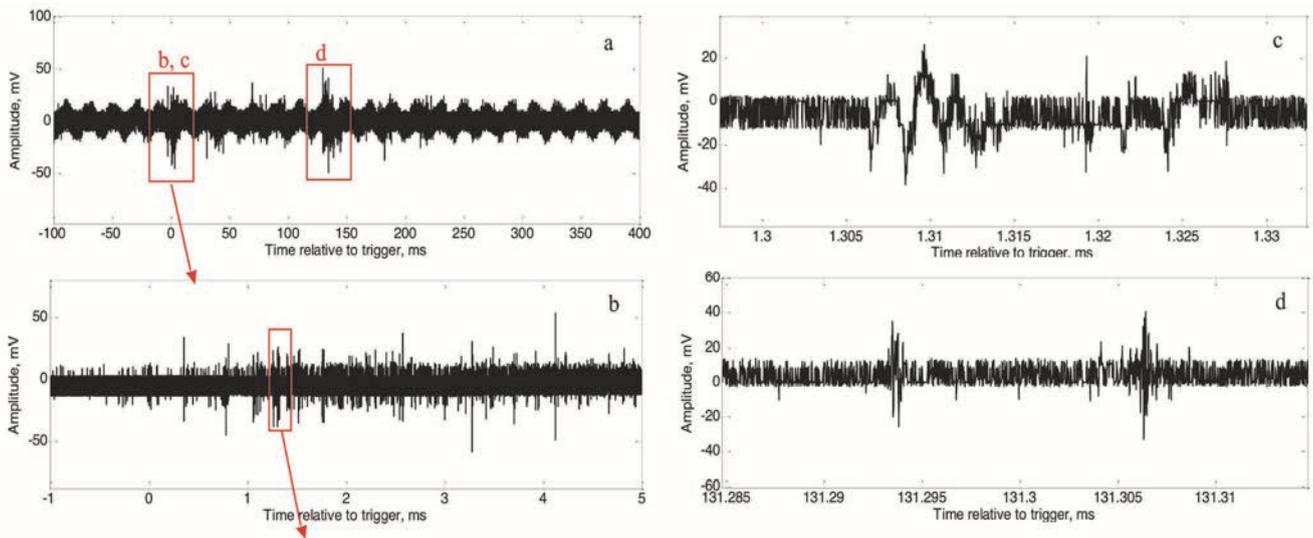
Figure 8. Fast waveforms registered on October 4 2015 at 17:51:01

In Fig. 9 we show UV/IR transient flashes in the Earth's atmosphere registered by the DUVIR device on board of Vernov satellite (Garipov et all., 2015).
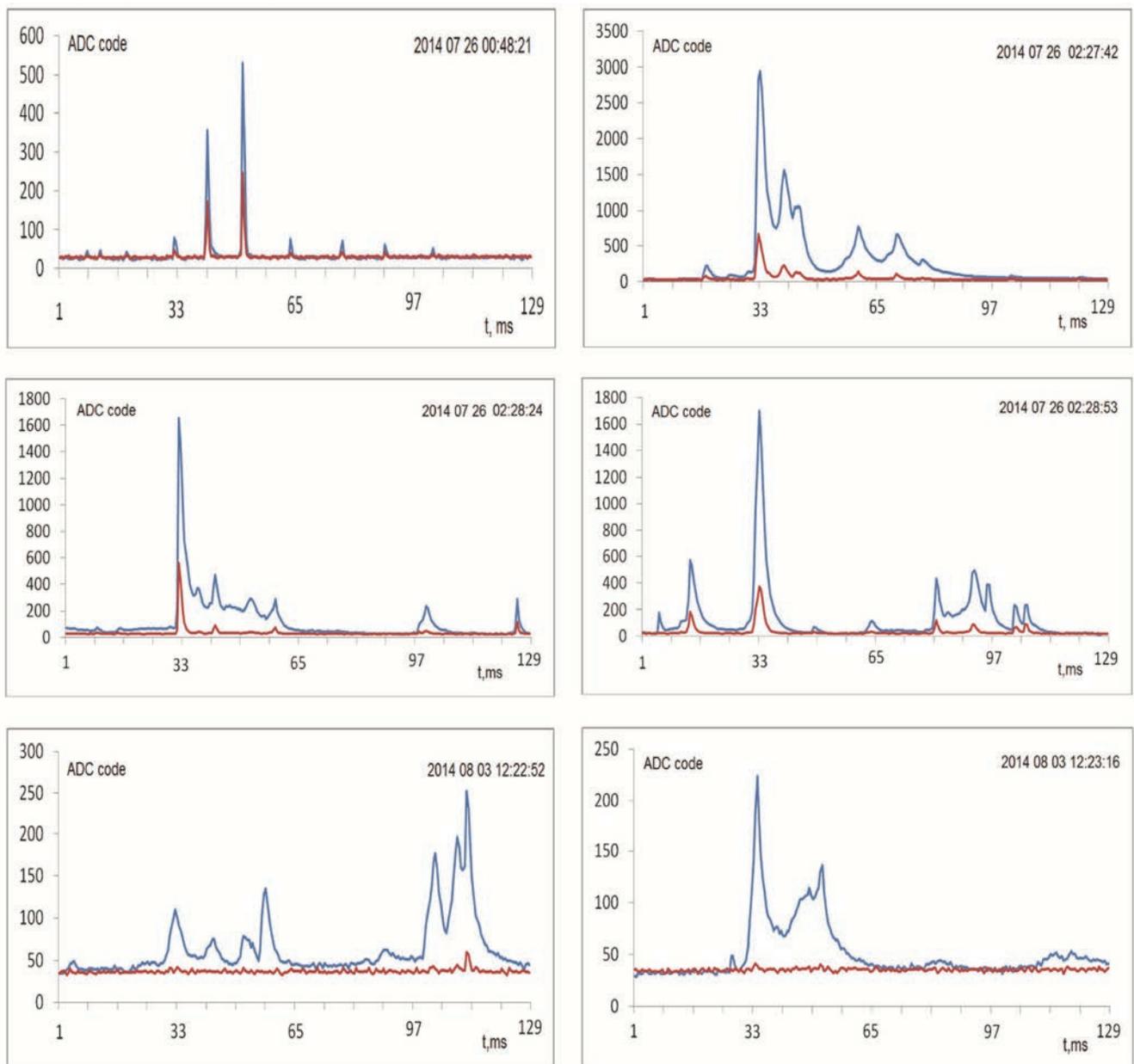
Figure 9. Examples of the waveforms of lightning flashes recorded on board of the "Vernov" satellitte.

62

4. DISCUSSION AND CONCLUSION

We have presented the preliminary results of the operation of a device designed to register the UV/IR radiation from the lightnings that occur above the Aragats research station in Armenia. The temporal structure of the lightnings as measured by the DUVIR device consists of random pulses of ultraviolet and infrared radiation between which there is no delay. In most of the coincident in time pulses, the infrared signal by the amplitude exceeds the ultraviolet radiation; in some of the pulses their amplitudes are equal. The variations of the amplitudes of the coincident pulses of infrared and ultraviolet radiation are caused by scattering and absorption on the way to the detector and by reflection and scattering of the lightning light in the stormy atmosphere.

It is evident that the temporal structure of the lightning observed at Aragats station and that observed from the orbit are very similar. In the flashes recorded on Aragats, there is somewhat less ultraviolet radiation as compared with the infrared radiation, which is explained by the non-ideal transparency of the lower atmosphere. In some flashes observed from space, the ultraviolet radiation sometimes appears in the absence of infrared radiation; it points to the difference in the discharge properties of the transient luminous events and conventional lightnings. This phenomenon has not been observed on high mountains, possibly due to insufficient statistics of the recorded events.

In the 2016 observations we plan to attach DUVIR to myRio board produced by National Instruments Company (see Figs. 10 and details in Pokhsraryan, 2016). With the help of this board we plan to register UV/IR emissions, fast waveforms from atmospheric discharges and particle fluxes on the nanosecond time's scale.
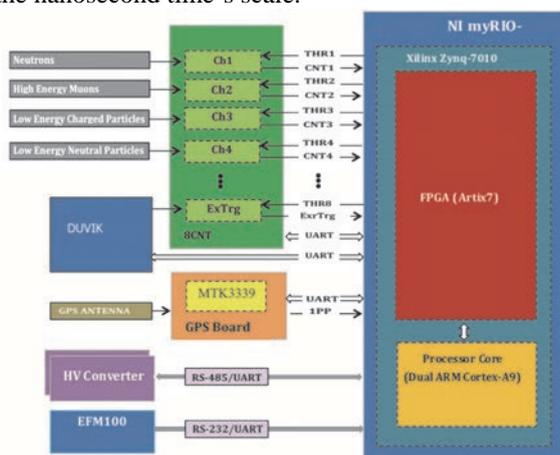

Figure 10. National Instruments myRio board for the synchronized detection of particle fluxes, UV and IR radiation and disturbances of the near-surface electrostatic field.

The myRio board keeps the GPS absolute time with an accuracy not worse than a few tens of nanoseconds. This accuracy can be improved down to a few nanoseconds by using calibration signals from the aircrafts or drones (Aab et al., 2016). Thus, files with microsecond scale waveforms of UV/IR radiation (DUVIR trigger) and files with nanosecond resolution from 5HGz frequency oscilloscope (fast waveform trigger) will be synchronized at least on the microsecond time's scale. As well we plan to synchronize fluxes of electrons, gamma rays and neutrons from TGEs. Moreover, arrival time of each particle in a time span of 100 msec before trigger and 400 msec after trigger will be enumerated also with a nanosecond accuracy. It will give us the possibility to check the hypothesis if the lightnings themselves are the source of high-energy particles. We are planning to use another myRio board that will be triggered by the Extensive air Showers (EAS), so that we can finally check the hypothesis on the relation between EASes and lightnings (RB-EAS hypothesis of Alex Gurevich et al., 1999).

REFERENCES

- Aab A., et al., 2016. Nanosecond-level time synchronization of autonomous radio detector stations for extensive air showers, Pierre Auger Array Collaboration: submitted to Journal of Instrumentation, arxiv.org/abs/1512.02216.

- Chilingarian, A., Arakelyan, K., Avakyan, K., et al., 2005. Correlated measurements of secondary cosmic ray fluxes by the Aragats Space-Environmental Center monitors. Nucl. Instrum. Methods Phys. Res., Sect. A 543 (2–3), 483–496.

- Chilingarian, A., A. Daryan, K. Arakelyan, A. Hovhannisyan, B. Mailyan, L. Melkumyan, G. Hovsepyan, S. Chilingaryan, A. Reymers, and L. Vanyan L., 2010. Ground-based observations of thunderstorm-correlated fluxes of high-energy electrons, gamma rays, and neutrons, Phys. Rev. D, 82, 043009.

- Chilingarian, A., Hovsepyan, G., Hovhannisyan, A., 2011. particle bursts from thunderclouds: natural particle accelerators above our heads. Phys. Rev. D: Part. Fields 83 (6), 062001.

- Garipov, G. K., Panasyuk, M. I., Rubinshtein, I. A. et all. 2006. Ultraviolet radiation detector of the MSU research educational microsatellite Universitetskii-Tatiyana Instruments and Experimental Techniques, 49, 126-130.

- Garipov, G. K., Panasyuk, M. I., Svertilov S., 2015. Vernov satellite mission: first results, study flashes of light in the ultraviolet and infrared optical range of the light spectrum, http://meetingorganizer. copernicus.org/ EGU2015/EGU2015-4584.pdf

- Gurevich A.V., Zybin K.P, Roussel – Dupre R.A., 1999. Lightning initiation by simultaneous of runaway breakdown and cosmic ray showers, Phys.Lett. A 254, 79.

- Pokhsraryan D, 2016. Very fast Data Acquisition system based on NI-myRIO with GPS time stamping capabilities, Proceedings of TEPA 2015, Nor Amberd, Tigran Mets.

- Soghomonyan S., Chilingarian A., Khanikyants Y, Kozliner L, 2016. Fast electric field waveforms of lightning discharges detected at the Aragats Mountain in Armenia, Proceedings of TEPA 2015, Nor Amberd, Tigran Mets.

Fast electric field waveforms and near-surface electric field images of lightning discharges detected on Mt. Aragats in Armenia

A. Chilingarian, Y. Khanikyants, L. Kozliner, S. Soghomonyan

A.Alikhanyan National Lab (Yerevan Physics Institute), 2, Alikhanyan Brothers, Yerevan 0036, Armenia

Abstract. We present the observational data on fast electric waveforms that are detected at 3200 m altitudes above sea level on Mt. Aragats in Armenia during thunderstorms. We analyse the relations of these forms with count rates of particle flux (during Thunderstorm Ground Enhancements -TGEs); to the slow disturbance of the near-surface electrostatic field; and to the lightning location data from the World Wide Lightning Location Network (WWLLN). An observed negative lightning that decreases a negative charge overhead often abruptly terminates TGEs. By analysing the recorded fast electric field waveforms and comparing them with similar classified waveforms reported previously, we could identify the type and polarity of the observed lightnings.

1. INTRODUCTION

The *in situ* observation of the numerous Thunderstorm Ground Enhancements (TGEs, Chilingarian et al., 2010, 2011, Chilingarian 2014), i.e. enhanced fluxes of electrons, gamma rays and neutrons detected by particle detectors located on the Earth's surface and related to the strong thunderstorms above, helped to establish a new scientific topic - high-energy physics in the atmosphere.

During the last 5 years, we experiment with the "beams" of the "electron accelerators" operating in the thunderclouds above the Aragats research station. Thunderstorms are very frequent above Aragats, peaking at May-June and almost all of them are accompanied with enhanced particle fluxes. The station is located on a plateau 3200 m above sea level, by a large lake. Numerous particle detectors and field meters are located in 3 experimental halls and outdoors; the facilities are operated all year round.

The runaway Breakdown (RB) process (Gurevich et al., 1992) which is nowadays mostly referred to as Relativistic Runaway Electron Avalanches (RREA, Babich et al., 2001, Dwyer, 2003) and Modification of the energy Spectra of the electrons (MOS, Chilingarian, Mailyan and Vanyan, 2012) are believed to be a central mechanism of the high-energy processes in the thunderstorm atmospheres. Numerous TGEs observed on Aragats Mt. in Armenia during strong thunderstorms and first simultaneous measurements of TGE electrons and gamma ray energy spectra proved that RREA is a robust and realistic mechanism for electron acceleration. The electrons giving rise to the RREA are accelerated by the electric field formed by the main negatively charged regions in the middle of the cloud and by the transient, lower, positively charged region (LPCR, Chilingarian and Mkrtchyan, 2012) at the bottom. LPCR charge is much less as compared with the thundercloud main charged regions; however, the local influence of LPCR can be essential, for instance LPCR prevents the lightning leader from reaching the ground and usually no −CG lightning occurs when the LPCR is mature (Nag and Rakov, 2009). Only after decaying of the LPCR, the stopped leader makes its path to the ground. Continuous attempts to start the stopped leader produce a large number of low-energy (few eV) electrons by ionizing the air. The low-energy electrons then drift in the thunderstorm electric field, producing discharges and radiofrequency emissions. Bipolar radiofrequency pulses, having possibly originated from these discharges, appear in the early stage of the formation of the conducting channel in the thundercloud (initial breakdown).

The paper is organized as follows. In the second section, we describe the facilities used for the particle-lightning research. In the third section, we review the TGE events abruptly terminated by lightning. In the fourth section, we analyse the fast waveforms of lightnings with an extended data capture length of the digital oscilloscope and in the fifth section, we relate the images of the slow near-surface electrostatic field to the fast electric waveforms. In conclusion, we discuss the preliminary results of our research.

2. INSTRUMENTATION

The data presented in this study were acquired in the fall 2014 and Spring-Summer 2015, at the Aragats Space Environmental Center (ASEC) on Mt. Aragats, Armenia (Chilingarian et al., 2005). Geographical coordinates of the research station are 40°28′N, 44°11′E, and the altitude is 3200 m above sea level. A 52 cm diameter circular flat-plate antenna followed by a passive integrator is used to record the fast electric field waveforms. The decay time constant RC of the integrator is 10 msec. The output of the integrator is directly coupled to a digital oscilloscope. The data presented here are recorded by two types of oscilloscopes: 1) Picoscope 3206 with a 100MS/s sampling rate and data capture length of 5 msec, including 1 msec of pre-trigger time, and 2) Picoscope 5244B with a 25MS/s sampling rate and a data capture length of 500 msec, including 100 msec of pre-trigger time. The amplitude resolution is 8 bit in both cases. The recording system is triggered by a signal from the high-frequency detecting system, which uses a commercial MFJ-1022 active whip antenna that covers a frequency range of 300 KHz to 200MHz. The disturbances of the near-surface electrostatic field are measured with the Boltek EFM-100 electric field mill. The measurements are taken 20 times per second, and the sensitivity range extends up to ~30 km. We use also the data of the World Wide Lightning Location Network (WWLLN) to locate the geographical coordinates and to get the estimated stroke energy for the lightnings simultaneously detected by the Network and by our recording system. The estimated stroke energy is the root-mean-square energy of the stroke from 1.3 msec waveform sampling between 7 to 18 kHz

(Hutchins et al., 2012). TGEs analyzed in the present study are detected by an outdoor 3 cm thick scintillator with a sensitive area of $1m^2$ operated in the particle counter mode. The detection efficiency is ~98% for electrons and ~5% for gamma rays, the energy threshold is ~2MeV.

3. TGEs TERMINATED BY LIGHTNING

We will consider six selected TGE events that have been terminated by lightning. The observation data involve 1 sec time series of the count rate of particle flux, 50 msec time series of slow disturbance of near-surface electrostatic field, fast wideband electric field waveforms, and lightning location and stroke energy data from WWLLN.

Three of the selected events, which were observed on the same day, May 11 2015, are shown in Figure 1, where the count rate of particle flux and the disturbances of the near-surface electrostatic field are presented.
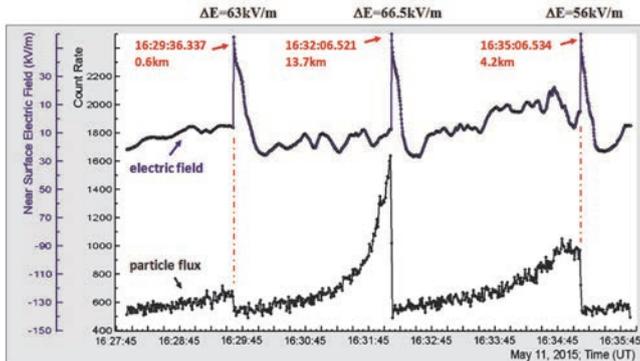

Figure 1. A sequence of three TGEs abruptly terminated by negative lightnings. The lower curve is the 1 sec time series of the count rate of the particle flux detected by the 3 cm thick outdoor scintillator; the upper curve is the 50 msec time series of the electrostatic field disturbances detected by the electric field mill. Lightning detection time and distance to the lightning is according to WWLLN data, and the electric field changes, ΔE, are indicated for each lightning.

As can be seen from Figure 1, all three TGEs are abruptly terminated by lightnings, which are characterized by a strong disturbance of the near-surface electrostatic field measured by the electric field mill. At 16:29:36, the electric field starts its sharp increase, in 100 msec changing from −5.7 kV/m to 57.3 kV/m, and the particle flux count rate is terminated at its rising edge. At 16:32:06, the electric field changes from −6.5kV/m to 60 kV/m, and the termination is observed at the maximum of the count rate. At 16:35:06, the electric field changes from 5.5kV/m to 61.5kV/m, and the termination is observed at the falling edge of the count rate. All three lightnings that terminated the TGEs shown in Figure 1, were detected by WWLLN.

The lightning detection time stamps and distance to lightning are indicated in Figure 1 as well. The distances to the lightning, according to the WWLLN data for the three selected events, are equal to ≈0.6km, ≈13.7km, and 4.2 km. However, the uncertainty in lightning location is rather high, ~5 km.

For all observed TGEs terminated by a lightning the electric field change measured at the ground is positive and it can be attributed to the decrease of negative charge overhead.

The "atmospheric electricity" sign convention (a downward-directed electric field or field change vector is considered positive) is used throughout this paper. Thus, a positive electric field change measured at the ground is produced by a negative lightning, which decreases the negative charge overhead.
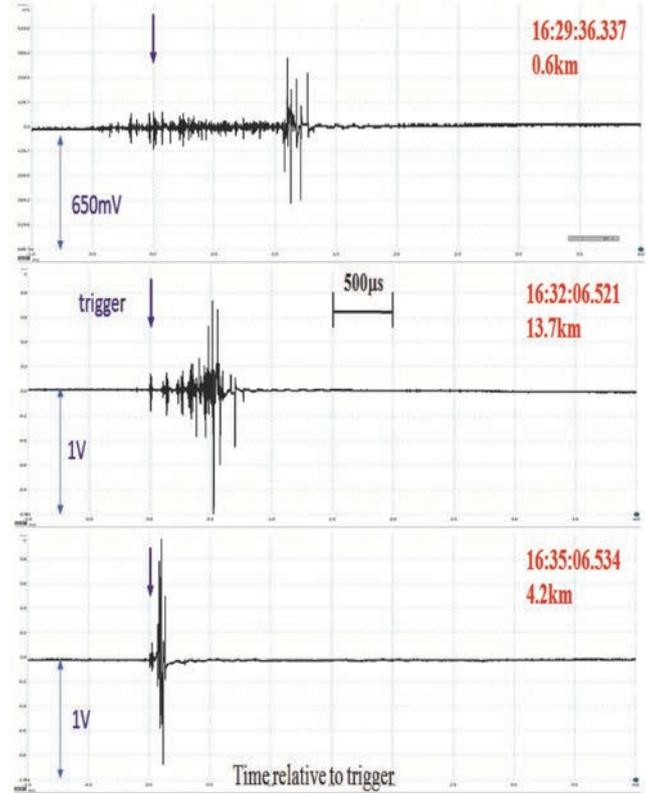
Figure 2. Fast electric field waveforms of three lightnings that terminated the TGEs corresponding to those shown in Figure 1. Data capture length is 5ms, including 1 msec pre-trigger time, sampling frequency is 100Ms/s.
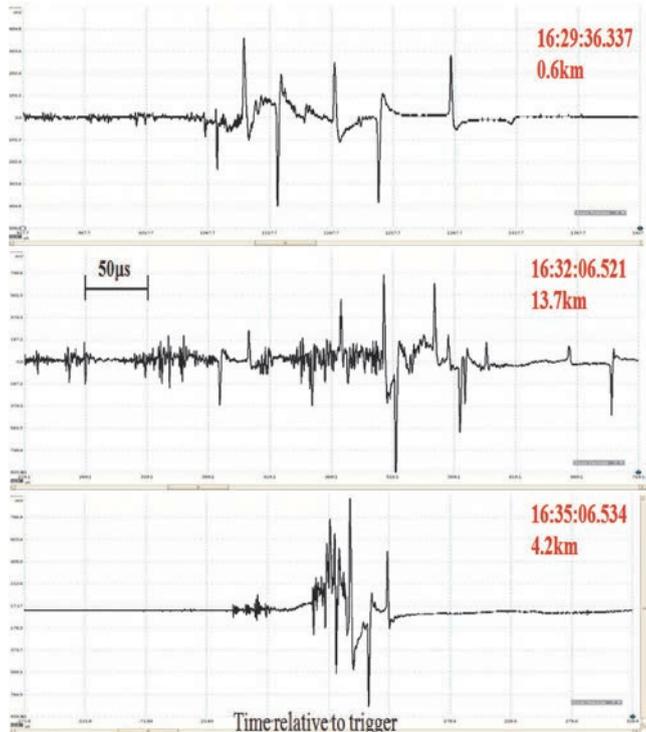
Figure 3. Fast electric field waveforms of Figure 2 are shown here with 10-fold time magnification. All three waveforms show multiple bipolar pulses with typical duration of 1-2 microseconds.

Fast electric field change waveforms for the three selected events are presented in Figures 2 and 3 with different time magnification. All three waveforms show trains of multiple short bipolar pulses of different polarity with typical duration of 1-2 microseconds, and with overall train

duration in the range from 150 microseconds to 1 msec. It should be noted, however, that due to short data capture length of 5 msec used in these measurements, the recorded waveforms may show only the preliminary stage of a lightning flash. Therefore, identification of the type of lightning discharge (cloud-to-ground, or intracloud) from the recorded fast electric field is problematic for these measurements.

In Figure 4, we present termination shapes for five selected events. An abrupt termination of the count rate was detected at the rising (c) and falling (b and e) edges of particle flux enhancement, as well as at the maximum of the burst (a and d).

We assume that, most probably, the cloud-to-ground lightning terminates these TGEs. An indirect argument supporting this assumption is that all three lightnings are detected by the WWLLN, which detects only the strongest lightnings with peak currents above 35-40kA with detection efficiency of ~10 %, and vast majority of lightnings detected by the network are cloud-to-ground lightnings. This is primarily because a CG lightning is a much stronger radiator in the frequency range from 3 to 30 kHz used by WWLLN for lightning detection. Nevertheless, we cannot ignore the possibility that a strong intracloud lightning, which can also be recorded by WWLLN, terminates TGE. Another method for the determination of the lightning type is discussed in (Chilingarian et. al., 2016).

The main characteristics of the electrostatic field changes for the six observed TGEs terminated by lightning are summarized in Table 1. Distance to the lightning given in the third column is calculated using latitude and longitude of the lightning determined by the WWLLN data and the coordinates of the Aragats station. The distance is calculated as the great-circle distance between the two points according to the well-known "haversine" formula on the basis of a spherical earth, ignoring the ellipsoidal effects. The estimated stroke energy and its uncertainty according to WWLLN data is given in the last column. All observed lightnings are characterized by very large positive change of the electric field strength. The "amplitude" of lightning as measured by the abrupt disturbances of the near-surface elec-

trostatic field $\Delta E = (E_{Maximum} - E_{start})$ ranges from 42.6 to 84kV/m.

However, the electric field strength at the start of its abrupt change is quite different for the six selected events, ranging from -25.5kV/m to +5.5kV/m. All six discussed lightnings occurred near the Aragats research station: the distance to the lightning according to the WWLLN data is in the range 0.6-13.7km.
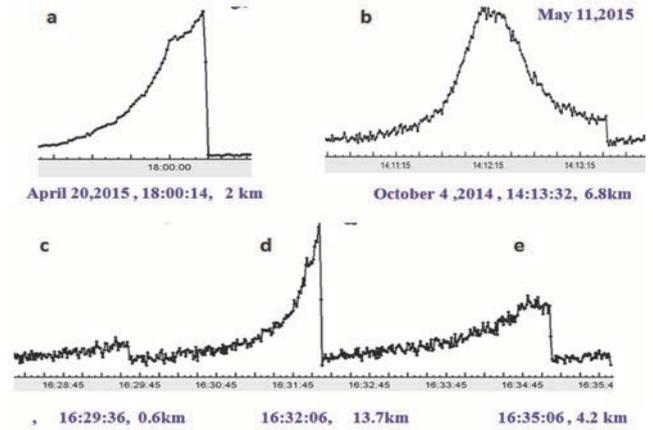
Figure 4. Various shapes of TGE termination observed for five selected events: at the maximum of particle flux (a, d); at the falling edge (b, e), at the rising edge(c).

We examined the time coincidences of the abrupt changes of the electrostatic field measured by EFM-100 field mills installed at the Aragats station and the time stamps of lightning detection by the WWLLN. The statistics for 137 event is presented in Figure 5, where the histogram shows the number of events as a function of time difference between WWLLN time stamps and corresponding maxima of electrostatic field disturbances.

As can be seen from Figure 5, the standard deviation of the distribution is ~350 msec. The shift of the center of the distribution towards negative values of the time difference by about 250 msec is due to the fact that the maximum of the electrostatic field change caused by lightning and measured by the field mill is achieved later than the time stamp WWLLN which detects the maximum of the electromagnetic emission pulse from the lightning.

Table 1. Parameters of electrostatic field change, distance to lightning, and estimated stroke energy observed for TGEs terminated by lightning.

ate	Time (UT)	Distance km	Start electric field E_{start}, kV/m	Max electric field E_{max}, kV/m	$\Delta E = E_{max} - E_{start}$ kV/m	FWHM of field change	Stroke Energy (J)
20-Apr-15	18:00:14	2	1.2	49.2	48	1.1sec	23513±14259
20-Apr-15	18:02:01	8	-3.41	39.2	42.6	1.2s	N/A
4-Oct-14	14:13:32	6.8	-25.5	58.5	84	5sec	N/A
11-May-15	16:29:36	0.6	-5.7	57.3	63	8sec	56516±40695
11-May-15	16:32:06	13.7	-6.5	60	66.5	6sec	N/A
11-May-15	16:35:06	4.2	5.5	61.5	56	5sec	5295±1660
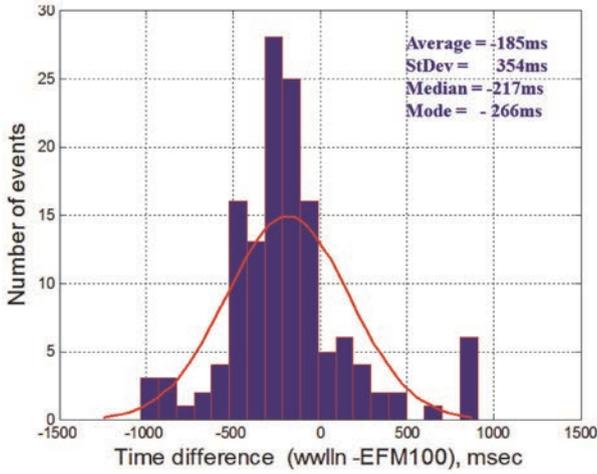
Figure 5. Histogram of time coincidences between WWLLN detection time stamps and the time stamps of electric field maximum measured by field mill EFM-100.

## 4. CLASSIFICATION OF LIGHTNINGS BY TYPE AND POLARITY

After installing a digital oscilloscope with an extended data capture length of 500 msec, we investigate the relations of the fast electric field waveforms and the disturbances of the near-surface electrostatic field. The waveforms of the selected lightnings recorded with a capture length of 500 msec have some typical features, which allow us to identify the type and polarity of a lightning flash.

Fast electric field waveforms for three selected lightnings are shown in Figures 6, 7 and 8. In all three waveforms, multiple weak microsecond-scale bipolar pulses are followed by a strong bipolar pulse, the amplitude of which is by an order of magnitude higher than that of the weak pulses. Typical amplitude is 10-20mV for weak pulses, and 200-300mV for the strong ones. Time interval between the beginning of weak pulses and start of the strong pulse is 160 msec, 74 msec, and 28 msec for the lightnings shown in Figures 6, 7, and 8, respectively. In order to identify the type and polarity of lightnings, we compare the waveforms shown in Figures 6-8 with the waveform of the negative cloud-to-ground (CG) lightning recorded at Lightning Observatory in Gainesville Florida, USA (Zhu et al 2014), shown in Figure 9. Multiple weak bipolar pulses around 4-5 msec are identified by as preliminary breakdown (PB) pulses, and the strong bipolar pulse at 21.5 msec with positive polarity of initial half cycle is identified as negative return stroke (RS). The typical duration of PB process is a few milliseconds; the time interval between PB pulses and strong bipolar pulse considered as stepped-leader duration (Zhu et al., 2014). We believe that fast electric field waveforms of lightning flashes detected on Aragats and shown in Figures 6-8 can be interpreted in a similar way.

Thus, weak bipolar pulses followed by a strong bipolar pulse in the waveforms of Figures 6-8 we identify as preliminary breakdown (PB) pulses (and stepped leader pulses in Figures 7 and 8) followed by the return stroke pulse. In waveforms of Figures 6 and 7, the PB pulses are followed by a positive return stroke at 162 msec and 74 msec after trigger, respectively. In both cases the return stroke is positive, because the polarity of the initial half cycle of the strong bipolar pulse is negative. In the waveform of Figure 8, the PB pulses are followed by a negative return stroke at 28.7 msec after trigger.
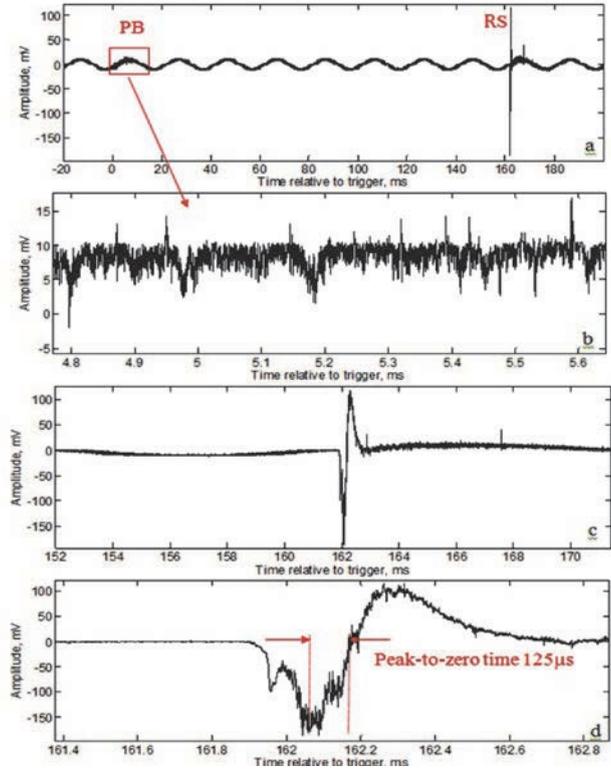
Figure 6. Fast electric field waveform detected at 15:51:21.446, August 6 2015. WWLLN data: distance to lightning 3.7 km, stroke energy (4586 ±1160) J.
Preliminary breakdown (PB) pulses are followed by the return stroke (RS) pulse. Frame b) shows expansion of PB pulses, frames c) and d) show expansion of RS. *Classification: positive cloud-to-ground lightning (+CG).*
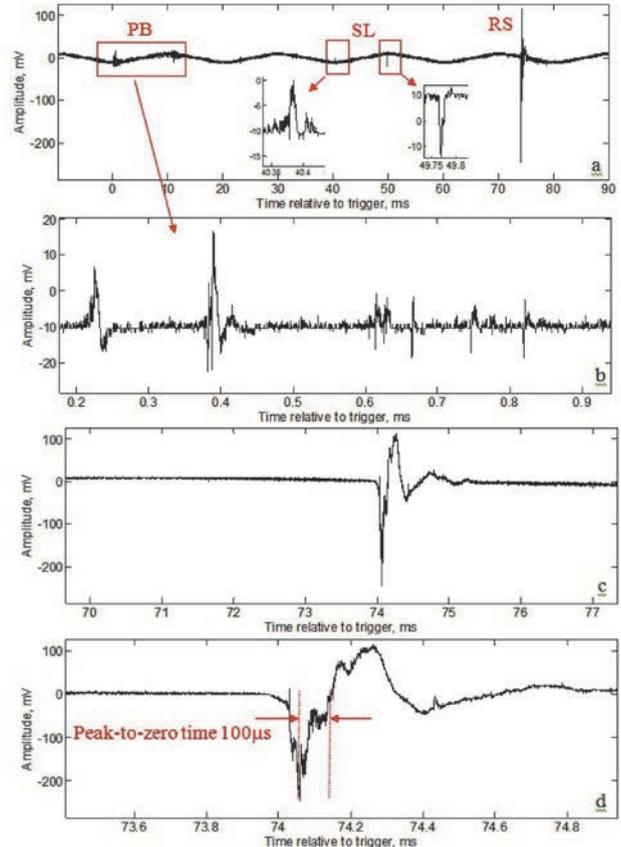

Figure 7. Fast electric field waveform detected at 02:58:49.244, August 2, 2015, WWLLN data: distance to lightning 5.9 km, stroke energy (3071 ±802) J. The pulses between the PB and RS shown in the insets of frame a) are presumably the stepped leader (SL) pulses. Classification: positive cloud-to-ground lightning (+CG).
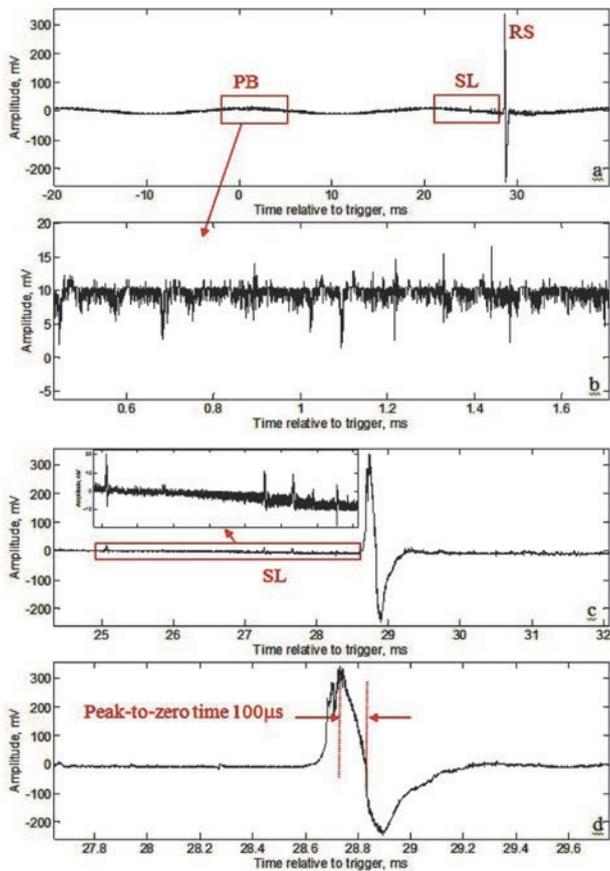
Figure 8. Fast electric field waveform detected at 15:42:31, August 6, 2015, distance to lightning estimated by EFM-100 field mill is in the range 6-28 km. Bipolar pulses in the inset of frame c) are presumably the stepped leader (SL) pulses. Classification: negative cloud-to-ground lightning (-CG).
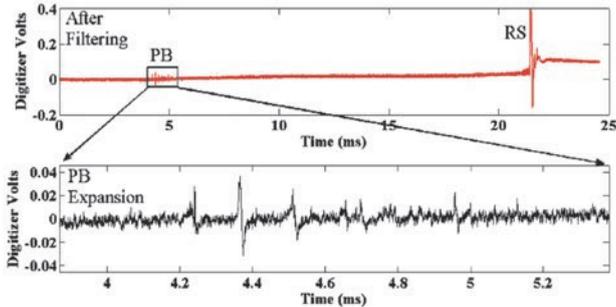

Fi
gure 9. Fast electric field waveform of negative CG lightning recorded at Lightning Observatory in Gainesville Florida, USA (Zhu et al 2014)

Here, the return stroke is negative because the polarity of the initial half cycle of the strong bipolar pulse is positive (as mentioned above, we use the "atmospheric electricity" sign convention for electric fields, in which a positive electric field change corresponds to negative return stroke). In the waveforms of Figure 7 and 8, some bipolar pulses are observed also in the time interval between PB pulses and the return stroke pulse. We assume that they can be interpreted as leader pulses.

We note that the peak-to-zero time of the initial half cycle is 125μs for the waveform of Figure 6, and about 100μs for the waveforms of Figures 7 and 8. This long fall time, or return from the minimum (or maximum) to zero supports the classification of the observed events as CG lightnings. According to the criterion used by (Heavener et al.,2003) at the Space and Atmospheric Science Group, Los Alamos National Lab, the classification of CG events is based solely on the relatively slow (greater than 30μs) fall time.

5. IMAGES OF THE CORRESPONDING NEAR-SURFACE ELECTROSTATIC FIELD

In Figure 10 we show the disturbances of the near-surface electrostatic field for three lightnings discussed in the previous section and measured by EFM-100 electric field mill.

The main characteristics of the electrostatic field changes, the distance to lightning and estimated stroke energy, are summarized in Table 2. The difference $\Delta E = (E_{max}-E_{start})$ between the electrostatic field at the maximum and at the start of its abrupt change is -64.6kV/m and -41.5kV/m for lightnings occurred on August 6. For the lightning that occurred on August 2, the electrostatic field abruptly rises from 11 kV/m to 39 kV/m during 100 msec and then drops down to -23 kVm in 50 msec with a subsequent long recovery time of (FWHM=30sec). These parameters of the slow electric field measured by the field mills fulfill the conditions for CG lightnings introduced in (Chilingarian et al., 2015, Tab. 1). Thus, we have the same classification of lightning type made by fast waveforms and "slow" near-surface electric field patterns.
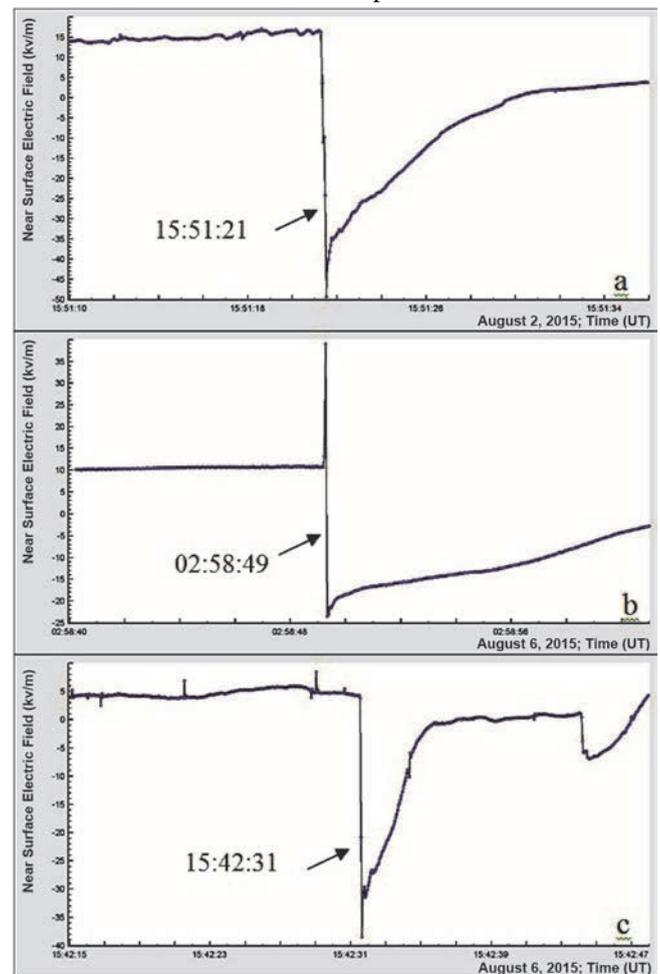
Figure 10. 50 msec time series of near-surface electrostatic field for three selected lightnings. a) 15:51:21 August 6,2015; b) 02:58:49 August 2,2015; c) 15:42:31 August 6,2015. Distance to lightning for a) and b) which were detected also by WWLLN is 3.7km and 5.9km, respectively. Distance to lightning for c) estimated by EFM-100 field mill is about 6km.

It is interesting to compare the disturbances of the electrostatic field and fast electric field waveforms for the three lightnings. For the lightning that occurred on August 6 at 15:51:21, the electrostatic field change is negative and hence, it is produced by a positive lightning, which neutralizes the positive charge overhead.

Table 2. Parameters of electrostatic field change, distance to lightning, and estimated stroke energy for three observed lightnings.

N	Date	Time (UT)	Distance km	Start electric field E_{start}, kV/m	Max electric field E_{max}, kV/m	$\Delta E = E_{max}\ E_{start}$ kV/m	FWHM of field change	Stroke Energy (J)
1	6-Aug-15	15:51:21	3.7	15.8	-48.8	-64.6	4sec	4586±1160
2	2Aug-15	02:58:49	5.9	11 39	39 -23	28 -62	35 msec 30sec	3071±802
3	6-Aug-15	15:42:31	6	3.5	-38	-41.5	2sec	N/A

This is consistent with the polarity of the lightning determined from the fast electric field waveform shown in Figure 6. For the lightning that occurred at 02:58:49, there are two changes of the electrostatic field having opposite polarity: a large positive change is immediately, within 100 msec, followed by a huge negative change. This negative change is produced by a positive lightning, which neutralizes the positive charge overhead, and this is again consistent with the polarity of the lightning determined from the fast electric field waveform shown in Figure 7. A question arises: what is the origin of the positive change of the electrostatic field in the beginning? The fast field waveform of Figure 7 shows that the positive return stroke is preceded by a long stage (about 50 msec) of multiple weak bipolar pulses, which can be identified as preliminary breakdown and stepped leader pulses, as it was already mentioned above. Even though these pulses are weak, the total charge neutralized by these multiple discharges can be quite large, and the electric field mill can detect the electrostatic field change produced by charge neutralization prior to the return stroke.

We also note that the lightning occurred on August 2 at 02:58:49.244 has the strongest PB pulses among the selected three, and only for this event (among the three) the electrostatic field change is not typical, showing a large positive change followed by an even larger negative one. If we assume that the positive change of the electrostatic field observed in the beginning of the lightning is related to the stage of preliminary breakdown and negative change then - to the stepped leader, we come to the conclusion, that prior to the positive return stroke which neutralizes positive charge overhead, the discharges of the preliminary stage neutralize the negative charge overhead.

For the lightning on August 6 at 15:42:31, the electrostatic field change is negative and hence, we can expect that a positive lightning, which neutralizes a positive charge overhead, could produce it. However, this conclusion is in contradiction with the lightning polarity determined from the fast electric field waveform shown in Figure 8, where the positive polarity of the initial half cycle (Figure 8 c, d) clearly indicates a negative lightning, which neutralizes a negative charge overhead.

We can suppose that a possible reason for this contradiction could be the sign reversal of the electrostatic field with distance (e.g., Rakov and Uman, 2003, p. 71.), and that the true polarity (negative) of this lightning is determined from fast field waveform, since the polarity of radiation field does not change with distance. However, no polarity reversal of electrostatic field has been detected by our three field mills for this lightning, so an unambiguous identification of the type and polarity is not possible.

6. CONCLUSION

The TGE events copiously measured on Aragats during thunderstorms are represented by the 50 ms, one-second and one-minute time series of the gamma ray and electron count rates as well as by gamma-ray energy spectra, meteorological conditions, fast and slow disturbances of the near-surface electric field, which allowed us to investigate their causal relation to lightning initiation (Chilingarian et al., 2015).

We monitor the particle fluxes from thunderclouds and atmospheric discharges by networks of near-surface electric field sensors and fast electric field waveforms. TGE slowly discharge the lower dipole allowing smooth decaying of the large negative electrostatic field on the ground. In contrast, lightnings "kill" the TGE immediately; the abrupt change of the near surface electric field by the negative cloud-to-ground lightning is accompanied by the abrupt termination of the TGE. Thus, investigation of the lightning-TGE relations can shed new light on the long-standing problem of lightning initiation.

Extended data capture length of digital oscilloscope allows investigating relations of the fast electric field waveforms and disturbances of near-surface electrostatic field. Weak bipolar pulses followed by strong bipolar pulse in the waveforms can be identified as preliminary breakdown (PB) pulses followed by stepped leader pulses and by the large return stroke pulse. Long fall time of the return stroke pulse supports the classification of observed events as CG lightnings.

For the lightning of August 6 at 15:51:21, the electrostatic field change is negative and hence, it is produced by a positive lightning, which neutralizes a positive charge overhead. This is consistent with the polarity of lightning determined from the fast electric field waveform.

The lightning of August 2 at 02:58:49.244 has the strongest PB pulses among the three selected, and only for this event (among the three analyzed) the electrostatic field change is not typical, showing a large positive change followed by an even larger negative one. We can speculate that the positive change of the electrostatic field observed in the beginning of the lightning of August 2 is related to the stage of the preliminary breakdown and negative change then - to the stepped leader. Thus, we conclude that prior to the positive return stroke, which neutralizes the positive charge overhead the discharges of the preliminary stage neutralize the negative charge overhead.

For the lightning of August 6 at 15:42:31, the electrostatic field change is negative and hence, we can expect that a positive lightning, which neutralizes a positive charge overhead, produce it. However, this conclusion is in a contradiction with the polarity of lightning determined from the fast electric field waveform. The question of an unambiguous identification of the type and polarity of this lightning remains open.

REFERENCES

- Alexeenko V.V., Khaerdinov N.S., Lidvansky A.S., Petkov V.B., 2002. Transient variations of secondary cosmic rays due to atmospheric electric field and evidence for pre-lightning particle acceleration Physics Letters A 301, 299–306.

- Babich, L.P., et al., 2001. Comparison of relativistic runaway electron avalanche rates obtained from Monte Carlo simulations and kinetic equation solution. IEEE Trans. Plasma Sci. 29 (3), 430–438.

- Chilingarian, A., Arakelyan, K., Avakyan, K.et al., 2005. Correlated measurements of secondary cosmic ray fluxes by the Aragats space-environmental center monitors, Nucl. Instrum. Methods A 543 (2–3) 483.

- Chilingarian, A., A. Daryan, K. Arakelyan, A. Hovhannisyan, B. Mailyan, L. Melkumyan, G. Hovsepyan, S. Chilingaryan, A. Reymers, and L. Vanyan L.,2010. Ground-based observations of thunderstorm-correlated fluxes of high-energy electrons, gamma rays, and neutrons, Phys. Rev. D, 82, 043009.

- Chilingarian A., Hovsepyan, G., Hovhannisyan, A., 2011. Particle bursts from thunderclouds: natural particle accelerators above our heads. Phys. Rev. D: Part. Fields 83 (6), 062001.

- Chilingarian A., Mailyan B., and Vanyan L., 2012. Recovering of the energy spectra of electrons and gamma rays coming from the thunderclouds, Atmospheric Research 114–115 ,1–16.

- Chilingarian A., 2014. Thunderstorm Ground Enhancements - model and relation to lightning flashes, Journal of Atmospheric and Solar-Terrestrial Physics 107 68–76.

- Chilingarian A., Hovsepyan G., Khanikyanc Y., Reymers A. and Soghomonyan S., 2015. Lightning origination and thunderstorm ground enhancements terminated by the lightning flash, EPL, 110, 49001.

- Chilingarian A., Hovsepyan G., Khanikyants Y., Pokhsraryan D., and Soghomonyan S.,2016.Atmospherics discharges - particle flux relations in the TGEs terminated by the lightning flash, Proceedings of TEPA 2015, Nor Amberd, Tigran Mets.

- Dwyer, J.R., 2003. A fundamental limit on electric fields in air, Geophys. Res. Lett., 30 (20), 2055.

- Gurevich, A.V., Milikh, G.M., Roussel-Dupre, R., 1992. Runaway electron mechanism of air breakdown and preconditioning during a thunderstorm. Phys. Lett. A 165 (5-6), 463–468.

- Heavner M.J., D.M. Suszcynsky, and D.A. Smith, 2003. LF/VLF Intracloud Waveform Classification, LA-UR 03-2078, presented at International Conference on Atmospheric Electricity, Versailles, France, June 9-13, 2003.

- Hutchins M. L., Holzworth R. H., Rodger C. J., and Brundell J. B., 2012.

- Far-Field Power of Lightning Strokes as Measured by the World Wide Lightning Location Network, Journal of Atmospheric and Oceanic Technology, v. 29, 1102.

- Kato Y, Kuroda Y., Tomita N., Minowa M., Thundercloud-related radiation bursts observed at a coastal area and a mountaintop using segmented organic scintillators, Proceedings of TEPA 2015, Nor Amberd, Tigran Mets, 2016.

- Rakov, V., and M. Uman, 2003.Lightning: Physics and Effects, Cambridge Univ. Press, Cambridge, U. K.

- Torii T.,et al., 2011. Migrating source of energetic radiation generated by thunderstorm activity Geophys. Res. Lett, VOL. 38, L24801.

- Tsuchiya H. et al., 2009. Observation of an Energetic Radiation Burst from Mountain-Top Thunderclouds PRL 102, 255003 (2009) Phys. Rev. Lett., 102, 255003.

- Tsuchiya H. et al., 2013. Hardening and Termination of Long-Duration gamma- Rays Detected Prior to Lightning PRL 111, 015001.

- Zhu Y., Rakov V. A., Mallick S., Tran M. D., Pilkey J., and Uman M. A., 2014. Preliminary Breakdown Pulse Trains in Electric Field Records of Negative Cloud-to-Ground Lightning XV International Conference on Atmospheric Electricity, 15-20 June 2014, Norman, Oklahoma, U.S.A.

Thunderstorm ground enhancements (TGEs) abruptly terminated by negative cloud-to-ground lightnings

A. Chilingarian, G. Hovsepyan, G. Khanikyanc, D. Pokhsraryan, and S. Soghomonyan

A. Alikhanyan National Lab (Yerevan Physics Institute), 2, Alikhanyan Brothers, Yerevan 0036, Armenia

Abstract. The relationship of lightnings and particle fluxes in the thunderclouds is not fully understood to date. Using the particle beams (the so-called Thunderstorm Ground Enhancements – TGEs) generated in the lower part of clouds by the strong electric fields as a probe, we investigate the characteristics of the related atmospheric discharges. The well-known effect of the TGE dynamics is the abrupt termination of the particle flux. We demonstrate that among 12 atmospheric discharges that abruptly terminated TGE all are the negative cloud-to-ground lightnings. The flux termination and lightning occurred at one and the same second.

With new precise electronics on millisecond time scales we can see that particle flux decline occurred simultaneously with abrupt increase of electrostatic field after the return stroke of the lightning. Therefore, the declining of particle flux is connected with rearranging of charge centers in the cloud involving removal of the Lower Positive Charged Region (LPCR).

1. INTRODUCTION

Thunderstorm Ground Enhancements (TGEs, Chilingarian et al., 2010, 2011) are abrupt enhancements of the secondary cosmic rays measured on the Earth's surface in correlation with thunderstorms and lasting from several seconds to several tens of minutes. The origin of TGEs are the very strong electric fields in the thunderclouds; if all electrostatic fields induced by the charge layers in the thundercloud join in a resulting field that accelerates the electrons downwards, the seeds from the ambient population of Cosmic Rays (CR) can gain energy from the field, multiply and produce bremsstrahlung gamma rays which are registered at the Earth's surface. Plenty of the seed electrons originate from the multiple Extensive Air Showers (EASs) unleashed by the galactic high-energy protons and stripped nuclei interacting with the atmosphere.

The mechanism of the acceleration and multiplication of seed electrons, namely Runaway Breakdown (RB), was suggested in (Gurevich et al., 1992) along with emphasizing its role in the lightning initiation. This mechanism recently is referred also as Relativistic Runaway Electron avalanches (RREAs, Dwyer, Smith, and Cummer, 2012; Dwyer and Uman, 2014). RB operates only at very high electric fields in the cloud and is capable to originate TGEs with energies up to 40-50 MeV and intensities tens of times exceeding the cosmic ray background (Chilingarian, et al., 2013).

In 2002 Chilingarian, Mailyan and Vanyan proposed a compatible with RB mechanism – Modification of electron energy Spectra (MOS), which can increase the secondary cosmic ray flux by a few fractions of a percent, but in a larger energy scale.

In 1999, Alex Gurevich and colleagues suggested that when the electric field in a thunderstorm cloud reaches the critical value of $E > E_c$, every cosmic ray secondary electron with "runaway" energies (0.1 – 2 MeV) initiates a micro-runaway breakdown (MRB). Usually it is very difficult to select these nanosecond-lasting showers originated in the cloud from the individual electrons (Extensive Cloud Showers – ECSs, Chilingarian et al., 2011) within the ongoing TGE of several minutes duration. ECSs (MRBs) should be distinguished from the plenty of large EASs originated

high in the atmosphere and containing millions of particles. Nonetheless, at Aragats research station where clouds sometimes are "sitting" on the surface we detect several large TGEs, within which "resolve" numerous very short (< 400 nsec) showers originated in the thundercloud from a seed electron (Chilingarian et al., 2011). Furthermore, by the 2-way classification we demonstrate systematic differences of ECSs and EASs. Thus, TGEs are superposition of the multiple avalanches initiated by the individual CR electrons in thundercloud and reaching the Earth's surface.

The relation of RBs, TGEs and lightnings are not yet fully discovered. If we can definitely state that RB is capable to initiate a TGE and a lightning cannot initiate a TGE (Chilingarian, 2014), then the role of RB in lightning initiation is still dimmed.

According to the theory of a combined effect of RB-EAS (Gurevich, et al., 1999), the ionization of the atmosphere by a high-energy EAS ($E > 10^{16}$ eV) in RB conditions is growing strong enough to produce spark-type local electric breakdown that can radiate a strong local pulse of electric current and serve for lightning leader initiation.

For proving this theory we need simultaneous and synchronized on nanosecond time scales detection of EASs, TGEs and lightnings by particle detectors with fast electronics, detectors of the fast waveforms of radio emission, sensitive fast cameras, precise lightning detectors and electrostatic field sensors. Certainly, *in-situ* measurements of the electric field in the cloud will be very helpful. Unfortunately to date there are no convincing experiments for solving the lightning origination enigma.

In the present paper we will try to approach this problem by the analysis of a special kind of TGEs, i.e. TGEs abruptly terminated by lightnings. To our knowledge, the Baksan group reported the first TGEs of this kind (Alexeenko et. al., 2002). They demonstrated that the particle count rate increased at energies of ~30 MeV then quickly returned to the background level when lightning occurred. In (Khaerdinov and Lidvansky, 2005) they correctly deduce that the detected flux enhancements are not directly related to the lightning activity; the lightnings serve rather as a switch-off for the electric field. Recently several groups report such special TGEs as well (Tsuchiya H. et al.,

2013, Chilingarian et al., 2015, Kelley et al., 2015, Kollarik et al., 2016, Kuroda et al., 2016).

With installing of new fast electronics at Aragats (Pokhsraryan, 2016) it became possible to investigate time series of the near-surface electric field, fast waveforms of atmospheric discharges and particle fluxes on the millisecond time scale. Various particle detectors and field meters are now synchronized by GPS receivers providing a time stamp with an accuracy of better than a few tens of a nanosecond.

In the paper we present the analysis of a TGE event occurred on 7 October 2015 for the first time detected on a millisecond time scale. We also consider a sample of TGEs observed during 2013-2015, all of them being abruptly terminated by lightnings, in order to deduce what kind of atmospheric discharge had ceased the particle flux.

2. INSTRUMENTATION: ARAGATS SOLAR NEUTRON TELESCOPE [1]

Aragats Solar Neutron Telescope (ASNT, Fig. 1) is a part of the worldwide network coordinated by the Nagoya University and aiming primarily to measure the fluxes of the neutrons born in the violent solar flares. Now ASNT is monitoring 7/24 charged and neutral fluxes of secondary cosmic rays. ASNT observation of the ever-largest TGE detected at Aragats Space Environmental Center (ASEC, Chilingarian et al., 2005) on 19 September 2009 (Chilingarian et al., 2011) allows for the first time to measure simultaneously the energy spectra of the electrons and gamma rays and firmly establish the neutrons production in the photonuclear reactions of gamma rays in the atmosphere.
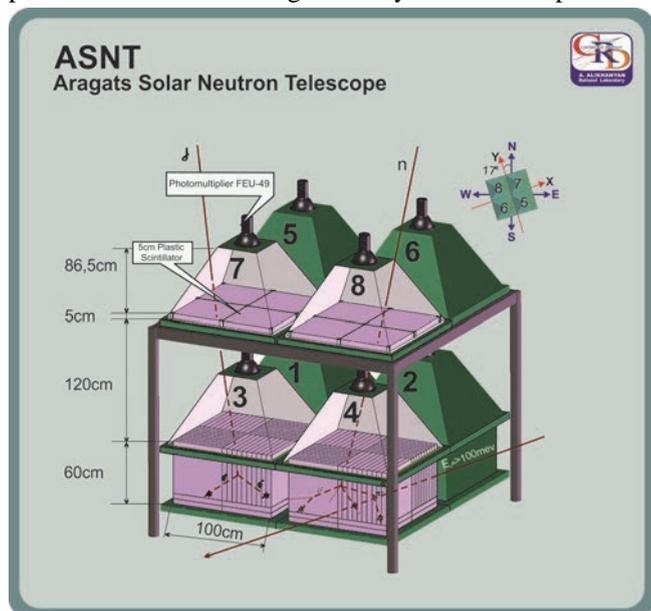

Figure 1. Setup of the Aragats Solar Neutron Telescope (ASNT)

ASNT consists of 4 upper and 4 lower scintillators, each having an area of 1m^2. The distance between the layers is ~1.2 m. The data acquisition system can register all coincidences of detector signals from the upper and lower layers, thus enabling measurements of the arrival of the particles from different directions. The signals ranging from 0.5 mV to 5 V, from each of 8 photomultipliers, are passed

---

[1]*Particle detectors and field meters used in the present research are described in other papers of proceedings. Here we present only description of the ASNT detector.*

---

to the programmable threshold discriminators. The output signals are fed in parallel to the 8-channel logical OR gate triggering device and to a buffer. If there is a signal in the channel we will denote it by 1 and the channels that were not fired within the ''opening'' time of the gate (~1 μs) by 0. The ASNT trigger condition is defined by detecting at least one signal in the 8 data channels. The trigger rate of the entire detector system does not exceed 10 kHz. The duration of the entire data readout and signal processing procedure is less than 10 μs. There are 23 different possibilities of so-called ''basic states''. Sixteen of them carry information about the direction of the incident particle. For example, the state configuration 0010 for the upper layer and 0010 for the lower layer corresponds to the charged particle traversal through the third upper and third lower scintillators (zenith angle between 0 and 30). Combination 0010 and 1000 corresponds to the traversal through the third upper and the first lower scintillator (zenith angle between 20 and 40). The other 7 possibilities give additional valuable information on the particle flux incident on the detector. For instance, the combination 01, i.e., no signal in the upper and the signal in the lower layer can be attributed to the traversal of a neutral particle. However, due to small sizes of the anticoincidence shielding (see Fig. 1), several charged particles can hit the detector from the side. Nonetheless, if the particle beam is near vertical (it is just the case of a TGE hitting ASNT), we can measure the energy release spectrum of the thunderstorm-correlated gamma rays. Histograms of the energy releases in the thick scintillators are measured and stored each minute, providing the exact pattern of the energy releases during solar transient events and during thunderstorms. The top scintillators have the thickness of 5 cm (energy release for the vertical electrons is ~10 MeV) the combination 11 will select charged particles with energy greater that 20 MeV. The advanced data analysis system (ADAS) provides registration and storage of all logical combinations of the detector signals for further offline analysis and for issuing warnings and alerts on the dangerous space weather conditions.

3. LARGE TGE OCCURRED ON 7 OCTOBER 2015

On 7 October 2015 the weather at Aragats was stormy. Disturbances of the near-surface electrostatic field started around 7:00 UT and followed with several lightnings to12:00. The atmospheric pressure was 685.3 mbar; wind speed 2.5 m/sec from ~270° N direction. The solar radiation decreased from 500 W/m^2 at 10:15 down to zero at 11:45 due to thick cloud preventing solar radiation to reach the Earth's surface. The temperature followed the decline of the solar radiation with a short delay decreasing from 2.8 C° down to 0.5 C°. The location of the cloud just above the particle detectors and developing of the Lower Positively Charged Region (LPCR) in the bottom of it assisted unleashing of the large TGE, which started at 14:40 and all the particle detectors of ASEC registered it. The relative humidity during TGE was very high – 97%. In Fig. 2 we show the two-second time series of the ASNT detector (Fig. 1). The upper blue time series correspond to the flux measured by the four 60 cm thick 1-m^2 plastic scintillators; the black time series are measured by the same scintillators conditioned on the absence of a signal in the upper (veto) scintillators; and the read one – the near-vertical flux of particles registered in both layers of detector (11-combination, mostly electrons with energies above 20 MeV).
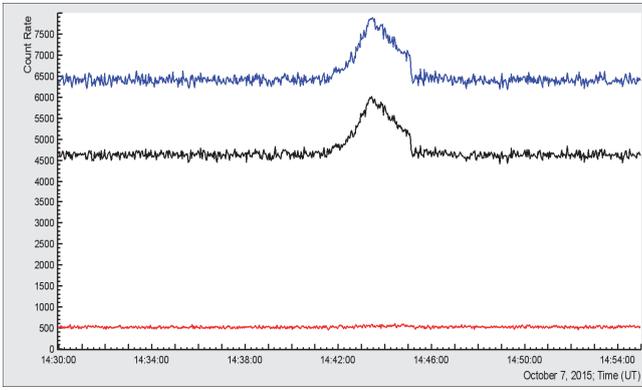
Figure 2. TGE seen in the two-second time series of the ASNT detector; blue time series – total flux; black time series – flux with veto on near-vertical charged particles; red time series – high energy particles with energies greater than 20 MeV.

In Fig. 3 we show p-values of the same two-second time series observed by ASNT detector. The significance of detecting peaks in the time series of the particle count rates is determined by the p-values of the peak significance test, i.e. by the value of the peak divided by the standard deviation of count rate (number of standard deviations contained in the peak, Nσ). The p-value is the most comprehensive measure of the reliability of detecting peaks in a time series. Large p-value corresponds to small chance probabilities that the observed peak is a background fluctuation and not a genuine signal. Therefore, we can safely reject the null hypothesis (background fluctuation) and confirm the TGE.
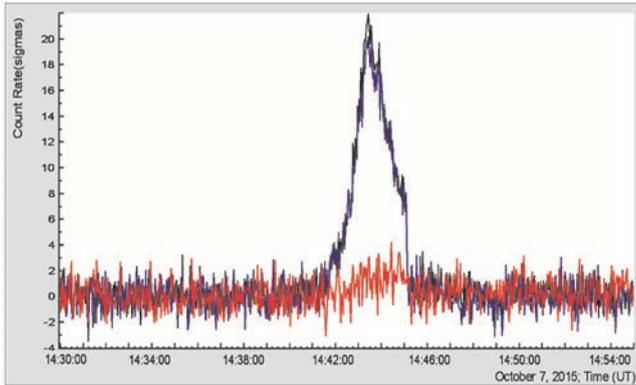

Figure 3. TGE as seen in the p-values of the two-second time series of the ASNT detector; black time series – total flux; blue time series – flux with veto on near-vertical charged particles; red time series – high energy particles with energies greater than 20 MeV.

Closeness of the particle flux with and without veto proves that most of the TGE particles were gamma rays.

The high-energy gamma ray flux was confirmed by directly measured differential energy spectrum with the network of NaI spectrometers, see Fig 4. Differential energy spectra measured by 3 NaI spectrometers extended at least up to 30 MeV (therefore the "parent" electrons have energies up to 40-50 MeV). The integral near-vertical energy spectra of the TGE event measured by the CUBE detector (energy threshold ~ 4 MeV) with capability of separating electron and gamma ray fluxes was: I_e ~ 350(min*m²)⁻¹; $I\gamma$ ~ 9500(min*m²)⁻¹; Ie/Iγ ~ 3.8%.

The particle flux reached the maximum at ~14:44 and on the declined phase at 14:45:07 the negative lightning "killed" it (see Fig. 5). The disturbances of the near-surface field started at 14:45:07, reaching the maximum at 14:45:07.10; the amplitude was ~70 kV/m and the distance to lightning was ~7 km.
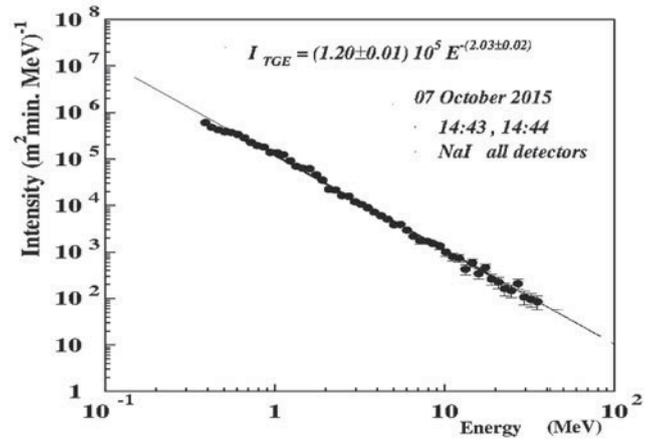

Figure 4. Differential energy spectrum of the TGE measured by the NaI spectrometer with energy threshold 0.4 MeV

After the shaping of the LPCR in the bottom of the cloud, the emerged strong electric field accelerated the electrons downward in the direction to the ground. The LPCR is usually small as compared to the main negative charge; so it can influence only the electrostatic field locally beneath the cloud. LPCR, as well, can control the development of the downward negative leader starting above in the cloud. The main negative charge region in the middle of the cloud and its image charge of the opposite sign (under the assumption of perfectly conducting ground) form much more extended field also accelerated electrons downward. The superposition of these two fields and electrostatic field induced by the main upper positively charged region is changing fast, dependent on the wind speed that moves LPCR above the particle detector location. Deposition of the negative charge to the ground by lightning leads to an abrupt increase of the positive charge overhead, resulting in the particle flux decay. We note that the "atmospheric electricity" sign convention (a downward-directed electric field or field change vector is considered positive) is used throughout this paper. Therefore, negative lightning depositing negative charge to the ground produces positive electrostatic field change as indicated in the Figure 5 (see the discussion on the atmospheric electricity sign convention in (Krehbiel et al., 2014).
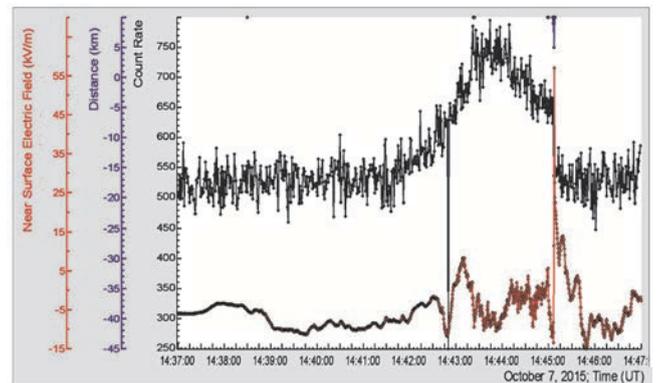
Figure 5. TGE abruptly terminated by the negative lightning; in the bottom are shown electric field disturbances detected by the electric mill EFM-100; in the middle – 1-sec time series of count rate of 3 cm thick outdoor plastic scintillator, on the top – distance to lightning; Lightning occurred at 14:45:07 coinciding with decline of particle flux by 14.4%.

In our previous paper (Chilingarian et al., 2015) we compared the 50 msec time series of the near-surface electrostatic field measurements with the 1-sec time series of the count rates of particle detectors. This, 20-fold inconsistency in the time series prevents definite inference on

start of the particle decline relative to lightning time. With installing of the new fast electronics (Pokhsraryan, 2016) it becomes possible to compare lightning and particle fluxes on the same temporal scale.

In Fig. 6 we demonstrate five seconds of the 50-ms time series of the count rates including abrupt increase of the near-surface electrostatic field and particle flux termination. Visible decline of the particle flux occurred within 100 ms from (14:45:07.175 to 14:45:07.275) of the abrupt increase of the near-surface electrostatic field that is manifestation of the negative lightning strike. It is expected that the maximum of electrostatic field change is reached later than the maximum of electromagnetic pulse from the lightning. Our statistics of the time difference between WWLLN time stamps and EFM-100 field maximum time stamps (137 coinciding detections, see Fig. 5 in Chilingarian et.al., 2016) shows a delay of electrostatic field maximal value of ~ 185 ms. Thus, the decline of the particle flux detected at ~14:45:07.175 was simultaneously with abrupt increase of the near-surface electrostatic field after the return stroke which deposited the negative charge on the ground. This is further supported by the fact that detection of the fast electric field waveform was triggered at 14:45:06.995 that is 180 ms prior to the abrupt termination of TGE.

The electric field measurements are fed to the myRio board by the TCP-IP connection (WiFi) scaled ~ 5 times less than the firmware application provided by Boltek via Internet cable (Pokhsraryan, 2016). It explains ~5-fold decrease of the electrostatic field strength of myRio output.
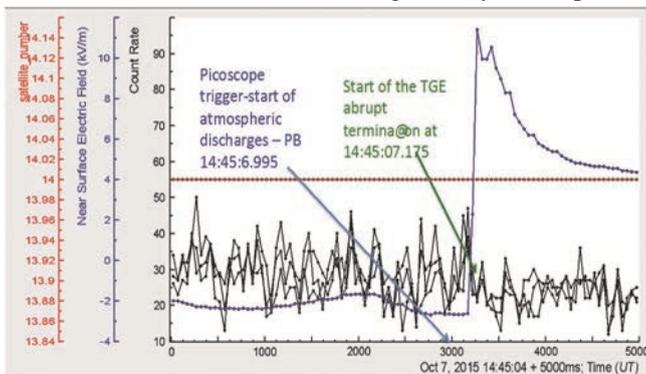

Figure 6. Five seconds of 50 ms time series of all 3 layers of the STAND1 detector (located near SKL hall) before and after sharp decline of particle flux at 14:45:07.225. The flux decline coincides with an abrupt increase (100 ms rise time) of the near-surface electrostatic field. 14 GPS satellites participate in the precise time synchronization.

4. TYPE OF ATMOSPHERIC DISCHARGE ABRUPTLY TERMINATING TGE

We add to the already published 5 TGE events terminated by lightning that occurred in 2014 (Chilingarian et al., 2015) 5 new TGE events observed in 2015 and 2 old events from 2013 and 2012 found in the databases. The goal of our analysis is the identification of the discharge type for all 12 TGEs.

First of all we can claim that only negative discharges terminate TGEs (see for instance, Chilingarian, Hovsepyan and Mnatsakanyan, 2016). However the question still to be answered is: are these discharges intracloud ones (IC-), or cloud-to ground (CG-)? In our analysis we will use the data from the network of near-surface electric field sensors, photographs from lightning monitoring cameras and data from the World Wide Lightning Locating Network (WWLLN).

All 12 TGE events terminated by an atmospheric discharge are shown in the Fig. 7. The abrupt decline of TGE is shown in the 1-second time series of count rates of 3-cm thick outdoor plastic scintillator of STAND1 detector. In 2012-2014 years the data from STAND1 near MAKET experimental hall was used (Fig 7 e-h); in 2015 – the data from STAND1 detector near SKL experimental hall (Fig 7 a-d). For all 12 TGEs the disturbances of electrostatic field and distances to lightning performed by the EFM-100 electric mill located on the roof of MAKET hall were used.

In the Tab. 1 we summarize characteristics of TGE events interrupted by lightnings. As we can see from Fig. 7 lightning occurred in the same second with the count rate decline. Negative lightning in the disturbances of near-surface electrostatic field is seen as abrupt positive change of the field with subsequent slow recovering.

Table 1 contains essential parameters of the selected TGEs. In the first column we put the date of the event, in the second – time of start of the abrupt change of electric field and corresponding value of the electrostatic field. In the third column we put the time and value of the reached maximal electric field. The fourth and fifth columns show the rise time (from start to maximum) and recovery time (Full width at half maximum - FWHM) of the measured disturbed electrostatic field respectively. In the sixth column we show the drop of the particle detector count rate. The seventh column shows the drop of electric field (difference between maximal and start values). The next two columns show the distance to lightning estimated by electric field mill EFM-100 and WWLLN, respectively. The WWLLN time stamp of detected lightning is shown in the last column. In the last 2 rows of the Table we show calculated values of measurements means and mean standard deviations (MSD). The typical features of the negative cloud-to-ground (-IC) lightnings terminated TGE are:

1. Mean rise time of the near-surface electrostatic field ~ 242 ± 88 ms;
2. Mean field recovery time (FWHM) ~ 4.3 ± 2.3 sec;
3. Mean particle flux drop – 37 ± 23%;
4. Mean field surge –60 ± 19 kV/m;
5. Mean distance to lightning ~ 5.3 ± 2.9 km.

Very large amplitude of the negative lightning field changes (~60 kV/m) achieved in very short time (~242 ms) and large recovery time of electric field (4.3 sec) indicate strong discharge processes at nearby distances (up to10 km) in the thunderclouds above Aragats.

To determine the type of lightning we incorporate in our analysis another type of evidence from the network of electric mills. Since our network is rather lengthy, extending from top of Aragats to Yerevan (~ 40 km) for the classification of the discharge types we can use the criterion described by (MacGorman and Rust, 1998), see also (Krehbiel et al., 2014). When measuring the disturbances of the electrostatic field by network of sensors, the electrostatic field can reverse polarity with distance from the lightning in case of the intracloud discharges (IC), whereas for the CG ones the polarity remain constant. All 12 lightnings (with exception of one not reliably classified event) did not reverse the polarity in the domain of electric mill network. Examples of IC lightning changing polarity with distance and confirming the type by the simultaneous photographs are shown in Figs. 8 and 9. Therefore we conclude that only – CG lightnings terminate the TGE.
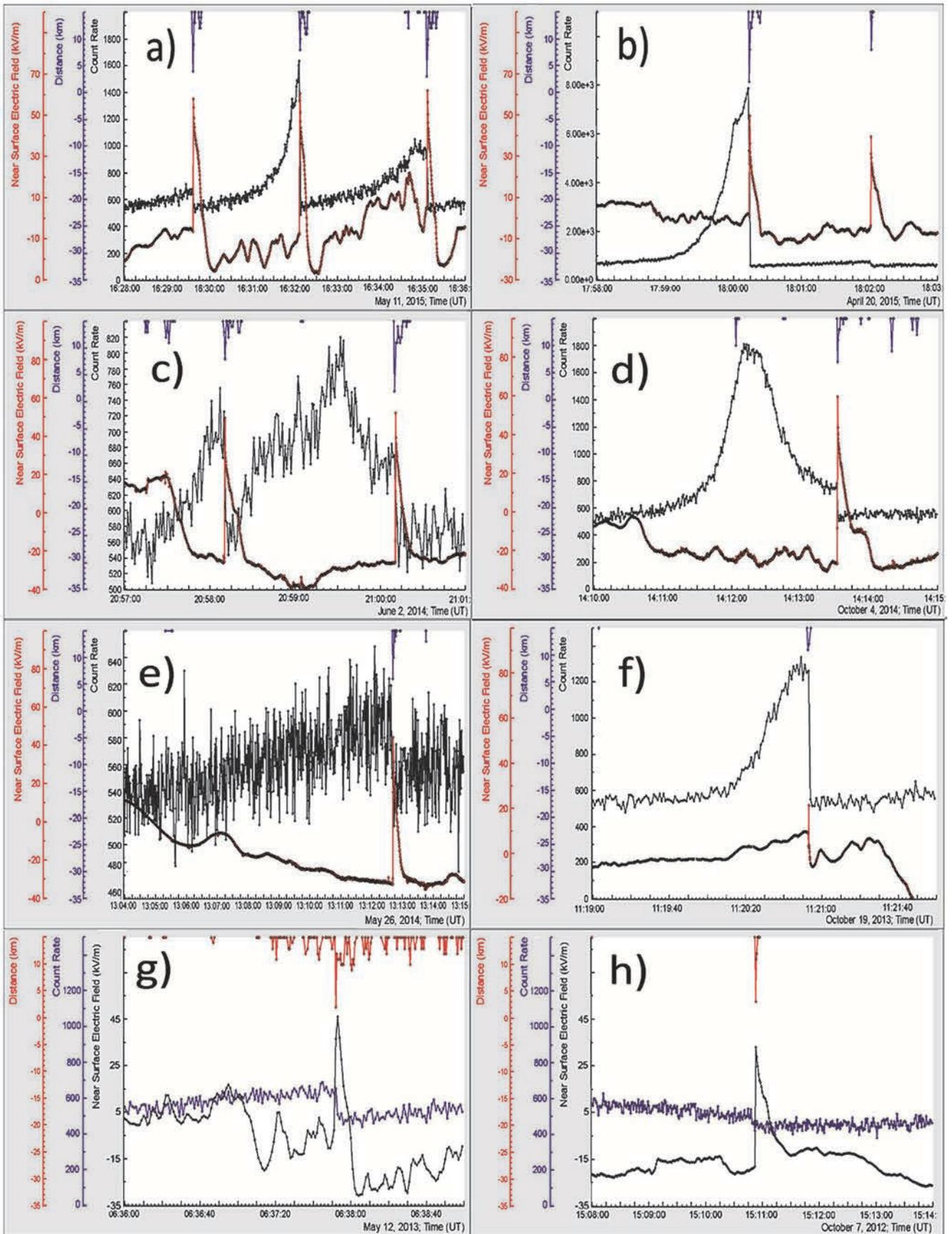
Figure 7. Time series of the 1 second count rates of the outdoor 3 cm thick scintillator sharply terminated by the lightning and disturbances of the near-surface electric field; in the top of figures the distance to lightning from particle detectors is shown. Electrostatic field and distance to lightning are measured by the EFM-100 electric mill located on roof of the MAKET experimental hall. Particle count rate was measured by the 3-cm thick scintillator of STAND1 detector located outdoors the SKL experimental hall and(a-d) and MAKET experimental hall (e-h).

Table 1. Main parameters of the TGE events terminated by lightnings

Date	Start of lightning (UT) and el. field value kV/m	Time of maximum (UT) and el. field max value kV/m	Rise time (ms)	Decay time fwhm sec	Drop of flux %	Surge of el. field kV/m	EFM Dist. km	WWLLN Dist km	WWLLN time (UT)
11/05 2015	16:29:36.380 -5.7	16:29:36.580 57.3	200	8	24	63	4.0	0.6	16:29:36.337
11/05 2015	16:32:06.550 -6.5	16:32:06.800 60	250	6	70	66.5	7.9	13.7	16:32:06.521
11/05 2015	16:35:06.550 5.5	16:35:06.800 61.5	250	5	44	56	2.9	4.2	16:35:06.534
20/04 2015	18:00:14.1001.2	18:00:14.350 49.2	250	1.1	91	48	2	6.7	18:00:14.757
20/04 2015	18:02:01.100 -3.4	18:02:01.300 39.2	200	1.2	25	42.6	7.8	N/A	N/A
4/10 2014	14:13:32.400 -25.5	14:13:32.550 58.5	150	5	32	84	6.8	N/A	N/A
2/06 2014	20:58:10.050 -25.2	20:58:10.350 48.8	300	4	24	74	7.8	N/A	N/A
2/06 2014	21:00:11.000 -23.2	21:00:11.000 52.2	350	4	22	75.4	2	N/A	N/A
26/05 2014	13:12:41.500 -32	13:12:41.800 43.6	300	7	13	75.6	6.3	N/A	N/A
19/10* 2013	11:20:53.000 9.3	11:20:53.050 21.1	50	0.05	58	11.8	11	4.9	11:20:53.392
12/05 2013	06:37:52.000 -10	06:37:53.000 45.6	400	4	20	55.6	2	N/A	N/A
7/10 2012	15:10:53.000 -17.9	15:10:53.000 50.2	200	6	22	68.1	2.9	N/A	N/A
Mean	-11.1	49	242	4.3	37	60.0	5.3		
MSD	12.8	11	88	2.3	23	19	2.9		

*According to measurements of the electric mill located near GAMMA array the lightning was much closer and amplitude of near-surface electric field disturbances was much larger. Unfortunately, lightning kills this electric mill and it is another evidence along with staff reports that lightning was much closer than 11 km.
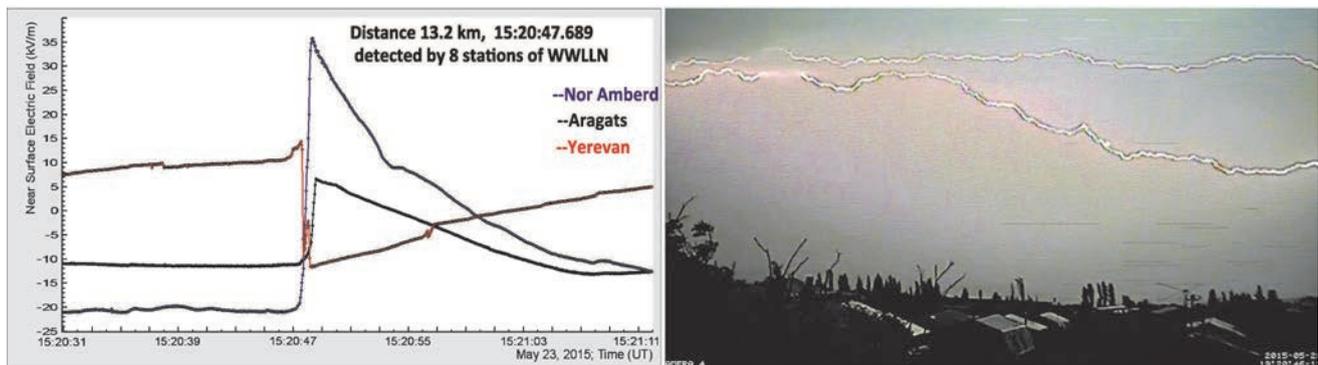
Figure 8. The disturbances of the near-surface electric field due to intracloud lightning shown on the photograph shot at Burakan village in direction of Mt. Ararat. On the top are shown the measurements of the near-surface electric field performed by the EFM-100 electric mills located at Aragats, Nor Amberd and Yerevan. Polarity reversal of electrostatic field change for the negative IC flash is apparent.
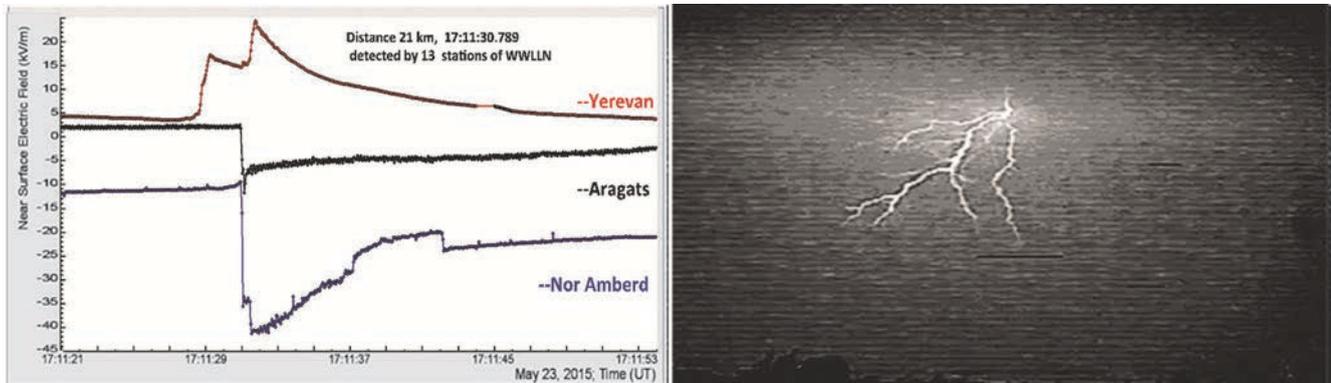

Figure 9. The disturbances of the near-surface electric field due to intracloud lightning shown on the photograph shot at Burakan village in direction of Mt. Ararat. On the top are shown the measurements of the near-surface electric field performed by the EFM-100 electric mills located at Aragats, Nor Amberd and Yerevan. Polarity reversal of electrostatic field change for the negative IC flash is apparent.

5. DISCUSSION AND CONCLUSIONS

We analysed TGE events abruptly terminated by the lightning discharge. The new fast electronics recently installed at Aragats allowed synchronization of particle fluxes, measurements of the near-surface electrostatic field and electric field waveforms on the millisecond time scale. By examining 13 TGE events, we have found that the atmospheric discharges that terminated the TGE at Aragats all are cloud-to-ground negative lightnings.

On 7 October 2015, ASEC particle detectors fixed a large TGE event. One-minute time series of low-threshold detectors demonstrate a huge enhancement equivalent to ~ 100 standard deviations. The differential energy spectrum of gamma rays extends till 30 MeV and more. The strong negative lightning seen as an abrupt enlarging of the near-surface electrostatic field with an amplitude of ~ 70 kV/m terminates the particle flux. On the 50 ms time scales we can see that the TGE decay started simultaneously with abrupt increase of the near-surface electrostatic field. Therefore, the initiation and termination of TGE is directly connected with rearranging of charged structures in the thundercloud, the most important of which is development and decay of the LPCR.

In (Chilinarian et al., 2016) we demonstrate that 3 electrostatic fields from the tripole structure of the electrified thundercloud contribute to the resulting field that accelerates electrons downward. The LPCR, as the nearest to the Earth positively charged layer has the biggest impact on the development of the resulting accelerating field and hence, on the TGE initiation.

We assume that the magnitude of accelerating field and hence, the particle flux intensity depend on the matureness (thickness) of LPCR. At the maximum of particle flux the LPCR is mature and thick, whereas at the beginning and at the decay phase the LPCR is thin.

12 TGEs terminated by lightning (Fig. 7) were equally distributed by 3 categories: terminated in the beginning, at maximum and on decaying phase (four TGEs in each category). It contradicts the model of the LPCR development and decay presented in (Nag and Rakov, 2009). According to their model, the negative lightning leader can penetrate LPCR only on its decaying phase. The mature LPCR do not allow the negative leader to punch throw and change it to intracloud lightning. Thus, maybe there are another players that influence the lightning initiation much more than the thickness of LPCR; i.e. the very large EAS occasionally hitting the cloud and unleashing –CG by the RB-EAS mechanism (Gurevich et al., 1999).

Based on TGE events detected on Aragats we conclude that only negative cloud-to-ground lightnings terminate TGEs and the particle flux decline starts after lightning strikes and rearrangement of the electric field in the cloud took place. Lightning can terminate TGE in the beginning, on the decaying phase or at maximum of development with equal frequencies. Only nearby lightnings (within 10 km) can terminate TGE.

REFERENCES

- Alexeenko V.V., Khaerdinov N.S. Lidvansky A.S. and Petkov V.B. 2002. Transient Variations of Secondary Cosmic Rays due to Atmospheric Electric Field and Evidence for Pre-Lightning Particle Acceleration, *Physics Letters A*, 301, 299-306.
- Chilingarian, A., Arakelyan, K., Avakyan, K.et al., 2005. Correlated measurements of secondary cosmic ray fluxes by the Aragats space-environmental center monitors, Nucl. Instrum. Methods A 543 (2–3) 483.
- Chilingarian, A., A. Daryan, K. Arakelyan, A. Hovhannisyan, B. Mailyan, L. Melkumyan, G. Hovsepyan, S. Chilingaryan, A. Reymers, and L. Vanyan L.,2010. Ground-based observations of thunderstorm-correlated fluxes of high-energy electrons, gamma rays, and neutrons, Phys. Rev. D, 82, 043009.
- Chilingarian, A., Hovsepyan, G., Hovhannisyan, A., 2011. particle bursts from thunderclouds: natural particle accelerators above our heads. Phys. Rev. D: Part. Fields 83 (6), 062001.
- Chilingarian, A., Mailyan, B., Vanyan, L., 2012. Recovering of the energy spectra of electrons and gamma rays coming from the thunderclouds. Atmos. Res. 114–115, 1–16.
- Chilingarian A., Thunderstorm Ground Enhancements - model and relation to lightning flashes, 2014. Journal of Atmospheric and Solar-Terrestrial Physics 107 68–76.
- Chilingarian, A., Chilingaryan, S., and A. Reymers, 2015. Atmospheric discharges and particle fluxes, J. Geophys. Res. Space Physics, 120, doi: 10.1002/2015JA021259.
- Chilingarian A., Hovsepyan G., Khanikyanc G., Reymers A. and Soghomonyan S., 2015. Lightning origination and thunderstorm ground enhancements terminated by the lightning flash, EPL, 110, 49001.
- Chilingarian A., Hovsepyan G., and Mantasakanyan E., 2016. Mount Aragats as a stable electron accelerator for atmospheric High-energy physics research accepted for publication in Phys. Rev. D: Part. Fields.
- Chilingarian A., Khanikyanc G., Kozliner L. and Soghomonyan S., 2016. Fast electric field waveforms and near-surface electric field images of lightning discharges detecte on Mt. Aragats in Armenia, Proceedings of TEPA 2015, Nor Amberd, Tigran Mets,
- Dwyer, J.R., Smith, D.M., Cummer, S.A., 2012. High-energy atmospheric physics: terrestrial gamma-ray flashes and related phenomena, Space Sci. Rev., 173, 133–196.
- Dwyer J.R., Uman M.A., 2013. The physics of lightning, Physics Reports Phys. Rep., 534(4), 147–241 .
- Gurevich A.V., MilikhG.M. and Rouseel-Dupre R, 1992. Runaway electron mechanism of air breakdown and preconditioning during a thunderstorm, Physics Letters A 1992, v.165, pp.463 – 468.
- Gurevich A.V., ZybinK.P, Roussel – Dupre R.A., 1999. Lightning initiation by simultaneous of runaway breakdown and cosmic ray showers, Phys.Lett. A 254, 79.
- Kuroda Y., Oguri S., Kato Y., et. al., 2016. Observation of gamma ray bursts at ground level under the thunderclouds, arXiv: 1601.06349v2 [astro-ph.HE], submitted to Physics Letters B.
- Kelley N.A., Smith D.M., Dwyer J.R., et al. 2015. Relativistic electron avalanches as a thunderstorm discharge competing with lightning, Nature communications, **6**, Article number: 7845, DOI: 10.1038/ncomms8845.
- Khaerdinov N.S., Lidvansky A.S. 2005. Cosmic rays and the electric field of thunderclouds: Evidence for acceleration of particles (runaway electrons) , Atmospheric Research 76, 346–354
- Krehbeil P., Mazur V., Rison W., Standardizing the sign convention for atmospheric electric field measurements, 2014. Newsletter on Atmospheric Electricity Vol. 25No 2, 5.
- Kollarik M., Kudela K., Langer R., Strharsky I., 2016. First results from the measuring equipment SEVAN on Lomnickýštít and possible connections with atmospheric phenomena, Proceedings of TEPA 2015, Nor Amberd, Tigran Mets.
- Nag A. and Rakov V. A., 2009. Some inferences on the role of lower positive charge region in facilitating different types of lightning Geophys. Res. Lett., 36, L05815.
- D.R. *MacGorman* and W. D. *Rust,* 1998, *Electrical Nature of Storms,* Oxford University press, Ch3, p.50.
- Pokhsraryan D, 2016. Very fast Data Acquisition system based on NI-my RIO with GPS time stamping capabilities, Proceedings of TEPA 2015, Nor Amberd, Tigran Mets,
- Soghomonyan S., Chilingarian A., Khanikyants Y, Kozliner L, 2016. Fast electric field waveforms of lightning discharges detected at the Aragats Mountain in Armenia, Proceedings of TEPA 2015, Nor Amberd, Tigran Mets.
- Tsuchiya H., Enoto T., Iwata K., et al., 2013. Detection of high-energy gamma rays from winter thunderclouds, Phys. Rev. Lett., 111, 015001.

Preliminary results of the measurements of the radiation background at Aragats and in Yerevan

E. Mnatsakanyan, R. Dallakyan

Yerevan Physics Institute, 2, Alikhanyan Brothers, 0036 Yerevan, Armenia

Abstract. The measurements of the gamma radiation background at mount Aragats and in Yerevan, by 3"x3" standard NaI ORTEC detector were performed. The measurements at fair weather conditions show that there are no differences between the forms of the radiation backgrounds at Aragats and Yerevan.

1. INTRODUCTION

The natural background radiation consists of nuclides radiation in the lithosphere, soil, water and air, and in contribution of cosmic rays and technogenic radioactive sources. The cosmic ray impact is expected to be higher on the mountains due to thinner atmosphere that allows penetration of the cosmic rays and radiation from the volcanic rocks. Radioactive nuclides can penetrate from the soil into the atmosphere, mostly radon isotopes (^{222}Rn, ^{220}Rn) and their daughter radionuclides.

Since 2009 hundreds of events of Thunderstorm ground enhancements (TGE), i.e. enhanced fluxes of electrons, gamma rays and neutrons detected by particle detectors located on the Earth's surface and related to the strong thunderstorms above, were observed by the network of particle detectors located at Aragats space-environment centre (ASEC, Chilingarian et al., 2005, 2010, 2011).

In order to measure the natural radiation background possibly influencing in the TGE observations at Aragats (3200 m above sea level) and Yerevan (1000 m above sea level) the background measurements were performed by 3"x3" standard NaI ORTEC detector.

2. MEASUREMENTS AND RESULTS

In the Fig. 1, 2 and 3 there are shown the background radiation spectrums inside the SKL experimental hall (Aragats), outside the SKL hall on territory of Aragats research station and at headquarters of Yerevan Physics Institute (YerPhI) respectively. All measurements were done during 600 s at the fair weather conditions.

In the Table 1 the total counts of the spectrums are shown.

Table 1.

Place of measurement	Total counts (600 s)
SKL building inside background, Aragats	381000±617
Outdoor background, Aragats	213000±462
22a building inside background, Yerevan	374000±612

Background radiation measurement in the SKL experimental hall was performed under the roof where five NaI(Tl) detectors of ASEC network are positioned. The gamma spectrometer was located on the concrete layer just below the roof. In the Fig. 1 we show the gamma lines of

identified radionuclides of Uranium (^{214}Pb (352 keV) and ^{214}Bi (768; 1120; 1764 keV)), Thorium (^{208}Tl (583; 2614 keV) and ^{228}Ac (911; 969 keV)) series and potassium ^{40}K (1460 keV).
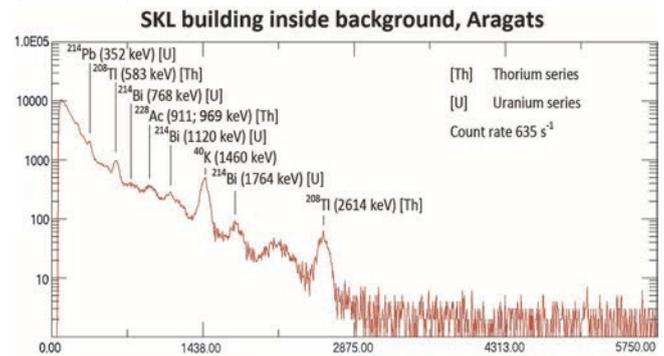
Figure 1. The background spectrum measured inside the SKL building.
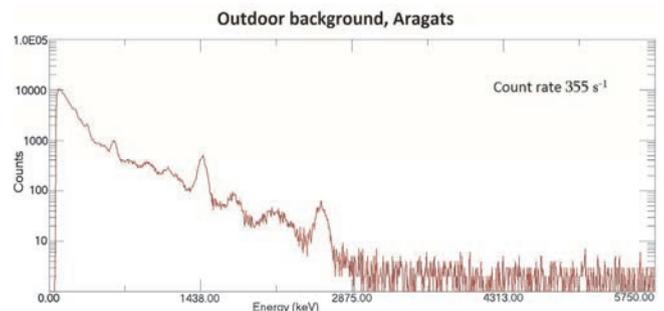
Figure 2. The background spectrum measured outside the SKL building.
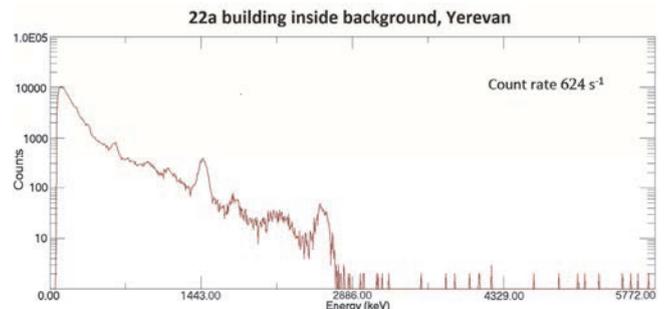
Figure 3. The background spectrum measured in Yerevan.

For the identification of radionuclides the gamma lines of ^{40}K (1460 keV) and ^{208}Tl (2614 keV) were used. For an additional calibration and testing of the energetic resolution of the spectrometer the gamma line of ^{137}Cs isotope (662 keV) was used. The extracted spectrum of ^{137}Cs is shown in Fig. 4. The energetic resolution of 3"x 3" standard NaI ORTEC spectrometer was 100%*FWHM/(Photo-peak en-

ergy) = 7.6 ±1.5 % (Full Width at Half Maximum of photopeak) at 662 keV when the background is extracted from ^{137}Cs spectrum. The total counts of the extracted spectrum was 2200000±1483 during 600 s.
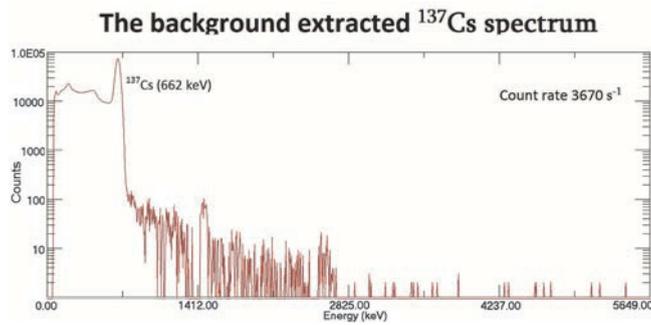
Figure 4. The background extracted spectrum of the ^{137}Cs isotope.

As it shown in the Table 1 total counts of inside the building is about two-fold higher than outdoor, which can be explained by the accumulation of radon gas (^{222}Rn, ^{220}Rn and their daughter radioactive nuclides) in the building and also by the contamination of radionuclides in the construction materials of the building. The measurements in Yerevan were performed by positioning spectrometer on the concrete layer in the building 22a of YerPhI (Fig. 3) for comparison with high-mountain results at Aragats.

3. CONCLUSION

The radiation background measurements were shown that they are gamma lines of radioactive nuclides of Uranium, Thorium series and ^{40}K in the spectrum.

The largest peak was the peak of ^{40}K (1460 keV) and the next one was the peak of ^{208}Tl (583 keV).

The total counts differences between Aragats inside and outdoor spectrums can be explained by the accumulation of radon gas (^{222}Rn, ^{220}Rn and their daughter radioactive nuclides) in the building and also by the contamination of the radionuclides of the constriction materials.

The measurements show that there are no special differences between the forms of the radiation background at Aragats and Yerevan.

More detailed measurements are provisioned during this year to find out the influence of different weather conditions on the local radiation background.

REFERENCES

- Chilingarian, A., Arakelyan, K., Avakyan, K.et al., 2005. Correlated measurements of secondary cosmic ray fluxes by the Aragats space-environmental center monitors, Nucl. Instrum. Methods A 543 (2–3) 483.
- Chilingarian, A., A. Daryan, K. Arakelyan, A. Hovhannisyan, B. Mailyan, L. Melkumyan, G. Hovsepyan, S. Chilingaryan, A. Reymers, and L. Vanyan L.,2010. Ground-based observations of thunderstorm-correlated fluxes of high-energy electrons, gamma rays, and neutrons, Phys. Rev. D, 82, 043009.
- Chilingarian, A., Hovsepyan, G., Hovhannisyan, A., 2011. Particle bursts from thunderclouds: natural particle accelerators above our heads. Phys. Rev. D: Part. Fields 83 (6), 062001.

Observation of TGFs and Relativistic Electron Precipitation in RELEC experiment on-board Vernov Mission

M.I. Panasyuk, S.I. Svertilov, V.V. Bogomolov, G.K. Garipov, E.A. A.V. Bogomolov, I.N. Myagkova, P.A. Klimov, A.V. Prokhorov[1]; S.I. Klimov, T.V. Grechko, V.A. Grushin, D.I. Vavilov[2]; V.E. Korepanov, S.V. Belyaev, A.N. Demidov[3]; Cs. Ferencz[4]; L. Bodnár, P. Szegedi[5]; H. Rothkaehl, M. Moravski[6];

1. Physics Department, D.V. Skobeltsyn Institute of Nuclear Physics, M.V. Lomonosov Moscow State University, Moscow, Russian Federation;

2. Space Research Institute, Russian Academy of Science, Moscow, Russian Federation;

3. Institute of Space Research, Ukrainian Academy of Science and National Space Agency, Lviv, Ukraina;

4. Eötvös University, Budapest, Hungary;

5. BL Electronics Ltd., Solymár, Hungary;

6. Space Research Centrum, Poland Academy of Science, Warsaw, Poland

Abstract. Experiment "RELEC" on-board satellite Vernov, launched July 2014, contains a suite of scientific instruments including gamma-spectrometer (0.01-3.0 MeV), spectrometer of electrons (0.2-15.0 MeV), UV (300-400 nm) and opticsl (600--800 nm) photometer and imager, radio wave low frequency (0.001 - 40.0 kHz) and high frequency (0.05 - 15.0 MHz) analyzers.

Gamma and electron spectrometers were used to study transient events, including terrestrial gamma-flashes (TGFs) and precipitations of relativistic electrons from the Earth magnetosphere with ~15 mcs time resolution. Comparative correlating analysis of the data taken by the on-board instruments were made.

First catalogue of TGFs detected by "RELEC" during is presented. Events that are included in this catalogue were selected by criterion of having at least 5 gamma-quanta during the time interval of 1 ms, simultaneously in at least two gamma-spectrometer detectors. TGFs included in this catalogue have a typical duration of about 400 microseconds, and in total contain from 10 to 40 gamma-quanta. For each selected for catalogue TGF candidate, we will show light curve and a correlating data of other instruments of "RELEC" on-board Vernov satellite.

Results of observations of trapped, quasi-trapped and precipitated electron flux and spectral variations in different areas in the near-Earth space including low L-shells in wide dynamical range from ~1 up to 104 part/cm2s are discussed in this report.

1. INTRODUCTION

The Atmospheric Transient Energetic Phenomena, such as Terrestrial Gamma Flashes (TGF) and Transient Luminous Events (TLE) are the main subject of scientific research in the RELEC experiment onboard the Vernov spacecraft.

TGFs and TLEs are observed both in stratosphere and mesosphere, i.e. at the source altitude from about 12 km up to a few dozen kilometers (Cummer et al, 2014). They are accompanied by short rising electron fluxes and electromagnetic radiation bursts in very wide bands from radio to gamma including optical ranging from ultraviolet to red.

The optical phenomena known as sprites, elves and blue jets are TLEs. The characteristics of TLEs including spatial and temporal structure, rate of occurrence and optical brightness in different ranges are found, for ex., In Vaughan and Vonnegut, 1989; Fischer, 1990; Lyons, 1994.

The intensive atmospheric X-ray and gamma-ray bursts were detected from space experiments in thunderstorm areas (Fishman, 1994; Nemiroff et al., 1997).

TGFs and TLEs might be the consequence of physical processes resulting from a different kind of high-energy release during short time intervals (from 10^{-6} to 10^{-3} seconds).

Despite more than 20 years of experimental and theoretical research, there are no clear interpretations of such phenomena. The runaway electron breakdown (REB), predicted in 1992 and studied theoretically in details (Gurevich et al., 1992; Dwyer et al., 2012), becomes of great interest. High-energy cosmic rays could play a principal role in the evolution of such breakdown (Gurevich et al., 2004). Auger showers (or Extensive Air Showers – EAS) generated by such cosmic rays contain a huge amount of high-energy electrons to be seeds of REB.

The simultaneous observation of radio, optical and gamma flashes as well as direct electron detection from the propagated from the thunderstorm electron-gamma ray avalanche will be the direct confirmation of the theory of runaway electron breakdown and the mechanism altitude discharges initiated by strong electric fields in the thunderstorm atmosphere.

The thunderstorm activity can produce the upward travelling beams of relativistic runaway electrons at the altitudes 60-80 km (Bell, 1995; Lehtinen 1997). Electrons with energies of E ~ 1 MeV and above are able to penetrate to the Earth's magnetosphere and fed to radiation belts. According to (Lehtinen et al., 2000), high-altitude discharges with REB can be one of the inner radiation belt sources. Such electrons can produce long (about 20-30 ms) signals in gamma ray detectors. However, attempts of direct measurements of runaway electrons by means of large area electron detector onboard Tatiana-2 satellite did not show any tangible results (Sadovnichy et al., 2011).

Relativistic electrons seeding the altitude discharges in the mesosphere may fall in thunderstorm area from space, for example, by precipitation from the Earth's radiation belts

(referred to as "up-down" model in contrast to the "down-up" model which describes the runaway electron avalanche spreading). Indeed, electron flux transients increasing at the lower edge of inner radiation belts and beneath the belts were observed in a number of experiments (for instance, see Nagata et al., 1988; Bogomolov et al., 2005).

If precipitation electrons generated TGFs or TLEs in the upper atmosphere, the influence of geomagnetic activity on the TGFs and TLEs generation in the mesosphere should be taken into account. The study of such influences on TGFs and TLEs is one of the main objectives in the RELEC project.

The dynamics of relativistic electrons in the Earth's radiation belt can be regarded as a separate physical problem that includes electron acceleration, drift and loss processes caused by pitch-angle diffusion and their local acceleration (for instance, see (Shprits et al., 2008a; Shpritz et al., 2008b)). Relativistic electron fluxes are now detected by satellites at high-apogee (Van Allen Probes, GPS and Glonass), at the geostationary orbit (GOES and electro) and at the low-altitude satellites (POES, Meteor). Measurements from the Vernov satellite complement these experiments for the study of relativistic electrons in the Earth's radiation belt.

The Vernov instrument parameters and the first results are presented in this paper.

2. INSTRUMENTATION
2.1. VERNOV SPACECRAFT

The scientific instruments complex of RELEC (acronym **R**elativistic **ELEC**trons) was developed and manufactured as a component of the small Vernov spacecraft (Khartov, 2011), which was named in honor of academician Sergey Nikolaevich Vernov, one of the founders of Russian space program The spacecraft was manufactured by the S.A. Lavochkin space corporation. Technical parameters of the spacecraft are following:

mass – 283 kg;

orientation accuracy – 6 angular minutes;

stabilisation accuracy – 0.0015^{o}/s;

data rate – 5 Mbit/s.

satellite orbit - solar-synchronous with apogee of

830 km, perigee of 640 km, inclination of 98.4^{o}, and

period of 100 min.

The main operational mode is the observation with all instruments operating simultaneously. The nominal data transfer to the Earth is about 1.2 GB/day. The satellite was launched on July 8, 2014.

2.2. SCIENTIFIC INSTRUMENTS

The onboard instruments the DRGE, DUV, MTEL (Telescope-T), low-frequency analyzer (LFA or NChA), radio frequency analyzer (RFA or RChA) and the electronic unit (BE) provide measurements of high-energy electron flux with high time resolution (~15 mcs in event by event mode) and anisotropy of flux, TEP detection in wide range of electromagnetic spectrum from radio to gamma with time resolution of ~15 μs,

and electric and magnetic field measurements in the frequency band from 0.1 Hz up to 15 MHz. All instruments are connected with electronic unit BE (see Fig. 1) which controls and powers the instruments and collects data from them.

The DRGE instrument is designed for flux and spectral measurements of X rays and gamma rays with energy values of $E = 0.01$-3.0 MeV, electrons with energy $E = 0.2$-15 MeV and protons with energy $E = 4$-100 MeV.

The instrument consists of three units: two identical units DRGE-1, DRGE-2 and unit DRGE-3. Physical and technical parameters of these instruments are presented in Table 1. All instrument units include detectors, electronics, frames and fixing elements. The instrument units are connected with BE as depicted in Fig. 1.

Each of DRGE-1and DRGE-2 units contains two identical detector blocks including a NaI(Tl)/CsI(Tl) phoswich read out by a photomultiplier tube (PMT). The diameter of both scintillators is 13cm, while the NaI(Tl) thickness is 0.3 cm, and the CsI(Tl) thickness 1.7 cm. An The 11 cm diameter Hammamatsu R877 PMT faces both scintillators. Electronic signals from the PMT are digitized and processed by special electronic circuitry. The axes of the DRGE-1 and DRHE-2 detectors are directed toward to the local nadir with a $\pm3^{o}$ accuracy.

The NaI(Tl) is placed on top of the CsI(Tl) crystal, both crystals seen by one PMT. In this way, the NaI(Tl) serves as the main detector for hard X-ray timing while the CsI(Tl) is used as an active shield against background gammas, and it can also detect gammas with energy up to few MeV.

DRGE-3 unit contains three identical detector blocks, whose axes are directed was follows: the DRGE-31 detector axis faces the local zenith, the DRGE-32 axis is principally directed against the satellite velocity vector, and the DRGE-33 axis is directed normal to the plane formed by the two other detectors axes. The orientation accuracy for the each of all three axes is $\pm3^{o}$.

Each DRGE-3 detector consists of the phoswich of a CsI(Tl)/BGO with a 0.3 cm thick CsI(Tl) and a 1.7 cm thick BGO. The diameter of both scintillators is 1.5 cm. The cylindrical copper collimator has a height of 1.0 cm and a 0.1 cm thickness arranged above the CsI(Tl) crystal. This collimator limits the FOV of the detector. The whole package is covered by an anticoincidence cup which consists of a 0.5 cm thick plastic scintillator. All scintillators are viewed by a single PMT. The input window of the CsI(Tl) crystal is closed off by100 μm thick Aluminum foil, which protects the scintillator crystals from light and absorbs electrons with energies of less than 0.2 MeV and protons and nuclei with energies of less than ~5 MeV/nucleon. The CsI(Tl)/BGO phoswich detector is also sensitive to X-rays and gamma-rays of energy of 0.05-3.0 MeV. Electrons, protons and gammas are separated by measuring energy release in each scintillator.
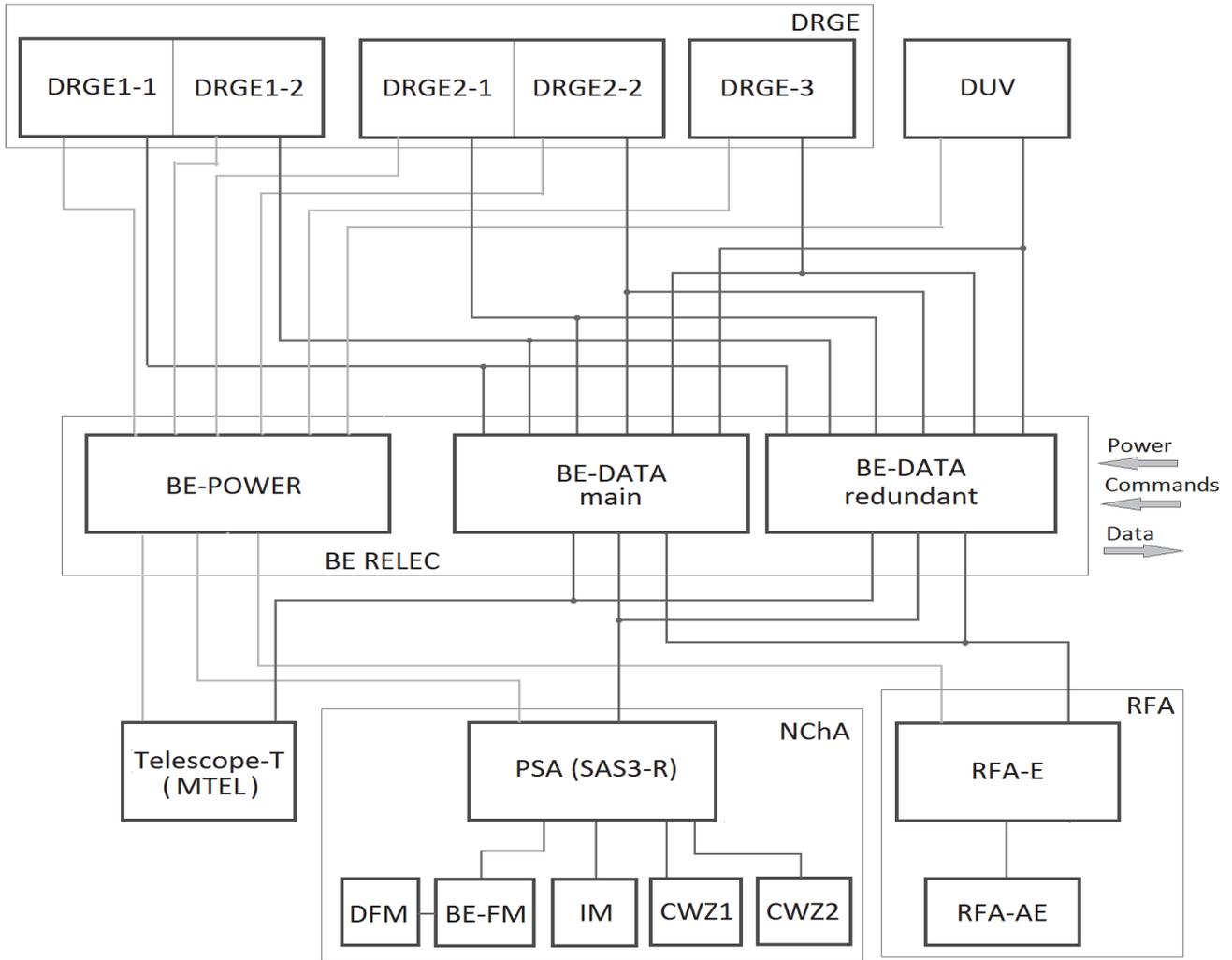
Figure 1. Wiring diagram of the instruments onboard Vernov satellite.

Table. 1.

	DRGE-1(2)	DRGE-3	Total

Energy range
  photons
  electrons
  protons
	0.01-3 MeV
	0.5-10 MeV
	10-100 MeV
		0.05-3 MeV
		0.2-15 MeV
		5-100 MeV	

Detector effective area	$4\times120=480$ cm^2 (for 4 detectors)	2.5 cm^2	
Field of view	2π sr ($\pm90^o$)	1.2 sr ($\pm60^o$)	
Mass	~10.4 kg (for each unit)	~2.8 kg	~23.6 kg
Size	$0.36\times0.36\times0.18$ m^3	$0.23\times0.3\times0.18$ m^3	
Data volume	~150 MByte/day	~70 MByte/day	~370 MByte/day
Power consumption	~9 W (for each unit)	~7 W	~25 W

The output off all DRGE detector units is recorded continuously. There are two types of data frames, both transferred to the Earth:

- Monitoring frame, containing the number of events in the NaI(Tl) or CsI(Tl) for exposure time equal the time passed from previous frame (usually 1 s);
- Event frame, containing the digital record of energy release amplitudes in the NaI(Tl) or CsI(Tl) on the basis of gamma by gamma, a ~15 μs timing accuracy for each event occurred during time equal the time passed from previous frame (usually 1 s). The number of events recorded in frame is

limited by 800 in the case of total count less than 10^3 s^{-1}, and 200 if the total count is higher 10^3 s^{-1}.

The DUV instrument is a monoblock unit consisting of two PMTs of R1463 type with 13 mm input window diameter, electronics boards and support structures. The instrument is $130\times95\times65$ mm in size and 0.7 kg in mass Power consumption with input voltage of 27 V is less than 2.5 W. The input windows of each PMT are closed by special filters, each of 2.5 mm thickness. The filter on one PMT is transparent in UV range (~240-400 nm), and the filter on the other PMT is transparent in red and infrared range (610-800 nm). Long-wavelength limit is determined

by PMT sensitivity. The part of infrared photons, which can penetrate UV filter, is not more than 2%.

The Telescope-T (MTEL) instrument is able to detect fine structures of atmospheric afterglow in space-time for UV (300-400 nm) and red (600-700 nm) ranges. It is a monoblock unit, consisting of two micro-electro-mechanical systems (MEMS) micromirrors, two 64 channel multi-anode PMTs (Hamamatsu H7546A) and electronics (B.W. Yoo et al., 2009). The size and mass of the instrument is 500×123×77mm and 3.9 kg, respectively. The power consumption at the input voltage of 27 V is not larger than 8.0 W. There are two optical systems with different focal length; one is the trigger optics with shorter focal length and thus wide FOV, and the other is the zooming optics with longer focal length equipped with MEMS which allows the fast steering of the interesting image onto the corresponding PMT (J.H. Park et al., 2008).. The rotational speed of two axes micromirror is 10^{-1} μs^{-1}. The field of view of the trigger and the zooming optics are 11.3° and 2.9°, respectively. The viewing area of MTEL is about 160x160 km^2, i.e. one pixel area is 20x20 km^2 for observations from ~1000 km altitude (J. Lee et al., 2012)..

The axes of both DUV and Telescope-T instruments are directed to the nadir with accuracy of $\pm 3^{\circ}$.

The complex of low-frequency (LFA or NChA) and radio-frequency (RFA or RChA) analyzers is intended to measure electromagnetic wave components and plasma current with wide frequency range. The instrument units are placed both on the special boom and on the thermostat panel. All units have no resonance frequencies below40 kHz.

The LFA instrument consists of 6 units including three-component fluxgate magnetometer DFM and its electronic unit BE-FM, induction magnetometer IM, two identical electrometers or complex wave probes CWZ-1, CWZ-2 and complex signal spectral analyzing processor PSA(SAS3-R). Fluxgate magnetometer provides measurements of constant magnetic field with intensity not less than 64000 nT. Component non-orthogonality is measured to be not large than 1°. The digitization frequency is 250 Hz. Mutual orthogonality of three measuring axes is provided by DFM unit configuration. Values and sign of three components of alternating magnetic field induction vector are measured by induction magnetometer IM and CWZ-1, 2 probes. The frequency range is from 0.1 Hz to 40 kHz. The CWZ-1, 2 probes are also able to measure plasma current density. Parameters of low-frequency analyzer units are presented in Table 2.

Table 2

Unit	Size (mm)	Mass (kg)	Consumption (W)
DFM	Ø(40±0.3)x62	0.13	< 0.1
BE-FM	148.4x85x40	0.30	< 0.25
CWZ-1, CWZ-2	Ø(64±0.3)x(325±0.8)	0.40	< 0.25
IM	Ø(24±0,3)x212	0.15	< 0.1
PSA (SAS3-R)	150x200x40	1.10	< 5

The RFA instrument consists of electronic unit RFA-E and antenna RFA-AE, which is able to measure three electric field components of electromagnetic wave in the range from 50 kHz to 15 MHz. The frequency resolution of the

instrument is 10 kHz and the time resolution is 25 ns. The size of RFA unit is 192x149x91.5 mm^3, and mass is 1.5 kg, while the size of the antenna unit RFA-AE is 54x26x66 mm, and mass is 0.2 kg. The total instrument power consumption is about 10 W.

The BE instrument provides power supply, command inputs and high accuracy time pulses on all instruments as well as scientific and telemetry data collected from the instruments and its transfer to the satellite onboard systems in daily volume about 1.2 GByte. It consists of three boxes: one box of power controller (BE-POWER or KPP) and two identical boxes of data controllers, the main (BE-DATA main or KTzImain) and the redundant (BE-DATA redundant or KTzIred).

3. RESULTS OF TGFS OBSERVATION

3.1. TERRESTRIAL GAMMA-RAY FLASHES

The DRGE-1 and DRGE-2 large area detectors with axes directed toward the Earth are the main instruments for TGFs observations during the operation of RELEC in space. To the extent that the TGFs are very short (<0.5 ms), the "gamma by gamma" data taking mode was chiefly used for their selection. The time of each gamma-quantum detection as well as the amplitude determining the energy release in each part of the detector (NaI(Tl) or CsI(Tl)) was recorded for every detected gamma-quantum in this mode. The energy threshold is about 10 keV for NaI(Tl) and about 25 keV for CsI(Tl).

Due to the limited volume of data transfer the number of recorded events in a row is restricted such that not more than 800 events per second in one detector can be recorded in the case of low background count (<1000 pulses/s in both crystals). If background is over 1000 pulses/s or 1500 pulses/s, then not more than first 200 events or 50 events, respectively, can be recorded consequently event by event for every second. In the near-equatorial regions, the total background in both crystals of each of the detector was less, than 800 pulses/s, so data on all detected gammas was stored. In the polar cap regions, the background exceeded 1000 pulse/s, and only one fifth of the events detected per second was stored. Thus, in the near-equatorial regions, gammas were detected without losses, which is very favorable for a TGF search, because these events are observed mainly in equatorial thunderstorm regions.

At the background on average near the equator not more than 1 noise event is detected every few milliseconds. Consequently, the trigger was chosen to have simultaneous detection of more than 5 gammas/ms by two detectors and 3 or more gammas by three detectors. Because the majority of TGFs have a rather hard energy spectrum, only events with energy release over 500 keV inside both sccintillators were triggered for selection. Besides, an additional condition was utilized in order to lower the trigger rate caused by charged particles background in the trapped radiation areas. This condition limits average background per second before firing trigger to 1 kHz.

The huge number of events was chosen which satisfied the trigger criterion. However, the most events were caused by cosmic rays, particularly heavy charge particles, passing through the scintillation crystals. Such events can be selected effectively from the "energy-time" diagrams which reflect the energy release values pointed againstthe time of detection. Events originated by heavy charged particles

have a typical form of very high energy release at the beginning and exponential decay because of large ionization taking place in the scintillators.
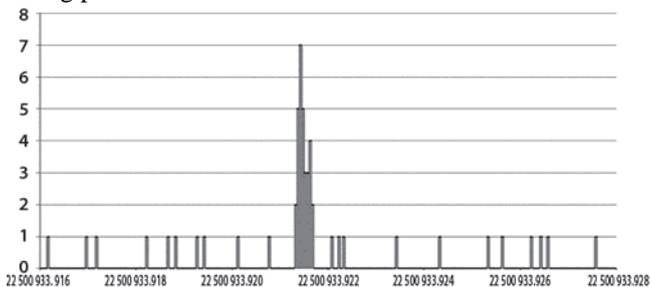

Figure 2. Time profile of TGF candidate detected on 18.09.2014.

The sample of TGF candidates is selected after excluding events caused by heavy charged particles. During the observation period from July 20 to December 10, 2014, five TGF candidates were found. The times of their detection were 08.08.2014 22:20:55 UTC, 08.08.2014 00:31:07 UTC, 16.08.2014 13:06:55 UTC, 18.09.2014 10:15:34 UTC, and 02.11.2014 03:34:14 UTC. The most intensive flare was detected on 18.09.2014. The time profile of this event is shown in Fig. 2, and the area of the source location is presented in Fig. 3. The area circle diameter is about 5000 km. As can be seen in the figure, this event was detected in the western part of the Pacific Ocean in the vicinity of active thunderstorm regions.
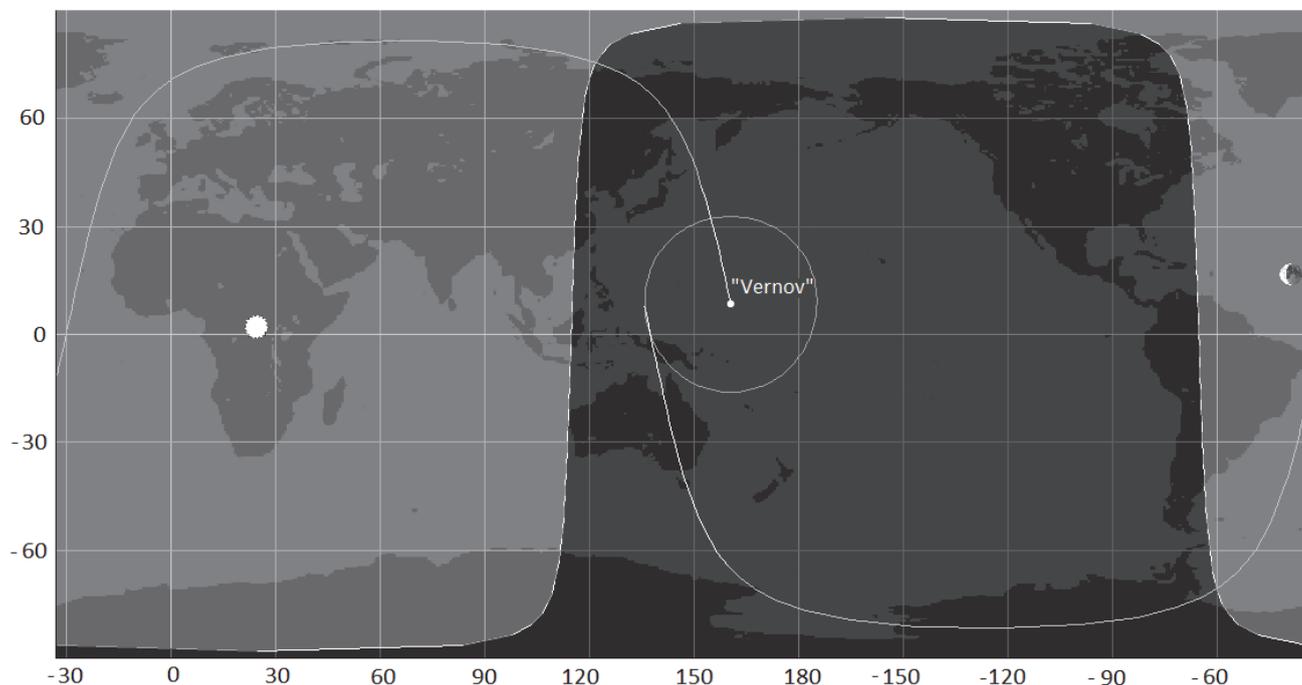

Figure 3. The location area of TGF candidate detected on 18.09.2014. It is a circle around the sub-satellite point in the detecting time. The circle diameter corresponds to the detector FOV. The satellite orbit as well as light and shadow areas, and the Sun and Moon projections are also marked according to Orbitron (http://www.stoff.pl/).

The total time for which TGF candidates were selected according to the trigger criterion, was 256.5 hours, or 10.7 days. Therefore the TGF detection rate is about 15 events per month, or one flash every few days. This rate is of the same order as estimated from RHESSI (Grefenstette et al., 2009), AGILE (Fuschino et al., 2011) and Fermi GBM (Briggs, 2013) trigger data, but more than an order less than the value obtained for Fermi non-triggered events (Briggs, 2011). It is conjectured that Fermi non-triggered events are on average low-intensity and thus more numerous.

Although TGF candidates were observed in the regions of rather high electromagnetic activity, there is no indication of these TGF candidates accompanied by short (i.e. comparable with typical TGF duration) events both in low and high frequency bands which could be caused by lightning. Additionally, no coincidences of TGF candidates with WWLLN events were found. However, these results are possibly explained by the low efficiency of WWLLN as well as poor TGF statistics in the RELEC experiment.

4. RESULTS OF ELECTRON FLUX MEASUREMENTS

Detector unit DRGE-3 is the main instrument for high-energy electron detection. Electrons can be detected also indirectly by gamma detectors DRGE-1 and DRGE-2 via Bremsstrahlung. An example of electron flux measurement is presented in Fig. 4, where the profiles of electron counts in DRGE-3 channels versus L-shell number $N(L)$ are plotted. The dotted lines indicate the counts in the detector unit with its axis directed to the local zenith (i.e. along the magnetic field lines at high latitudes), while the solid lines (black and gray) correspond to the counts in detector units whose axes are predominantly normal to the magnetic field line at high latitudes. This means that for relatively high latitudes (L>1.5) the thin lines indicate the $N(L)$ dependences of electrons with pitch-angles of ~0° (i.e. precipitated), and thick lines represent $N(L)$ for electrons with pitch-angles ~90° (i.e. trapped or quasi-trapped).

The data presented refer to the magnetic-quiet time interval of September 5, 2014 15.30-18.50 UT, with the following interplanetary parameters: $Kp < 2$, $Dst > -8$ nT, $AE < 550$ nT, solar wind velocity< 375 km/s, $Bz > -5$ nT. A magnetic storm with $Dst = -80$ nT occurred on August 27, 2014, however, it ended on the first of September, 2014.

Fig. 4 shows the electron data for three consecutive satellite orbits in the Southern Hemisphere for the longitudes of ~ 112°, 135°, and 157° W at $L = 2.5$. Each subsequent orbit, top down in Fig. 6, moves further away from

the South Atlantic Anomaly (SAA) and magnetic field increases for each subsequent orbit.

The lower edge of outer radiation belt at $L \sim 3.5$ and adjacent gap are shown in the figure for all profiles. The inner belt with electron flux intensity maxima at $L \sim 1.5\text{-}1.6$ is also seen for all orbits. As distance SAA increases inner belt peak narrows and its intensity decreases. The intermediate structure at $L \sim 2\text{-}3$ with maximum at $L \sim 2.4\text{-}2.6$ is revealed in the gap between the inner and outer belts. This structure is rather stable because it was observed on all presented orbits and occurred not less than 300 min, i.e. observed on the subsequent orbits. At the inner belt it becomes narrower and less intensive as distant from SAA. Moreover, unlike the inner belt, it is shifted gradually to the higher L. Perhaps, it is caused by magnetic and electric field pulsations.

*Figure 4. The space-time variation of counting rates $N(s^{-1})$ for electrons with energy E = 235-300 keV (left panel) and E = 400-570 keV (right panel) at $L \sim 1.3\text{-}3.8$ for three (a, b, c) consecutive orbits of the Vernov satellite in the Southern Hemisphere to the right of SAA. In order to obtain electron fluxes, N values should be divided by the instrument geometry factor (see Table 1). Dotted lines indicate the counting rate in the detector with axis directed to the local zenith, solid black lines in the detector with axis directed against the satellite velocity , and solid gray lines in the detector with axis normal to previous ones.*

The smaller structures are also observed at $L \sim 1.7\text{-}2.2$. These are revealed more clearly in the 235-300 keV channel on the second orbit. Unlike the inner belt and structure at $L \sim 2\text{-}3$ these structures are non-regular, short-time effects. Possibly, they are caused by natural electromagnetic field pulsations (thunderstorms, seismic) or artificially (power radio transmitters) as well as by equatorial electrojet field pulsations.

During the electron flux measurements onboard the Van Allen Probe satellites, it was indicated that the background of the inner belt protons penetrated through the instrument side shield was very high (Li et al., 2015). Thus, electron fluxes at $L < 2.5$ were too high (on 3-5 orders of magnitude) and isotropy on the data from this experiment. In (Li et al., 2015) significant overestimation of electron fluxes at $L < 2.5$ was also indicated for the AE-8 & AE-9 models, whereas AP-8 & AP-9 models are in good agreement with newest experiments at all L.

Electron fluxes at $L < 2.5$ were obtained from the DE-METER and REPTile satellite data only for the SAA region. The orbits of these satellites were similar to those off the Vernov probe. From these measurements only background levels were obtained for electron fluxes at $L < 2.5$ outside SAA (for instance, see (Li et al., 2015)).

Geometry factors of the RELEC electron detectors were significantly larger than the ones of Van Allen Probes, DEMETER and REPTile satellites. Besides, using a combination of anti-coincidence shield and phoswich detectors removes fake counts in electron channels caused by proton background. As a result, significant electron fluxes were detected at $L < 2.5$ outside of the SAA. They are a few orders lower than proton fluxes according to the AP-8 model.

Fluxes of electrons with $E \sim 300\text{-}600$ keV at $L < 2.5$ recover very slowly over dozens of days. Thus, we were unable to exclude that the local structures of such electrons at $L < 2.5$ given in Fig. 4 could have been formed during the magnetic storm of August 27, 2014.

5. RESULTS OF ELECTROMAGNETIC WAVE MEASUREMENTS

The complex of LFA-RFA (or NChA-RChA) instruments onboard the Vernov satellite provides the physical study in the following:

- Electric and magnetic field spectral analysis in the extremely low, very low and high frequency bands in different helio- and geomagnetic conditions;
- Detection and analysis of electromagnetic events called spherics or whistlers, which are generated in thunderstorm discharges in the VLF band;
- Analysis of the relationship of electromagnetic phenomena in ELF-VLF-HF bands in different regions of the near-Earth space by comparing with synchronous wave measurements at spacecraft and ground-based stations;
- Space weather monitoring in order to refine its prediction taking into account impacts from the top (i.e. from space) as well as perturbations coming from the bottom, of both natural (earthquakes, typhoons, tsunamis etc) and artificial origin (explosions, man-made disasters etc).

So far only the database of spectra and detailed signal shapes (time-functions) measured by the LFA - SAS3-R

instruments is available. Each spectrum in this database gives the averaged values for 6.5 s of electric field **E** and three orthogonal components of magnetic field: **Bx**, **By**, **Bz**.

Measurements with higher temporal resolution, called wave-form mode, were also made for a number of time intervals. One of the interesting examples of such measurements will be discussed below.

The LFA instruments worked in the wave-form mode on December 10, 2014 from 08:54:50.0 to 08:57:10.3 UTC (140 s) in the range of 0.1 – 39062.5 Hz, channels CH0 (**E** – electric field tension) and CH3 (**Bx**-component of magnetic field tension).

The Vernov satellite orbit for this time is shown in Fig. 5.

The **E** and **Bx** signal wave-forms, dynamic spectrograms and spectra averaged for the total time of observation are presented in Fig. 6 for the time interval marked in Fig. 5. The wave-form of **E** indicates that anthropogenic disturbances with 1 Hz frequency does not lead signal to any high level due to the amplitude high dynamic range (~ 120 dB). Such a disturbance was not observed clearly in **Bx** signal.
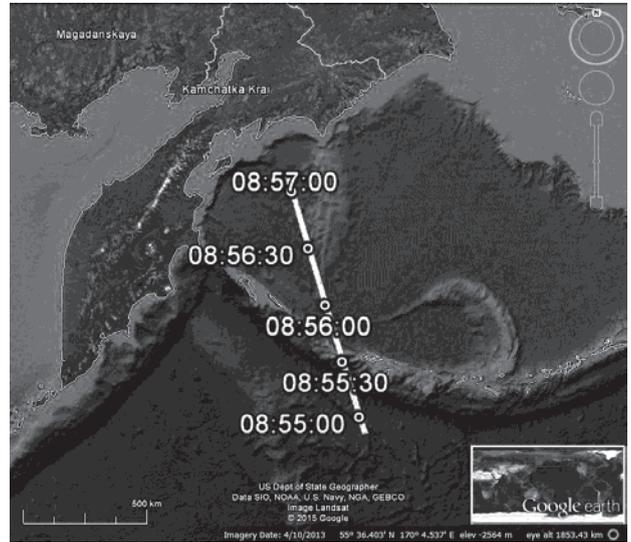
Figure 5. The Vernov satellite orbit on December 10, 2014 from 08:54:50.0 till 08:57:10.3 UTC. Altitude ~ 670 km, local time ~ 21:10 LT, magnetic latitude ~ 75⁰.
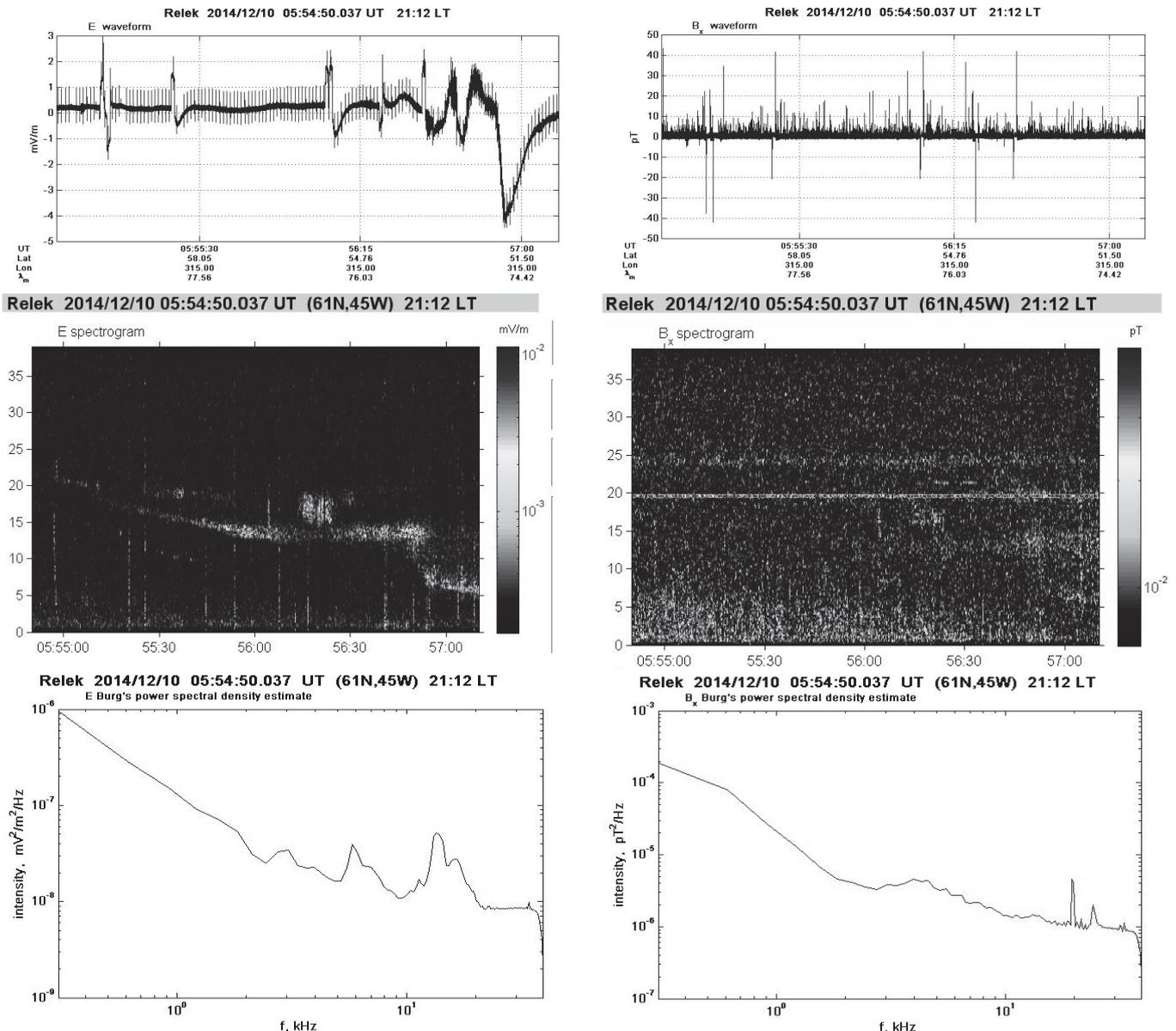

Figure 6. LFA (or NChA) instrument data. Left panel is E, right panel – Bx. Top down: wave forms, dynamic spectrograms, and frequency spectra averaged for the total observation time interval. Time scales (UTC – 3 h) of wave forms and dynamic spectra are synchronous.

87

Dynamic cyclograms, mainly *E*, indicate the satellite crossing over geographic regions with different kinds of wave activity. Accurate identification requires additional data about thermal plasma concentration and low energy (about 10 keV) particle spectra. Using the data on satellite geomagnetic coordinates suggests that revealed areas are in the night sector of the main ionosphere laydown and longitudinal current regions.

The presence of three band-pass frequencies in the *E* spectrum may be caused by 2- or, possibly, 3-wave decay from ~ 20 kHz on ~ 18, ~ 15 and 11 kHz, which is more pronounced in the dynamical spectrogram in the dedicated range of frequencies, as shown in Fig. 6. Separation of this range into two structures at 08:56:20 UTC also could be seen. These structures have a size about of 30 km and both band-pass 15017 kHz and narrow band ~13 kHz emissions are observed in *E.*

Transformation of *E* frequencies is also observed at the end of observation time interval ~ 08:56:50 – 08:57:05 UTC, when a frequency jump from ~ 13 to ~ 6 kHz took place.

Component *Bx* changed considerably less, than *E* on this orbit. The narrow band emission was observed constantly in this component at ~19 kHz as in dynamic as in averaged spectra. Probably this emission was generated by navigation transmitters.

The "large-scale" analysis made above indicates the detection of geophysical processes by means of LFA instrument that allows turning to the small-scale processes.

Emission near ~5 kHz with increasing frequency can be seen clearly in the right part of Fig. 6 left panels. The details of this process are presented in Fig. 7, in which as in Fig. 6 after "noise cloud" at 6-23 kHz on time scale ~ 1 s (Fig. 7a) signal with increasing frequency 6 – 7 kHz (Fig. 10b) is observed on time scale ~ 0.4 s (Fig. 7c). Here frequency parameters of this signal are similar to the long time Aurora emission of the choir type. Possibly, due to the satellite quick motion under the emission region only one choir emission element was detected. However, the strict linear increase of the emission frequency (Fig. 9c) provides a reason to consider this signal as technogenic from other scientific instruments.
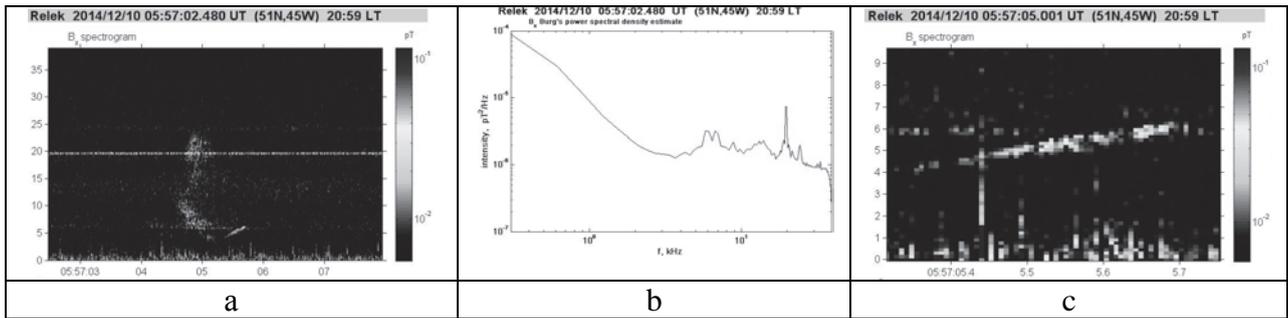

Figure 7. Dynamic spectrogram on time scale ~ 1 s (a), frequency spectrum (b), dynamic spectrogram on time scale ~ 0.4 s (c) for time interval December 14, 2014, 08:57:02 – 08:57:08 UTC.

It is noted that events presented in Fig. 8 also clearly show the well-known geophysical emissions of spheric or electron whistler type, which were detected both in *E* (Fig. 8a), and in *Bx* (Fig. 8b). However, in the Fig. 8 records simultaneously with the "normal" electron whistlers some interesting, co-existing and strange signal parts appeared too, below and above 20 kHz. The whistler-group propagating at the satellite with whistlers having slightly different dispersions also generated some yet unanswered questions about the propagation mechanism.
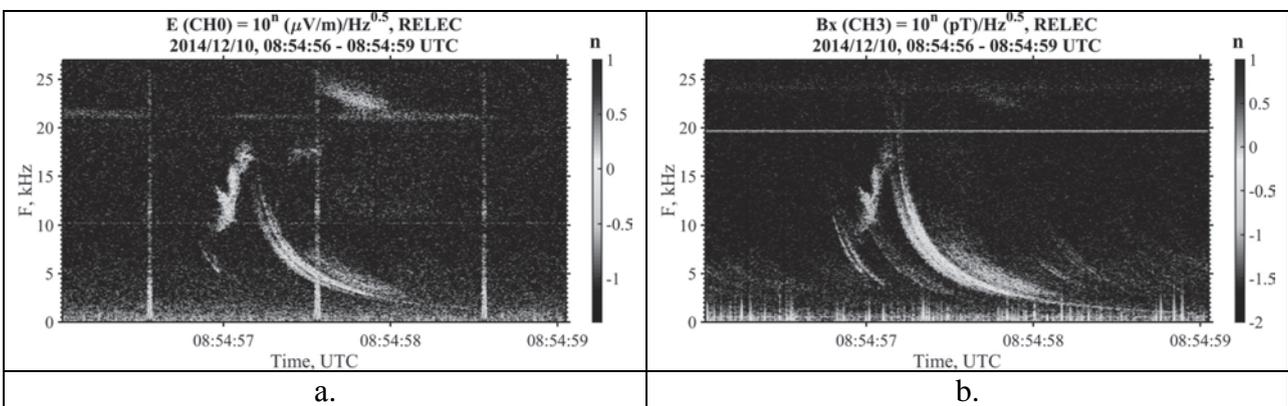
Figure 8. Examples of electron whistler detection.

As is seen from Fig. 6, a noteworthy specific rare emission was detected at 08:54:57. This is the same event that was detected first from the Chibis M microsatellite and called "dovetail" (Klimov et al., 2014).

6. CONCLUSION

Several candidates of TGFs were detected from the RELEC/*Vernov* gamma-detectors.

A new phenomenon previously discovered from the experiment onboard the Universitetski-Tatiana-2 satellite, i.e. the series of UV flashes, was confirmed by the optical detectors, especially by the DUV instrument. These series of UV flashes connection with radiation from lightning bolts is most likely hypothesis of their origin.

Nonlinear processes in low frequency bands were detected by means of the NChA-SAS3-R instrument, including two - and three-wave decay. The new type of "dovetail"

whistler previously observed during the Chibis M mission was confirmed.

Measurements of flux of electrons with energy of hundreds keV onboard the Vernov satellite indicate the formation of isolated quasi-stationary structures of sub-relativistic electrons in the gap between inner and outer belts even during very quiet periods.

The first reliable experimental estimations of anisotropy index ($A \sim 15$-20) for the fluxes of electrons with energy $E \sim 300$-600 keV at $L < 2.5$ were obtained from longitude and latitude variations in our experiment.

Our measurement of local structures of electrons with $E \sim 300$-600 keV at $L < 2.5$ that were formed during the storm on August 27, 2014.

REFERENCES

- Bell, T. F., V. P. Pasko, and U.S. Inan, Runaway electrons as a source of red sprites in the mesosphere, Geophys. Res. Leftt., 22, 2127 (1995)
- Bogomolov A.V., Denisov Yu.I., Kolesov G.Ya., Kudryavtsev M.I., Logachev Yu.I., Morozov O.V., and Svertilov S.I., Fluxes of Quasi-Trapped Electrons with Energies >0.08 MeV in the Near-Earth Space on Drift Shells L < 2, *Cosmic Res., 43 (5),* p. 307, 2005.
- Briggs et al. 2013, JGR, 118, 3805, doi:10.1002/jgra.50205.
- Briggs, M. S., Connaughton, V., Wilson-Hodge, C. et al. (2011), Electron-positron beams from terrestrial lightning observed with Fermi GBM, *Geophysical Research Letters*, *38*(2), doi:10.1029/2010GL046259.
- Cummer et al., GRL, 2014, doi:10.1002/ 2014GL062196
- Dwyer, J.R., Smith, D. M., and Cummer, S.A. (2012), High-energy atmospheric physics: Terrestrial gamma-ray flashes and related phenomena, Space Sci. Rev., 173, 133-196, doi: 10.1007/s11214–012-9894-0.
- Fisher J.R. Wether 45 451 (1990)
- Fishman, G.J., Bhat, P.N., Mallozzi, R., et al. (1994), Discovery of intense gamma-ray flashes of atmospheric origin, Science, 264(5163), 1313–1316, doi:10.1126/science.264.5163.1313.
- Gurevich, A.V., et. al., Phys. Lett., 2004
- Gurevich, A.V., Milikh, G.M., Roussel-Dupre, R. Runaway electron mechanism of air breakdown and preconditioning during a thunderstorm. Phys. Lett. A. 1992. V. 165, 463– 468.
- Klimov Stanislav, Csaba Ferencz, Laszlo Bodnar, Perter Szegedi, Perter Steinbach, Vladimir Gotlib, Denis Novikov, Serhiy Belyayev, Andrey Marusenkov, Orsolya Ferencz, Valery Korepanov, Jarnos Lichtenberger, Darniel Hamar. First results of MWC SAS3 electromagnetic wave experiment on board of the Chibis-M satellite. Advances in Space Research 54 (2014) 1717–1731
- Khartov V.V. Next step of automated spacecraft development for fundamental space research. Vestnik of S.A. Lasvochkin space corporation. 2011. N3, pp.3-11.
- Lehtinen, N. G., T. F. Bell, V. P. Pasko, and U.S. Inan, A two-dimensional model of runaway electron beams driven by quasi-electrostatic thundercloud fields, Geophys.Res.Lett., 24, 2639 (1997)
- Li, X., Selesnick, R. S., Baker, D. N., et al. (2015), Upper limit on the inner radiation belt MeV electron intensity, *J. Geophys. Res. Space Physics*, *120*, 1215-1228, doi: 10.1002/2014J020777.
- Lyons W.A. Geophys. Res. Lett. 21 875 (1994)
- Nagata, K., Kohno T., Murakami H. et al. (1988), Electron (0.19-3.2 MeV) and proton (0.58-35 MeV) precipitations observed by OHZORA satellite at low latitude zones L=1.6-1.8, Planet. Space Sci., 36, 591–606.
- Nemiroff, R.J., Bonnell, J.T., Norris, J.P. *J. Geophys. Res.* 102 9659 (1997) Orbitron http://www.stoll.pl
- Sadovnichy V. A., Panasyuk M. I., Yashin I. V. et al. Investigations of the space environment aboard the Universitetsky-Tat'yana and Universitetsky-Tat'yana-2 microsatellites // Solar System Research. 2011. V. 45. No. 1. P. 3–29.
- Shprits Y.Y., Elkington S.R., Meredith N.P., Subbotin D.A. (2008a), Review of modeling of losses and sources of relativistic electrons in the outer radiation belt I: Radial transport, J. Atmos. Sol. Terr. Phys., 70, 1679–1693.
- Shprits Y.Y., Subbotin D.A., Meredith N.P., Elkington S.R. (2008b), Review of modeling of losses and sources of relativistic electrons in the outer radiation belt II: Local acceleration and loss, J. Atmos. Sol. Terr. Phys., 70, 1694–1713.
- Vaughan O.H., Vonnegut B. J. Geophys. Res. 94 13179 (1989)

2015

5-th International TEPA Symposium
Thunderstorms and Elementary Particle Acceleration
October 5-9 | Nor Amberd | Aragatsotn Province | Armenia

Thundercloud electrodynamics and its influence on high-energy radiation enhancements and lightning initiation

E.A. Mareev[1], D.I. Iudin[1], V.A. Rakov[1, 2], A.Yu. Kostinskiy[1, 3], V.S. Syssoev[1, 4]

1. Institute of Applied Physics of the Russian Academy of Sciences, Nizhny Novgorod, Russian Federation;
2. Department of Electrical and Computer Engineering, University of Florida, USA;
3. National Research University Higher School of Economics, Moscow, Russian Federation;
4. High-Voltage Research Center of the All-Russia Institute of Electrical Engineering, Istra, Moscow region,
Russian Federation

Abstract. We analyze multi-scale dynamics of thunderstorm electric structure as related to high-energy radiation enhancements and lightning initiation. First, we review experimental data on the multi-layer charge structure of thunderstorm clouds. A special attention is paid to the lower positive charge region (LPCR) and its possible effects on the development of CG and IC discharges and thunderstorm ground enhancements (TGEs). Based on the graph theory, we have developed a fractal simulation code to examine the occurrence of lightning flashes of different type as a function of the cloud charge structure. We show in particular that presence of relatively intense lower positive charge region prevents the occurrence of negative CG flashes by "blocking" the progression of descending negative leader from reaching ground. Further, based on our recent observations of electrical discharges in the artificial cloud of charged water droplets, we present the description of a complex hierarchical network of interacting channels at different stages of development (some of which are hot and live for milliseconds), which can possibly be considered as a missing link in the still poorly understood lightning initiation process.

1. INTRODUCTION

The paper presents some results of experimental and theoretical studies illustrating a key role of thunderstorm electrodynamics in high-energy radiation enhancements and lightning initiation. The main attention is paid to the role of so-called lower positive charge region (LPCR) and recently discovered unusual plasma formations (UPF) in electrified cloud. Both phenomena can be substantial for lightning initiation. But first of all, we review some necessary information on the experimental data showing the complicated charge structure of thunderstorm clouds.

The gross charge structure of a "normal" thundercloud can be viewed as a vertical tripole consisting of three charge centers (regions), main positive at the top, main negative in the middle, and additional positive below the main negative [Krehbiel et al.(1986), Williams(1989)]. The model also includes a negative screening charge at the top of the cloud. The magnitudes of the main positive and negative charges are typically some tens to hundreds of coulombs, while the lower positive charge magnitude is considerably less. The negative charge region is apparently related to the − 10 to − 25°C temperature range, while the lower positive charge is typically found just below the freezing level, five or less kilometers above ground, depending on season and latitude.

It should be noted that the charge structure of real thunderstorm cloud is often far from idealized picture given above. Conceptual model of the electrical structure in mature, mid-latitude convection is presented in Fig.1.

Four main charge regions (with red + for positive charge, blue – for negative charge) are typically found in soundings through updrafts, while soundings outside updrafts have at least six charge regions in common. Representative electric field (E) and electrostatic potential (V) profiles in the nonupdraft (left) and updraft (right) of the convective region are also shown; the altitudes in these soundings do not correspond exactly to the conceptual model. Schematic representations of an intracloud flash (in

green) and a cloud-to-ground flash (in purple) are shown as they might appear in lightning mapping data [Stolzenburg and Marshall, 2009].
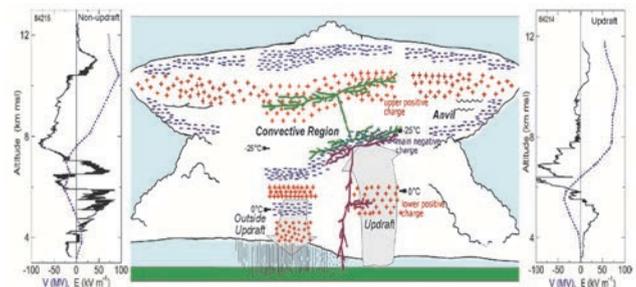

Figure 1. Conceptual model of the electrical structure in mature, mid-latitude convection.

2. MODELING OF LPCR AND ITS INFLUENCE ON LIGHTNING INITIATION

The presence of the LPCR (lower positive charge region, see Figure 1) is an essential feature of the cloud charge structure. Whatever the source of the LPCR [Rakov and Uman, 2003; Nag and Rakov, 2009], it is generally thought that it serves to enhance the electric field at the bottom of the main negative charge region and thereby facilitate the launching of a negatively-charged leader toward ground [Tessendorf et al., 2007; Nag and Rakov, 2009]. Also, it may play an important role in the facilitating of so-called Thunderstorm Ground Enhancements (TGEs), a sizable flux of electrons and gamma rays correlated with thunderstorms [Chilingarian et al., 2010, Chilingarian and Mkrtchyan, 2012]. Negative CG flashes produced by the model suggested in [Mansell et al., 2002] are consistent with the hypothesis that a lower positive charge region is critical for their development. On the other hand, the presence of excessive lower positive charge may prevent the occurrence of negative cloud-to-ground discharges by "blocking" the progression of descending negative leader from reaching ground [Qie et al., 2005]. The role of the

lower positive charge (LPC) as a potential well has been examined previously observationally [e.g., Coleman et al., 2008], statistically [e.g., Nag and Rakov, 2009] and in cloud model simulations [e.g., Mansell et al., 2010]. Coleman et al. [2008] examined potential profiles derived from electric field soundings to relate the relative strength of the LPC region to the amount of lightning channel branching and the time delay between initiation and ground contact. They found that a stronger LPC resulted in more branching and larger time delay, which makes sense from basic physics. Nag and Rakov [2009] developed the qualitative picture of the inferred dependence of lightning type on the magnitude of the lower positive charge region. Mansell et al. [2010] suggested that the electric potential of the channel could be a determining factor for whether a discharge reaches ground. Both of these results were based on complicated (real or simulated) configurations and could be nicely tested in a more controlled and methodical idealized setup.

We have developed a fractal simulation code to examine the detailed space and temporal evolution of the lightning discharges initiated at the main negative charge region and the corresponding structure of the electric field and potential in the cloud [Iudin et al., 2016]. We can demonstrate how changes in the cloud charge structure can facilitate development of lightning flashes of different type, paying the special attention to the role of the lower positive charge region.

Our model employs the four-layer charge structure described above and located above a flat, perfectly conducting ground plane, as illustrated in Figure 1. Each charge layer is assumed to have a cylindrically symmetric charge density distribution with Gaussian shape:

$$\rho_i = \rho_i(0) \cdot exp\left(-\left(\frac{z-z_i}{h_i}\right)^{2\alpha} - \left(\frac{r}{R_i}\right)^{2\alpha}\right), \quad (1)$$

where $\rho_i(0)$ is the volume charge density magnitude of the ith layer, z_i, h_i and R_i are its altitude, depth (thickness), and lateral extension (radius), respectively. The power exponent α determines the width w_ρ of transition zone from charge density magnitude $\rho_i(0)$ in the center of the layer to nearly zero value at the boundary of the computational domain; w_ρ $\sim R_i /\alpha$. In this paper, we use a relatively sharp transition zone with $\alpha = 4$. Similar to the characteristic time from cloud–to–ground lightning initiation to the return-stroke onset at ground of a few tens of milliseconds, the IC discharge formation characteristic time is some tens of milliseconds [Rakov and Uman, 2003]. Since this time is much shorter than the Maxwell relaxation time of the charges in the cloud and in the air, the conduction currents in the latter can be neglected. The electric potential $\phi(r)$ produced by a distribution of charges specified by the volume charge density $\rho(r)$ is obtained as a solution of the Poisson equation. In turn, the electric field vector $\mathbf{E}(r)$ is obtained from $\phi(r)$ as $\mathbf{E}(r) = -\nabla\phi(r)$.

Electric field lines produced by four charge layers, each described by equation (1), for three different charge configurations that are summarized in Table 1 (#1, #2, and #3), are shown in Figure 2 by cross-sectional views in the x–z plane at y = 0. The sets of parameters in Tables 1-3 are in agreement with observations and well correlate with those used by [Krehbiel et al., 2008].

Table 1. Parameters of different charge layers - configuration #1

Charge layer	Height, z, km	Depth, h, km	Radius, R, km	Charge density, ρ_0, $nC \cdot m^{-3}$	Charge, Q, C
NS	11	0.4	4	-0.77	-20
P	9.8	0.6	4	0.727	40
N	6.5	0.55	3	- 2.185	-60
LP	4.7	0.7	1.8	0.855	11

Table 2. Parameters of different charge layers - configuration #2

Charge layer	Height, z, km	Depth, h, km	Radius, R, km	Charge density, ρ_0, $nC \cdot m^{-3}$	Charge, Q, C
NS	11	0.4	4	-0.77	-20
P	9.8	0.6	4	0.727	40
N	6.5	0.55	3	- 2.185	-60
LP	4.7	0.7	1.8	0.967	12.5

Table 3. Parameters of different charge layers - configuration #3

| Charge layer	Height, z, km	Depth, h, km	Radius, R, km	Charge density, ρ_0, $nC \cdot m^{-3}$	Charge, Q, C
NS	11	0.4	4	-0.77	-20
P	9.8	0.6	4	0.727	40
N	6.5	0.55	3	- 1.82	-50
LP	4.7	0.7	1.8	1.32	17
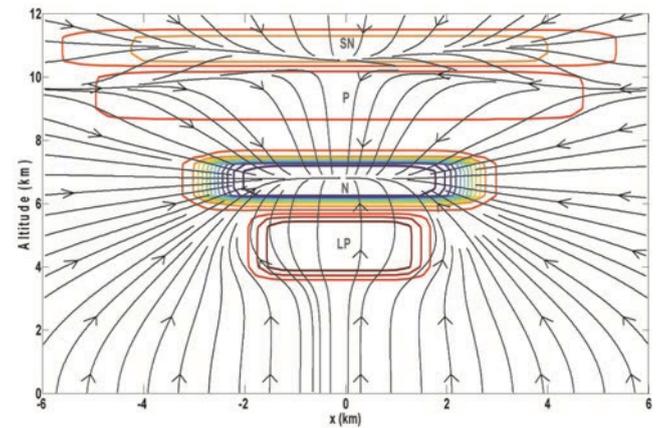
Figure 2. (a) A cross-sectional view in the x – z plane at y = 0 of the model thundercloud with negative screening (NS), main positive (P), main negative (N) and lower positive (LP) charge layers for charge configuration # 1. Electric field lines produced by the charges are also shown for reference.
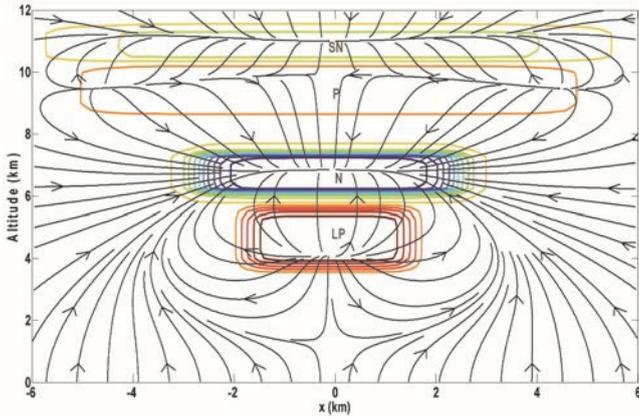
*Figure 2. (b) The same as in Figure 2(a), for charge configuration # 2.*
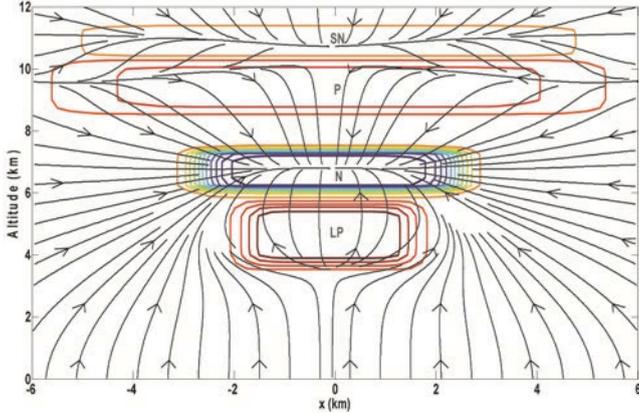
*Figure 2. (c) The same as in Figure 2(a), for charge configuration # 3.*
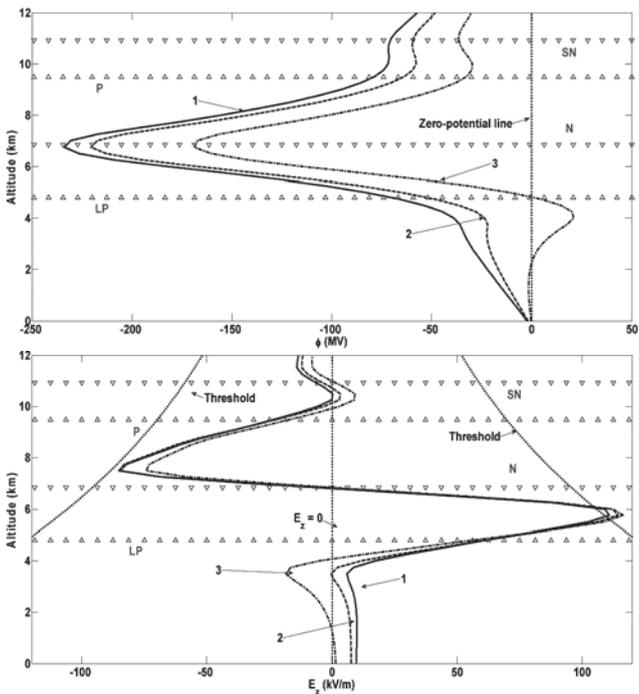
Figure 3. Electric potential (at the top) and z-component of electric field (at the bottom) before lightning discharge initiation. Curves 1, 2, and 3 correspond to 3 different cloud charge configurations that are summarized in Tables 1-3

Lightning discharge initiation starts with an electrical breakdown between two adjacent cells of the computational domain having the voltage drop (potential difference) that exceeds the breakdown value *Eith*. For an adequate description of the discharge tree dynamics, we introduce the physical time *t* that is discretized with model time steps. Each stage or step in the growth of the lightning structure between moment's *t* and *t* +1 corresponds to an interval of

physical time. Our calculations were made using = 50 μs. The discharge develops as a bidirectional leader from its parent pair of adjacent cells. Positive and negative leaders are propagated from opposite ends of the initial parent channel. Positive branches gather net negative charge and extending preferentially into and through regions of lower electric potential. Negative branches distribute negative charge and tend to propagate toward and through regions of net positive charge and higher electric potential.
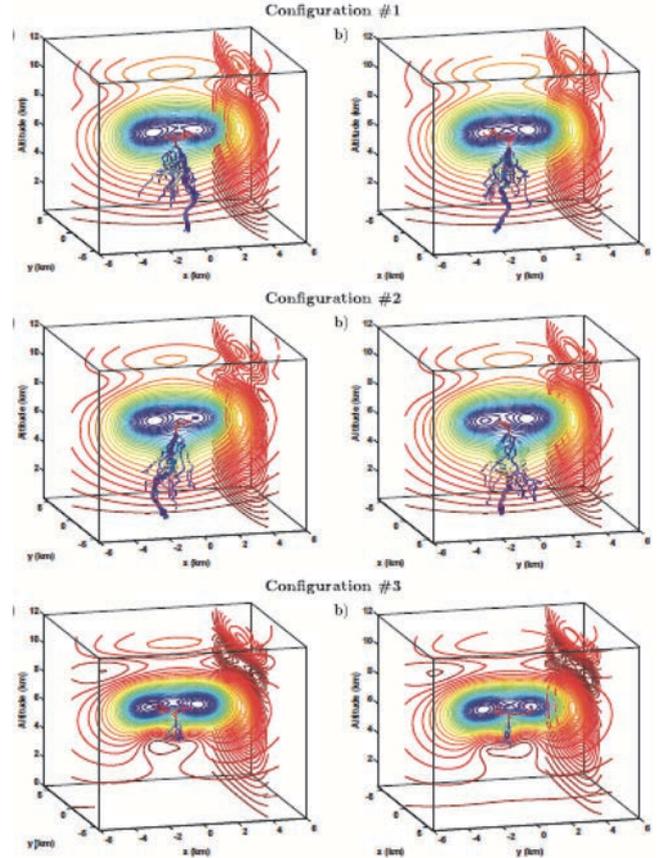

Figure 4. Three-dimensional views of model-predicted lightning discharges for three configurations (see Tables 1-3). We specify the viewpoint in terms of azimuth and elevation. The azimuth, (a) 75° and (b) 15°, is the horizontal rotation about the z-axis (labeled Altitude) measured in degrees with respect to the negative y-axis. Positive values indicate counterclockwise rotation of the viewpoint. The elevation of the viewpoint is 15°. Color-coded equipotentials are shown in each plot in two orthogonal planes: (a) x = 0 and y = 5 km and (b) x = 5 km and y = 0.

Fractal modeling arises as a phenomenological approach and thus our choice of critical fields and thresholds should be based on experimentally testable and reasonable estimations. The first spark can initiate discharges in neighboring pairs of cells with the electric field that is considerably smaller than the critical one (required for initiation of the first spark). Following Wiesmann and Zeller (WZ model) ideas we choose the electric field required for discharge propagation at sea level air pressure makes $E^{\pm}_{pth} = E^{+}_{pth} = E^{-}_{pth} = 50$ kV/m the same for both positive and negative directions. It is assumed that values $E^{\pm}_{pth}$ also vary proportionally to the neutral atmospheric density.

To take into account both the breakdown value E_{ith} and propagation threshold $E^{\pm}_{pth}$ we use the following weibullized distribution of the probability of the channel growth associated with candidate link i.

$$P^{\pm}\big(E(r_i)\big) = \begin{cases} 1 - exp\left\{-\left|\dfrac{E(r_i) - E^{\pm}_{pth}}{E_{ith}}\right|\right\}, & if\ E(r_i) \geq E^{\pm}_{pth} \\ 0, & if\ E(r_i) < E^{\pm}_{pth} \end{cases}$$

where r_i (i = 1,...N) is the candidate link position vector and m is a weibullized distribution index. For relatively small values of m (slowly increasing function P(E)), the probability of formation of several new segments from the streamer/leader tip is larger than that for rapidly in- creasing P(E). In the present study we use m = 1.

Most implementations of the WZ discharge model (including the most prominent one by Mansell et al. [2002]]) add only one new extension at a time and then update the potential of the surrounding grid for the effect of extending the conducting channel. In reality, growth may occur simultaneously on different branches or even come to a stop in development. Charge transfer dq along the lightning channels is proportional to the potential difference dj$i$ j across the link and obeys Ohm's law

$$\delta q = \tau \cdot I = \tau \cdot \sigma \cdot a^2 \frac{\delta \varphi_{ij}}{a_{ij}} = \tau \cdot \sigma E_{ij} \cdot a^2,$$

Here I is the current, t is the model time step, Ei j is the local electric field amplitude, s is the conductivity of the plasma channel, ai j is the channel length and a is the lattice spacing. The charge distribution on the discharge tree nodes obeys the continuity equation

$$\frac{\partial q}{\partial t} = \sum I,$$

where the right-hand term denotes the algebraic sum of all the currents I that flow in and flow out the node. The variation in the channel conductivity s is determined by the balance between the production and dissipation of Joule heat in the plasma lightning channel. As a first approximation, it is assumed that the increase in the channel conductivity is directly proportional to the energy release, i.e.

$$\frac{\partial \sigma}{\partial t} = \eta(E^2 - E_0^2) \cdot \sigma + \eta E_0^2 \sigma_0(z),$$

where h is the growth rate parameter for the conductivity and dissipation critical level is determined by plasma channel internal field threshold.

Figure 4 shows examples of fully developed discharges for the three different cloud charge configurations. The simulated discharge is initiated at an altitude of 5.9 km above ground level, where the maximum electric field (exceeding the breakdown value) is achieved (see Fig. 3b). Figures 3a and 3b compare, respectively, the total electric field and potential at the center of the simulation domain, along the vertical axis before and after the flash for the three cloud charge configurations presented in Figure 2 and summarized in Tables 1-3 (configurations #1, #2, and #3). The altitude of each new discharge tree node that gives rise to more than three new links (channel segments) is plotted in Figure 6 versus time represented by model steps. Our simulations show that the characteristic time of CG discharge formation gradually in- creases with increasing the lower positive charge density (compare the LP rows in Tables 1-2 for configurations #1, and #2). The dying out of nodes with incident links is a unique feature of the model compared to the previous cellular automata models that account for discharge tree extension only [Dulzon et al.(1999), Petrov and Petrova(1995), Riousset et al.(2007) , Krehbiel et al.(2008)]. This feature allows us to include the difference between sreamer and leader velocities.

Figures 4a and 4b show that, when LPCR is relatively weak, the altitude of negative part of discharge rapidly decreases leading in either case to a negative CG flash. On the contrary, Figure 4c demonstrates that the presence of relatively large (excessive) LPCR prevents the occurrence of

negative CG flash by "blocking" the progression of descending negative leader from reaching ground. Statistically, this "blocking" effect occurs when a negative potential well at the cloud bottom is present and the electric field at the cloud bottom is negative, as opposed to being positive or zero for configurations #1 and #2, respectively, as seen in Figure 2. Next, starting with configuration #2 we show that the LPCR "blocking" effect can be achieved by slightly changing the geometrical parameters, while keeping the charge magnitudes the same. Note that changes in the dimensions of the cloud charge regions lead to changes in their charge densities. When the LPCR radius decreases and its depth increases in such a way that its charge density increases, a negative potential well at the cloud bottom appears again, and the electric field at the cloud bottom changes polarity. Such a configuration change prevents the progression of descending negative leader from reaching ground and leads to an IC flash, in contrast with configuration #2 that leads to a negative CG flash. Conversely, when both the LPCR radius and its depth increase in such a way that its charge density appreciably decreases, the magnitude of electric field between the main negative and lower positive charge layers falls below the threshold level (see Figure 3b). We observed that a noticeable depletion of the lower positive charge density eliminates the possibility of negative CG flashes and leads to IC flashes between main positive and main negative charge layers instead. Figures 3a and 3b show the total potential and electric field, respectively, before the discharge initiation at the center of the simulation domain, along the vertical axis for three different cloud charge configurations that are summarized in Tables 1-3. It is clear from the previous analysis that the dynamics of thunderstorm cloud at the stage preceding a lightning discharge, are very sensitive to the cloud electrical structure, so that even minor changes in the geometrical parameters and charge magnitudes can lead to significant alteration of discharge activity, including its fine structure and LCPR "blocking" effect. This observation illustrates once again that the thunderstorm cloud is a good example of self-organized criticality. Our model is capable of reproducing such a behavior and, moreover, finding quantitative criteria for the prediction of the discharge development based on available experimental data. On the other hand, the model is in need of further elaboration to include the processes responsible for the formation of the cloud charge structure, such as corona beneath the cloud and charging currents inside the cloud.

3. UNUSUAL PLASMA FORMATIONS FORMING A HIERARCHICAL NETWORK OF CHANNELS IN CLOUDS

We have observed unusual plasma formations (UPFs) in artificial clouds of charged water droplets using a high-speed infrared camera operating in conjunction with a high-speed visible-range camera [Kostinskiy et al., 2015]. Inferred plasma parameters were close to those of long-spark leaders observed in the same experiments, while the channel morphology was distinctly different from that of leaders, so that UPFs can be viewed as a new type of in-cloud discharge. These formations appear to be manifestations of collective processes building, from scratch, a complex hierarchical network of interacting channels at different stages of development (some of which are hot and live for milliseconds). We believe that the phenomenon should commonly occur in thunderclouds and might give invites on the

missing link in the still poorly understood lightning initiation process.

We used (a) artificial clouds of negatively charged water droplets with an average radius of 0.3–0.5 μm and (b) an infrared (IR) camera sensitive in the wavelength range of 2.7–5.5 μm to "see" what happens inside the cloud. We are not aware of any previous IR observations of electric discharges. Our cloud (10–15 m^3 in size), when negatively charged, is capable of drawing long sparks from nearby grounded objects and, hence, can be viewed as a model of some natural charged aerosol systems. Our unique combination of cloud parameters (relatively small droplet size) and relatively long recorded wavelengths allowed us to observe a new class of in-cloud plasma formations, both in the presence and in the absence of sparks between the cloud and nearby grounded sphere. In our experiments, typically the best images of these unusual plasma formations are obtained when a spark is formed nearby. For this reason, most of the presented images correspond to this latter kind of the phenomenon.

Fig. 5a and 5b show two consecutive frames taken by the IR camera viewing the upper part of cloud (the lower frame boundary was about 70 cm above the grounded plane). All the discharge processes seen in these frames were hidden inside the cloud and, hence, were not imaged in the visible range (only flashes of scattered light were observed). Each frame had 6.7 ms exposure and 2ms dead time, so that the two images could be separated in time by 2 to 15.4 ms. It follows that most of the discharge processes recorded in the two frames were visible in IR for at least 2 ms. The processes seen in the IR images include (1) the upper, in-cloud part of the upward positive leader from the grounded sphere, whose lower part, developing in clear air, was outside the field of view of the IR camera; (2) a large streamer zone, crossing each frame from the lower right to the upper left corner (presumably positive corona from the upward positive leader channel, including its branches that are outside the camera field of view); and (3) unusual plasma formation (UPF) that is the focus of this paper. Both the imaged part of upward positive leader and the UPF appear to be inside or in the immediate vicinity of the streamer zone. The upward positive leader current had a peak of 5 A, lasted 35 μs, and transferred 15 μC of charge. No return-stroke-type process was observed. This UPF was formed as early as within 1.4 μs of the initial corona burst from the grounded sphere.

It is clear from Fig. 5 that the UPF is very different from either the upward positive leader or the streamer zone. Its brighter parts are much (an order of magnitude) brighter than streamers. Further, in Fig. 5a, the intensity of the IR radiation coming from some elements of UPF is similar to that coming from the hot upward-leader channel (this was determined both visually and quantitatively, using image analysis software). On the other hand, UPF morphology (a complex network of channels pervading a relatively large cloud region) does not resemble that of leader (main channel with branches indicating its direction of propagation and streamer zones at its extremities). In Fig. 5b, the UPF radiates even stronger than the decaying upward leader channel.
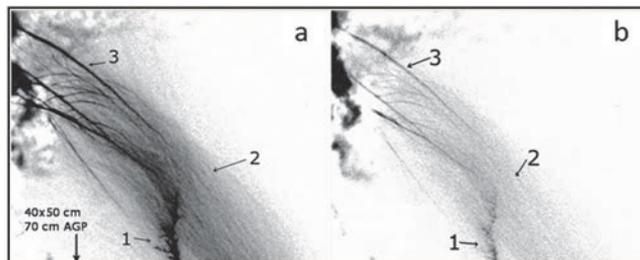

Figure 5. Two consecutive infrared images (negatives) obtained with 6.7 ms exposure and separated by 2ms that show various discharge processes inside the cloud. Only flashes of scattered light, as opposed to distinct channels, were observed during this event in the visible range. 1: upper part of the upward positive leader (its lower part, developing in clear air, is outside the field of view of the IR camera), 2: streamer zone, 3: unusual plasma formation (UPF). AGP stands for "above the grounded plane."

The IR images of UPF shown in Fig. 5a and 5b are typical in the presence of upward positive leader from the grounded sphere entering a negatively charged cloud. More than 100 of such events have been recorded to date. We observed that UPFs can take different forms and occur in different contexts, essentially anywhere in the cloud and in its immediate vicinity, with or without a spark discharge (Figure 6). In Figure 7, we show an example of simultaneous IR and rare visible-range images of the same UPF inside the cloud.
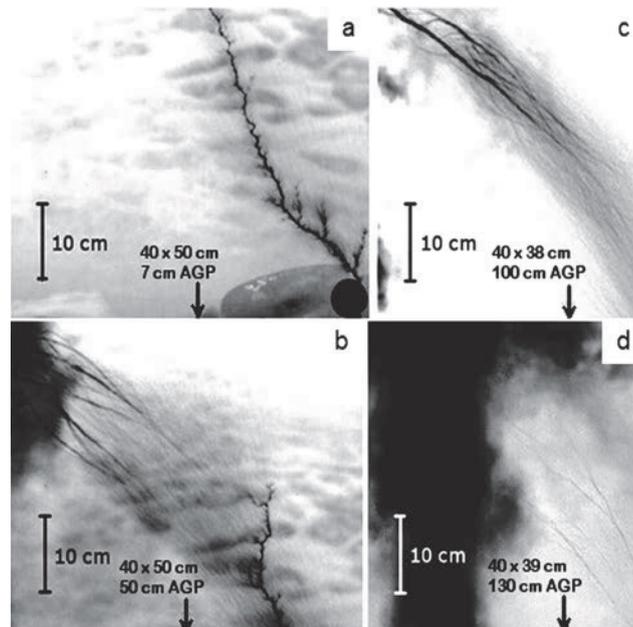

Figure 6. Infrared images (negatives) obtained with 6.7 ms exposure that show the processes at different heights above the grounded plane (AGP) and different horizontal distances from the cloud axis: (a) The upward positive leader from the grounded sphere. No UPF is seen. (b) The upper part of the upward positive leader (bottom right) and UPF (top left), both inside the cloud. The two appear to be distinct discharge processes which interact, via their streamer zones. Relative to Figure 5a, the field of view of the IR camera was moved up and left (closer to the axis of the cloud). (c) The lower part of UPF (inside the cloud). The upward positive leader is outside the IR camera field of view, which was moved (relative to Figure 5b) further up and left. The upward positive leader and the UPF apparently interact (outside of the field of view) via their streamer zones. (d) Same as Figure 5c, but for the upper part of UPF near the central part of the cloud (see the dark formation on the left). Note that relatively faint UPF channels branch toward the axis of the cloud, but do not cross the axis This direction of branching is opposite to that seen in Figure 5c, suggesting that UPFs extend bidirectionally.
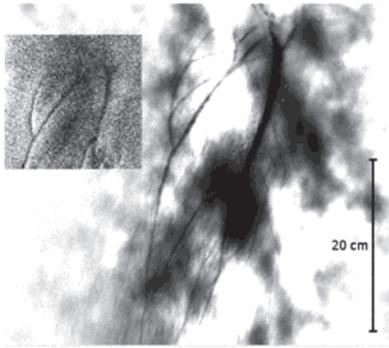
Figure 7. Simultaneous IR (right) and visible-range (left) images of UPF inside the cloud. The latter (smaller) image corresponds to a fragment of the former, but main features of the IR image are clearly identifiable in the visible-range one. Exposure time of the IR camera was 8 ms vs. 1 μs for the visible-range camera. Note the much greater level of detail provided by the IR camera. IR image size: height – 40 cm, width – 50 cm; visible-range image size: height – 25 cm, width – 28 cm. The lower IR frame boundary was about 100 cm above the grounded plane. The lower visible-range frame boundary was about 120 cm above the grounded plane. It can be seen that the contours of the brightest UPFs are similar in both images.

Based on our analysis, we conclude that the brightness of the IR images of UPFs reasonably represents the final gas temperature, which is reached as a result of the discharge process (leaving aside the issue of their size, since the brightness of optically thin objects is proportional to their spatial extent along the line of sight). A more detailed analysis of the air vibrational kinetics during the entire discharge process (including afterglow), needed for determination of quantitative relationship between the intensity of the IR radiation and the final gas temperature, is in progress.

The UPF often involves multiple and more or less parallel channels of relatively high brightness that are repeatedly interconnected by a great variety of fainter channels or branches. As a result, the overall structure of UPF looks like a network of channels of irregularly varying brightness, which pervade a relatively large cloud region, in contrast with leaders which have a main channel with branches indicating its direction of propagation, more of less regularly varying brightness, and streamer zones at its extremities. Thus, the morphology of UPFs is distinctly different from that of leaders. Further, the secondary channels often appear to originate from and terminate on different points of the same trunk or originate from a common point in space and terminate on a neighboring channel, forming kind of loops or splits in the overall channel structure. The latter behavior has never been observed in leaders. Based on the above, we conclude that UPF is a unique phenomenon, distinctly different from leader. Further, IR brightness of streamers in spark discharges differs substantially from that of leader, and a rather sharp boundary between the bright leader channel and the weakly glowing streamer zone is observed. In contrast, UPFs typically exhibit a more gradual change of luminosity along the channel (compare, for example, Figures 6a (leader) and 6c (UPF)).

We conclude with a brief discussion of some implications of our observations of UPFs in artificial clouds of charged water droplets for the improving of our understanding of lightning initiation process in thunderclouds. The lightning initiation mechanism remains a mystery, but researchers agree that it must involve the creation of a relatively large ionized region ("lightning seed") in the cloud that is capable of locally enhancing the electric field at its extremities. Such field enhancement is likely to be the main process leading to the formation of a hot, self-propagating

lightning leader channel. In our opinion, it is possible that UPFs are the key to understanding the "lightning seed" formation mechanism. Indeed, UPFs appear to be manifestations of collective processes building, from scratch, a complex hierarchical system of interacting channels at different stages of development, some of which are hot and live for at least a few milliseconds. In fact, it is possible that a UPF (a network of electrically floating plasma channels interacting with each other via positive and negative streamers) can serve to "metalize" a region of thundercloud, as described by Iudin et al. [2003], thereby creating a "seed" needed for lightning initiation. The basis for our speculation/prediction regarding UPF's being possibly the missing link in the lightning initiation process is the fact that UPFs (1) occurred in charged cloud regions that did not previously host any other discharge activity and (2) contained hot channel segments in their overall network-like structure, while being distinctly different in their morphology from leaders. We believe that such formations can be an intermediate stage between virgin air (in the presence of water droplets) or initial low-conductivity streamer and a hot, self-propagating leader channel, provided that the hot segments of UPF can get polarized and grow within its overall channel network pervading a relatively large cloud volume.

ACKNOWLEDGEMENTS

REFERENCES

- Chilingarian, A., Daryan, A., Arakelyan, K., et al., (2010), Ground-based observations of thunderstorm-correlated fluxes of high-energy electrons, gamma rays, and neutrons. Phys. Rev. D 82, 043009.
- Chilingarian, A., Mkrtchyan, H., (2012), Role of the lower positive charge region (LPCR) in initiation of the thunderstorm ground enhancements (TGEs). Phys. Rev. D: Part. Fields 86, 072003.
- Coleman, L. M., M. Stolzenburg, T. C. Marshall, and M. Stanley (2008), Horizontal lightning propagation, preliminary breakdown, and electric potential in New Mexico thunderstorms, J. Geophys. Res., 113, D09208, doi: 10.1029/2007JD009459.
- Dulzon, A. A., Lopatin V. V., Noskov M. D. and Pleshkov O. I., 1999, Modelling the development of the stepped leader of a lightning discharge, J. Tech. Phys. 3948 (Translated from Russian 1999 Zh. Tech. Fiz. 69(4) 4853).
- Iudin, D.I., V. A. Rakov, E. A. Mareev, F. D. Iudin, and A. A. Syssoev, Thundercloud lower positive charge region and lightning type: A study based on a cellular automata model, J. Geophys.Res. Atmos., 2016 (submitted).
- Iudin, D. I., V. Y. Trakhtengerts, M. Hayakawa (2003), Fractal dynamics of electric discharges in a thundercloud, Phys. Rev. E, 68(1), 016601, doi:10.1103/PhysRevE.68.016601.

- Kostinskiy, A. Y., V. S. Syssoev, N. A. Bogatov, E. A. Mareev, M. G. Andreev, L. M. Makalsky, D. I. Sukharevsky, and V. A. Rakov (2015), Infrared images of bidirectional leaders produced by the cloud of charged water droplets, J. Geophys. Res. Atmos., 120, doi: 10.1002/2015JD023827.
- Kostinskiy, A. Y., V. S. Syssoev, N. A. Bogatov, E. A. Mareev, M. G. Andreev, L. M. Makalsky, D. I. Sukharevsky, and V. A. Rakov (2015), Observation of a new class of electric discharges within artificial clouds of charged water droplets and its implication for lightning initiation within thunderclouds, Geophys. Res. Lett., 42, 8165–8171, doi: 10.1002/2015GL065620.
- Krehbiel, P.R., J.A. Riousset, V.P. Pasko, R.J. Thomas, W. Rison, M.A. Stanley and H.E. Edens, Upward electrical discharges from thunderstorms // 2008, Nature, doi:10.1038/ngeo162.
- Mansell, E. R., C. L. Ziegler, and C.E. Bruning, Simulated Electrification of a Small Thunderstorm with Two-Moment Bulk Microphysics, J.Atm.Sci., 2010, V.67, p.171-194.
- Mansell, E. R., C. L. Ziegler, and C.E. Bruning, Simulated three-dimensional branched lightning in a numerical thunderstorm model, Journal of Geophysical Research, Vol. 107, NO. D9, 4075, 10.1029/2000JD000244, 2002.
- Nag, A., and V. A. Rakov, Some inferences on the role of lower positive charge region in facilitating different types of lightning, Geophysical Research Letters, VOL. 36, L05815, doi:10.1029/2008GL036783, 2009.
- Petrov, N. I., and Petrova G. N., 1995, Mathematical modeling of the trajectory of a leader discharge and the vulnerability to lightning of isolated and grounded objects // J. Tech. Phys. 40 42736 (Translated from Russian 1995 Zh. Tech.Fiz. 65 4158).
- Qie, X., T. Zhang, C. Chen, G. Zhang, T. Zhang, and W. Wei (2005), The lower positive charge center and its effect on lightning discharges on the Tibetan plateau, Geophys. Res. Lett., 32, L05814, doi: 10.1029/ 2004GL022162.
- Rakov, V. A., and M. A. Uman (2003), Lightning: Physics and Effects, Cambridge Univ. Press, New York.
- Riousset, J.A., V.P. Pasko, Krehbiel P.R., R.J. Thomas, W. Rison, Three dimensional fractal modelling of intracloud lightning discharge in a New-Mexico thunderstorm and comparison with lightning mapping observations, J. Geophys Res., 2007, V112, D15203, doi:10.1029/2006JD007621.
- Stolzenburg, M., and T.C. Marshall (2009), Electric Field and Charge Structure in Lightning-Producing Clouds, in Lightning: Principles, Instruments and Applications, Eds. H.Betz, U, Schumann, and P.Laroche, p. 57-82.
- Tessendorf, S. A., S. A. Rutledge, and K. C. Wiens (2007), Radar and lightning observations of normal and inverted polarity multicellular storms from STEPS, Mon. Weather Rev., 135, 3682- 3706, doi:10.1175/2007MWR1954.1.
- Williams, E.R., The tripole structure of thunderstorm, J. Geophys.Res., 94 (D11), 13,151–13,167, 1989.

2015

5-th International TEPA Symposium
Thunderstorms and Elementary Particle Acceleration
October 5-9 | Nor Amberd | Aragatsotn Province | Armenia

List of participants

|		
1	Evgeny Mareev, Institute of Applied Physics of the RAS, Nizhny Novgorod, Russian Federation	evgeny.mareev@gmail.com
2	Svertilov Sergey, SINP Moscow State University, Moscow, Russian Federation	lidvansk@lebedev.ru
3	Alexander Lidvansky, Institute for Nuclear Research, RAS, Moscow, Russian Federation	lidvansk@lebedev.ru
4	Gali Garipov, SINP Moscow State University, Moscow, Russian Federation	ggkmsu@yandex.ru
5	Yo Kato, The University of Tokyo, Tokyo, Japan	ykato0310@hotmail.co.jp
6	Michael Briggs, University of Alabama in Huntsville, Alabama, Huntsville, United States	briggsms@uah.edu
7	Nicole Kelley, University of California, Berkeley; Berkeley, United States	nkelley@ssl.berkeley.edu
8	Leonid Sorokin , Peoples' Friendship University of Russia, Moscow, Russian Federation	leonid.plasma@gmail.com
9	Alexei Pozanenko, Space Research Institute (IKI), Moscow, Russian Federation	apozanen@iki.rssi.ru
10	Vitaly Bogomolov, Moscow State University, Moscow, Russian Federation	vit_bogom@nm.ru
11	Alain Sarkissian, LATMOS / CNRS / UVSQ, Guyancourt, France	alain.sarkissian@free.fr
12	Meftah Mustapha, CNRS – LATMOS, Guyancourt, France	mustapha.meftah@latmos.ipsl.fr
13	Johannes Knapp, DESY, Berlin, Germany	johannes.knapp@desy.de
14	Hartmut Gemmeke, IPE, KIT, Karlsruhe, Germany	hartmut.gemmeke@kit.edu
15	Mikhail Khaerdinov, Institute for Nuclear Research of the RAS, Moscow, Russian Federation	khaerdinovmn@gmail.com
16	Ashot Chilingarian, Yerevan Physics Institute, Yerevan, Armenia	chili@aragats.am
17	Eduard Mnatsakanyan, Yerevan Physics Insitute, Armenia	eduardmnats@gmail.com
18	Hripsime Mkrtchyan, Yerevan Physics Institute, Yerevan, Armenia	hripsime@yerphi.am
19	Lev Kozliner, Tel-Aviv University, Israel	lkozliner@mail.ru
20	Tigran Karapetyan, Yerevan Physics Institute, Yerevan, Armenia	ktigran79@yerphi.am
21	Yeghia Khanikyants, Yerevan Physics Insitute, Yerevan, Armenia	khanikync@yerphi.am
22	Suren Soghomonyan, Yerevan Physics Insitute, Yerevan, Armenia	surensog@gmail.com
23	David Pokhsraryan, Yerevan Physics Institute, Yerevan, Armenia	davitpo@gmail.com
24	Harut Dermenjyan, Yerevan Physics Institute, Yerevan, Armenia	h.dermenjyan@gmail.com
25	Suren Hovakimyan, Ministry of Territorial Administration of the RA, Ashtarak, Armenia	suren.hovakimyan@gmail.com
26	Haik Avdishyan, Yerevan Physics Institute, Yerevan, Armenia	h.avdishyan@gmail.com
27	Gagik Hovsepyan, Yerevan Physics Institute, Yerevan, Armenia	hgg@yerphi.am
28	Arsen Ghalumyan, Yerevan Physics Institute, Yerevan, Armenia	ghalumyan@yandex.ru
29	Hovik Bagdasarya, Armenian State Technical University, Yerevan, Armenia	hovik_b@yahoo.com
30	Zaruhi Asaturyan, Yerevan Physics Institute, Yerevan, Armenia	zara@mail.yerphi.am

# High-energy Physics in Atmosphere: Particle fluxes and lightnings at Aragats

http://crd.yerphi.am/Conferences/tepa2015/home